

Washington University in St. Louis

Washington University Open Scholarship

All Theses and Dissertations (ETDs)

5-24-2009

Design and Synthesis of Nanomaterials for Surface-Enhanced Raman Scattering, Fuel Cell Technology, and Photonics

Pedro Camargo

Washington University in St. Louis

Follow this and additional works at: <https://openscholarship.wustl.edu/etd>

Recommended Citation

Camargo, Pedro, "Design and Synthesis of Nanomaterials for Surface-Enhanced Raman Scattering, Fuel Cell Technology, and Photonics" (2009). *All Theses and Dissertations (ETDs)*. 883.

<https://openscholarship.wustl.edu/etd/883>

This Dissertation is brought to you for free and open access by Washington University Open Scholarship. It has been accepted for inclusion in All Theses and Dissertations (ETDs) by an authorized administrator of Washington University Open Scholarship. For more information, please contact digital@wumail.wustl.edu.

WASHINGTON UNIVERSITY IN ST. LOUIS

School of Engineering
Department of Biomedical Engineering

Dissertation Examination Committee:

Younan Xia, Chair

Donald Elbert

Lihong Wang

Jin-Yu Shao

Da-Ren Chen

Sophia Hayes

DESIGN AND SYNTHESIS OF NANOMATERIALS FOR SURFACE-ENHANCED RAMAN
SCATTERING, FUEL CELL TECHNOLOGY, AND PHOTONICS

By

Pedro Henrique Cury Camargo

A dissertation presented to the
Graduate School of Arts and Sciences
of Washington University in
partial fulfillment of the
requirements for the degree
of Doctor of Philosophy

August 2009

Saint Louis, Missouri

copyright by
Pedro Henrique Cury Camargo
2009

ABSTRACT OF THE DISSERTATION

Design and Synthesis of Nanomaterials for Surface-Enhanced Raman Scattering, Fuel

Cell Technology, and Photonics

by

Pedro Henrique Cury Camargo

Doctor of Philosophy in Biomedical Engineering

Washington University in St. Louis, 2009

Professor Younan Xia, Chairperson

In the first part of my dissertation, I developed two approaches for selectively probing the SERS activities of individual hot spots, i.e., experimentally detect the SERS signals only for the molecules that are trapped within the hot-spot region in individual Ag nanoparticle dimers. Then, I performed a systematic investigation on the SERS activity of individual dimers composed of two closed spaced Ag nanoparticles. By utilizing Ag nanoparticles displaying a variety of well-defined shapes, sizes and orientations to construct the dimers, I were able to precisely correlate the detected SERS signals to the specific geometry of individual hot spots.

In the second part of this dissertation, I performed a systematic investigation on the galvanic replacement reaction between PtCl_6^{2-} and Pd nanocrystals with well-defined shapes including octahedra, nanocubes, and nanorods. The resultant hollow Pd-Pt bimetallic nanostructures were employed as electrocatalysts for the oxygen reduction reaction (ORR). Our results demonstrated that the nanostructures derived from Pd

octahedra displayed the highest ORR activity, being 1.7 times more active based on equivalent Pt mass than the commercial Pt/C. I also conducted a mechanistic study on the galvanic replacement reaction between AuCl_4^- and Pd nanorods. Differently from the Pd-Pt system, a new type of hybrid nanostructure in the tadpole shape consisting of a Au head and a Pd tail was obtained due to a localized galvanic replacement mechanism. As an extension of my work to develop new electrocatalysts for the ORR, a template-engaged reaction was utilized for the synthesis of $\text{RuSe}_{2+\delta}$ nanotubes. The $\text{RuSe}_{2+\delta}$ nanotubes were active towards the ORR and displayed no loss in activity in the presence of methanol, as opposed to commercial Pt/C.

Finally, the template-engaged reaction was applied to the synthesis of $\text{Se}@M\text{Se}$ ($M = \text{Zn}, \text{Cd}$ or Pb) colloidal spheres having similar sizes but different compositions. They were utilized as building blocks to obtain 3D photonic crystals via self-assembly. Moreover, superparamagnetic properties could be obtained via the incorporation of Fe_3O_4 nanoparticles into the α -Se cores. Taken together, this represents a versatile approach to the synthesis of magnetoactive spheres with similar dimensions but a variety of compositions and properties.

ACKNOWLEDGMENTS

First and foremost, I would like to thank my academic advisor Professor Younan Xia. I would like to express my deepest gratitude and appreciation for his tutelage and patience. His enthusiasm, perseverance and hard-work are motivational and have inspired me to become a better scientist. I would like to thank Dr. Dong Qin for her friendship, support and advice during my study. I am grateful to Prof. Hong Yang and Zhenmeng Peng at the University of Rochester for the collaboration in part of this work. I would like to demonstrate my special recognition to Eric Lee, Dr. Xianmao Lu, Dr. Leslie Au and Dr. Jesse McCann, whose friendship and help I will never forget. I would like to express my acknowledgement and appreciation to all past and current members of the Xia group, in particular Dr. Byungkwon Lim, Majiong Jiang, Young Hwan Lee, Dr. Unyong Jeong, Dr. Yujie Xiong, Dr. Jingyi Chen, Dr. Eric Formo, Dr. Eun Chul Cho, Claire Copley, Matthew Rycenga, Dr. Jingwei Xie, Weiyang Li, Dr. Joseph McLellan, Dr. Ben Wiley, Xiaoran Li, Dr. Alex Briseno, Maureen McKiernan, Dr. Meng-Yi Bai, Dr. Sung-Wook Choi, Dr. Hirokazu Kobayashi and Dr. Marta Ibisate. I would like to express my gratitude to Prof. Frank Yin for his help during my transfer to WashU and all the staff in the BME department, in particular, Glen Reitz, Lori Williams and Karen Teasdale. I am grateful to Prof. Michael Heinekey and Nectaria Llywelyn from the Chemistry Department at UW for their assistance and help during the beginning of my Ph.D. study in the US.

I would like to express my gratefulness and appreciation to my family, especially my Mother and Grandmother, for their endless love, understanding and support. I would like to thank the Brazilian Government (CAPES - Ministry of Education) and the Fulbright Foundation for providing me with a scholarship and opportunity to conduct my Ph.D. study in the US. Finally, I would like to thank all the staff at CAPES, the Fulbright Foundation office in Brazil and the International Institute of Education (IIE) for their assistance and handling the paperwork/logistics during my study.

DEDICATION

To my family and friends

“The real voyage of discovery consists not in seeking
new landscapes but in having new eyes”

Marcel Proust

TABLE OF CONTENTS

	Page
List of Figures.....	ix
Abstract	ii
Chapter 1. Introduction.....	1
1.1. Nanoscience and Nanomaterials.....	1
1.2. Surface-Enhanced Raman Scattering.....	2
1.3. Direct Methanol Fuel Cells.....	6
1.4. Photonic Crystals.....	8
1.5. Synthesis of Nanomaterials: the Template-Directed Approach.....	9
1.6. Scope of This Work.....	11
1.7. Notes to Chapter 1.....	15
Chapter 2. Dimers of Silver Nanoparticle as Substrates for SERS: Probing the SERS Acitivity for Hot Spots Formed between Two Closely Spaced Nanoparticles.....	20
2.1. Introduction.....	20
2.2. Probing the Enhancement Factor for the Hot Spots Formed in Dimers of Silver Nanospheres.....	22
2.2.1. Results and Discussion.....	22
2.2.2. Summary.....	24
2.3. Isolating and Probing the Hot Spots Formed between Two Silver Nanocubes.....	25
2.3.1. Results and Discussion.....	26
2.3.2. Summary.....	34
2.4. Measuring the SERS Enhancement Factors of Hot Spots Formed between an Individual Ag Nanowire and a Single Ag Nanocube.....	35
2.4.1. Results and Discussion.....	36
2.4.2. Summary.....	45

2.5. Measuring the SERS Enhancement Factors for Hot-Spots with Different Morphologies in Dimers Consisting of Ag Nanospheres and Nanocubes.....	46
2.5.1. Results and Discussion.....	48
2.5.2. Summary.....	55
2.6. Experimental Section.....	57
2.7. Notes to Chapter 2.....	92
Chapter 3. A Mechanistic Study of the Galvanic Replacement Reaction between PtCl_6^{2-} and Pd Nanocrystals Enclosed by Different Facets.....	96
3.1. Introduction.....	96
3.2. Results and Discussion.....	99
3.3. Summary.....	110
3.4. Experimental Section.....	112
3.5. Notes to Chapter 3.....	126
Chapter 4. Facile Synthesis of Tadpole-Like Nanostructures Consisting of Au Heads and Pd Tails.....	130
4.1. Introduction.....	130
4.2. Results and Discussion.....	131
4.3. Summary.....	134
4.4. Experimental Section.....	135
4.5. Notes to Chapter 4.....	144
Chapter 5. Synthesis and Application of $\text{RuSe}_{2+\delta}$ Nanotubes as a Methanol Tolerant Electrocatalyst for the Oxygen Reduction Reaction.....	146
5.1. Introduction.....	146
5.2. Results and Discussion.....	149
5.2.1. Synthesis of $\text{RuSe}_{2+\delta}$ Nanotubes.....	149
5.2.2. Evaluation of Electrochemical Performance.....	150
5.3. Summary.....	156
5.4. Experimental Section.....	157

5.5. Notes to Chapter 5.....	165
Chapter 6. Cation-Exchange: A Simple and Versatile Route to Inorganic Colloidal Spheres with the Same Size but Different Compositions and Properties.....	169
6.1. Introduction.....	169
6.2. Results and Discussion.....	171
6.2.1. Synthesis of a-Se and Se@Ag ₂ Se Monodispersed Colloidal Spheres	171
6.2.2. Synthesis of Se@MSe (M=Zn, Cd, Pb) Colloidal Spheres via Cation-Exchange Reactions.....	173
6.2.3. Crystallization of MSe (M=Zn, Cd, Pb) Hollow Spheres.....	178
6.2.4. Synthesis of Superparamagnetic Colloidal Spheres of Fe ₃ O ₄ /Se, (Fe ₃ O ₄ /Se)@Ag ₂ Se, and (Fe ₃ O ₄ /Se)@CdSe.....	181
6.3. Summary.....	184
6.4. Experimental Section.....	185
6.5. Notes to Chapter 6.....	199
Bibliography.....	202

LIST OF FIGURES

Figure Number	Page
1.1. Electromagnetic field enhancement contours calculated for a dimer composed of two Ag nanospheres.....	12
1.2. Schematic representation of a direct methanol fuel cell.....	13
1.3. Schematic illustration of photonic crystals.....	14
2.1. (A) SERS spectra from a dimer of silver nanospheres, two silver nanospheres separated by ~600 nm, and a single silver nanosphere. (B) Approach for the calculation of the field-enhancement from a hot spot.....	63
2.2. SERS spectra from a dimer of silver nanospheres with different orientations relative to laser polarization.....	64
2.3. SEM image of the sharp Ag nanocubes employed in our SERS studies.....	65
2.4. Functionalization and removal and of a Ag nanocube with 4-MBT via plasma etching and re-immersion in a 4-MBT solution.....	66
2.5. Schematic of the approach employed for replacing 4-MBT (probe-A) with 1,4-BDT (probe-B), and vice-versa, on a Ag nanocube.....	67
2.6. SERS spectra from a Ag nanocube (4-MBT as probe), followed by plasma etching and immersion in a 1,4-BDT solution.....	68
2.7. SERS spectra from a Ag nanocube (1,4-BDT as probe), followed by plasma etching and immersion in a 4-MBT solution.....	69
2.8. SERS spectra from a Ag nanocube (4-MBT as probe), followed by plasma etching, immersion in a 1,4-BDT and plasma etching for another 2 min.....	70
2.9. (A) Isolation of hot spot in a Ag nanocube dimer. (B-D) SERS spectra from a Ag nanocube dimer (4-MBT as probe), followed by plasma etching and immersion in a 1,4-BDT solution.....	71
2.10. Enhancement factors calculated for nanocube dimers and single nanocubes..	72

2.11. SEM images of (A) Ag nanowires and (B) Ag nanocubes.....	73
2.12. SERS spectra from (A) a Ag nanowire and (B) a Ag nanocube.....	74
2.13. SERS spectra from seven different individual Ag nanowires.....	75
2.14. SERS spectra from dimers made of a Ag nanowire and a Ag nanocube.....	76
2.15. Schematic representation of the dimers probed in Fig. 2.14.....	77
2.16. Enhancement factors obtained for a Ag nanocube, a Ag nanowire, and dimers consisting of a Ag nanowire and a Ag nanocube.....	78
2.17. SERS spectra from (A) a Ag nanowire and (B) a Ag nanocube functionalized with 4-MBT, followed by plasma etching for 6 min, and immersion in a 1,4-BDT solution.....	79
2.18. Plasma etching of a dimer made of a Ag nanowire and a Ag nanocube.....	80
2.19. Cross-section representation for dimers made of (A) two Ag nanocubes and (B) a Ag nanowire and a Ag nanocube.....	81
2.20. SERS spectra from dimers composed of a Ag nanowire and a Ag nanocubes or a Ag right bipyramid.....	82
2.21. SEM images of the (A) Ag nanospheres and (B) Ag nanocubes.....	83
2.22. SERS spectra from a (A) Ag nanosphere and (B) Ag nanocube.....	84
2.23. SERS spectra from ten individual Ag nanospheres.....	85
2.24. SERS spectra from Ag nanospheres and Ag nanocubes in solution.....	86
2.25. Finite-difference time-domain calculation for a supported Ag nanocube.....	87
2.26. SERS spectra from dimers constructed from two Ag nanospheres and two Ag nanocubes (parallel polarization).....	88
2.27. Schematic representation of the dimers probed in Fig. 2.26.....	89
2.28. SERS spectra from dimers constructed from two Ag nanospheres and two Ag nanocubes (perpendicular polarization).....	90
2.29. Enhancement factors for individual Ag nanocubes, individual Ag nanospheres and their dimers probed in Fig. 2.26 and 2.28.....	91
3.1. TEM and HRTEM images of Pd nanocrystals (sacrificial templates).....	116

3.2. (A-C) TEM images and (D) EDX spectra for Pd _{oct.} -Pt samples obtained by titrating the Pd octahedra with 0.4 mM PtCl ₆ ²⁻	117
3.3. HRTEM images of Pd _{oct.} -Pt samples.....	118
3.4. (A-C) TEM images of and (D) EDX spectra from Pd _{cube} -Pt samples obtained by titrating the Pd nanocubes with 0.4 mM PtCl ₆ ²⁻	119
3.5. HRTEM images of Pd _{cube} -Pt samples.....	120
3.6. (A-C) TEM images of and (D) EDX spectra from Pd _{rod} -Pt samples obtained by titrating the Pd nanorods with 0.4 mM PtCl ₆ ²⁻	121
3.7. HRTEM images of Pd _{rod} -Pt samples.....	122
3.8. (A-C) TEM images of and (D) EDX spectra from the samples that were obtained by titrating the Pd nanobars with 0.4 mM PtCl ₆ ²⁻	123
3.9. CV curves for Pt/C, Pd _{oct.} -Pt, Pd _{cube} -Pt and Pd _{rod} -Pt nanocrystals.....	124
3.10. ORR polarization curves, and mass and specific activities for Pt/C, Pd _{oct.} -Pt, Pd _{cube} -Pt, and Pd _{rod} -Pt nanostructures.....	125
4.1. TEM images of (A) Pd nanorods and (B-D) samples that were obtained by titrating the Pd nanorods with 0.4 mM AuCl ₄ ⁻	138
4.2. STEM/EDS analysis of the Pd-Au hybrid nanostructures in Figure 4.1B.....	139
4.3. Titration of Pd nanorods with 10 mL of 0.4 mM AuCl ₄ ⁻	140
4.4. UV-vis spectra taken from a suspension of Pd nanorods after they had been titrated with 1, 2, 4 and 10 mL of 0.4 mM AuCl ₄ ⁻	141
4.5. HRTEM and STEM/EDS of a Pd-Au nanotadpole from Fig. 5.1C.....	142
4.6. Schematic detailing all major steps involved in the galvanic replacement reaction between a Pd nanorod and AuCl ₄ ⁻ ions.....	143
5.1. (A) SEM and TEM (inset) images of <i>t</i> -Se nanowires. (B) TEM and (C, D) HRTEM images of RuSe _{2+δ} nanotubes.....	160
5.2. (A) XRD diffractograms and (B) EDX spectra taken from the <i>t</i> -Se nanowires and RuSe _{2+δ} nanotubes.....	161
5.3. CV curves for the (A) Pt/C and (B) RuSe _{2+δ} nanotubes.....	162

5.4. ORR polarization curves for the Pt/C and RuSe _{2+δ} nanotubes in the absence and in the presence of 0.1 M methanol, respectively.....	163
5.5. Durability tests for Pt/C and RuSe _{2+δ} nanotubes in the absence and in the presence of 0.1 M methanol.....	164
6.1. Synthesis of core-shell colloidal spheres of Se@Ag ₂ Se, Se@ZnSe, Se@CdSe, and Se@PbSe	189
6.2. SEM images and TEM (insets) images of (A) Se@Ag ₂ Se, (B) Se@ZnSe, (C) Se@CdSe, and (D) Se@PbSe colloidal spheres.....	190
6.3. XRD patterns taken from Se@Ag ₂ Se, Se@ZnSe, Se@CdSe, and Se@PbSe colloidal spheres.....	191
6.4. EDX spectra recorded from Se@Ag ₂ Se, Se@ZnSe, Se@CdSe, and Se@PbSe colloidal spheres.....	192
6.5. SEM images of (A) Se@CdSe and (B) Se@PbSe colloidal spheres prepared via cation-exchange with Se@Ag ₂ Se at 70 °C.....	193
6.6. SEM images of colloidal crystals assembled from CdSe hollow spheres doped with (A) 0, (B) 5 % and (C) 20 % of ZnSe hollow spheres.....	194
6.7. Near-IR reflectance spectra from the colloidal crystals in Figure 6.6.....	195
6.8. Synthesis of (Fe ₃ O ₄ /Se)@Ag ₂ Se and (Fe ₃ O ₄ /Se)@CdSe superparamagnetic colloidal spheres.....	196
6.9. SEM and TEM images of (A) Fe ₃ O ₄ /Se, (B) (Fe ₃ O ₄ /Se)@Ag ₂ Se, and (C) (Fe ₃ O ₄ /Se)@CdSe. (D) Optical microscopy image of (Fe ₃ O ₄ /Se)@CdSe colloidal spheres.....	197
6.10. Magnetization curves for (Fe ₃ O ₄ /Se)@Ag ₂ Se (■) and (Fe ₃ O ₄ /Se)@CdSe (▼) colloidal spheres.....	198

Chapter 1

Introduction

1.1. Nanoscience and Nanomaterials

Over the years, the quest for innovative knowledge to produce materials with suitable properties to meet the needs of emerging applications has been the driving force of our technological progress and the improvement of our quality of life. At present, nanoscience and nanotechnology offers the unique opportunity to the creation of new materials to fulfil currently challenging demands. In the energy sector, notable examples include the development of more environmentally friendly energy generation systems, such as fuel cells and solar cells with improved performances and at reduced costs.¹ In medicine, nanoscience and nanotechnology is enabling the development of new approaches for ultrasensitive detection of chemical agents and disease biomarkers, non-invasive and targeted therapies for cancer treatment, new contrast agents for clinical imaging diagnostics, and site specific drug-delivery systems displaying controlled release properties.² In the information and communication industries, examples include the creation of new electronic and optoelectronic devices as well as memory storage systems displaying superior performances.³

Nanoscience and nanotechnology encompasses the design, synthesis, characterization, and utilization of nanomaterials -- a novel class of materials in which at

least one of its dimensions is in the range of 1-100 nm.⁴ More specifically, nanoscience and nanotechnology involves relating the desired properties and relative performance of a material in a certain application to the morphology and structure of the atoms and phases in that material. In this dissertation, I will address the synthesis, characterization, and application of a variety of nanomaterials in areas such as *i*) surface-enhanced Raman scattering, *ii*) fuel-cell technologies, and *iii*) photonic crystals.

1.2. Surface-Enhanced Raman Scattering

In the Raman effect, incident light is inelastically scattered from the molecules in a sample.⁵ The change in wavelength that is observed when a photon undergoes Raman scattering is attributed to the excitation (or relaxation) of vibrational modes of a molecule. Raman spectroscopy is then based on vibrational transitions that yield very narrow spectral features. In accordance with the Raman selection rule, the molecular polarizability changes as the molecular vibrations displace the constituent atoms from their equilibrium positions.^{5,6} The intensity of Raman scattering (P_{RS}) is then proportional to the magnitude of the change in molecular polarizability:

$$P_{RS} \propto N \times \sigma_R \times I_L \quad (1.1)$$

where N is the number of molecules within the probed volume, σ_R is the Raman cross section (determined by the polarizability derivative of the molecular vibration) and I_L is the excitation laser intensity. Because different functional groups have different

characteristic vibrational energies, every molecule has a unique Raman spectrum. Thus, Raman spectroscopy has long been regarded as a valuable tool for the identification of chemical and biological samples as well as the elucidation of molecular structure. Despite such advantages, Raman scattering suffers from the disadvantage of extremely poor efficiency due to its inherently small cross sections (e.g., 10^{-30} - 10^{-25} cm²/molecule), precluding the possibility of analyte detection at low concentration levels without special enhancement processes. Consequently, Raman spectroscopy has been considered a technique for structural analysis, rather than a method for ultra-sensitive trace detection.⁷ It is important to note that the characterization of the chemical structure of a single molecule and screening structural changes at the single-molecule level, for example, represents the ultimate limit in chemical and biomedical analysis.

There has been a renewed interest in Raman techniques in the past three decades owing to the discovery of the surface-enhanced Raman scattering (SERS) effect, which results in strongly increased Raman signals when probe molecules are adsorbed on or near nanometer-sized structures of metals such as silver (Ag) and gold (Au).^{8,9} The mechanism of SERS enhancement falls into two categories: chemical and electromagnetic enhancements. The chemical enhancement is related to chemical interactions, including charge-transfer, which may occur when the analyte molecules are directly adsorbed onto the metal surface. This interaction creates a charge-transfer state between the metal and the adsorbate that can increase the probability of Raman transitions via resonant excitation. This mechanism is both site-specific and analyte-dependent, and it is thought to contribute an average enhancement factor (EF) on the

order of 10^2 .¹⁰ The electromagnetic enhancement is a near-field effect and it occurs when the incident light is in resonance with the localized surface plasmon resonance (LSPR) mode of a metal nanoparticle.^{9,11} Excitation of the LSPR mode results in selective absorption/scattering of the incident light and generation of strong electromagnetic fields at the metal surface. These surface electromagnetic fields lead to large enhancement in the Raman scattering intensity (P_{SERS}):

$$P_{\text{SERS}} \propto N \times \sigma_{\text{R}} \times l_{\text{L}} \times |E(\nu_{\text{L}})|^2 \times |E(\nu_{\text{S}})|^2 \quad (1.2)$$

where $E(\nu_{\text{L}})$ and $E(\nu_{\text{S}})$ refer to the field enhancement factors for the excitation and scattered frequencies, respectively. The electromagnetic enhancement mechanism requires analyte molecules to be confined within the surface electromagnetic fields, but not necessarily adsorbed to the metal surface.¹² The EM can contribute an additional EF of $\geq 10^5$,¹³ with the exact magnitude being dependent on a number of parameters, such as the excitation wavelength employed in the Raman scattering experiments as well as the size, shape and composition of the metal nanostructures (which determine the resonant frequency of the conduction electrons and the magnitude/concentration of surface electromagnetic fields).

Despite the technological importance of SERS and the extensive efforts devoted to studying this phenomenon, attempts to understand its physical origin and thus maximize its potential have had limited success. Since the discovery of SERS in the 1970s, this field has struggled to achieve reproducible measurements and to justify

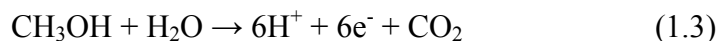
discrepancies between results reported by different research groups. Most of these inconsistencies can be attributed to the lack of uniform nanoparticles with well-controlled shapes. In addition, most SERS experiments are performed with an ensemble of nanoparticles produced via uncontrolled aggregation, making it difficult to correlate the EF to a specific parameter. Recent advances in nanofabrication and the discovery of single-molecule SERS detection in 1997 for substrates composed of aggregated Ag colloids have generated a boom in this field, bringing SERS from a structural analytical tool to a structurally sensitive single-molecule probe.^{14,15} At present, SERS is the only way to detect a single molecule and simultaneously probe its chemical structure.

It is generally accepted that the giant field enhancements that enabled single molecule detection in substrates comprised of Ag nanoparticles occurred only at particular sites, the so-called hot spots.¹⁶ Hot spots can be defined as junctions or gaps between two or more closely spaced particles in which enormous electromagnetic enhancements often arise in contrast to individual particles (Figure 1.1). Theoretical calculations indicate that the dimeric structure formed by placing two silver nanospheres next to each other with a gap of 1-2 nm can give a hot spot with a EF as high as 10^8 .¹⁷ These results demonstrate that hot spots hold the key to the understanding of the field-enhancement mechanisms that enable SERS for single-molecule detection. In order to study the hot-spot phenomena, I report in Chapter 2 the utilization of individual dimers consisting of two closely spaced Ag nanoparticles having a variety of well-defined shapes as substrates for SERS. Even though Ag and Au are the most commonly used noble metals for fabricating SERS-active substrates, it is well-documented that Ag outperforms

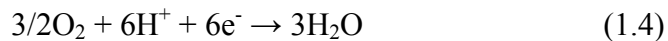
Au by at least three orders in magnitude in terms of average EF, which is typically in the range of 10^6 - 10^7 and 10^3 - 10^4 for conventional Ag and Au colloids, respectively.^{12,18} As a result, I have focused on the utilization Ag nanoparticles in this research.

1.3. Direct Methanol Fuel Cells

Fuel cells convert chemical energy directly into electrical energy with high efficiency and low emission of pollutants.¹⁹ A fuel cell is an electrochemical device that produces electricity from a fuel (at the anode) and an oxidant (at the cathode) that react in the presence of an electrolyte. In direct methanol fuel cells (DMFCs), methanol (CH_3OH) is fed directly to the anode (Figure 1.2).²⁰ The utilization of methanol as a direct fuel is especially attractive due to its low cost, large availability, and easy handling and distribution. The DMFCs rely upon the oxidation of methanol on a catalyst layer at the anode to form carbon dioxide:



Positive ions (H^+) are then transported across the proton exchange membrane to the cathode, where they react with oxygen to produce water:



Electrons are transported through an external circuit from anode to cathode, generating power.^{20,21} Currently, platinum (Pt) and Pt-based alloys are employed as the catalysts for both half-reactions, i.e. methanol oxidation and oxygen reduction reaction (ORR).²² Although Pt is an effective catalyst, several drawbacks associated with its utilization have hampered the widespread commercialization of DMFCs. For example, current proton exchange membranes are permeable to methanol. In this case, any methanol that accidentally crosses through the membrane and reaches the cathode chamber will be oxidized in the presence of Pt. This process is referred as methanol crossover and contributes to the loss of cell voltage potential.²³ Also, Pt is very expensive, resulting in the high cost per kilowatt for such cells. Even though the Pt loading at the anode has been reduced to economically acceptable levels by allowing with ruthenium (Ru), relatively high Pt loadings are still required at the cathode in order to achieve a sufficient surface area and thus desired ORR activity.²⁴ Currently, the major challenges that need to be addressed to enable the widespread utilization of fuel cells include the development of *i*) ORR electrocatalysts with high activity and reduced Pt loading and *ii*) methanol-tolerant ORR electrocatalysts or electrolyte membranes which have high ionic conductivity and low methanol permeability.²⁰ In Chapter 3, I demonstrate that the Pt loading can be reduced at the cathode by employing hollow Pd-Pt bimetallic nanocrystals as electrocatalysts for ORR. In order to tackle the methanol crossover problem, I describe in Chapter 5 the application of RuSe_{2+δ} nanotubes as an active and 100 % methanol-tolerant ORR electrocatalyst.

1.4 Photonic Crystals

Photonic crystals are spatially periodic structures composed of dielectric materials with different refractive indices (Figure 1.3).²⁵ This long-range order creates a gap in the photonic band structure that prohibits the passage of photons with a specific range of wavelengths.^{25,26} Therefore, a photonic crystals offers an opportunity to control the propagation of photons similarly to what a semiconductor does for electrons, allowing one to localize photons to specific areas, to manipulate a spontaneous or stimulated emission process and to guide the propagation of light. All of these properties can be applied to the fabrication of new types of optical filters, switches, and mirrors, as well as to improve the performance of semiconductor lasers and other electronic devices.²⁷

The effective manipulation and control of light propagation in all three dimensions requires photonic crystals presenting complete (or full) band gaps. A complete band gap is defined as one that extends over the entire Brillouin zone in a band structure. An incomplete one is often referred to as a pseudo gap (or stop band) because it only appears along a certain direction of propagation. In general, the development of a complete band gap strongly depends on the structural type of the lattice, the symmetry of the lattice points and the refractive index contrast. One of the major challenges in this field is the fabrication of photonic crystals with complete band gaps in the optical regime, which requires three-dimensionally periodic structures with lattice constants $<1 \mu\text{m}$. Although this fabrication task can be accomplished using conventional microlithographic techniques, a number of technical problems still need to be solved before this approach becomes practical for large-scale production.²⁸ In contrast, self-assembly of colloidal

spheres with diameters ranging from 0.1 to 1 μm provides a simple and versatile method for producing the desired structures. The success of this route relies on the spontaneous organization of pre-designed building blocks into a lattice with long range order that is very close to or at a thermodynamic equilibrium state.²⁹ In this research, I employed a self-assembly route for the fabrication of three-dimensional (3D) photonic crystals. In particular, I have focused on the synthesis and utilization of Se@MSe (M = Zn, Cd and Pb) colloidal spheres presenting high-refractive indices as building blocks to generate 3D opalline lattices via self-assembly, followed by characterization of their photonic bandgap properties. A detailed description of this project is presented in Chapter 6.

1.5. Synthesis of Nanomaterials: the Template-Directed Approach

The synthetic methods for the fabrication of nanoscale materials can be classified into two different groups: the “top-down” and the “bottom-up” approaches. The top-down approach involves the utilization of advanced techniques such as e-beam or ion beam writing, proximal probe patterning, and X-ray or extreme UV lithographies to pattern nanoscale features.³⁰⁻³³ Although these techniques provide excellent control over morphology, dimensions, position, and orientation, they are severely limited in terms of throughput and cost. On the other hand, the bottom-up approach generates nanomaterials directly from atoms.³⁴ In this approach, a precursor compounds is decomposed, reduced, or hydrolyzed to form nuclei that grow into the final nanostructure. The major advantage of bottom-up syntheses is that it allows the fabrication of nanomaterials at relatively low

cost and with high throughput, and together with the potential for high volume production.³⁴

The template-directed approach represents a versatile strategy for bottom-up synthesis of nanomaterials. In the template-directed approach, a pre-formed nanostructure is employed as a template for the synthesis of new nanostructures with a range of different compositions and properties. The template nanostructure can serve as a physical or chemical scaffold on which other materials are assembled (physical templating) or chemically converted (chemical templating) into the final nanostructure. In this case, the product displays a morphology similar or complementary to that of the original template. In the chemical templating, a pre-formed nanostructured material is employed as a reactant in a chemical reaction. This approach is usually referred as a template-engaged reaction and the morphology of the final product can be controlled by using starting templates with different shapes and/or by controlling the extent of the reaction. Examples of template-engaged methods include galvanic replacement and ion-exchange reactions. In this work, I employed the template-engaged approach for the synthesis of a variety of nanomaterials as described in Chapters 3-6. It is important to note that all starting materials employed in the template-engaged reactions were synthesized with well-defined shapes and monodisperse sizes by bottom-up strategies recently described in our group.³⁵⁻³⁸

1.6. Scope of This Work

In the first part of this dissertation (Chapter 2), I report a systematic investigation on the SERS activity of individual dimers consisting of two closely spaced Ag nanoparticles having a variety of well-defined shapes and hot-spot configurations. I also present two different methods for detecting the SERS signals and their corresponding field enhancements exclusively for probe molecules trapped in the hot-spot region. In the second part of this research, I report on the use of a template-engaged reaction approach for the synthesis of Pd-Pt bimetallic nanocrystals (Chapter 3), Pd-Au nanotadpoles (Chapter 4), RuSe₂ nanotubes (Chapters 5) and Se@MSe (M = Zn, Cd or Pb) colloidal spheres (Chapter 6). While the Pd-Pt bimetallic nanocrystals and RuSe₂ nanotubes were employed as new electrocatalysts for the ORR in DMFCs, the Se@MSe colloidal spheres were applied as building blocks to fabricate 3D photonic crystals via self-assembly. Each Chapter begins with an introduction explaining the significance of each project and ends with a summary emphasizing the relevance of the results to their corresponding fields.

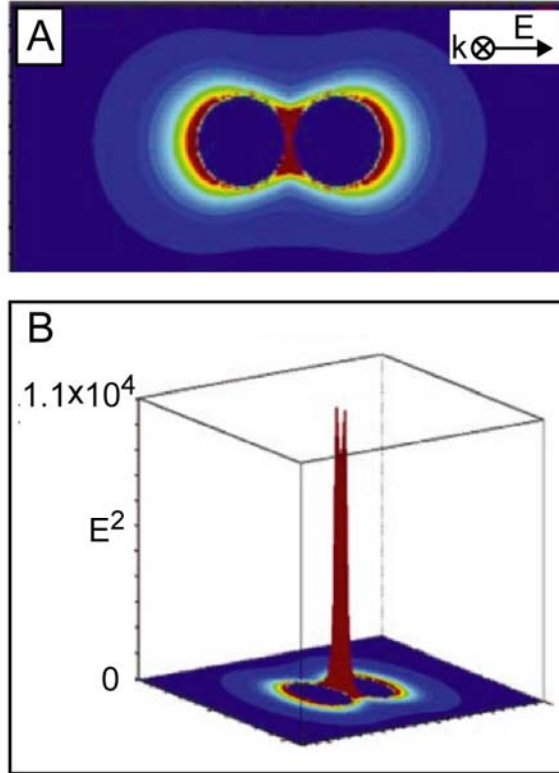


Figure 1.1. Electromagnetic field enhancement contours that were calculated for a dimer composed of two Ag nanospheres separated by 2 nm, for a plane that is along the inter-particle axis and that passes midway through the two spheres. (A) Two-dimensional map of the electromagnetic field intensity showing the polarization of the incident light. (B) Three-dimensional plot where the axis perpendicular to the selected plane represents the amount of electromagnetic field enhancement around the dimer. As the SERS enhancement factor (EF) typically scales as $|E|^4$, the expected EF for this example is on the order of 10^8 (adapted from ref. 17, copyright American Institute of Physics, 2004).

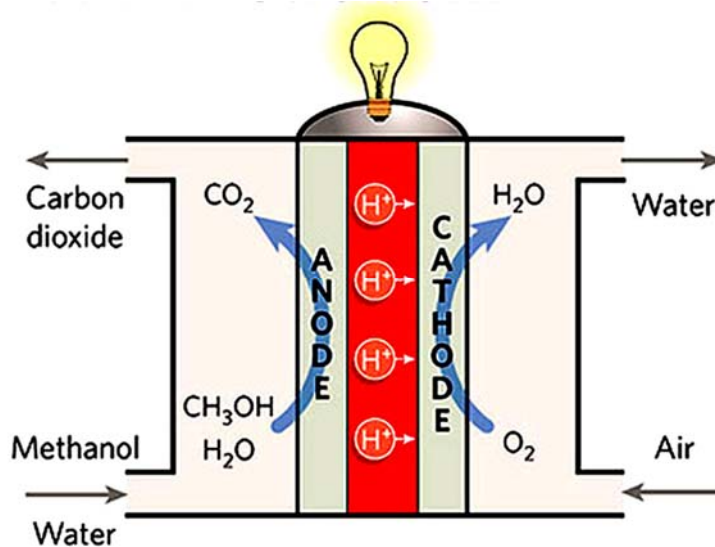


Figure 1.2. Schematic representation of a direct methanol fuel cell. Methanol is oxidized at the anode producing CO_2 and H^+ ions, which migrate to the cathode through the proton-exchange membrane to reduce O_2 and produce H_2O . Electrons are transported from anode to cathode through an external circuit to generate power (adapted from ref. 20b, copyright Nature Publishing Group, 2006).

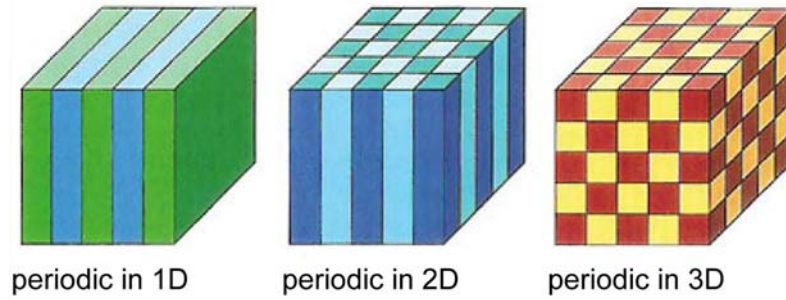


Figure 1.3. Illustration of one-, two-, and three-dimensional photonic crystals. The different colors represent materials with different dielectric constants. The defining feature of a photonic crystal is the periodic variation in the dielectric constant along one or more axes (adapted from ref. 25, copyright Princeton University Press, 2006).

1.7. Notes to Chapter 1

- [1] (a) Kamat, P. V.; *J. Phys. Chem. C* **2008**, *112*, 18737. (b) Aricò, A. S.; Bruce, P.; Scrosati, B.; Tarascon, J. M.; Van Schalkwijk, W. *Nature Mater.* **2005**, *4*, 366.
- [2] (a) Boisselier, E.; Astruc, D. *Chem. Soc. Rev.* **2009**, *38*, 1759. (b) Riehemann, K.; Schneider, S. W.; Thomas, A. L.; Godin, B.; Ferrari, M.; Fuchs, H. *Angew. Chem. Int. Ed.* **2009**, *48*, 872. (c) Muthu, M. S.; Singh, S. *Nanomedicine* **2009**, *4*, 105. (d) A special issue in *Adv. Mater.* **2007**, *19*.
- [3] (a) Ferry, D. K. *Science* **2008**, *319*, 579. (b) Bhushan, B. (ed.), *Springer Handbook of Nanotechnology*, Springer, Verlag Berlin Heidelberg **2004**. (b) A special issue in *Nature*, **2000**, 406.
- [4] (a) Odom, T. M.; Pileni, M. -P. *Acc. Chem. Res.* **2008**, *41*, 1565. (b) Cao, G. *Nanostructures & Nanomaterials*, Imperial College Press, London **2004**.
- [5] Raman, C. V.; Krishnan, K. S. *Nature* **1928**, *121*, 501.
- [6] Kneipp, K.; Kneipp, H.; Itzkan, I.; Dasari, R. R.; Feld, M. S. *Chem. Rev.* **1999**, *99*, 2957.
- [7] McCreery, R. L. *Modern Techniques in Raman Spectroscopy*, ed. J. J. Laserna, John Wiley & Sons, Chichester-NY, Brisbane-Toronto-Singapore, **1996**.
- [8] (a) Jeanmaire, D. L.; Duyne, R. P. V. *J. Electroanal. Chem.* **1977**, *84*, 1. (b) Albrecht, M. G.; Creighton, J. A. *J. Am. Chem. Soc.* **1977**, *99*, 5215.
- [9] (a) Pieczonka, N. P. W.; Aroca, R. F. *Chem. Soc. Rev.* **2008**, *37*, 946. (b) Stiles, P. L.; Dieringer, J. A.; Shah, N. L.; Van Duyne, R. P. *Annu. Rev. Anal. Chem.* **2008**, *1*, 601. (c) Willets, K. A.; Van Duyne, R. P. *Annu. Rev. Phys. Chem.* **2007**, *58*, 267.

- [10] Campion, A.; Kambhampati, P. *Chem. Soc. Rev.* **1998**, 27, 241.
- [11] (a) Haynes, C. L.; McFarland, A. D.; Van Duyne, R. P. *Anal. Chem.* **2005**, 77, 338A. (b) Lu, X.; Rycenga, M.; Skrabalak, S. E.; Wiley, B. and Xia, Y. *Ann. Rev. of Phys. Chem.* **2009**, 60, 167.
- [12] Schatz, G. C.; Van Duyne, R. P. In *Handbook of Vibrational Spectroscopy*, Eds. Chalmers, J. M.; Griffiths, P. R. John Wiley & Sons: New York, **2002**.
- [13] (a) Xiao, T.; Ye, Q.; Sun, L. *J. Phys. Chem. B* **1997**, 101, 632. (b) Garcia-Vidal, F. J.; Pendry, J. B. *Phys. Rev. Lett.* **1996**, 77, 1163. (c) Zeman, E. J.; Schatz, G. C. *J. Phys. Chem.* **1987**, 91, 634-43. (d) Inoue, M.; Ohtaka, K. *J. Phys. Soc. Jpn.* **1983**, 52, 3853.
- [14] (a) Nie, S.; Emory, S. R. *Science* **1997**, 275, 1102. (b) Kneipp, K.; Wang, Y.; Kneipp, H.; Perelman, L. T.; Itzkan, I.; Dasari, R. R.; Feld, M. S. *Phys. Rev. Lett.* **1997**, 78, 1667.
- [15] Kneipp, K.; Wang, Y.; Kneipp, H.; Perelman, L. T.; Itzkan, I.; Dasari, R. R.; Feld, M. S. *Phys. Rev. Lett.* **1997**, 78, 1667.
- [16] (a) Otto, A. *J. Raman Spectrosc.* **2006**, 37, 937. (b) Le Ru, E. C.; Etchegoin, P. G.; Meyer, M. *J. Phys. Chem.* **2006**, 125, 104701. (c) Doering, W. E.; Nie, S. *J. Phys. Chem. B* **2002**, 106, 311.
- [17] Hao, E.; Schatz, G. C. *J. Chem. Phys.* **2004**, 120, 357.
- [18] Kelly, K. L.; Coronado, E.; Zhao, L. L.; Schatz, G. C. *J. Phys. Chem. B* **2003**, 107, 668.
- [19] B. C. H. Steele and A. Heinzl, *Nature*, 2001, **414**, 345.

- [20] (a) Aricò, A. S.; Srinivasan, S.; Antonucci, V. *Fuel Cells*, **2001**, 2, 133. (b) Macilwain, C. *Nature* **2006**, 441, 1046. (c) Winter, M.; Brodd, R. J. *Chem. Rev.* **2004**, 104, 4245. (d) Dresselhaus, M. S.; Thomas, I. L. *Nature* **2001**, 414, 332. (e) Wasmus, S.; Küver, A. *J. Electroanal. Chem.* **1999**, 461, 14.
- [21] Shukla A. K.; Raman, R. K.; *Annu. Rev. Mater. Res.*, **2003**, 33, 155.
- [22] (a) Liu, H.; Song, C.; Zhang, L.; Zhang, J.; Wang, H.; Wilkinson, D. P. *J. Power Sources* **2006**, 155, 95. (b) Gasteiger, H.; Kocha, S. S.; Sompalli, B.; Wagner, F.T. *Appl. Catal. B* **2005**, 56, 9. (c) Paulus, U. A.; Schmidt, T. J.; Gasteiger, H. A.; Behm, R. J. *J. Electroanal. Chem.* **2001**, 495, 134.
- [23] (a) Liu, L.; Kim, H.; Lee, J. W.; Popov, B. N. *J. Electrochem. Soc.* **2007**, 154, A123. (b) Baranton, S.; Coutanceau, C.; Roux, C.; Hahn F.; Leger, J.-M. *J. Electroanal. Chem.* **2005**, 577, 223. (c) Jusys Z.; Behn, R. J. *Electrochim. Acta* **2004**, 49, 3891.
- [24] Gasteiger, H. A.; Kocha, S. S.; Sompalli, B.; Wagner, F. T. *Appl. Catal. B* **2005**, 56, 9.
- [25] Joannopoulos, J. D.; Johnson, S. G.; Winn, J. N.; Meade, R. D. *Photonic Crystals: Molding the Flow of Light*, 2nd edition, Princeton University Press, Princeton, 2008.
- [26] Camargo, P. H. C.; Li, Z. -Y.; Xia, Y. *Soft Matter*, **2007**, 3, 1215. (b) López, C. *Adv. Mater.*, 2003, **15**, 1679.
- [27] (a) Wu, M. C.; Solgaard, O.; Ford, J. E. *J. Lightw. Technol.* **2006**, 24, 4433. (b) Vlasov, A.; O'Boyle, M.; Harmann, H. F.; McNab, S. J. *Nature* **2005**, 438, 65. (c)

- Noda, S.; Imada, M.; Okano, M.; Ogawa, S.; Mochizuki, M.; Chutinan, A. *IEEE J. Quantum Electron.* **2002**, *38*, 726.
- [28] Fleming, J. G.; Lin, S. Y.; El-Kady, I.; Biswas, R.; Ho, K. M. *Nature* **2002**, *417*, 52.
- [29] Whitesides, G. M.; Grzybowski, B. *Science* **2002**, *295*, 241.
- [30] (a) Gibson, J. M. *Phys. Today* **1997**, *October*, 56. (b) Matsui, S.; Ochiachi, Y. *Nanotechnology* **1996**, *7*, 247.
- [31] (a) Hong, S. H.; Mirkin, C. A. *Science* **1999**, *286*, 523. (b) Dagata, J. A. *Science* **1995**, *270*, 1625.
- [32] (a) Levenson, D. V. *Solid State Technology*, **1995**, *September*, 81. (b) Dunn, P. N. *Solid State Technology* **1994**, *June*, 49.
- [33] Gates, B. D.; Xu, Q.; Stewart, M.; Ryan, D.; Willson, C. G.; Whitesides, G. M. *Chem. Rev.* **2005**, *105*, 1171.
- [34] (a) Xia, Y.; Xiong, Y.; Lim, B.; Skrabalak, S. E. *Angew. Chem. Int. Ed.* **2009**, *48*, 60. (b) Kwon, S. G.; Hyeo, T. *Acc. Chem. Res.* **2008**, *41*, 1696. (c) Xia, Y.; Rogers, J. A.; Paul, K. E.; Whitesides, G. M. *Chem. Rev.* **1999**, *99*, 1823.
- [35] Jeong, U.; Xia, Y. *Adv. Mater.* **2005**, *17*, 102
- [36] (a) Mayers, B.; Liu, K.; Sunderland, D.; Xia, Y. *Chem. Mater.* **2003**, *20*, 3852. (b) Gates, B.; Mayers, B.; Grossman, A.; Xia, Y. *Adv. Mater.* **2002**, *14*, 1749.
- [37] (a) Lim, B.; Jiang, M.; Tao, J.; Camargo, P. H. C.; Zhu, Y.; Xia, Y. *Adv. Funct. Mater.* **2009**, *19*, 189. (b) Lim, B.; Xiong, Y.; Xia, Y. *Angew. Chem. Int. Ed.* **2007**, *46*, 9279. (c) Xiong, Y.; Cai, H.; Wiley, B. J.; Wang, J.; Kim, M. J.; Xia, Y. *J. Am. Chem. Soc.* **2007**, *129*, 3665.

- [38] (a) Skrabalak, S. E.; Au, L.; Li, X.; Xia, Y. *Nat. Protoc.* **2007**, *2*, 2182. (b) Im, S. H.; Lee, Y. T.; Wiley, B.; Xia, Y. *Angew. Chem. Int. Ed.* **2005**, *44*, 2154. (c) Sun, Y.; Xia, Y. *Science* **2002**, *298*, 2176. (d) Chen J.; Wiley, B.; Xia, Y. *Langmuir* **2007**, *23*, 4120. (e) Sun, Y.; Mayers, B.; Herricks, T.; Xia, Y. *Nano Lett.* **2003**, *3*, 955.

Chapter 2

Dimers of Silver Nanoparticle as Substrates for SERS: Probing the SERS Activity for Hot Spots Formed between Two Closely Spaced Nanoparticles

2.1. Introduction

The commonly employed method for producing SERS substrates containing hot spots for ultrasensitive detection relies on the uncontrolled aggregation of Ag or Au nanoparticles induced by a salt.¹⁻⁵ While these aggregates can provide strong SERS signals, the poor reproducibility on the fabrication as well as the broad distribution in terms of size and shape for the nanoparticles imposes many challenges for effectively correlating the detected SERS signals to the specific attributes of a hot spot. As a result, although the hot-spot phenomenon has been extensively investigated, it still remains a poorly understood subject.

In this context, individual dimers consisting of two nanoparticles represent an ideal system for quantitatively investigating the hot-spot phenomenon. In particular, the dimers enable one to easily correlate the SERS signals and their polarization dependencies to the hot-spot morphology.^{6,7} Also, enhancements strong enough for ultrasensitive analysis and even single-molecule detection have recently been reported for

dimers composed of Ag nanoparticles.⁸ A number of dimeric systems have recently been investigated as SERS substrates, including dimers constructed from rounded particles, nanoshells, nanowires, and nanowires decorated with nanoparticles.⁶⁻¹⁰ These studies suggest that the field enhancements are strongly dependent on the direction of the laser excitation polarization. Typically, the strongest enhancement occurred when the laser excitation was polarized across the interparticle junction, i.e., parallel to the hot-spot axis. Nevertheless, shape irregularity and surface roughness associated with the employed dimer nanoparticles still imposes some challenges to precisely calculate the number of molecules being probed and, consequently, the enhancement factor (EF) from an individual dimer and hot spot. As the EF provides a direct quantification of how much the Raman signals are enhanced in the SERS as compared to the ordinary Raman spectrum, an accurate estimate of its magnitude is crucial to the fundamental understanding of the hot-spot phenomenon.⁴

In order to address this issue, I report on the utilization of a variety of dimers made of two closely-spaced Ag nanoparticles as substrates for SERS, followed by the estimation of their respective EFs. In my studies, the use of well-defined, uniform particles with smooth surface was critical to a meaningful correlation of the EFs and their dependence on laser polarization to the hot-spot structure. In Section 6.2, I describe the probing of the EF for the hot-spot formed in individual dimers comprised of two Ag nanospheres that were 30 nm in diameter. In Section 6.3, I report on a new strategy based on plasma etching for exclusively measuring the SERS signals from those molecules located in the hot-spot region formed between two Ag nanocubes that were 100 nm in

edge length. In Section 6.4, I describe the utilization of a new class of well-defined nanoparticle dimer as a substrate for SERS: an individual Ag nanowire decorated with a single Ag nanocube. Finally, in Section 6.5, I report on a systematic investigation on the SERS activity of hot spots displaying a variety of well-defined morphologies formed between two Ag nanospheres and two Ag nanocubes.

2.2. Probing the Enhancement Factor for the Hot Spots Formed in Dimers of Silver Nanospheres

2.2.1. Results and Discussion

Figure 2.1 shows SERS spectra taken from a sample of an individual Ag nanosphere, two Ag nanospheres separated by ~ 600 nm and a two barely touching Ag nanospheres that had been functionalized with 4-MBT. Owing to the relatively small size (~ 30 nm in diameter) of the silver nanospheres, I expect that probe molecules outside the hot spot region will not contribute to the detected SERS signals.¹¹ Hence, these dimers provide an ideal model system for investigating the enhancement factor and polarization effect of an individual hot spot. The top trace in Figure 2.1A shows the SERS spectrum taken from a single dimer with the laser polarization parallel to the longitudinal axis. The two characteristic peaks for 4-MBT at 1079 and 1594 cm^{-1} were clearly resolved, albeit at low intensity. The peak at 1079 cm^{-1} is due to a combination of the phenyl ring-breathing mode, CH in-plane bending, and CS stretching, while the peak at 1594 cm^{-1} can be assigned to phenyl stretching motion (8a vibrational mode).^{12,13} The low intensity reflects

the small number of molecules trapped in the hot spot region and the relatively smaller Raman cross-section for the 4-MBT molecules as compared to organic dyes usually employed in single-molecule SERS studies.² Figure 2.1A also gives the SERS spectra recorded from two silver nanospheres separated by ~600 nm (middle trace) and a single silver nanosphere (bottom trace). In these two cases, there was no hot spot involved. In the case of two silver nanospheres separated by 600 nm, both of them were within the laser focal volume, and the total number of probed 4-MBT molecules should be similar to the case of a dimer. The absence of detectable SERS signals confirm that only 4-MBT molecules trapped in the hot spot region are responsible for the SERS peaks at 1079 and 1594 cm^{-1} .

When determining the number of trapped molecules ($N_{\text{hot-spot}}$) in the hot spot region, I assume that the 4-MBT molecules will be absorbed as a monolayer with a 0.19 nm^2 molecular footprint onto a spherical cap having $h = r/6.6$ located on each silver nanosphere of the dimer (i.e., the interparticle region), as shown in Figure 2.1B. This approximation yielded $N_{\text{hot-spot}} = 2510$. This number represents a theoretical maximum number of molecules and is surely an overestimate, thus the EF reported here is likely an underestimate rather than an overestimate of the actual EF value. According to this approach, the EF of the hot spot was calculated to be 1.9×10^7 . Alternatively, if I assume that the hot spot region is enclosed by two hexagonal (111) faces, $N_{\text{trap}} = 1904$ and the EF became 2.5×10^7 , which is also close to 1.9×10^7 . It is important to note that 4-MBT does not exhibit any absorption bands around 785 nm, which excludes the possibility of any resonance Raman effects for the excitation laser employed in my study. Further

enhancement of the SERS effect can be achieved by employing probe molecules with resonance effects and/or by optimizing the laser wavelength employed in the measurements.

Figure 2.2 illustrates the dependence of the SERS signals on the laser polarization for the silver nanosphere dimer. It can be observed that the 4-MBT peaks were maximized when the laser was polarized parallel to the longitudinal axis of the dimer. The 4-MBT signals were gradually reduced when the laser was rotated by 22.5 and 45° away from the longitudinal axis. At 45°, the area of the peak at 1079 cm⁻¹ was reduced by a factor of ~3. Finally, the 4-MBT peaks disappeared when the polarization was off from the longitudinal axis by angles larger than 45° (e.g., 77 and 90°).

2.2.2. Summary

With 4-MBT as a probe molecule, the enhancement factor for the hot-spot region of a silver nanosphere dimer was estimated to be 1.9×10^7 . The SERS signals taken from the hot spot were polarization dependent; they were maximized when the laser was polarized parallel to the longitudinal axis and vanished when the polarization was in the orthogonal direction. These well-defined dimers hold great promise for ultrasensitive detection and even single-molecule detection by SERS and are expected to find a range of applications in fields such as life sciences, environmental science, and photonics.

2.3. Isolating and Probing the Hot Spots Formed between Two Silver Nanocubes

Despite the advantages of using individual nanoparticle dimers as substrates for SERS, there are still limitations associated with their utilization for studying the hot-spot phenomenon. Due to the size and shape of the usually employed nanoparticles, SERS molecules absorbed inside and outside the hot-spot region can both contribute to the detected SERS signals.^{6-8,14} As a result, the experimentally determined enhancement factor (EF) represents an average enhancement from the entire surface of the dimer. In this regard, determination of EFs exclusive from the hot-spot region still remains a great challenge.

In this section, I describe a new strategy based on plasma etching for exclusively measuring the SERS signals from those molecules located in the hot-spot region formed between two Ag nanocubes. In this approach, the dimer of Ag nanocubes was functionalized with SERS probe molecules and then briefly exposed to plasma etching to selectively remove those molecules outside the hot-spot region. With the aid of registration marks, I was able to experimentally determine the SERS enhancement factor associated with the hot spot at different orientations relative to the laser polarization. To our knowledge, this work represents the first attempt to isolate the hot spot formed between two Ag nanoparticles, followed by measurements of the SERS enhancement factor intrinsic to a hot spot.

2.3.1. Results and Discussion

Figure 2.3 shows a typical SEM image of the sharp Ag nanocubes used in my SERS studies, which had an edge length of 100 ± 5.7 nm. I chose them for a number of reasons. For example, they can be routinely synthesized with good uniformity in terms of shape and size distribution via the polyol method.¹⁵ Their sharp corners and relatively large dimensions ensure that I will be able to obtain strong SERS signals as compared to smaller or rounded particles.¹⁶ Also, they represent an ideal system for the isolation of the hot spot through plasma etching. I employed 4-methyl-benzenethiol (4-MBT) and 1,4-benzenedithiol (1,4-BDT) as the SERS probe molecules because they are known to form well-defined monolayers on Ag surfaces via a strong Ag-S linkage with characteristic molecular footprints. These attributes are critical to estimating the total number of molecules being probed and therefore the EF.¹⁷ Moreover, these molecules are expected to be able to penetrate into the hot-spot region between two Ag nanocubes owing to their relatively small sizes.

I started my measurements by investigating the effect of plasma etching on individual Ag nanocubes (Figure 2.4A). Specifically, I would like to know whether 4-MBT molecules adsorbed on the surface of a Ag nanocube could be removed by brief plasma etching. I was also interested in understanding if the plasma etching would lead to any physical and/or chemical changes to the Ag nanocube, including its capability to enhance the SERS signals from 4-MBT re-deposited on the Ag nanocube. Figure 2.4B shows a set of SERS spectra taken from the same Ag nanocube, which was functionalized with 4-MBT, plasma etched for 2 min, and then re-functionalized with 4-

MBT by immersing into its solution. With the assistance of registration marks, I was able to locate the same Ag nanocube (see the inset) and take SERS spectra from it during these steps. I also repeated the cycle of functionalization, etching, and re-functionalization a number of times to see if plasma etching would eventually cause any irreversible change to the Ag surface. As clearly shown in Figure 2.4B, the initial spectrum (top trace) presents the characteristic SERS peaks for 4-MBT at 1072 and 1582 cm^{-1} .¹² Here, the nanocube was oriented with one of its edges parallel to the laser polarization. The peak at 1072 cm^{-1} is due to a combination of the phenyl ring-breathing mode, CH in-plane bending, and CS stretching, while the peak at 1582 cm^{-1} can be assigned to phenyl ring stretching motion (8a vibrational mode).¹³ The broad band at 900-1000 cm^{-1} came from the Si substrate. After the sample had been plasma etched for 2 min, both the 4-MBT peaks disappeared from the SERS spectrum (second trace from the top), indicating complete removal of the 4-MBT molecules from the surface of the nanocube. Interestingly, both peaks of 4-MBT appeared again in the SERS spectrum (third trace from the top) after the etched sample had been re-immersed in the 4-MBT solution. No significant change was observed for the SERS peaks of 4-MBT when the first and third spectra were compared. This result suggests that the number of 4-MBT molecules that were re-deposited on the Ag nanocube after plasma etching was essentially the same as the number of molecules initially adsorbed on the Ag nanocube. It also implies that plasma etching merely removes the 4-MBT molecules from the surface of the Ag nanocube when the exposure time is relatively short. The complete cycle comprising of plasma etching and re-immersion in 4-MBT could be repeated up to three

times without observing major deterioration in the SERS spectrum. However, after the fourth cycle, no 4-MBT peaks could be detected. It is possible that surface oxidation after an extended exposure to the oxygen-based plasma will hamper the adsorption of 4-MBT onto the surface.

The plasma etching could also be employed to change the probe molecules adsorbed on the surface of an individual Ag nanocube. This concept is illustrated in Figure 2.5. In the first step, the nanocube is functionalized with 4-MBT (probe-A). Then, the probe-A molecules are removed by briefly subjecting the sample to plasma etching. Finally, the sample is immersed in a solution containing 1,4-BDT (probe-B). Figure 2.6 shows the SERS spectra recorded from a sample going through these steps. In Figure 2.6A, the nanocube was oriented with one of its edges parallel to the laser polarization. The initial spectrum (top trace) presents the characteristic peaks for 4-MBT at 1073 and 1583 cm^{-1} ,¹² which completely disappeared after plasma etching (middle trace). After immersion in a 1,4-BDT solution, the characteristic peaks for 1,4-BDT appeared in the SERS spectrum as a result of the adsorption of 1,4-BDT onto the nanocube. In this case, we observed a shift in phenyl ring stretching motion band (8a mode) from 1582 cm^{-1} (for 4-MBT) to 1562 cm^{-1} (for 1,4-BDT).¹⁸ The same trend was also observed when the nanocube was orientated with one of its face diagonals parallel to the laser polarization, as shown in Figure 2.6B. In this case, the intensities of the SERS signals were much stronger as compared to those in Figure 2.6A. As previously reported by our group, the SERS signals taken from a single Ag nanocube had a strong dependence on the laser polarization, which could be attributed to the difference in near-field distribution over the

surface of a nanocube under different polarization directions.¹⁹ In addition to the shift in position for the 8a band from 1583 to 1562 cm^{-1} , broadening was observed for the band at 1072 cm^{-1} for 1,4-BDT as compared to 4-MBT. This is because the ordinary Raman spectrum of 1,4-BDT displays two bands in this region (1080 and 1065 cm^{-1}), which tend to broaden and overlap in the SERS spectrum due to interactions between the Ag surface and the π -orbital system of the benzene ring.¹⁸ The SERS spectrum for 1,4-BDT also displayed a weak signal at 1180 cm^{-1} that could be assigned to the 9a vibrational mode (CH bending).¹⁸

Figure 2.7 and 2.8 illustrate the effect of plasma etching over single a Ag nanocube functionalized with 1,4-BDT. In these cases, no changes in the SERS spectra were observed after plasma etching. Moreover, the SERS spectra didn't change after immersing the sample in a 4-MBT solution. While 4-MBT interacts with Ag through one sulfur atom assuming a vertically tilted orientation with respect to the Ag surface, 1,4-BDT interacts with Ag as a dithiolate in which the aromatic ring assumes a flat orientation.^[13-15,17] Consequently, it is reasonable that the 4-MBT molecules, due to their vertical orientation, are more susceptible to the oxygen plasma and, therefore, can be more easily etched away from the Ag surface. In addition, the interaction between Ag and 1,4-BDT (via 2 sulfur atoms) is expected to be much stronger than the interaction between Ag and 4-MBT (via 1 sulfur atom). Combined together, it is not hard to understand why the adsorbed 1,4-BDT molecules could not be displaced by 4-MBT. The scale bar in the inset corresponds to 100 nm.

After the experimental details for surface functionalization and plasma etching

had been established for individual Ag nanocubes, I turned my attention to dimers of Ag nanocubes. In this case, I aimed at isolating the 4-MBT molecules located in the hot-spot region by exposing the sample to plasma etching under similar conditions as employed for the individual nanocubes. It is important to note that under the conditions used in this work, both 4-MBT and 1,4-BDT are expected to be present on the Ag surface as a complete monolayer. Therefore, for individual Ag nanocubes, the plasma etching was responsible for the removal of a 4-MBT monolayer adsorbed on the Ag surface. Similarly, for nanocube dimers, the plasma etching is expected to remove a monolayer of 4-MBT molecules present on the surface. As the hot-spot region in the nanocube dimers comprises a narrow gap between two nearly touching nanocubes, the 4-MBT molecules in the hot spot can be considered as a multilayer resist relative to the oxygen plasma (Figure 2.9A). If each 4-MBT molecule has a 0.19 nm^2 footprint, each 4-MBT molecule can be assumed to occupy a circular area of 0.249 nm in diameter on the Ag surface. As the nanocubes have an edge length of 100 nm , approximately 200 layers of 4-MBT molecules can be present in the hot-spot region along the vertical direction. Therefore, it will require a much longer time to remove the 4-MBT molecules located in the hot spot as compared to those molecules outside the hot-spot region. This scenario explains why plasma etching can serve as an effective method for isolating the hot spot formed between two Ag nanocubes. In order to demonstrate that no significant change took place on the surface of the nanocube dimers during plasma etching, the sample was also immersed in a 1,4-BDT solution after the hot spot had been isolated.

Figure 2.9, B-D, shows the SERS spectra from a nanocube dimer that was

functionalized with 4-MBT (top trace), followed by plasma etching for 2 min (middle trace) and then immersion in a 1,4-BDT solution (bottom trace). In Figure 2.9B, the long axis of the dimer was parallel to the laser polarization. The SERS spectrum from the Ag nanocube dimer functionalized with 4-MBT clearly showed the characteristic peaks for 4-MBT at 1072 and 1582 cm^{-1} .^{12,13} The much stronger intensity of the SERS signals as compared to Figures 2.4B and 2.6A reflects a higher SERS activity for the dimer relative to the individual nanocubes due to the presence of a hot spot. I employed the peak at 1582 cm^{-1} to estimate the EF as described in the experimental section. Based on my assumptions, the EF for the initial nanocube dimer (EF_{dimer}) functionalized with 4-MBT (Figure 2.9B, top trace) was 2.2×10^7 . In comparison, the EF calculated for an individual Ag nanocube (EF_{cube}) under the same polarization (Figure 2.6A, top trace) was 5.9×10^5 . This indicates that the EF_{dimer} was ~ 37 times higher than EF_{cube} . After plasma etching (Figure 2.9B, middle trace), a slight decrease in the intensity was observed for the 4-MBT bands at 1072 and 1582 cm^{-1} . This slight reduction due to the removal of 4-MBT molecules from the region outside the hot-spot region indicates that the molecules in the hot spot were the major contributors to the SERS signals from the dimer. By assuming that only the 4-MBT molecules adsorbed in the hot-spot region were present in the nanocube dimer after plasma etching, the calculated EF for the hot-spot ($EF_{hot-spot}$) was 1.0×10^8 . In this case, $EF_{hot-spot}$ was higher than EF_{dimer} and EF_{cube} by a factor of 4.5 and 170, respectively. After the sample was immersed in a 1,4-BDT solution, all the peaks due to 4-MBT were replaced by the characteristic peaks of 1,4-BDT (Figure 2.9B, bottom trace), as it can be observed from the shifting of the 8a band to 1561 cm^{-1} and the

broadening of the 1073 cm^{-1} peak. This result indicates that, in addition to be adsorbed onto the faces of the nanocubes outside the hot spot, 1,4-BDT replaced the 4-MBT molecules in the hot-spot region. The stronger interaction between 1,4-BDT and Ag than 4-MBT and Ag may provide the driving force for this process (Figure 2.7 and 1.8).^{12,13,18,20} After complete replacement of 4-MBT by 1,4-BDT, EF_{dimer} was 1.9×10^7 , which is close to the initial EF_{dimer} obtained with 4-MBT, indicating that no significant change on the surface of the nanocube dimers occurred as a result of plasma etching.

Figure 2.9C illustrates the SERS spectra from the nanocube dimer in which the long axis of the dimer was at 45° relative to the laser polarization. The SERS signals were weaker compared to those in the spectra shown in Figure 2.9B as a result of inferior SERS activities under this configuration. The initial spectrum for the nanocube dimer presents the characteristic peaks for 4-MBT. EF_{dimer} was calculated as 2.0×10^6 , representing a 11-fold decrease as compared to the EF_{dimer} calculated from Figure 2.9B. Comparatively, when the individual nanocube was orientated with a face diagonal parallel to the laser polarization (Figure 2.6A, top trace), EF_{cube} was 2.3×10^6 . The fact that EF_{dimer} is close to EF_{cube} under this configuration suggests that the molecules in the hot-spot did not contribute additionally towards the SERS signals observed for the dimer. This is also confirmed by inspecting the SERS spectrum after plasma etching (Figure 2.9C, middle trace). In this case, a significant decrease in intensity for both the 1072 and 1584 cm^{-1} peaks were observed as the 4-MBT molecules were removed from the region outside the hot spot. $EF_{hot-spot}$ was calculated to be 4.1×10^6 , indicating that $EF_{hot-spot}$ is within the same order of magnitude as EF_{dimer} and EF_{cube} . After the sample was immersed

in a 1,4-BDT solution, all the peaks due to 4-MBT were replaced by the characteristic peaks of 1,4-BDT (Figure 2.9C, bottom trace) and EF_{dimer} was calculated as 1.6×10^6 , which agrees with the initial EF_{dimer} obtained with 4-MBT.

Figure 2.9D shows the SERS spectra for which the long axis of the dimer was perpendicular to the laser polarization direction. In this case, the SERS signals further decreased in comparison to Figure 2.9C, and were much weaker relative to Figure 2.9B. EF_{dimer} was calculated as 6.8×10^5 , which is close to the value of 5.9×10^5 obtained for single Ag nanocubes (Figure 2.6A), suggesting that the molecules in the hot spot did not make any additional contribution toward SERS signals observed for the dimer. After plasma etching, while the peak at 1072 cm^{-1} completely disappeared, the peak at 1583 cm^{-1} became very weak and $EF_{hot-spot}$ became 4.4×10^5 , which was on the same order of magnitude as EF_{dimer} and EF_{cube} . After immersion in 1,4-BDT, all the 4-MBT were replaced by the characteristic peaks of 1,4-BDT and EF_{dimer} was found to be 5.4×10^5 . Figure 2.10 summarizes the EFs obtained for the Ag nanocubes and their dimers during the steps of functionalization with 4-MBT, plasma etching, and immersion in 1,4-BDT.

According to near-field calculations by the discrete-dipole approximation (DDA) method for Ag nanocubes 100 nm in size at 514 nm excitation,¹⁹ the near-field distribution is expected to be concentrated on the faces that form the hot-spot region when the laser polarization is parallel to the dimer long axis. This could lead to a SERS enhancement of 170 folds stronger for $EF_{hot-spot}$ as compared to EF_{cube} . However, when the long axis of the dimer is at 45° and 90° relative to the laser polarization direction, the near-field distributions are expected to be mostly concentrated outside the hot-spot

region, i.e., at the corners and on the faces that are perpendicular to the dimer's long axis, respectively. This reduction of near-field distribution in the hot-spot region can be considered to be responsible for the significant decrease in the $EF_{hot-spot}$ when the long axis of the dimer is at 45° and 90° relative to the laser polarization.

2.3.2. Summary

I have demonstrated a simple and versatile approach based on plasma etching for isolating and exclusively probing the hot spot in a dimer of Ag nanocubes. In this approach, the dimer of Ag nanocubes was first functionalized with 4-MBT and the hot spot was then isolated by exposing the sample to plasma etching. The plasma etching only led to the removal of molecules adsorbed on the surface outside the hot-spot region. Finally, the sample was functionalized with 1,4-BDT to demonstrate that the surface of the dimer did not undergo any significant changes during plasma etching. Based on this approach, $EF_{hot-spot}$ was calculated as 1.0×10^8 , 4.1×10^6 , and 4.4×10^5 as the long axis of the dimer was oriented at 0 (parallel), 45, and 90 (perpendicular) degrees relative to the laser polarization, respectively. Likewise, EF_{dimer} (without isolating the hot spot) was calculated as 2.2×10^7 , 2.0×10^6 and 6.8×10^5 , respectively. These results indicate that $EF_{hot-spot}$ displayed a strong dependence on the laser polarization, increasing by a factor of *ca.* 10 and 230 as the long axis of the dimer was rotated from 90 to 45 degrees and from 90 to 0 (relative to the laser polarization). Similarly, EF_{dimer} displayed an increase by a factor of *ca.* 3 and 30. By comparing $EF_{hot-spot}$ with EF_{cube} , $EF_{hot-spot}$ was increased by *ca.* 170 folds when the dimer's long axis was parallel to the direction of laser polarization.

2.4. Measuring the SERS Enhancement Factors of Hot Spots Formed Between an Individual Ag Nanowire and a Single Ag Nanocube

In this section, I wish to report on the utilization of a new class of well-defined nanoparticle dimer as a substrate for SERS: an individual Ag nanowire decorated with a single Ag nanocube. More specifically, I investigated two distinct dimer geometries: *i*) a sharp Ag nanocube having one side face nearly touching the side face of a nanowire (face-to-face configuration) and *ii*) a sharp Ag nanocube having one edge nearly touching the side face of a nanowire (edge-to-face configuration). In addition to measurement of EF for the dimers (EF_{dimer}) and its correlation with the hot-spot structure, I compared my results to those obtained from individual nanowires and nanocubes. It is important to note that both finite Ag nanowires and sharp Ag nanocubes present interesting features that make them attractive as substrates for SERS. For example, they can be routinely synthesized with good uniformity in terms of shape, size distribution and surface smoothness by the polyol method.^{15,21} Individual nanowires, nanocubes and their dimers can be easily found under a dark-field optical microscope during SERS measurements. In addition, the dimerization between a nanowire and a nanocube is expected to generate a hot spot region with increased field enhancement as compared to individual components.¹⁰ Finally, because the SERS signals for sharp Ag nanocubes present strong laser polarization dependency, the relative orientation of the nanocube with respect to the nanowire side face in the dimers may provide another venue for the maximization the SERS intensities and their correlation with different hot-spot structures.¹⁹

2.4.1. Results and Discussion

Figure 2.11 shows SEM images of the Ag nanowires and nanocubes employed in my SERS studies. The Ag nanowires had a mean diameter of 95.2 ± 8.8 nm and were 2-5 μm in length. They are characterized by a pentagonal cross section and pyramidal tips. The sharp Ag nanocubes had a mean edge length of 141.7 ± 3.8 nm. I employed 1,4-BDT as the SERS probe molecules because they are known to form well-defined monolayers on Ag surface via a strong Ag-S linkage with a characteristic molecular footprint.¹⁸ These attributes are critical to estimating the total number of molecules being probed and therefore the EF.¹² Moreover, these molecules are expected to be able to penetrate into the hot-spot region between a Ag nanowire and a Ag nanocube owing to the relatively small size.

I started my studies by evaluating the SERS properties of individual Ag nanowires and nanocubes. Figure 2.12A shows typical SERS spectra for an individual Ag nanowire that was 105 nm in diameter under two different laser polarizations: perpendicular and parallel to the longitudinal axis (top and bottom traces, respectively). Since I was interested in a systematic investigation of the SERS signals from the nanowires, the laser beam was focused at the center of the nanowire (relative to its longitudinal axis) in all my measurements. This was performed in order to ensure that a maximum number of SERS probe molecules can be located within the laser spot and avoid any signal contributions or fluctuations arising from the tips. This concept is illustrated in Figure 2.13, which presents SERS spectra for seven different Ag nanowires having similar diameters. Although their lengths varied from 2.5 to 4.8 μm , no significant

variation in the detected SERS intensities was observed. As shown in Figure 2.12A, the SERS spectra from an individual Ag nanowire present a strong laser polarization dependence, in which the signals were more strongly enhanced when the polarization direction was perpendicular to the longitudinal axis (transverse polarization, top trace). In this case, the characteristic 1,4-BDT peaks at 1069, 1181 and 1562 cm^{-1} could be easily resolved in the spectrum.¹⁸ Here, the peak at 1069 cm^{-1} is due to a combination of the phenyl ring breathing mode, CH in-plane bending, and CS stretching, while the peak at 1181 cm^{-1} can be assigned to the 9a vibrational mode (CH bending). The peak at 1562 cm^{-1} can be assigned to the phenyl ring stretching motion (8a vibrational mode).¹⁸ The broad band at 900-1000 cm^{-1} came from the silicon substrate. The shoulder at $\sim 1600 \text{ cm}^{-1}$ is due to direct interactions between the Ag surface and the π -orbital system of the benzene ring in the 1,4-BDT molecule. This interaction occurs as the 1,4-BDT molecule binds to Ag as a dithiolate (via two sulfur atoms), in which the aromatic ring assumes a flat orientation with respect to the Ag surface. This shoulder peak at $\sim 1600 \text{ cm}^{-1}$ was intensified and more easily visualized in the spectra involving the nanowire-based dimers. Based on the area of the peak at 1562 cm^{-1} , the EF for an individual nanowire (EF_{wire}) was 6.4×10^5 in the transverse direction. Conversely, the 1,4-BDT peaks could not be detected in the SERS spectrum when the laser was polarized parallel to the longitudinal axis (longitudinal polarization, bottom trace). This strong polarization dependence for an individual Ag nanowire agrees with previously reported results and finite difference time domain calculations.^{22,23} For Ag nanowires of 50-100 nm in diameter, the transverse plasmon resonance is peaked at $\sim 400 \text{ nm}$ and could be excited by

the 514 nm laser source employed in my measurements.²²⁻²⁴ However, considering the large aspect ratio of the nanowires, it is unlikely that the longitudinal plasmon mode could be excited at this wavelength.

Figure 2.12B shows typical SERS spectra for an individual Ag nanocube under two different laser polarization directions: along a face diagonal and along an edge (top and bottom traces, respectively). The SERS signals from the Ag nanocubes also present a strong dependence on laser polarization, which is consistent with our previous reports.^{19,25} As shown in Figure 2.12B, the 1,4-BDT signals were more strongly enhanced when the nanocube was oriented with one of its face diagonals parallel to the laser polarization direction. This strong dependence on laser polarization could be attributed to the difference in near-field distribution over the surface of the nanocube under different excitation directions.¹⁹ The EF for the nanocube (EF_{cube}) was 3.0×10^6 and 5.8×10^5 for laser polarization along a face diagonal and an edge, respectively.

After the SERS spectra for individual Ag nanowires and nanocubes had been investigated, I turned my attention to dimers comprised of an individual Ag nanowire decorated with a single Ag nanocube. It is worth pointing out that a variety of dimeric structures can exist in this system. For example, during dimerization, a Ag nanocube can approach a nanowire with one of its faces or edges nearly touching the side face of the nanowire. In addition, the nanocube can approach the nanowire at different locations, i.e., in the central region, close to or at the tips of the nanowire. This diversity of structures can complicate a systematic correlation between the hot spots and their corresponding field enhancements. In order to address this issue, I only concentrated on situations in

which the dimerization between a Ag nanowire with a Ag nanocube took place at the midpoint of the Ag nanowire (with respect to its longitudinal axis). This enables maximization of the signal intensities and estimate of the number of probe molecules located within the laser spot size (N_{sers}) by focusing the laser beam directly on the hot spot, i.e., at the nanocube-nanowire intersection. I was interested in two particular dimer geometries: *i*) a Ag nanocube with one side face nearly touching the side face of a Ag nanowire (face-to-face configuration) and *ii*) a Ag nanocube with one edge nearly touching the side face of a Ag nanowire (edge-to-face configuration).

Figure 2.14 shows SERS spectra for two dimers presenting the aforementioned configurations. In Figure 2.14A, the dimer has a face-to-face configuration, in which the hot-spot region involves the narrow gap between a nanocube's face and a nanowire's side face. The inset in Figure 2.14A presents an SEM image of the probed dimer. The nanowire was 93 nm in diameter and 4.1 μm in length, while the nanocube had an edge length of 142 nm. The SERS spectra for the dimer were recorded for two different laser polarization directions: perpendicular and parallel to the long axis of the nanowire. It can be clearly seen that the SERS signals displayed a strong polarization dependence. When the laser was polarized perpendicular to the nanowire's long axis (top trace), the SERS signals were strongly enhanced. In fact, the characteristic peaks for 1,4-BDT were so strong that the Si peak arising from the substrate in the 900-1000 cm^{-1} region essentially disappeared in the baseline. It is important to note that this polarization direction is parallel to the hot-spot axis. In this case, the stronger SERS intensities as compared to the individual components shown in Figure 2.12 are due to the formation of a hot spot

between the nanowire and the nanocube. Under this polarization, EF_{dimer} was calculated as 1.4×10^7 . This corresponds to an increase in EF of 22 and 24 folds relative to the individual EF_{wire} and EF_{cube} . When the laser polarization was parallel to the nanowire's long axis (perpendicular to the hot-spot axis), the intensity of the SERS signals were significantly reduced (bottom trace). The EF_{dimer} was calculated as 1.9×10^5 , which is on the same order of magnitude as EF_{wire} and EF_{cube} . This result suggests that the molecules adsorbed in the hot-spot region did not make any additional contribution towards the SERS signals when the laser was polarized perpendicular to the hot-spot axis. The fact that EF_{dimer} is smaller than EF_{cube} can be explained as follows: N_{sers} for the dimer is higher than N_{sers} for the individual nanocube, as 1,4-BDT molecules are also adsorbed on the surface of the nanowire that is enclosed by the laser spot (outside the hot spot region). However, because the nanowires did not contribute to the detected SERS signals under longitudinal polarization, they did not contribute to I_{sers} . Therefore, under this polarization, there is an increase in N_{sers} that is not accompanied by an increase of I_{sers} for the dimer, leading to an overall reduction in EF_{dimer} as compared to EF_{cube} according to eq. 2.

Figure 2.14B shows SERS spectra for a dimer having an edge-to-face orientation. The inset in Figure 2.14B shows an SEM image of the probed dimer. Here, the hot-spot region comprises the space between a nanocube edge and a nanowire side face. The nanowire was 108 nm in diameter and 3.1 μm in length, while the nanocube had an edge length of 138 nm. Similar to the dimer probed in Figure 2.14A, the SERS spectra displayed a strong dependence on laser polarization. When the laser was polarized

perpendicular to the nanowire's long axis (top trace), the SERS signals were enhanced as compared to the individual components shown in Figure 2.12. In this case, EF_{dimer} was calculated as 4.3×10^6 , which is 3.3 folds smaller than the EF_{dimer} obtained from Figure 2.14A (top trace). Moreover, even though EF_{dimer} is 6.7 folds higher than EF_{wire} , it lies within the same order of magnitude as EF_{cube} (polarization along a face diagonal), indicating that the hot-spot region contributed only moderately to the intensity of the detected SERS signals for the dimer having an edge-to-face configuration under transverse polarization.

According to our DDA calculations for an individual Ag nanocube, the maximum E^4 is roughly 4 folds higher for polarization parallel to a face diagonal than E^4 for polarization along an edge.¹⁹ Since the near fields are concentrated along the laser polarization direction, it can be expected that the dimer having an edge-to-face configuration will display a stronger near field in the hot-spot region. However, there is another important factor that needs to be taken into consideration in order to explain the observed field-enhancements: the number of SERS probe molecules trapped at the hot-spot region. The SERS intensity coming from a hot spot is determined by both the near-field strength in the hot spot region and the number of molecules that will have their scattering cross-sections enhanced when they are subjected to the near field.

A schematic representation of dimers probed in Figure 2.14 and their respective hot-spot configurations are shown in Figure 2.15. In Figure 2.14A (face-to-face configuration), the nanocubes are ~142 nm in edge length and they contribute ~37,340 1,4-BDT molecules to the hot-spot region (based on a molecular footprint of 0.54 nm^2 for

1,4-BDT). However, for the dimer in Figure 2.14B (edge-to-face orientation), the number of 1,4-BDT molecules trapped in the hot-spot region is expected to be much lower. For example, if I assume that only 1,4-BDT molecules enclosed by a 4 nm distance (from the nanocube surface to the nanowire surface) in the nanocube-nanowire junction are enclosed by the hot-spot region (Figure 2.15), the nanocubes only contributed $\sim 2,900$ 1,4-BDT molecules to the hot spot. This corresponds to a difference of 34,440 molecules (92 %). Therefore, it is plausible to assume that when the hot spot possesses an edge-to-face orientation, the smaller number 1,4-BDT molecules trapped in the hot-spot region compared to the face-to-face orientation can lead to significantly lower scattering intensities. More specifically, the increased near field strength in the hot spot is not sufficiently large to compensate for the significant reduction in number of molecules trapped within the hot-spot region, leading to an overall decrease in the SERS intensities.

When the laser polarization was parallel to the nanowire's long axis, the intensity of the SERS signals was decreased and EF_{dimer} was calculated as 7.9×10^5 (bottom trace, Figure 2.14B). Similar to what was observed for the dimer displayed in Figure 2.14A, EF_{dimer} is within the same order of magnitude as EF_{cube} , suggesting that the molecules adsorbed in the hot-spot region did not make any additional contribution towards the SERS signals when the laser was polarized perpendicular to the hot-spot axis.

Figure 2.16 summarizes the EFs measured for individual Ag nanowires, nanocubes, and their respective dimers probed in Figures 1.12 and 1.14. It is clear that the highest EF was obtained for the dimer in which the Ag nanocube was oriented with one of its faces nearly touching the side face of a Ag nanowire. In this case, the face-to-face

geometry allows for the highest number of SERS probe molecules to be trapped within the hot spot. In general, when the laser was polarized perpendicular to the nanowire's long axis and parallel to the hot-spot axis, a higher strength in near field is expected to be enclosed in the hot-spot region, leading to increased SERS signals for the dimers in comparison to EF_{wire} and EF_{cube} . However, when the laser was polarized perpendicular to the hot-spot axis, the near field is expected to be concentrated outside the hot-spot region, leading to a decrease in EF_{dimer} , which becomes equaled to the EFs for the individual nanoparticle components.

I have also tried to isolate and selectively probe the hot-spot region formed between a Ag nanowire and a Ag nanocube in a face-to-face configuration using my previously reported approach based on plasma etching (see Figure 2.17 and 2.18).²⁵ In this case, the dimer was first functionalized with 4-MBT and the SERS spectrum was recorded. Then, the sample was plasma etched. As previously demonstrated in a dimer made of two sharp Ag nanocubes, the plasma etching was able to remove only the SERS probe molecules absorbed outside the hot-spot region, leading to the isolation of the hot spot.²⁵ After plasma etching, the SERS spectrum was taken and the detected signals originated only from the probe molecules trapped in the hot-spot region. Finally, the sample was immersed in a different SERS probe, such as 1,4-BDT to confirm that no significant changes to the surface of the dimer took place during these steps and that the final spectrum resembles the initial with respect to its signal intensities. Figure 2.18 shows the SERS spectra recorded for transverse polarization during each of these steps for a dimer having a face-to-face orientation (inset). The SERS spectrum from the dimer

functionalized with 4-MBT (top trace) clearly shows the characteristic 4-MBT peaks at 1072 and 1582 cm^{-1} .^{12,13} After plasma etching (middle trace), all the 4-MBT signals disappeared from the spectrum, indicating complete removal of 4-MBT molecules from the dimer, including those trapped in the hot-spot region. This result suggests that, in this system, the plasma etching did not enable hot-spot isolation. This can be interpreted in terms of the hot-spot geometry, as shown in Figure 2.19. In the dimers made of two sharp Ag nanocubes, the hot-spot region comprises a narrow gap between two nearly touching nanocube faces. Therefore, the 4-MBT molecules in the hot spot can be considered as a multilayer resist relative to the oxygen plasma, which allows for their incomplete removal and thus hot spot isolation during the plasma etching process. However, in the dimer comprising a nanowire and a nanocube, the 4-MBT molecules trapped in the hot-spot region are readily exposed to the oxygen plasma owing to the pentagonal cross-section of the nanowire, enabling their complete removal by plasma etching. After the sample was immersed in 1,4-BDT, all the characteristic peaks for 1,4-BDT were detected in the spectrum again, indicating that no significant changes took place on the surface of the dimers during the plasma etching.

I also probed systems in which the dimerization between a nanocube and the side face of a nanowire took place at a position close to the tip of the nanowire instead of its midpoint. Figure 2.20 shows SEM images of the probed dimers together with their SERS spectra recorded with the laser polarization being parallel to the hot-spot axis. Similarly, I was interested in two particular configurations for the nanowire-nanocube dimers: *i*) face-to-face and *ii*) edge-to-face. The signal intensities in the SERS spectra for the dimers

presented in Figure 2.20 are consistent with those in Figure 2.14. The SERS intensities were the highest for the dimer having a face-to-face configuration as compared to the edge-to-face orientation (see the insets and spectra *i* and *ii*, respectively). Interestingly, the signal intensities were further reduced for dimers comprised of a Ag right bipyramid (instead of a Ag nanocube) having one of its tips nearly touching the side face of a Ag nanowire, as shown in the insets and spectra *iii* and *iv*, respectively. In the dimer involving a right bipyramid, the hot-spot region can be described as the narrow gap between one of the bipyramid's tips and the side face of the Ag nanowire (tip-to-face configuration). In this context, it can be expected that the number of 1,4-BDT molecules trapped within the hot-spot region would be further reduced in comparison to the dimer in which the nanocube approaches the nanowire in an edge-to-face orientation. These results also suggest that the number of molecules trapped in the hot-spot region played a key role in determining the SERS intensities in dimers comprised of an individual Ag nanowire and a nanocube or right bipyramid. Taken together, it is plausible that the gradual reduction in the number of molecules trapped within the hot-spot region (face-to-face, edge-to-face and tip-to-face configurations, respectively) was responsible for the corresponding decrease in signal intensities detected in the nanowire-based dimers (*i-iv*).

2.4.2. Summary

I have measured the SERS EFs for dimers comprised of an individual Ag nanowire and a single Ag nanocube. My results showed that the largest field enhancement was obtained when the laser was polarized parallel to the hot-spot axis.

Moreover, the detected SERS intensities were dependent on the hot-spot structure, i.e., the relative orientation of the Ag nanocube with respect to the nanowire's side face. The strongest enhancement was observed when the nanocube was oriented with one of its side faces nearly touching the side face of the nanowire (face-to-face configuration). In this case, the EF_{dimer} was 1.4×10^7 , which corresponds to an increase of 22 and 24 folds relative to an individual nanowire and nanocube, respectively. Conversely, when the nanocube was oriented with one of its edges nearly touching the side face of the nanowire, the EF_{dimer} was 4.3×10^6 , which represents a decrease of 3.3 folds as compared to the dimer having a face-to-face configuration. In these systems, the difference in the measured EF_{dimer} could be explained based upon different hot-spot structures, in which the strongest EF was obtained when the hot-spot configuration allowed for a larger number of probe molecules to be trapped in the hot-spot region. The results presented herein indicate that, in addition to the concentration of near fields in the hot-spot region, the number of molecules trapped at the narrow gap between almost touching particles (interparticle hot-spot) plays an important role in determining the SERS intensities of dimers constructed from a Ag nanowire and a Ag nanocube.

2.5. Measuring the SERS Enhancement Factors for Hot-Spots with Different Morphologies in Dimers consisting of Ag Nanospheres and Nanocubes

In nanocube-nanowire dimers (Section 2.4.), I found that the different orientations of the Ag nanocube with respect to the nanowire's side face played a central role over the

detected SERS EF.²⁶ In this context, it is important to note that there have been very few investigations regarding how different dimer configurations, i.e., hot-spot morphologies, would affect the EFs.^{10a,26} As the near-field distribution and the number of probe molecules at the hot spot are dependent upon the particle shape and hot-spot morphology, such a systematic investigation would be very attractive not only for the fundamental understanding of the hot-spot phenomenon, but also from a practical aspect, providing a venue for the maximization of SERS signals coming from individual hot spots.

In this section, I report on a systematic investigation of the SERS activity of hot spots presenting a variety of well-defined morphologies formed between two Ag nanospheres and two Ag nanocubes. Specifically, I investigated four distinct dimer geometries: *i*) two nearly touching Ag nanospheres; *ii*) a sharp Ag nanocube having one face nearly touching the face of another Ag nanocube; *iii*) a sharp Ag nanocube having one edge nearly touching the face of another Ag nanocube and *iv*) a sharp Ag nanocube having one edge nearly touching the edge of another Ag nanocube. In these systems, the hot spot region can be described as the narrow gap between: *i*) two spherical caps, *ii*) two nanocube faces, *iii*) a nanocube edge and a nanocube face and *iv*) two nanocube edges (cap-to-cap, face-to-face, edge-to-face and edge-to-edge configurations, respectively). Taken together, by probing the EFs for these dimeric structures (EF_{dimer}) presenting well-defined hot-spot morphologies, I expect to systematically investigate how the concentration of near fields and probe molecules at the hot-spot region impacts EF_{dimer} relative to their individual nanosphere and nanocube counterparts.

2.5.1. Results and Discussion

Figure 2.21 displays SEM images for the Ag nanospheres and nanocubes employed in my SERS studies. The Ag nanospheres were 81.1 ± 5.3 nm in diameter, while the sharp Ag nanocubes had an edge length of 100.7 ± 5.7 nm. It is important to note that the utilization of Ag nanospheres and nanocubes as substrates for SERS is attractive for a number of reasons. For example, they can be routinely synthesized with good uniformity in terms of shape, size and surface smoothness by the polyol method.^{15,27} Due to their dimensions, individual nanospheres, nanocubes and their dimers can be easily found under a dark-field optical microscope during the SERS measurements. Also, as they present similar sizes, they allow for a direct correlation among the detected SERS signals, their corresponding EFs and specific hot-spot morphologies. Finally, Ag nanospheres and nanocubes are suitable building blocks to generate dimers presenting a variety of hot-spot configurations, in which hot-spot region can be comprised of rounded, flat and sharp surfaces.

I started my study by evaluating the SERS properties of individual Ag nanospheres and nanocubes. Figure 2.22A shows typical SERS spectra for an individual Ag nanosphere under two different laser polarization directions: parallel and perpendicular to the nanosphere equatorial axis relative to the SEM image depicted in the inset (top and bottom traces, respectively). The SERS spectra for the Ag nanospheres display no laser polarization dependency, as no significant variations on signal intensities were observed for the different laser polarization directions. In both spectra, the characteristic 4-MBT peaks at 1072 and 1582 cm^{-1} could be easily resolved.¹⁷ Here, the

peak at 1072 cm^{-1} is due to a combination of the phenyl ring-breathing mode, CH in-plane bending, and CS stretching, while the peak at 1582 cm^{-1} can be assigned to phenyl ring stretching motion (8a vibrational mode).^{12,13} The broad band at $900\text{-}1000\text{ cm}^{-1}$ came from the Si substrate. Based on the area of the peak at 1582 cm^{-1} , the EF for an individual nanosphere (EF_{sphere}) was 1.7×10^7 and 1.6×10^7 (top and bottom traces, respectively). Figure 2.23 displays the SERS spectra for 10 distinct individual Ag nanospheres. In all cases, no significant variations in the signal intensities were observed, indicating the SERS spectra for the Ag nanospheres were consistent and reproducible. Figure 2.22B shows typical SERS spectra for an individual Ag nanocube under two laser polarization directions: along a face diagonal and along an edge (top and bottom traces, respectively). The SERS signals from the Ag nanocubes presented a strong dependence on laser polarization, which is consistent with our previous reports.^{19,25} As shown in Figure 2.22B, the 4-MBT signals were more strongly enhanced when the nanocube was oriented with one of its face diagonals parallel to the laser polarization direction. This strong dependence on laser polarization could be attributed to the differences in the near-field distribution over the surface of the nanocubes under different excitation directions.¹⁹ The EF for the nanocube (EF_{cube}) was 3.0×10^6 and 5.8×10^5 for laser polarization along a face diagonal and an edge, respectively.

These results show that EF_{sphere} was higher than EF_{cube} when the SERS spectrum is taken for the individual nanosphere and nanocube supported over a Si substrate. This is an intriguing observation. Generally, theoretical calculations predict that sharp nanoscale features can provide stronger Raman scattering intensities than rounded counterparts as

they allow for a higher concentration of near fields (lightning rod effect).¹⁶ Therefore, the nanocubes can be expected to display a higher concentration of near fields at their surface (concentrated at the corners) as compared to nanospheres of similar size (concentrated at opposite sides of the equatorial axis). In fact, SERS measurements in solution agree with this prediction. We have previously shown that, for solution-based SERS measurements employing Ag nanospheres and nanocubes having similar sizes, EF_{cube} were higher than EF_{sphere} .²⁸ Figure 2.24 displays SERS measurements performed in solution for the Ag nanospheres and Ag nanocubes employed in this work. According to the solution spectra, EF_{sphere} and EF_{cube} were 3.0×10^5 and 1.4×10^6 , respectively, confirming that EF_{cube} is higher than EF_{sphere} in the solution-based SERS spectra.

In order to explain the results observed herein for the supported nanoparticles, I have to consider the effect of the substrates over the plasmon resonance of the metal nanoparticles. It has been reported that an adjacent or an isotropically surrounding medium (metallic, semiconducting or dielectric) alters the plasmonic properties of a nanoparticle.^{29,30} In this respect, we have previously performed finite-difference time-domain (FDTD) calculations to study the effect of an adjacent substrate (glass) over the plasmonic properties of an individual Ag nanocube that was 90 nm in edge length (Figure 2.25).³⁰ These calculations have shown that, the single dipole resonance associated with the solution spectrum splits into two peaks when the nanocube approaches the substrate (Figure 2.25A). More specifically, the dipole resonance broadens and splits into a peak at 430 nm associated with large near fields away from the substrate and a peak at 550 nm associated with large near fields towards the substrate (Figure 2.25B and C). Thus, it is

plausible to assume that the near field distribution for the supported nanocube will have a significant contribution from large near fields pointing towards the substrate (Figure 2.25C) under the 514 nm excitation wavelength employed in my SERS measurements. However, because the Ag nanocubes were functionalized with 4-MBT after they had been deposited over the substrate, the bottom face of the nanocube that is in contact with the Si surface is expected to not contain any 4-MBT molecules (see inset Figure 2.25C). Here, it is possible that the EF for the supported nanocube is lower than expected because there were no SERS probe molecules absorbed on the region containing a high concentration of near fields, i.e., region encompassing the near fields that point towards the substrate.

Similar FDTD calculations for an individual Ag nanosphere showed that, differently from the nanocube, the presence of an adjacent substrate does not alter its near field distribution. In this case, only one dipolar plasmon resonance was observed as the nanosphere approached the substrate, in which the near-fields were concentrated along the equatorial position parallel to the laser polarization direction. As 4-MBT molecules are present along the equatorial positions in the sphere (region enclosed by the near field-distribution), the signal intensities were not affected. In this context, the “damping” observed for the supported nanocube is significant enough to cause EF_{cube} to be smaller than EF_{sphere} . It is important to note that a complete study of the substrate effect over the SERS spectra of Ag nanoparticles of different shapes is currently being investigated in our group. Our preliminary results indicate that the SERS spectrum of a supported nanocube having 6 faces functionalized with a SERS probe display, indeed, stronger

field-enhancements as compared to supported nanospheres of similar size, which is in agreement with my observations.

After the SERS spectra for the individual nanospheres and nanocubes had been investigated, I turned my attention to dimers composed of two Ag nanospheres and two Ag nanocubes, in which the hot-spot region displays a *i*) cap-to-cap, *ii*) face-to-face, *iii*) edge-to-face and *iv*) edge-to-edge configurations. Figure 2.26 presents the SERS spectra obtained for individual dimers displaying the aforementioned configurations and the insets show their corresponding SEM images. Here, the laser was polarized parallel to the dimer's longitudinal axis, i.e., parallel to the hot-spot axis. Under this polarization, the characteristic 4-MBT SERS signals were enhanced as compared to Figure 2.22 due to the formation of a hot spot. Also, it can be clearly seen from the spectra that the SERS intensities gradually decreased from the (*i*) cap-to-cap towards the (*iv*) edge-to-edge configuration. Under this polarization, EF_{dimer} for the cap-to-cap configuration (two Ag nanospheres) was calculated as 1.7×10^8 . This corresponds to an increase of 10 folds relative to EF_{sphere} . For the Ag nanocube dimers, EF_{dimer} were calculated 2.0×10^7 , 1.5×10^7 , and 5.6×10^6 for the face-to-face, edge-to-face and edge-to-edge configurations, respectively. This corresponds to an increase of 28, 9 and 2 folds, respectively, as compared to EF_{cube} . According to these results, the highest field-enhancement was obtained for the dimer composed of two Ag nanospheres (cap-to-cap configuration). However, if we consider the relative increase on EF_{dimer} with respect to EF_{sphere} and EF_{cube} , the highest field-enhancement was obtained for the dimer made of two Ag nanocubes displaying a face-to-face configuration. Moreover, the lowest field-

enhancement was observed for the dimer presenting an edge-to-edge geometry. In this case, EF_{dimer} was within the same order of magnitude as EF_{cube} (polarization along a face diagonal), indicating the hot-spot did not significantly contribute to the obtained field enhancements.

As I previously described in dimers made of an individual Ag nanowire and a single Ag nanocube, the SERS intensity coming from a hot spot is determined by both the near-field concentrations at the hot spot and the number of molecules that have their scattering cross-sections enhanced when they are subjected to the near fields, i.e., the number of SERS probe molecules trapped at the hot-spot region.²⁶ A schematic representation of dimers probed in Figure 2.26 and their respective hot-spot configurations are shown in Figure 2.27. Here, the relative increase in EF_{dimer} with respect to their individual nanoparticle counterparts could be directly correlated to number of molecules trapped within the hot-spot region ($N_{hot-spot}$). Based on the molecular footprint for 4-MBT and the dimensions of the nanocubes and nanospheres, $N_{hot-spot}$ was $\sim 105,263$ for the face-to-face configuration. This corresponds to 20 % of total number of 4-MBT molecules in the dimer (N_{sers}). When the dimers presented a cap-to-cap and edge-to-face configuration, $N_{hot-spot}$ was reduced to 16,033 and 10,210 molecules (8 and 2 % of N_{sers}), respectively. Finally, further reduction in $N_{hot-spot}$ took place for the dimer displaying an edge-to-edge orientation. Here, $N_{hot-spot}$ was 5,894 molecules (1 % of N_{sers}). In these systems, it is plausible that this gradual and significant reduction in $N_{hot-spot}$ (face-to-face > cap-to-cap > edge-to-face > edge-to-edge) was responsible for the corresponding decrease in EF_{dimer} with respect to their individual

nanoparticle counterparts.

According to our DDA calculations for an individual Ag nanocube, the $|E|_{\max}$ was estimated as 26.5 and 37.8 for laser polarizations along an edge and along a face diagonal, respectively.¹⁹ For a Ag nanosphere, $|E|_{\max}$ was estimated as ~ 4.0 . As the near-fields are distributed along the laser polarization direction, it can be expected that the concentration of near fields at the hot-spot region in the dimers probed in Figure 2.26 decreases in the order: edge-to-edge > edge-to-face > face-to-face > cap-to-cap. This corresponds to the opposite trend with respect to the detected SERS intensities and EF_{dimer} . Therefore, my results indicate $N_{hot-spot}$ was the most important factor dictating the SERS intensities and their relative field-enhancements in the dimers probed in Figure 2.26. More specifically, the increased concentration of near fields at the hot spot region in the dimer configurations that allow for sharp features to be located within the hot-spot region was not sufficiently large to compensate the associated reduction in $N_{hot-spot}$.

Figure 2.28 presents the SERS spectra obtained for the dimers presenting cap-to-cap, face-to-face, edge-to-face and edge-to-edge configurations in which the laser was polarized perpendicular to the longitudinal axis in the dimers, i.e., perpendicular to the hot-spot axis. It can be observed that the intensity of the SERS signals were significantly decreased for all dimers as compared to Figure 2.24. Here, EF_{dimer} were calculated as 1.5×10^7 , 6.6×10^5 , 1.9×10^6 and 3.0×10^6 for the cap-to-cap, face-to-face, edge-to-face and edge-to-edge configurations, respectively. These EFs are within the same order of magnitude as their corresponding single-particle counterparts, suggesting that the molecules adsorbed in the hot-spot region did not make any additional contribution

towards the SERS signals when the laser was polarized perpendicular to the hot-spot axis. Figure 2.29 summarizes all the EFs calculated for the individual nanospheres, nanocubes, and their respective dimers probed in Figures 2.26 and 2.28. When the laser was polarized parallel to the hot-spot axis, near-fields can be expected to be concentrated along the hot-spot region, leading to increased SERS signals for the dimers as compared to the individual nanospheres and nanocubes. However, when the laser was polarized perpendicular to the hot-spot axis, the near fields are expected to be concentrated outside the hot-spot region, leading to a decrease in EF_{dimer} , which becomes equaled to the EF_{sphere} and EF_{cube} for the individual nanoparticle components.

2.5.2. Summary

I have measured the SERS EFs for individual nanoparticle dimers presenting a variety of distinct and well-defined hot-spot morphologies. In particular, I probed dimers comprised of two Ag nanospheres (hot-spot displaying a cap-to-cap configuration) and two Ag nanocubes (hot-spot displaying face-to-face, edge-to-face and edge-to-edge configurations). My results showed that the largest field enhancements were obtained when the laser was polarized parallel to the hot-spot axis. Moreover, the detected SERS intensities and were strongly dependent on the hot-spot morphology. The calculated EF_{dimer} were 1.7×10^8 , 2.0×10^7 , 1.5×10^7 , and 5.6×10^6 for the cap-to-cap, face-to-face, edge-to-face and edge-to-edge configurations, respectively. This corresponds to an increase of 10, 28, 9 and 2 folds, respectively, as compare to their individual nanoparticle counterparts. Although the highest EF was observed for the dimer displaying cap-to-cap

configuration, the highest increase in EF_{dimer} as compared to EF_{sphere} and EF_{cube} was obtained for the dimer in a face-to-face configuration. In this case, a direct correlation between $N_{hot-spot}$ and the relative increase in EF_{dimer} as compared to EF_{sphere} and EF_{cube} was observed, in which the highest field enhancements were obtained for the configurations that allowed for a higher number of molecules to be trapped within the hot-spot region. The results presented herein indicate that, regardless of the concentration of near fields, the number of molecules trapped at the hot-spot region was the most important factor determining the field-enhancements in dimers constructed from Ag nanospheres and nanocubes.

Overall, I developed in this chapter two approaches for selectively probing the SERS activities of individual hot spots, i.e., experimentally detect the SERS signals only for the molecules that are trapped within the hot-spot region in individual Ag nanoparticle dimers (Sections 2.2 and 2.3). To our knowledge, these demonstrations represented the first attempt to isolate the hot spot formed between two Ag nanoparticles with subsequent measurements of the SERS enhancement factor intrinsic to a hot spot. I also performed a systematic investigation on the SERS activity of individual dimers composed of two closed spaced Ag nanoparticles. For the first time in this field, by employing Ag nanoparticles displaying a variety of well-defined shapes, sizes, and orientations, I was able to precisely and systematically correlate the experimentally detected field-enhancements to the specific geometry of a hot-spot. My results demonstrated that the number of probe molecules at the hot-spot region was the most important factor to the detected field-enhancements for the dimers. In this case, the

highest field enhancements ($EF \sim 10^7$ - 10^8) were detected for dimer configurations that allowed for a higher number of probe molecules to be trapped within the hot-spot region.

2.6. Experimental Section

Chemical and Materials. Silver nitrate (AgNO_3 , 99%), poly(vinyl pyrrolidone) (PVP, $M_w \approx 55,000$), Hydrochloric acid (HCl, 37%), Iron Nitrate ($\text{Fe}(\text{NO}_3)_3$, 98+%) and 4-methylbenzenethiol (4-MBT, 98%) were all obtained from Sigma-Aldrich and used as received. 1,4-benzenedithiol (1,4-BDT, 98%) was obtained from Alfa Aesar. Ethylene glycol (EG) was obtained from J. T. Baker, and Ethanol (200 proof) was obtained from Pharmco Products Inc. All aqueous solutions were prepared with deionized water (18.1 $M\Omega$ cm).

Synthesis of Ag nanosphere dimers (30 nm in diameter). Our developed approach was based upon the polyol process in which ethylene glycol (EG) serves as a solvent and a precursor to the reducing agent. By introducing a small amount of sodium chloride into the reaction solution,¹⁴ we could obtain single-crystal silver nanoparticles as a result of oxidative etching and at the same time induce dimerization due to a change to colloidal stability. In a typical synthesis, we obtained dimers consisting of silver nanospheres ~ 30 nm in diameter and separated by 1.8 nm in the solution phase with a yield $>50\%$.

Synthesis of Ag nanocubes 100 nm in edge length. The Ag nanocubes were synthesized according to our previously reported procedures.¹⁵ In a typical synthesis, 5 mL of EG was placed in a 20-mL vial, capped, and heated with magnetic stirring in an oil

bath at 150 °C for 1 h. 0.75 mL of 12 mM HCl in EG was then quickly added into the vial, and the vial was recapped. After 10 min, 1.5 mL each of 94 mM AgNO₃ and 147 mM PVP, both dissolved in EG, were simultaneously added through a two-channel syringe pump (KDS-200, KD Scientific, Holliston, MA) at a rate of 22.5 mL per hour into the vial. The vial was then capped and continued with heating at 150 °C until the solution turned into an ocher color. Upon injection of the AgNO₃ solution, the reaction mixture went through a series of color changes that included milky white, light yellow, transparent, red, and ocher. The final product, silver nanocubes with sharp corners, was obtained via centrifugation (30 min at 3,900 rpm) and washed with acetone once and ethanol twice to remove excess EG and PVP and finally re-dispersed in ethanol water for further use in the preparation of SERS substrates.

Synthesis of Ag nanowires and nanocubes. The Ag nanowires and nanocubes were synthesized according to our previously reported procedures.^{15,21} For the Ag nanocubes, AgNO₃ was reduced in EG at 140 °C in the presence of PVP and HCl. EG served as the solvent and source of the reducing agent (glycolaldehydes), while HCl acted as a oxidative etchant. In a typical synthesis, 25 mL of EG was placed in a 100-mL round bottom flask, capped, and heated with stirring in an oil bath at 140 °C for 1 h. HCl (5 mL of a 3 mM solution in EG) was then quickly added, and the vial was recapped. After 10 min, AgNO₃ (15 mL of a 94 mM solution in EG) and PVP (15 mL of a 147 mM solution in EG) were simultaneously added with a two-channel syringe pump (KDS-200, Stoelting, Wood Dale, IL) at a rate of 45 mL per hour to the stirring solution. The flask was then capped and heated at 140 °C. The reaction was allowed to continue overnight

before quenching in an ice bath and washing with acetone and water. A similar protocol (with the exception that the amount of HCl employed in the synthesis was 1 mL of 3 mM solution in EG) was used to produce the Ag nanowires, which were then mixed with Ag nanocubes at a ratio of 1 to 1. The mixture was then washed with acetone and ethanol to remove EG and excess PVP, and then re-dispersed in ethanol for further use in the preparation of SERS substrates.

Synthesis of Ag nanospheres 80 nm in diameter. The Ag nanospheres were prepared via the truncation of the Ag nanocubes in the presence of $\text{Fe}(\text{NO}_3)_3$.²⁷ In brief, 0.01 g of PVP was dissolved in 1.5 mL of ethanol. A suspension containing the Ag nanocubes dispersed in H_2O was added into this ethanol solution and kept under stirring. 50 μl of 10 mM $\text{Fe}(\text{NO}_3)_3$ aqueous solution was added to this mixture and the reaction was allowed to proceed at room temperature for 2 hours. The final the product was collected by centrifugation at 10,000 rpm and washed three times with ethanol. The sample was then re-dispersed in ethanol for further for further use in the preparation of SERS substrates.

Preparation of substrates for correlated SERS/SEM experiments. Samples for correlated SEM and SERS experiments were prepared by drop-casting an ethanol suspension of the Ag nanoparticles (nanocubes, nanowires and nanospheres) on a Si substrate that had been patterned with registration marks and letting it dry under ambient conditions. In this case, dimers could form spontaneously via aggregation during solvent evaporation. Functionalization with 1,4-BDT or 4-MBT was performed by immersing the substrate containing Ag nanocubes in a 5 mM ethanol solution (5 mL) of 1,4-BDT or 4-

MBT, respectively, for 1 h. The sample was then taken out, washed with copious amounts of ethanol, and finally dried under a stream of air. All samples were used immediately for SERS measurements after preparation.

Instrumentation. The SERS spectra were recorded using a Renishaw inVia confocal Raman spectrometer coupled to a Leica microscope with 50× objective (NA = 0.90) in backscattering geometry. The 514 nm wavelength was generated with an argon laser coupled to a holographic notch filter with a grating of 1200 lines per millimeter. For the 785 nm wavelength, diode laser was used under similar conditions. The backscattered Raman signals were collected on a thermoelectrically cooled (-60 °C) CCD detector. The scattering spectra were recorded in the range of 800-2000 cm^{-1} , in one acquisition, 30 s accumulations, and 0.5 or 0.7 mW (514 nm) or 1.5 mW (785 nm) at the sample. For 514 nm laser excitation wavelength, the laser spot size was approximated as 730 nm using the following expression for a focused Gaussian beam, which is valid when a laser light is focused by a microscopy objective and the beam diameter is smaller than the back diameter of the objective:

$$w_0 = (4 \times \lambda) / (\pi \times NA) \quad (2.1)$$

where w_0 is the minimum waist diameter for a laser beam of wavelength λ , focused by an objective with a numerical aperture NA . In the spectra, the broad band at 900-1000 cm^{-1} can be attributed to the Si substrate and was used in this work as a reference for intensity normalization. SEM images were taken using an FEI field-emission microscope (Nova

NanoSEM 230) operated at an accelerating voltage of 15 kV. Plasma etching was performed in a plasma cleaner/sterilizer (Harrick Scientific Corp., PDC-001) operated at 60 Hz and 0.2 Torr of air, with power being set to high. In a typical process, the sample was placed in the plasma cleaner chamber and exposed to the oxygen plasma for 6 min. Since plasma etching is highly sensitive to many parameters, one needs to at least optimize the etching time/air pressure when this protocol is applied to a specific system.

Calculation of the Enhancement Factors (EF). We employed the peak at 1562 cm^{-1} (for 4-MBT) or the peak at 1582 cm^{-1} (for 1,4-BDT) to estimate the EF through the following equation:

$$EF = (I_{\text{sers}} \times N_{\text{bulk}}) / (I_{\text{bulk}} \times N_{\text{sers}}) \quad (2.2)$$

where I_{sers} and I_{bulk} are the intensities of the same band for the SERS and bulk spectra, N_{bulk} is the number of molecules probed for a bulk sample, and N_{sers} is the number of molecules probed in the SERS. The areas of the 1562 cm^{-1} or 1582 cm^{-1} bands were used for the intensities I_{sers} and I_{bulk} . We chose this band because it was the strongest band in the spectra. N_{bulk} was determined based on the Raman spectrum of a 0.1 M 1,4-MBT or 0.1M 1,4-BDT solution in 12 M $\text{NaOH}_{(\text{aq})}$ and the focal volume of our Raman system (1.48 μL). When determining N_{sers} , we assumed that the 4-MBT molecules were adsorbed as a complete monolayer with a molecular footprint of 0.19 nm^2 .^{12,13} For 1,4-BDT, the molecular footprint was 0.54 nm^2 .¹⁸ These assumptions represent the theoretically maximum number of molecules and is therefore an overestimate. Thus, the calculated EF

will likely be an underestimate rather than an overestimate of the enhancement. A laser spot of 730 nm in diameter (eq. 2.1) was employed for calculating N_{SERS} in the nanowires, nanocubes and their respective dimers. As 4-MBT and 1,4-BDT do not present any absorption bands matching the laser wavelengths used in this study, any possibility of resonance Raman effects can be ruled out from the calculated EFs.

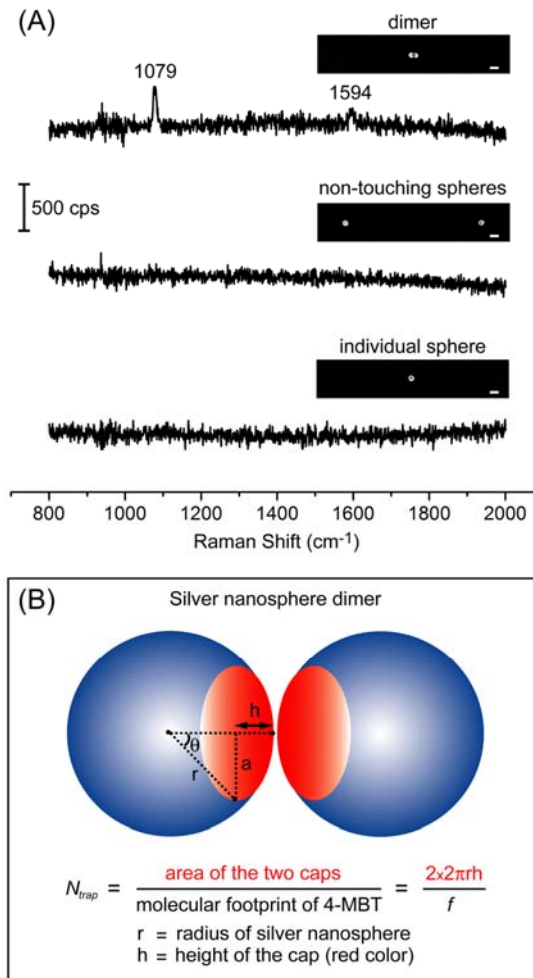


Figure 2.1. (A) SERS spectra taken from (top) a dimer of silver nanospheres, (middle) two silver nanospheres separated by ~ 600 nm, and (bottom) a single silver nanosphere. The scale bars in the insets correspond to 50 nm. (B) A schematic showing my approach to estimate the number of probe molecules trapped in the hot spot (N_{trap}) of a dimer. The hot spot region is assumed to comprise a cap on the surface of each nanosphere in the interparticle region of the dimer (red color). N_{trap} is obtained by calculating the total surface area of the hot spot region (surface area of the two caps) and dividing it by the molecular footprint of a 4-MBT molecule. In my calculations, $h = r/6.6$ (where h is the height of the cap and r is the radius of the nanosphere).

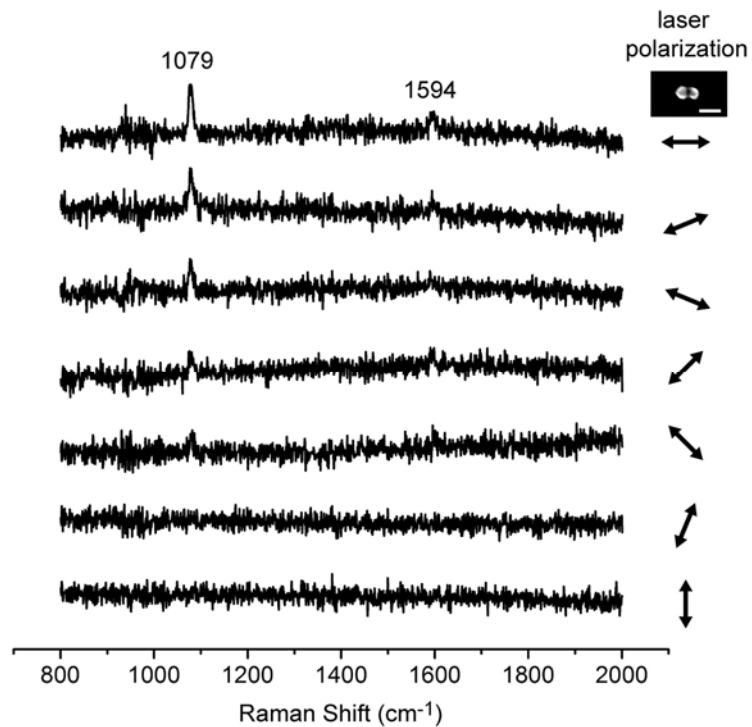


Figure 2.2. SERS spectra taken from a dimer of silver nanospheres (same as the one shown in Figure 2.1A) under different orientations relative to laser polarization. The 4-MBT peaks were maximized when the laser polarization was parallel to the longitudinal axis of the dimer. All spectra were taken with 785 nm excitation laser, 30 s accumulation, 1.5 mW at the sample. The scale bar in the inset corresponds to 50 nm.

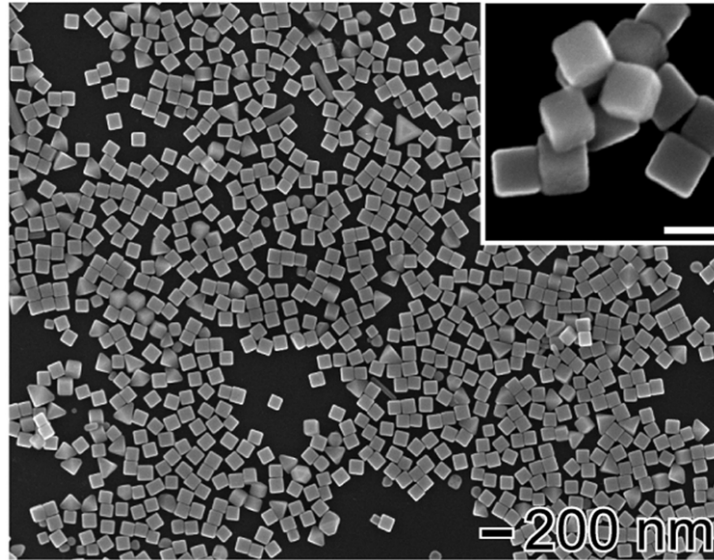


Figure 2.3. SEM image of the sharp Ag nanocubes employed in my SERS measurements. Their average edge length was 100 ± 5.7 nm. The scale bar in the inset corresponds to 100 nm.

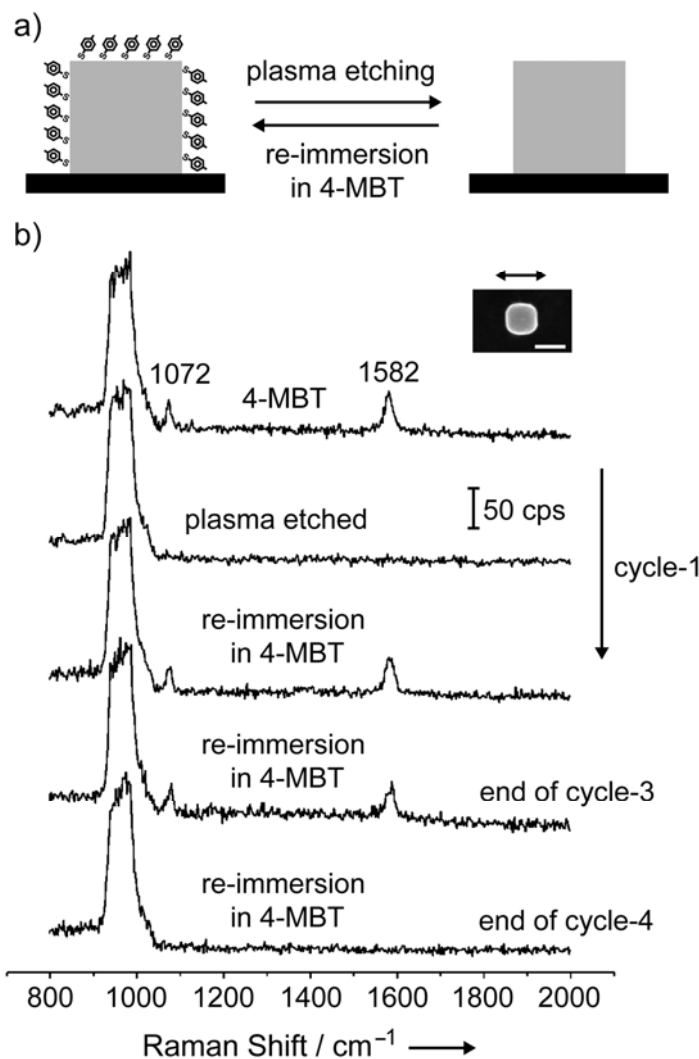


Figure 2.4. (a) Schematic of the approach employed for removal and functionalization of a single Ag nanocube with 4-MBT via plasma etching and re-immersion in a 4-MBT solution. (b) SERS spectra from a single Ag nanocube functionalized with 4-MBT, followed by successive cycles of plasma etching and re-immersion in 4-MBT (from top to bottom, respectively). The exchange process could occur up to three cycles of plasma etching and re-immersion in 4-MBT solution. After the fourth round of plasma etching, the Ag nanocubes could not be re-functionalized with 4-MBT any further. The SEM image in the inset was taken after the fourth round of plasma etching; the slight truncation at corners is probably due to surface oxidation under extended exposure to the oxygen-plasma. The scale bar in the inset corresponds to 100 nm.

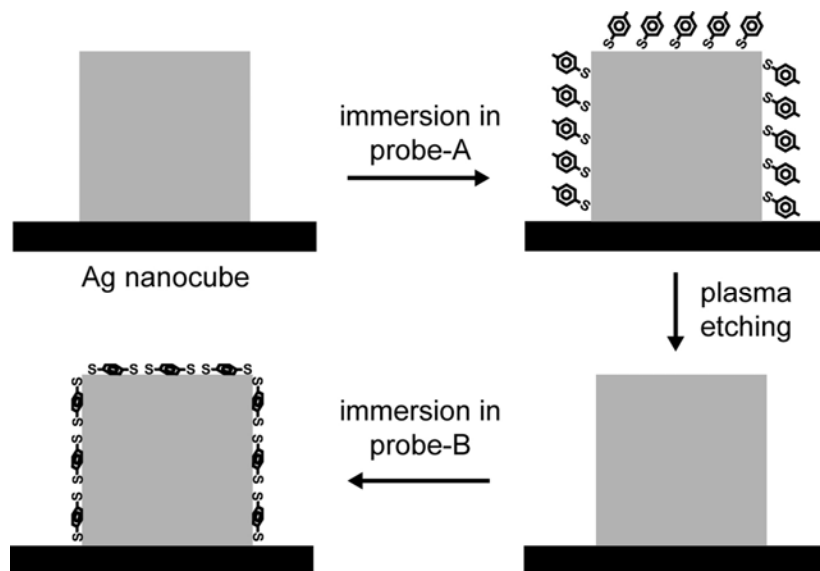


Figure 2.5. Schematic of the approach employed for the exchange between 4-MBT (probe-A) and 1,4-BDT (probe-B) on a single Ag nanocube. The Ag nanocube is functionalized with probe-A and then exposed to plasma etching to remove the adsorbed probe-A molecules from the surface of the nanocube. In the next step, the nanocube is immersed in a solution of probe-B molecules. As 4-MBT and 1,4-BDT present different Raman signatures, the exchange process can be readily monitored by observing the shift in the 8a band ($1550\text{-}1600\text{ cm}^{-1}$) for the benzene ring.

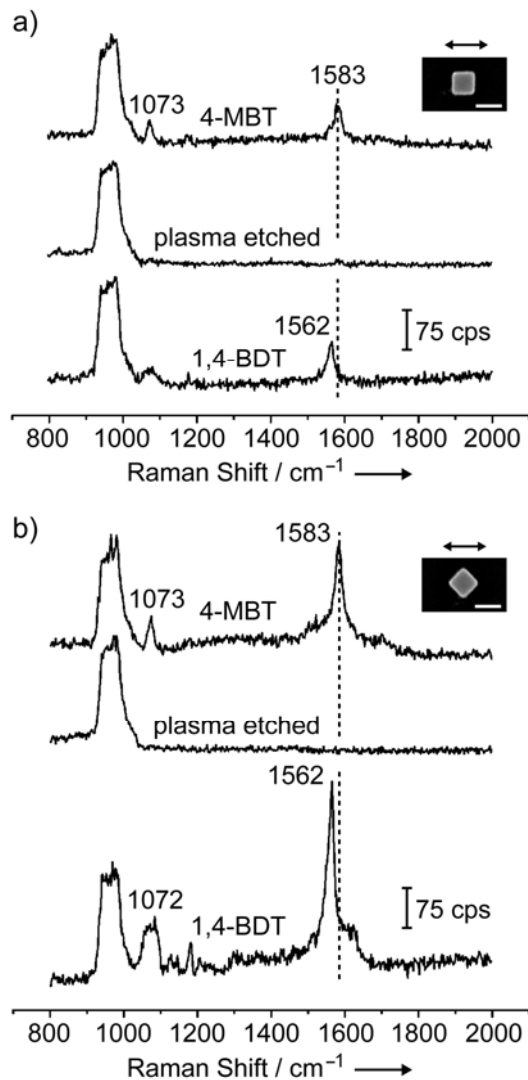


Figure 2.6. SERS spectra from a single Ag nanocube functionalized with 4-MBT (top trace), followed by plasma etching for 2 min (middle), and immersion in a 1,4-BDT solution (bottom). In (a) and (b), the laser was polarized along an edge and a face diagonal of the Ag nanocube, respectively. The scale bar in the inset corresponds to 100 nm.

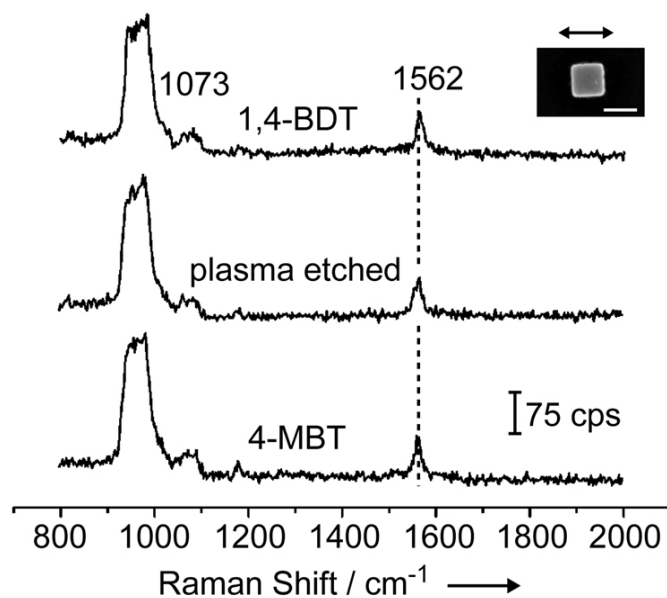


Figure 2.7. SERS spectra from a single Ag nanocube functionalized with 1,4-BDT (top), followed by plasma etching for 2 min (middle) and immersion in a 4-MBT solution (bottom). No major change in the SERS spectrum (middle trace) was observed after plasma etching. Also, the SERS spectrum did not change after immersing the sample in a 4-MBT solution, indicating that the 1,4-BDT molecules could not be displaced by 4-MBT.

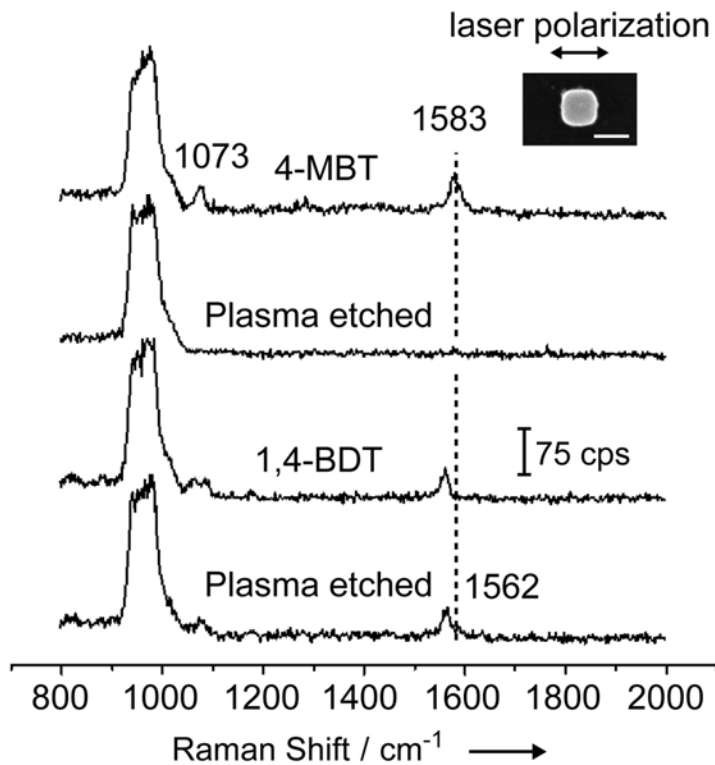


Figure 2.8. SERS spectra from a single Ag nanocube functionalized with 4-MBT (top), plasma etching for 2 min (second trace), followed by immersion in a 1,4-BDT (third trace) and plasma etching for another 2 min (bottom). When 1,4-BDT molecules were adsorbed on the surface of the nanocube, they could not be easily removed via plasma etching. The scale bar in the inset corresponds to 100 nm.

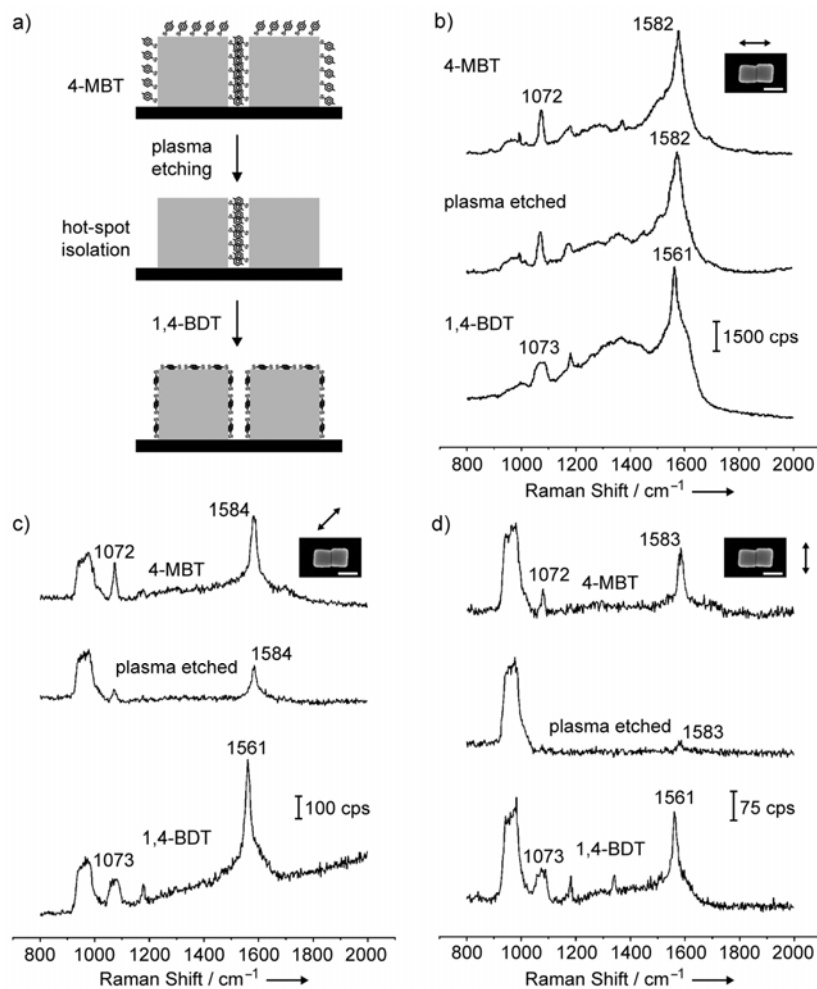


Figure 2.9. (a) Schematic of the approach employed for probing the hot spot formed in a dimer of Ag nanocubes. The dimer was functionalized with 4-MBT and then exposed to plasma etching to remove the adsorbed 4-MBT molecules. In this case, only the 4-MBT molecules outside the hot-spot region (i.e., outside the two touching faces) were removed during the plasma etching. The nanocube dimer was then immersed in a 1,4-BDT solution, resulting in the complete replacement of 4-MBT by 1,4-BDT over its entire surface. (b-d) SERS spectra from a Ag nanocube dimer functionalized with 4-MBT (top), followed by after plasma etching for 2 min (middle) and then immersion in a 1,4-BDT solution (bottom). The laser was polarized at 0, 45 and 90 degrees with respect to the long axis of the dimer. The scale bars in the insets correspond to 100 nm.

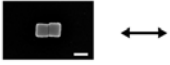
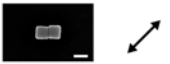
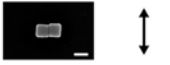


	4-MBT	Plasma etched (hot-spot isolation)	Re-immersion in 1,4-BDT
	2.2e+7	1.0e+8	1.9e+7
	2.0e+6	4.1e+6	1.6e+6
	6.8e+5	4.4e+5	5.4e+4
	5.9e+5	—	3.7e+5
	2.3e+6	—	1.9e+6

Figure 2.10. Summary of the Enhancement Factors (EFs) calculated using Eq. (1) for the dimers and individual Ag nanocubes functionalized with 4-MBT, followed by plasma etching for 2 min and immersion in a 1,4-BDT solution. The arrow denotes the laser polarization direction in each case. The scale bars in the insets correspond to 100 nm.

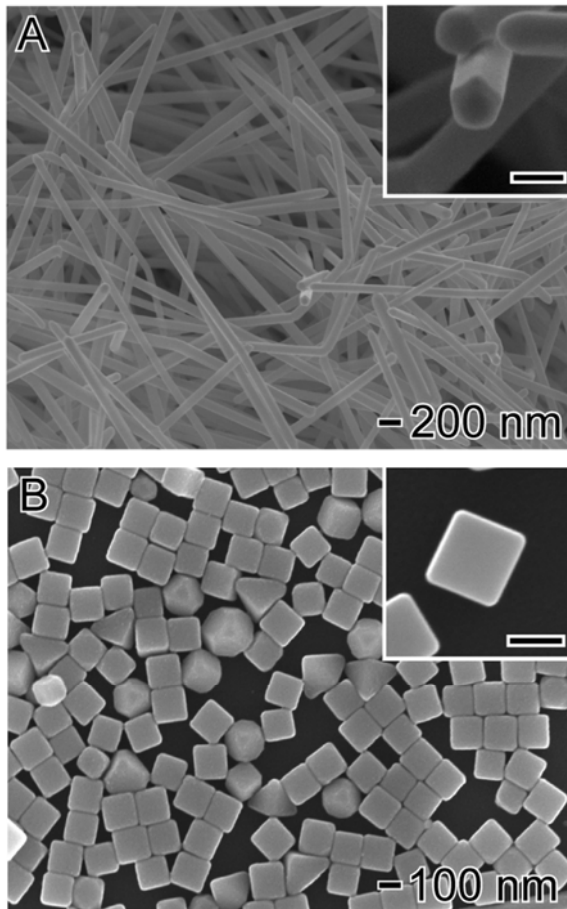


Figure 2.11. SEM images of (A) Ag nanowires and (B) Ag nanocubes with sharp corners used for the SERS measurements. The average width of the Ag nanowires was 95.2 ± 8.8 nm and the pentagonal cross section can be clearly observed from the image in the inset. The average edge length of the Ag nanocubes was 141.7 ± 3.8 nm. The scale bars in the insets correspond to 100 nm.

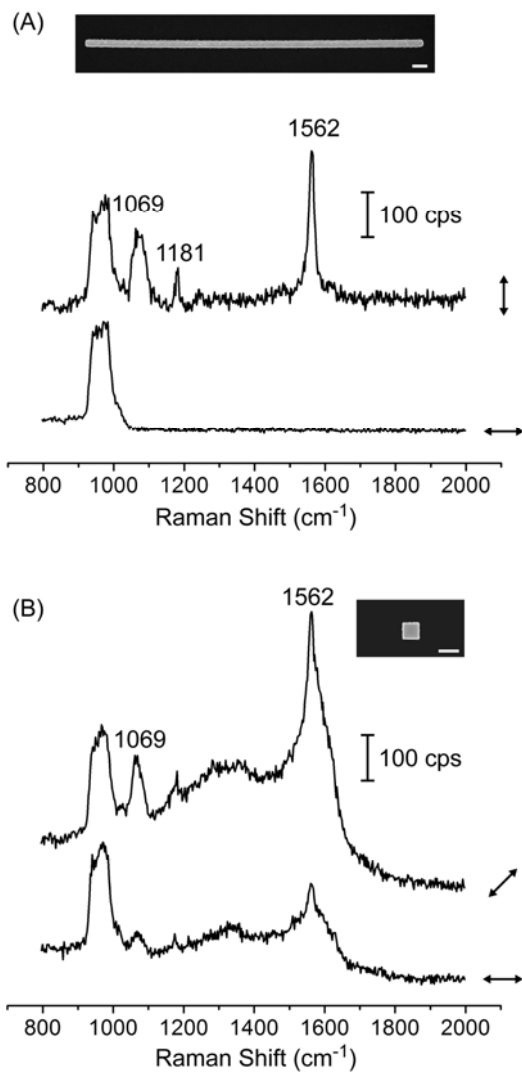


Figure 2.12. SERS spectra taken from (A) a single Ag nanowire and (B) a single Ag nanocube, respectively, which were functionalized with 1,4-BDT. The arrow indicates the laser polarization direction relative to the nanowire or nanocube in the inset. For a Ag nanowire, the SERS signals were more strongly enhanced when the laser polarization direction was perpendicular to the nanowire's long axis, top trace in (A). For a Ag nanocube, the SERS signals were more strongly enhanced when the laser was polarized along a face diagonal, top trace in (B). The insets show SEM images of the Ag nanowire and Ag nanocube being probed for SERS. The scale bars in the insets correspond to 200 nm.

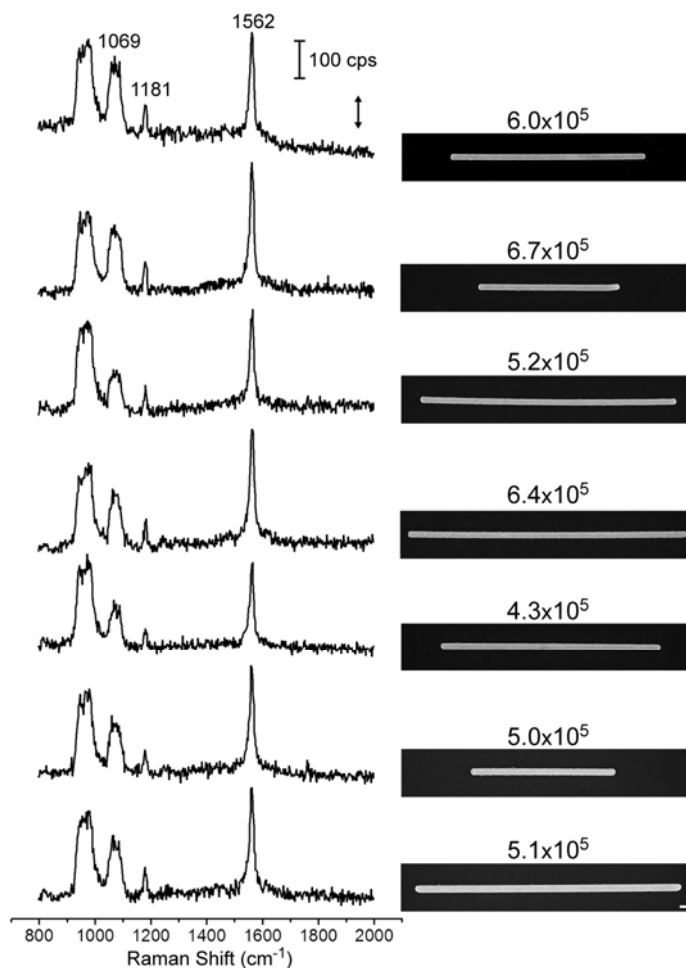


Figure 2.13. SERS spectra for seven different individual Ag nanowires that were functionalized with 1,4-BDT. The laser polarization direction was perpendicular to the nanowire longitudinal axis in all spectra, as indicated by the double arrow. The numbers on the insets indicate the calculated EF_{wire} for each spectrum. Although the nanowires present different lengths (varying from 2.5 to 4.8 μm), no significant changes in the detected SERS intensities and EFs were observed. This is because the number of probe molecules within the laser spot size was maximized in all cases by focusing the laser beam at the center of each nanowire, eliminating any potential fluctuations in N_{sers} that could arise from probing the regions close to the tips. The scale bar applies to all insets and corresponds to 200 nm.

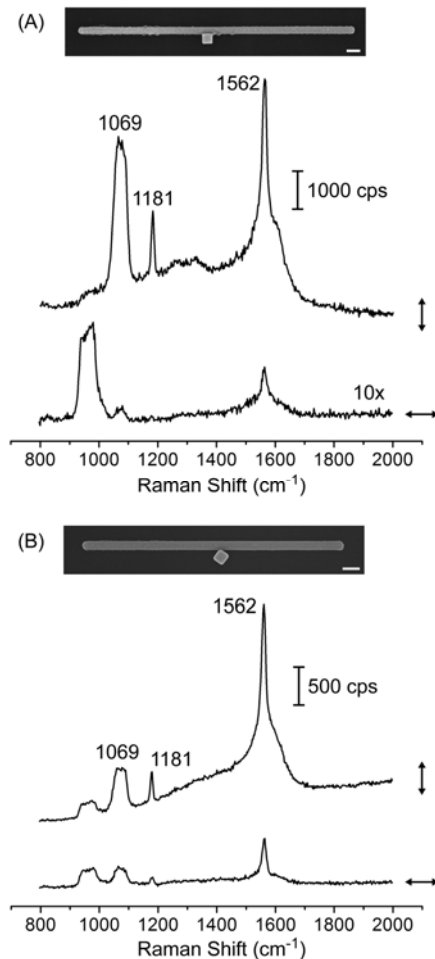


Figure 2.14. SERS spectra taken from two dimers made of an individual Ag nanowire and a single Ag nanocube. In (A), the nanocube was oriented with one side face nearly touching the side face of the nanowire. In (B), the nanocube was oriented with one edge nearly touching the side face of the nanowire. In both cases, the nanocubes were positioned at the center region relative to the nanowire’s long axis. The samples were functionalized with 1,4-BDT and the arrows indicate the laser polarization directions relative to the dimers shown in the insets. The SERS signals were more strongly enhanced when the laser was polarized parallel to the hot-spot axis (top traces). The insets show SEM images of the dimers being probed for SERS. The scale bars in the insets correspond to 200 nm.

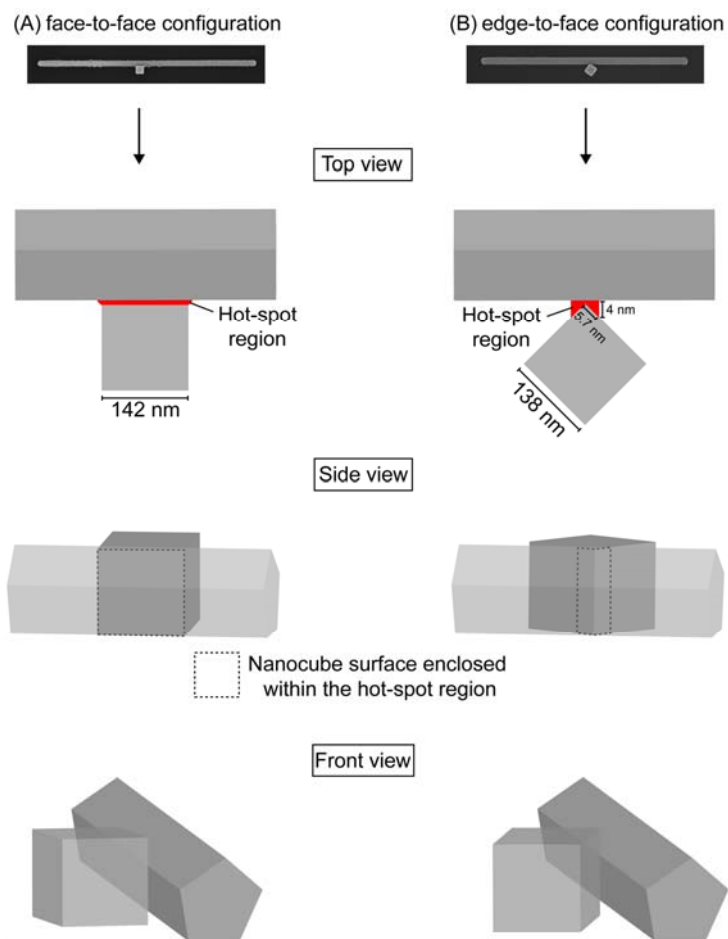


Figure 2.15. Schematic representation of the dimers probed in Figure 2.14. In (A), the Ag nanocube approached the nanowire with one side face nearly touching the side face of the Ag nanowire. The hot-spot region can be described by the narrow gap between the nanocube's face and the nanowire's side face (face-to-face configuration). In (B), the Ag nanocube approaches the nanowire with one edge nearly touching the side face of the Ag nanowire. In this case, the hot-spot region can be described by the narrow gap between the nanocube's edge and the nanowire's side face (edge-to-face configuration). As shown in the scheme, the number of probe molecules trapped in the hot-spot region is expected to be the lower for the dimer in an edge-to-face configuration. This smaller number of probe molecules in the hot-spot region is believed to be responsible for the observed reduction in the SERS intensities when the dimer displayed an edge-to-face geometry.





Enhancement factors	
	<p>↔ 5.8×10^5</p> <p>↗ 3.0×10^6</p>
	<p>↔ NA</p> <p>↕ 6.4×10^5</p>
	<p>↔ 1.9×10^5</p> <p>↕ 1.4×10^7</p>
	<p>↔ 7.9×10^5</p> <p>↕ 4.3×10^6</p>

Figure 2.16. Summary of the SERS EFs obtained for an individual Ag nanocube, an individual Ag nanowire, and dimers consisting of a Ag nanowire and a Ag nanocube probed in Figure 2.14. The highest EF was obtained under transverse polarization for a dimer in which the Ag nanocube was oriented with one side face nearly touching the side face of a Ag nanowire (face-to-face orientation). In this case, EF_{dimer} displayed an increase of 22 and 24 folds relative to EF_{wire} and EF_{cube} , respectively. For both dimers, no significant enhancement as compared to EF_{wire} and EF_{cube} was observed when the laser polarization direction was parallel to the long axis of the nanowire. The arrow denotes the laser polarization directions in each case. The scale bars in the insets correspond to 200 nm.

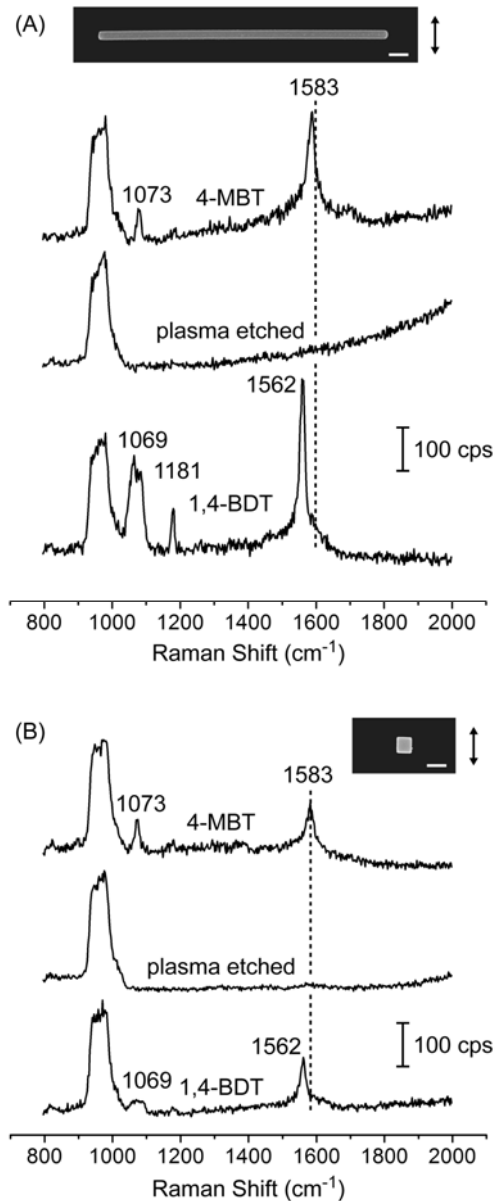


Figure 2.17. SERS spectra from (A) a single Ag nanowire and (B) a single Ag nanocube functionalized with 4-MBT (top trace), followed by plasma etching for 6 min (middle), and immersion in a 1,4-BDT solution (bottom). In both cases, the laser was polarized perpendicular to the nanowire's long axis, and along an edge or a face diagonal of the nanocube, as indicated by the arrows. The scale bars in the insets correspond to 200 nm.

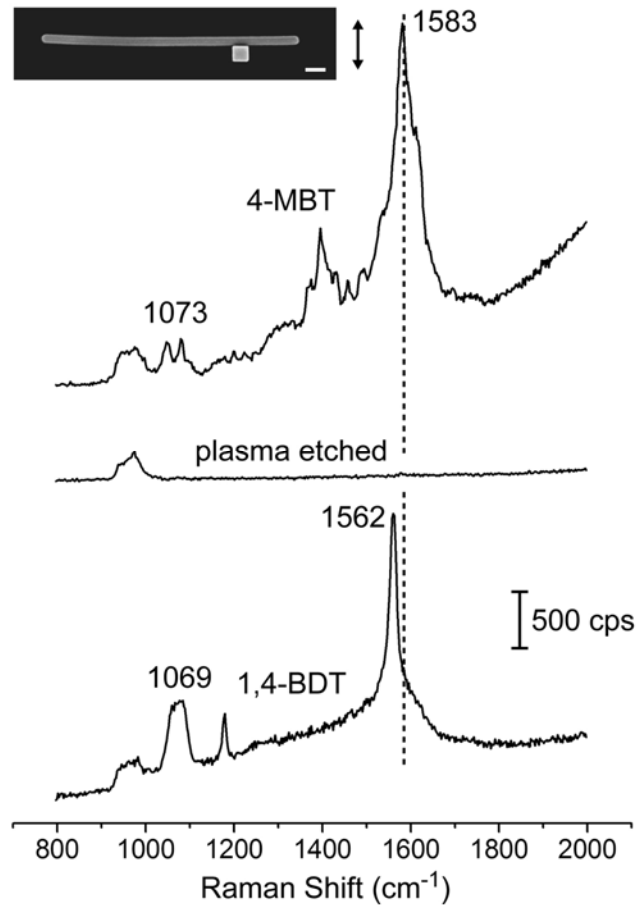


Figure 2.18. Attempt to isolate the hot-spot region in a dimer made of a Ag nanowire and a Ag nanocube via my previously demonstrated plasma etching approach. In this case, the dimer presents a face-to-face configuration. The dimer was functionalized with 4-MBT (top trace) and then exposed to plasma etching to remove the adsorbed 4-MBT molecules (middle trace). The dimer was then immersed in a 1,4-BDT solution, resulting in the complete replacement of 4-MBT by 1,4-BDT over its entire surface (bottom trace). The laser was polarized parallel to the hot-spot axis, as indicated by the arrow. The scale bar in the inset corresponds to 200 nm.

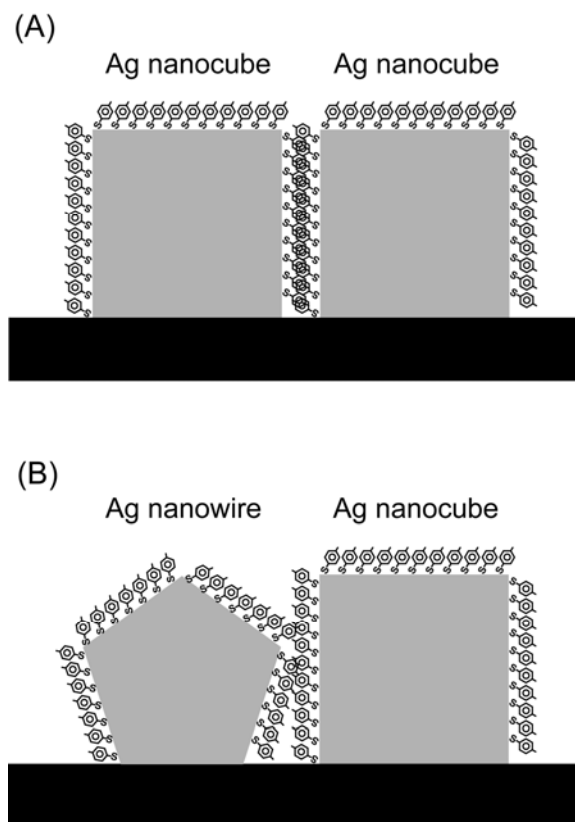


Figure 2.19. Representation of the cross-section region in a dimer containing (A) two sharp Ag nanocubes and (B) a Ag nanowire and a Ag nanocube. For a dimer made of two sharp Ag nanocubes, the hot-spot region comprises a narrow gap between two nearly touching nanocubes and, therefore, the 4-MBT molecules in the hot-spot can be considered as a multilayer resist relative to the oxygen plasma. In this case, removal of 4-MBT molecules from the hot-spot region can be expected to require longer plasma etching times as compared to the 4-MBT molecules absorbed outside the hot-spot region. For a dimer made of a Ag nanowire and a Ag nanocube (B), the SERS probe molecules adsorbed at the hot spot region are readily exposed to the oxygen plasma, owing to the pentagonal cross section of the Ag nanowires. This enables the complete removal of 4-MBT molecules (include those located in the hot-spot region) during plasma etching.

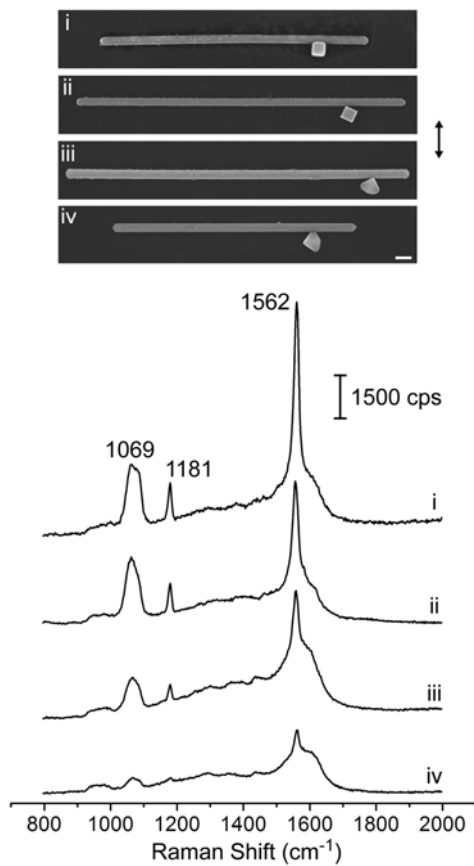


Figure 2.20. SERS spectra taken from four different dimers containing Ag nanowires, where *i*) the Ag nanocube was oriented with one side face nearly touching the side face of a Ag nanowire; *ii*) the Ag nanocube was oriented with one edge nearly touching the side face of a Ag nanowires; and *iii*, *iv*) the Ag right bipyramids were oriented with one of their tips nearly touching the side face of the Ag nanowires. The sample was functionalized with 1,4-BDT and the laser polarization direction was parallel to the hot-spot axis. The spectra show that the SERS signals were more strongly enhanced when the dimer had a face-to-face configuration (top trace), which allowed for the largest number of probe molecules to be located in the hot-spot region. The insets show SEM images of the probed dimers. The scale bar applies to all insets and corresponds to 200 nm.

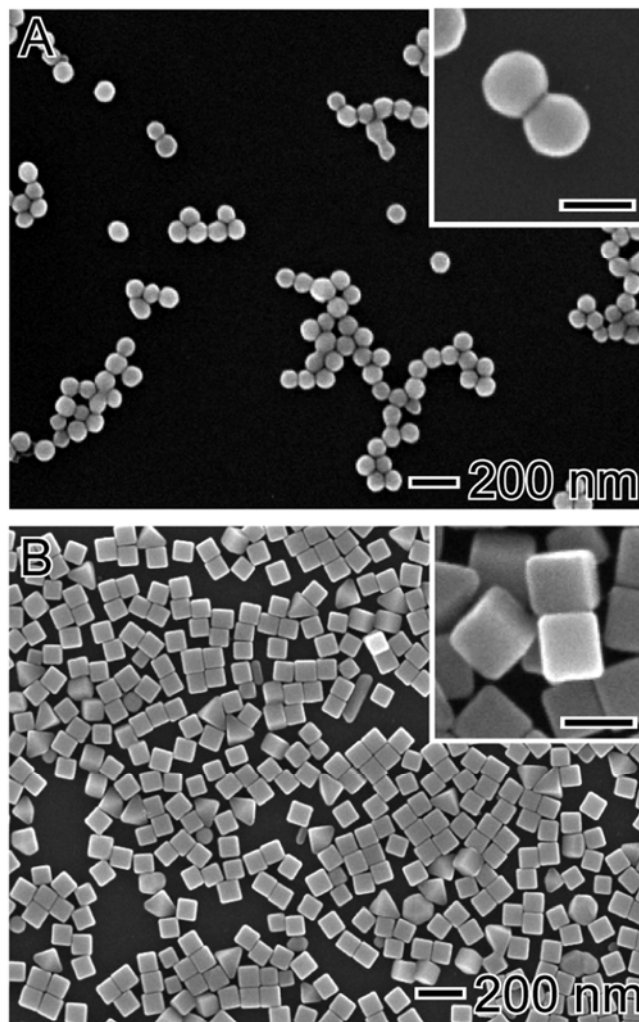


Figure 2.21. SEM images of the (A) Ag nanospheres and (B) Ag nanocubes employed in my SERS measurements. Their average diameter (nanospheres) and edge length (nanocubes) were 81.1 ± 5.3 and 100.7 ± 5.7 nm, respectively. The scale bars in the insets correspond to 100 nm.

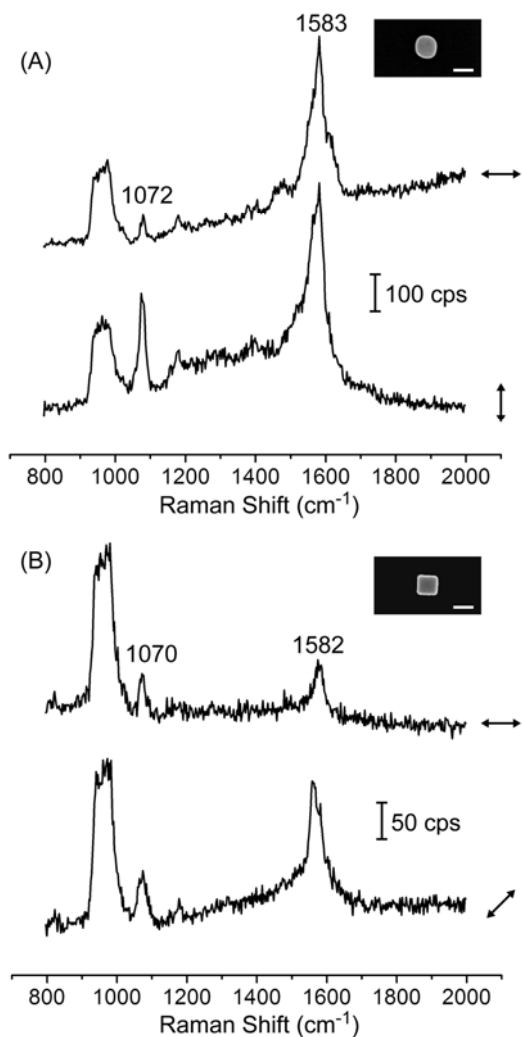


Figure 2.22. SERS spectra from a single Ag nanosphere (A) and a single Ag nanocube (B). The samples were functionalized with 4-MBT and the arrows indicate the laser polarization direction relative to the nanosphere and nanocube, respectively. For the Ag nanosphere, no significant variation in SERS signal intensity was observed for different polarization directions. For the Ag nanocube, the SERS signals were more strongly enhanced when the laser was polarized along a face diagonal (bottom trace in B). The insets show SEM images of the probed Ag nanosphere and nanocube. The scale bars in the insets correspond to 100 nm.

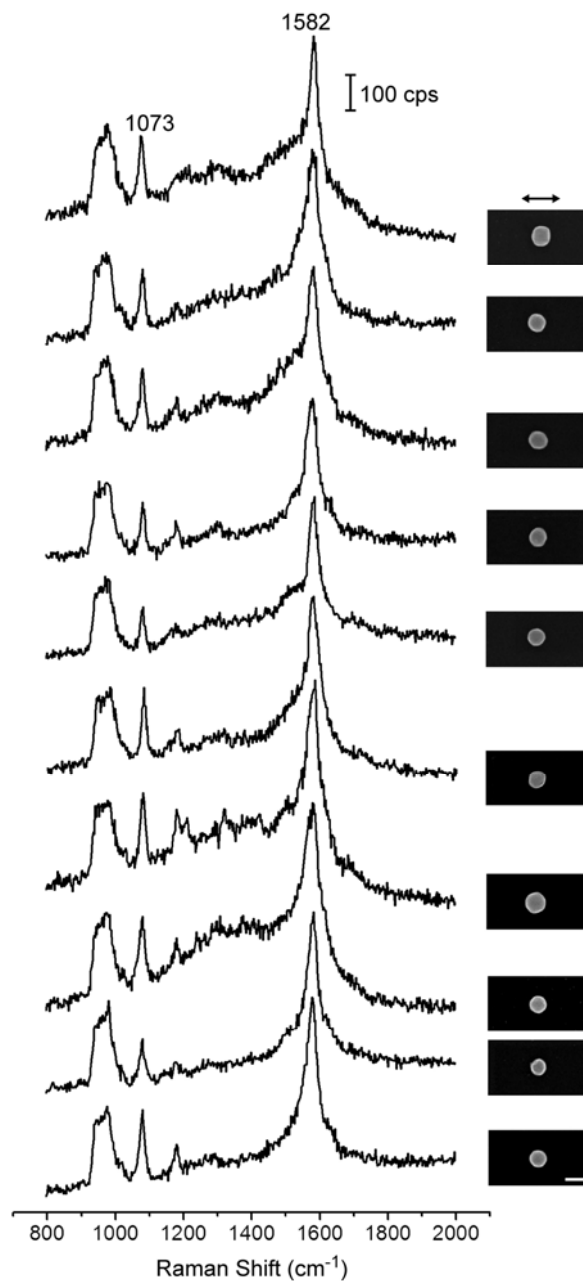


Figure 2.23. SERS spectra taken from 10 individual Ag nanospheres. The laser polarization direction is indicated by the double arrow. In all cases, no significant variation in the SERS signal intensity was observed for the different Ag nanospheres. The scale bar applies to all insets and corresponds to 100 nm. The average EF_{sphere} obtained from these spectra was 1.2×10^7 .

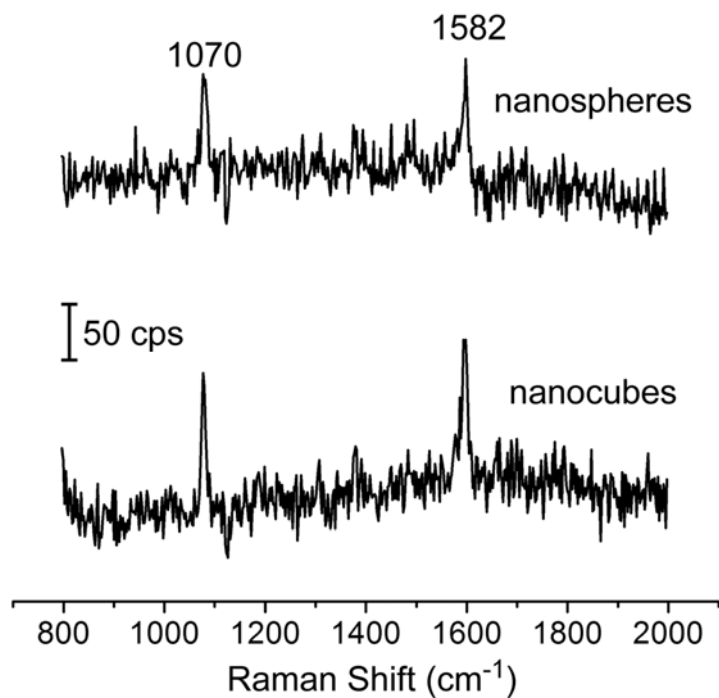


Figure 2.24. SERS spectra recorded from aqueous suspensions of the Ag nanospheres (top trace) and Ag nanocubes (bottom trace) that had been functionalized with 4-MBT. The measurements were performed with an excitation wavelength of 514 nm. EF_{sphere} and EF_{cube} calculated from the solution-phase spectra were 3.0×10^5 (top trace) and 1.4×10^6 (bottom trace), respectively.

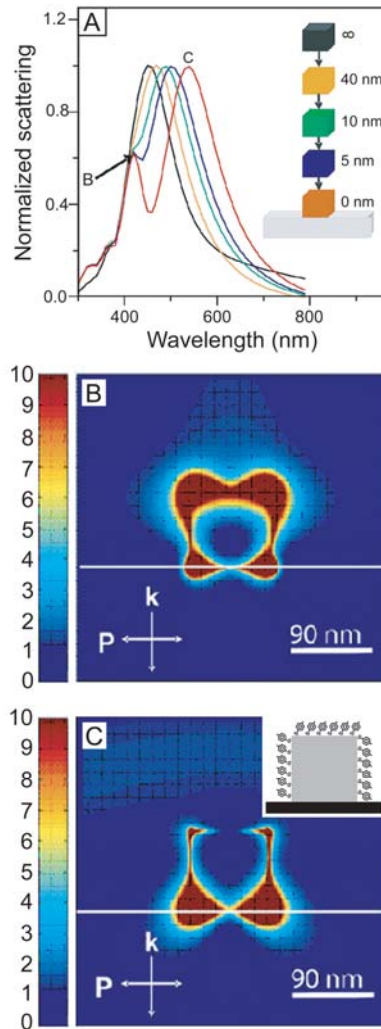


Figure 2.25. (A) Finite-difference time-domain (FDTD) simulation (Ref. 30) illustrating how the extinction peak of a nanocube 90 nm in edge length splits as the nanocube approaches a glass substrate. (B) The peak at 430 nm is associated with near fields away from the substrate. (C) The peak at 550 nm is associated with near fields impinging on the substrate. The white line in (B) and (C) represents the substrate. The inset in (C) displays a schematic representation of the Ag nanocube functionalized with 4-MBT employed in my measurements. In this case, no 4-MBT molecules are expected to be present at the bottom face of the nanocube that was in contact with the substrate.

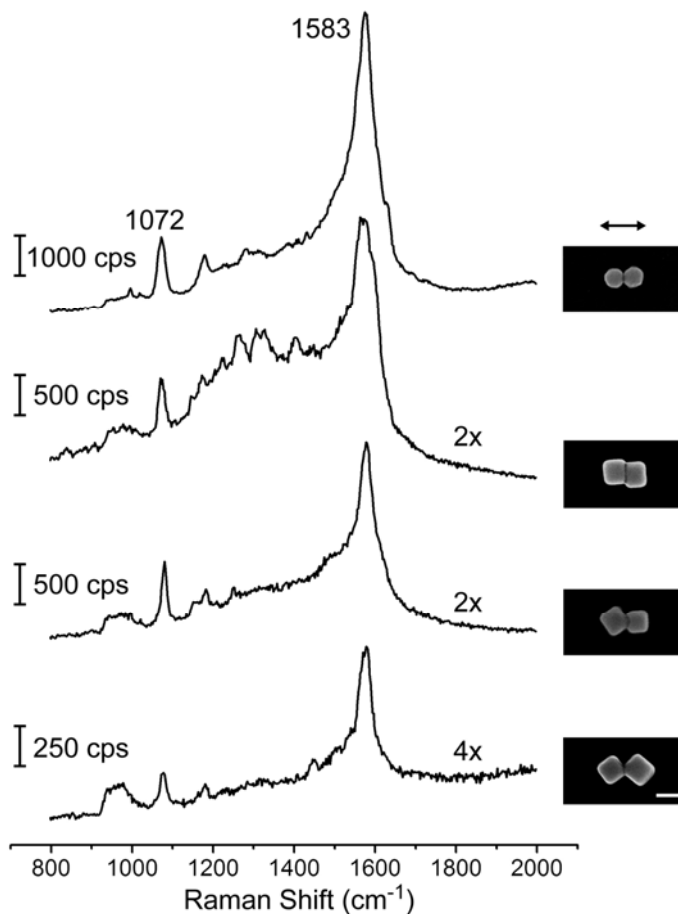


Figure 2.26. SERS spectra for dimers consisting of two Ag nanospheres or two Ag nanocubes with well-defined hot-spot structures: two Ag nanospheres (top trace) and two Ag nanocubes in a face-to-face (second trace from the top), edge-to-face (third trace from the top), or edge-to-edge (bottom trace) configuration. The samples were functionalized with 4-MBT and the laser was polarized along the longitudinal axis of each dimer, as indicated by the arrow. The insets give SEM images of the probed dimers. The scale bar applies to all insets and corresponds to 100 nm.

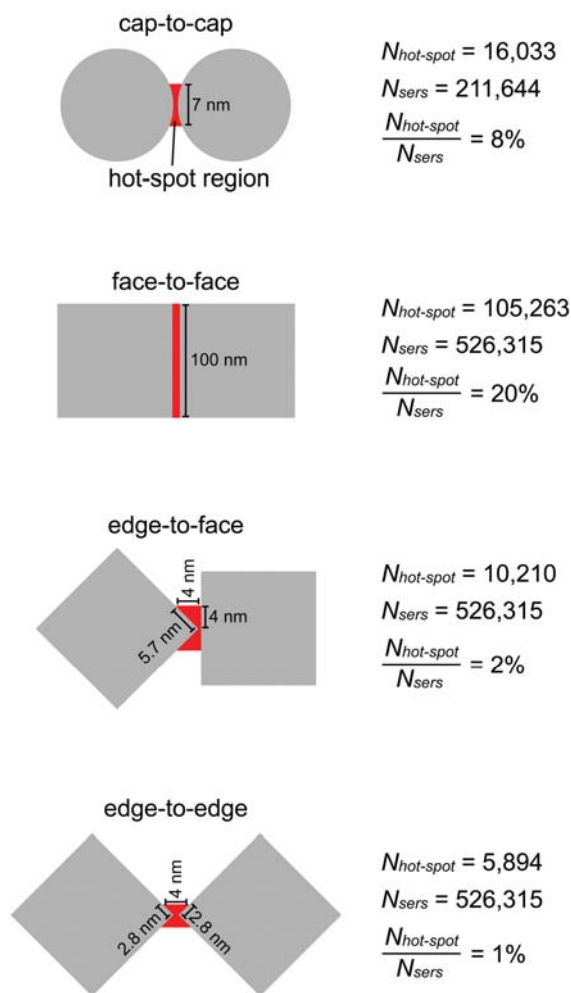


Figure 2.27. Schematic illustrations (top view) of the dimers probed in Figure 2.26 their corresponding hot-spot structures. The red color marks the hot-spot region for each dimer. In the dimer of nanospheres (A), the hot spot can be described by the narrow gap between two nearly touching semispherical caps (cap-to-cap configuration). In the dimers of nanocubes (B-D), the hot-spot region can be described by the narrow gap between: (B) two nearly touching side faces, (C) an edge and a side face, and (D) two nearly touching edges (face-to-face, edge-to-face, and edge-to-edge configurations, respectively). $N_{hot-spot}$ refers to the number of 4-MBT molecules trapped in the hot-spot region, while N_{sers} refers to the total number of molecules adsorbed on the entire surface of the dimer.

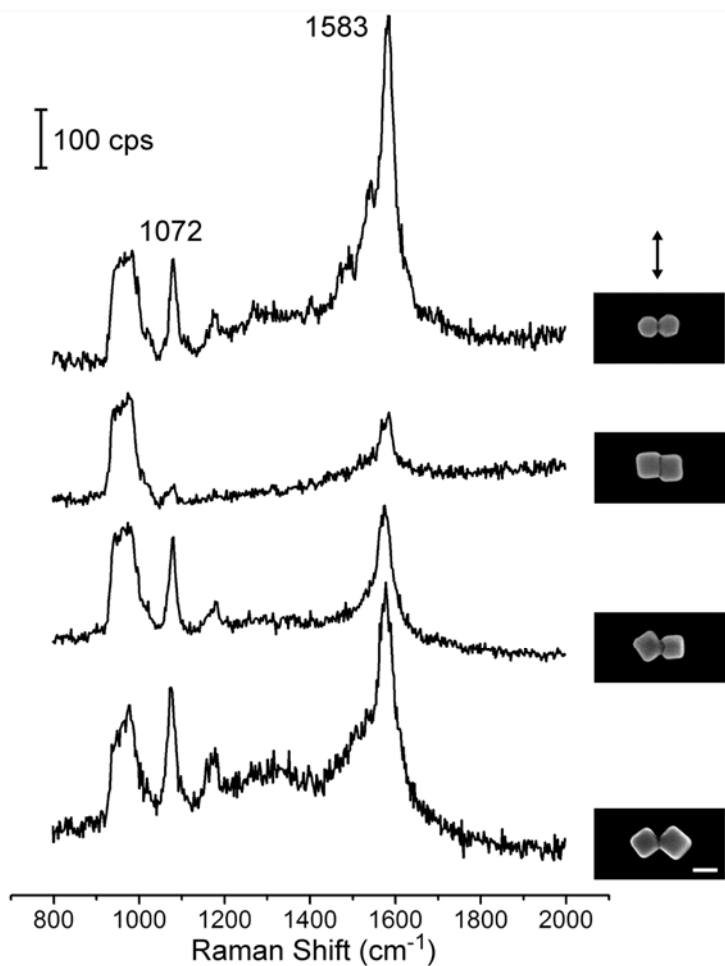


Figure 2.28. SERS spectra for dimers composed of two Ag nanospheres or two Ag nanocubes with well-defined hot-spot structures: two Ag nanospheres (top trace) and two Ag nanocubes in a face-to-face (second trace from the top), edge-to-face (third trace from the top), or edge-to-edge (bottom trace) configuration. The samples were functionalized with 4-MBT and the laser was polarized perpendicular to the longitudinal axis of the dimer, as indicated by the arrow. The insets give SEM images of the probed dimers. The scale bar applies to all insets and corresponds to 100 nm.

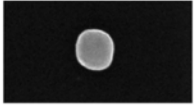
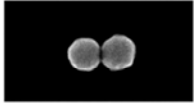
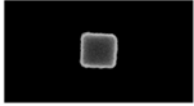
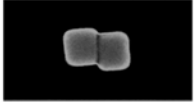
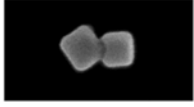
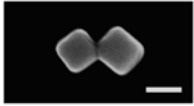
	Enhancement Factor (EF)	
	$\longleftrightarrow 1.7 \times 10^7$	$\updownarrow 1.6 \times 10^7$
	$\longleftrightarrow 1.7 \times 10^8$	$\updownarrow 1.5 \times 10^7$
	$\longleftrightarrow 7.2 \times 10^5$	$\nearrow 2.5 \times 10^6$
	$\longleftrightarrow 2.0 \times 10^7$	$\updownarrow 6.6 \times 10^5$
	$\longleftrightarrow 1.5 \times 10^7$	$\updownarrow 1.9 \times 10^6$
	$\longleftrightarrow 5.6 \times 10^6$	$\updownarrow 3.0 \times 10^6$

Figure 2.29. Summary of the enhancement factors calculated for the individual Ag nanosphere, nanocube, and the dimers of nanocubes probed in Figure 2.26 and 1.28. The highest EF_{dimer} was obtained for the dimer composed of two Ag nanospheres in a cap-to-cap configuration. However, when we compare the magnitudes of EF_{dimer} with respect to their single particle counterparts, the strongest field enhancement was obtained for the dimer consisting of two Ag nanocubes in a face-to-face configuration.

2.7. Notes to Chapter 2

- [1] (a) Pieczonka, N. P. W.; Aroca, R. F. *Chem. Soc. Rev.* **2008**, *37*, 946. (b) Stewart, M. E.; Anderton, C. R.; Thompson, L. B.; Maria, J.; Gray, S. K.; Rogers, J. A.; Nuzzo, R. G. *Chem. Rev.* **2008**, *108*, 494. (c) Stiles, P. L.; Dieringer, J. A.; Shah, N. L.; Van Duyne, R. P. *Annu. Rev. Anal. Chem.* **2008**, *1*, 601. (d) Willets, K. A.; Van Duyne, R. P. *Annu. Rev. Phys. Chem.* **2007**, *58*, 267. (e) Kneipp, K.; Kneipp, H.; Kneipp, J. *Acc. Chem. Res.* **2006**, *39*, 443.
- [2] (a) Nie, S.; Emory, S. R. *Science* **1997**, *275*, 1102. (b) Kneipp, K.; Wang, Y.; Kneipp, H.; Perelman, L. T.; Itzkan, I.; Dasari, R. R.; Feld, M. S. *Phys. Rev. Lett.* **1997**, *78*, 1667.
- [3] (a) Etchegoin, P. G.; Le Ru, E. C.; Meyer, M. *J. Am. Chem. Soc.* **2009**, *131*, 2713. (b) Otto, A. *J. Raman Spectrosc.* **2006**, *37*, 937.
- [4] (a) Le Ru, E. C.; Meyer, M.; Blackie, E.; Etchegoin, P. G. *J. Raman Spectrosc.* **2008**, *39*, 1127. (b) Le Ru, E. C.; Blackie, E.; Meyer, M.; Etchegoin, P. G. *J. Phys. Chem. C* **2007**, *111*, 13794.
- [5] (a) Kneipp, K.; Kneipp, H.; Itzkan, I.; Dasari, R. R.; Feld, M. S. *Chem. Rev.* **1999**, *99*, 2957. (b) Etchegoin, P. G.; Le Ru, E. C. *Phys. Chem. Chem. Phys.* **2008**, *10*, 6079.
- [6] (a) Olk, P.; Renger, J.; Härtling, T.; Wenzel, M. T.; Eng, L. M. *Nano Lett.* **2007**, *7*, 1736. (b) Svedberg, F.; Li, Z.; Xu, H.; Käll, M. *Nano Lett.* **2006**, *6*, 2639.
- [7] (a) Talley, C. E.; Jackson, J. B.; Oubre, C.; Grady, N. K.; Hollars, C. W.; Lane, S. M.; Huser, T. R.; Nordlander, P.; Halas, N. J. *Nano Lett.* **2005**, *5*, 1569. (b) Brandl, M.; Huser, T. R.; Nordlander, P.; Halas, N. J. *Nano Lett.* **2005**, *5*, 1569.

- D. W.; Oubre, C.; Nordlander, P. *J. Chem. Phys.* **2005**, *123*, 024701. (c) Wang, H.; Halas, N. J. *Nano Lett.* **2006**, *6*, 2945.
- [8] Camden, J. P.; Dieringer, J. A.; Wang, Y.; Masiello, D. J.; Marks, L. D.; Schatz, G. C.; Van Duyne, R. P. *J. Am. Chem. Soc.* **2008**, *130*, 12616.
- [9] Tao, A. R.; Yang, P. *J. Phys. Chem. B* **2005**, *109*, 15687.
- [10] (a) Wei, H.; Hao, F.; Huang, Y.; Wang, W.; Nordlander, P.; Xu, H. *Nano Lett.* **2008**, *8*, 2497. (b) Hutchison, J. A.; Centeno, S. P.; Odaka, H.; Fukumura, H.; Hofkens, J.; Uji-i, H. *Nano Lett.* **2009**, *9*, 995. (c) Lee, S. J.; Baik, J. M.; Moskovits, M. *Nano Lett.* **2008**, *8*, 3244.
- [11] Le Ru, E. C.; Etchegoin, P. G.; Meyer, M. *J. Phys. Chem.* **2006**, *125*, 104701.
- [12] (a) Khan, M. A.; Hogan, T. P.; Shanker, S. *J. Raman Spectrosc.* **2008**, *39*, 893. (b) Sauer, G.; Brehm, G.; Schneider, S. *J. Raman Spectrosc.* **2004**, *35*, 568.
- [13] (a) Osawa, M.; Matsuda, N.; Yoshii, K.; Uchida, I. *J. Phys. Chem.* **1994**, *98*, 12702. (b) Gui, J. Y.; Stern, D. A.; Frank, D. G.; Lu, F.; Zapien, D. C.; Hubbard, A. T. *Langmuir* **1991**, *7*, 955.
- [14] Li, W.; Camargo, P. H. C.; Lu, X.; Xia, Y. *Nano Lett.* **2009**, *9*, 485.
- [15] (a) Skrabalak, S. E.; Au, L.; Li, X.; Xia, Y. *Nat. Protoc.* **2007**, *2*, 2182. (b) Im, S. H.; Lee, Y. T.; Wiley, B.; Xia, Y. *Angew. Chem. Int. Ed.* **2005**, *44*, 2154. (c) Sun, Y.; Xia, Y. *Science* **2002**, *298*, 2176.
- [16] (a) Kelly, K.; Coronado, E.; Zhao, L.; Schatz, G. C. *J. Phys. Chem. B* **2003**, *107*, 668. (b) Hao, E.; Schatz, G. C. *J. Chem. Phys.* **2004**, *120*, 357. (c) Wiley, B. J.; Im,

- S. H.; Li, Z.-Y.; McLellan, J.; Siekkinen, A.; Xia, Y. *J. Phys. Chem. B* **2006**, *110*, 15666.
- [17] (a) Natan, N. J. *Faraday Discuss.* **2006**, *132*, 321. (b) McFarland, A. D.; Young, M. A.; Dieringer, J. A.; Van Duyne, R. P. *J. Phys. Chem. B* **2005**, *109*, 11279.
- [18] (a) Joo, S. W.; Han, S. W.; Kim, K. *J. Colloid Interface Sci.* **2001**, *240*, 391. (b) Cho, S. H.; Han, H. S.; Jang, D. -J.; Kim, K.; Kim, M. S. *J. Phys. Chem.* **1995**, *99*, 10594.
- [19] McLellan, J. M.; Li, Z. -Y.; Siekkinen, A. R.; Xia, Y. *Nano Lett.* **2007**, *7*, 1013.
- [20] Seo, K.; Borguet, E. *J. Phys. Chem. C* **2007**, *111*, 6335.
- [21] (a) Chen J.; Wiley, B.; Xia, Y. *Langmuir* **2007**, *23*, 4120. (b) Sun, Y.; Mayers, B.; Herricks, T.; Xia, Y. *Nano Lett.* **2003**, *3*, 955.
- [22] Mohanty, P.; Yoon, I.; Kang, T.; Seo, K.; Varadwaj, K. S. K.; Choi, W.; Park, Q. – H.; Ahn, J. P.; Suh, Y. D.; Ihee, H.; Kim, B. *J. Am. Chem. Soc.* **2007**, *129*, 9576.
- [23] Jeong, D. H.; Zhang, Y. X.; Moskovits, M. *J. Phys. Chem. B* **2004**, *108*, 12724.
- [24] Tao, A.; Kim, F.; Hess, C.; Goldberger, J.; He, R.; Sun, Y.; Xia, Y.; Yang, P. *Nano Lett.* **2003**, *3*, 1229.
- [25] Camargo, P. H. C.; Rycenga M, Au L and Xia Y 2009 *Angew. Chem. Int. Ed.* **48**, 2180.
- [26] Camargo, P. H. C.; Cobley, C. M.; Rycenga, M.; Xia, Y. *Nanotechnology* **2009**, in press
- [27] Li, W.; Camargo, P. H. C.; Au, L.; Zhang, Q.; Xia, Y. *Angew. Chem. Int. Ed.* **2009**, submitted.

- [28] (a) Rycenga, M.; Kim, M. H.; Camargo, P. H. C.; Cobley, C.; Li, Z. -Y.; Xia, Y. J. *Phys. Chem. A*, **2009**, *113*, 3932. (b) McLellan, J. M.; Siekkinen, A.; Chen, J.; Xia, Y. *Chem. Phys. Lett.* **2006**, *427*, 122.
- [29] (a) Dmitriev, A.; Hägglund, C.; Chen, S.; Fredriksson, H.; Pakizeh, T.; Käll M.; Sutherland, D. S. *Nano Lett.* **2008**, *8*, 3893. (b) Pinchuk, A.; Hilger, A.; von Plessen, G. Kreibig, U. *Nanotechnology* **2004**, *15*, 1890. (c) Malinsky, M. D.; Kelly, K. L.; Schatz, G. C.; Van Duyne, R. P. *J. Phys. Chem. B* **2001**, *105*, 2343.
- [30] Sherry, L. J.; Chang, S. H.; Schatz, G. C.; Van Duyne, R. P.; Wiley, B. J.; Xia, Y. *Nano Lett.* **2005**, *5*, 2034.

Chapter 3

A Mechanistic Study of the Galvanic Replacement Reaction between PtCl_6^{2-} and Pd Nanocrystals Enclosed by Different Facets

3.1. Introduction

Galvanic replacement represents a remarkably simple and versatile route to the synthesis of bimetallic nanostructures with hollow interiors and ultrathin walls.¹⁻⁶ In a galvanic replacement reaction, the electrical potential difference between the sacrificial template and the metal ions in solution provides the driving force for the reaction, i.e., oxidation and dissolution of the template accompanied by reduction of metal ions and deposition of resultant atoms on the template's surface. The morphology of the final product can be controlled by using sacrificial templates with different shapes and/or by controlling the extent of replacement. As the most extensively studied system, we have demonstrated that Ag nanostructures with a variety of shapes, including nanocubes, nanospheres, nanorods, and nanowires, could react with Au(III) or Au(I), Pt(II), and Pd(II) salt precursors to generate bimetallic nanoboxes,² nanocages,³ nanoshells,⁴ nanorattles,⁵ and nanotubes.^{5,6} In addition to their tunable optical properties, these hollow nanostructures are of particular interest for catalytic applications as they can provide high

surface areas and large surface-to-bulk atomic ratios and thus enhance the catalytic activity as compared to their solid counterparts.⁷

Although Platinum (Pt) is the most effective element for catalyzing the oxygen reduction reaction (ORR) in a proton-exchange membrane (PEM) fuel cell, high Pt loadings are required at the cathode in order to achieve a sufficient surface area and thus desired ORR activity.⁸⁻¹⁰ In an effort to decrease the Pt loading at the cathode, the galvanic replacement reaction has been recently employed for the one-step synthesis of hollow Pt nanostructures.^{11,12} Most of these studies have focused on the utilization of silver (Ag) and cobalt (Co) nanocrystals as sacrificial templates and PtCl_4^{2-} or PtCl_6^{2-} as the Pt source.^{3c,11,12} While the synthesis of the Ag and Co templates can be tightly controlled in terms of shape and size distribution, a good control over the morphology of the deposited Pt shell has not been achieved so far. In these systems, Pt deposition typically follows an island growth mode, yielding two typical morphologies: *i*) the formation of a dendritic or branched Pt shell and *ii*) deposition of small Pt nanoparticles on the surface of the sacrificial template. Interestingly, similar morphologies have also been reported when gold (Au) nanocrystals served as seeds for the growth of Pt.¹³ Although these strategies yield Pt nanostructures displaying high surface areas, they still presents drawbacks for practical applications. For example, any residual Co or Ag in the product can oxidize during fuel-cell operation, leading to detrimental effects over their catalytic performances. More importantly, little is know about the mechanism of Pt deposition and the reported morphologies have been explained based on the large lattice mismatch between Pt and the template nanocrystal (Ag-Pt, Co-Pt and Au-Pt display 4.3,

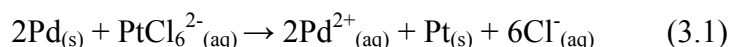
10.0 and 4.2 % lattice mismatch, respectively). Recently, we have shown that Pd nanocrystals with well-defined sizes and shapes can serve as supports for growing Pd-Pt bimetallic nanostructures with controllable morphologies.^{14,15} The epitaxial deposition of a smooth Pt shell took place when Pd nanoplates were employed as nanocrystal seeds.¹⁴ Conversely, the growth of Pt branches was observed upon the utilization of Pd cuboctahedra as seeds (producing Pd-Pt nanodendrites).¹⁵ This observation suggests that the shape of the template nanocrystal and/or the employed reaction conditions play an important role over the Pt growth mechanism (Pd-Pt lattice mismatch is 0.77 %). As the ORR catalytic performance is related to the morphology, a systematic investigation on the mechanisms of Pt growth onto the surface of a specific substrate is highly desirable to design catalysts with maximized ORR activities.

Here, I report on the use of galvanic replacement reaction for generating a variety of Pd-Pt bimetallic nanostructures. Compared to other galvanic replacement systems, very little is known about the mechanistic details involved in the heterogeneous nucleation and growth of Pt on Pd nanocrystals. I performed a systematic study on the galvanic replacement reaction between PtCl_6^{2-} ions and Pd nanocrystals with well-defined shapes as sacrificial templates, including octahedra, nanocubes, and nanorods. Even though a galvanic approach has been recently employed to the synthesis of Pd-Pt hollow nanocubes and Pd-Pt bimetallic nanoparticles,^{7,16} this work represents, to the best of my knowledge, the first systematic investigation on the utilization of Pd nanocrystals with distinct and well-defined shapes as sacrificial templates. The use of Pd octahedra, nanocubes, and nanorods in this study is motivating for various reasons. Because Pd is

dissolved during the course of the galvanic reaction, hollow Pd-Pt nanocrystals can be obtained in a single-step, i.e., without any post-treatment procedure for the removal of the core. Also, these Pd nanocrystals can be readily synthesized in terms of good uniformity and size distribution via water- or polyol-based protocols developed by our group.^{17,18} Owing to their well-defined morphologies and the minor lattice mismatch between Pd and Pt, their utilization as allows the systematic study on the effect of the shape (thus facets on the surface) of the template over the mechanism of Pt growth. Finally, Pd-Pt systems are especially attractive for ORR applications. It has been shown that deposition of Pt on a single-crystal Pd surface can considerably reduce the material cost while enhancing their catalytic activity.^{19,20} For instance, it has been demonstrated that a Pt monolayer supported on a Pd(111) surface had much higher activity for ORR relative to the Pt(111) surface.²¹ Very recently, we found that Pd-Pt bimetallic nanodendrites exhibited greatly improved ORR activity as compared to the commercial Pt/C and Pt-black catalyst.¹⁵

3.2. Results and Discussion

Figure 3.1 shows TEM and HRTEM images of the Pd octahedra, nanocubes, and nanorods that were employed as sacrificial templates for the galvanic replacement reaction with PtCl_6^{2-} :



It is clear that the nanocrystals in each sample had a uniform size and well-defined shape. The Pd octahedra were 20.0 ± 1.5 nm in edge length by 24.5 ± 1.8 nm (vertex-to-vertex direction). The nanocubes were 10.4 ± 0.5 nm in edge length. The Pd nanorods were 3.2 ± 0.4 nm in width and 23.8 ± 7.0 nm in length. Both HRTEM images and FFT operations confirm that the Pd octahedra were enclosed by $\{111\}$ facets, while the nanocubes were enclosed by $\{100\}$ facets. As the Pd nanorods had an octagonal cross section with the side surface enclosed by a mix of $\{100\}$ and $\{110\}$ facets, an individual nanorod can sit on the TEM grid against either one of the $\{100\}$ or $\{110\}$ facets.²² Figure 3.1F shows a nanorod that grew along the $[100]$ direction and lies on the TEM grid against one of its $\{100\}$ facets.

Figure 3.2 shows TEM images of the samples that were obtained after the Pd octahedra had reacted with different volumes of 0.4 mM PtCl_6^{2-} . Specifically, after the addition of 0.9 mL of PtCl_6^{2-} , small Pt islands (~ 1 nm in size) started to appear on the surface of the Pd octahedra (Fig. 3.2A). As more PtCl_6^{2-} was added (1.8 mL, Fig. 3.2B), Pd oxidation together with Pt nucleation and growth on the surface of the octahedra was observed, producing a core-shell morphology. Here, the core was comprised of a hollow octahedron and the shell was made of Pt branches that cover the entire surface of the core. The Pd-Pt bimetallic nanocrystal ($\text{Pd}_{\text{oct.}}\text{-Pt}$) presented an overall size of 35.0 ± 3.0 by 40.4 ± 2.1 nm (edge length and vertex-to-vertex direction, respectively), indicating that the Pt shell was ~ 7 nm thick. Finally, after addition of 2.7 mL of PtCl_6^{2-} (Fig. 3.2C), further growth of Pt on the template led to an increase of the shell thickness to ~ 11 nm and the overall size to 41.7 ± 2.1 by 53.0 ± 3.0 nm (edge length and vertex-to-vertex direction,

respectively). Figure 3.2D shows EDX spectra for the products depicted in Figure 3.2, A-C. The Pt atomic percentages for the bimetallic nanocrystals obtained with 0.9, 1.8 and 2.7 mL of 0.4 mM PtCl_6^{2-} were 16.8, 72.5 and 84.6, respectively. This result is in agreement with the gradual consumption of Pd from the octahedral core concurrent with the deposition of Pt at the surface as the volume of PtCl_6^{2-} added to the reaction mixture was increased during the replacement reaction.

Figure 3.3, A and B, shows HRTEM images for the Pd_{oct} -Pt nanocrystals obtained after titration with 0.9 mL of 0.4 mM PtCl_6^{2-} (shown in Fig. 3.2A). The epitaxial growth of small Pt islands on the surface of the Pd octahedron can be clearly observed at this stage. Figure 3.3, C and D, shows HRTEM images for the Pd-Pt nanostructures obtained after titration with 1.8 mL of 0.4 mM PtCl_6^{2-} (shown in Fig. 3.2B). Even though there was a high Pt coverage on the surface of the Pd octahedron, epitaxial correlation was still observed for the branched arms of Pt that were formed directly on the surface of the Pd octahedron, as indicated by the HRTEM image and FFT operation (inset) in Figure 3.3C. Conversely, the Pt branches that did not grow directly from the surface of the Pd octahedron (i.e., those deposited on the surface of pre-formed Pt branches) did not present an epitaxial relationship with the Pd surface. The presence of several spots forming an incomplete diffraction ring in the FFT operation (inset in Fig. 3.3D) supports this observation and indicates that the Pt coating was polycrystalline. Based on these results, the galvanic replacement reaction between a Pd octahedron and PtCl_6^{2-} can be understood as follows: in the early stages, Pt nucleation and growth occurred via the epitaxial deposition of small Pt islands on the surface of the octahedron. Then, as more Pt

atoms were produced via the reduction of PtCl_6^{2-} , further nucleation and growth of Pt led to the formation of branched arms on the template.

Figure 3.4 shows TEM images of the samples that were obtained after the Pd nanocubes had been titrated with different volumes of 0.4 mM PtCl_6^{2-} . The use of Pd nanocubes as sacrificial templates led to similar results as those previously described for Pd octahedra. Here, the formation of small Pt islands on the surface of the Pd nanocube was observed at the early stages of the reaction (Fig. 3.4A, titration with 0.9 mL of 0.4 mM PtCl_6^{2-}). As the reaction progressed (titration with 1.8 mL of 0.4 mM PtCl_6^{2-}), the formation of Pt branches that cover the entire surface of the nanocubes accompanied by Pd dissolution from the core was detected (Fig. 3.4B). The overall size for the $\text{Pd}_{\text{cube}}\text{-Pt}$ product at this stage was 25.2 ± 1.9 nm (shell was ~ 7 nm thick). Interestingly, the Pt branches deposited at the surface of the nanocubes are less densely packed as compared to the $\text{Pd}_{\text{oct.}}\text{-Pt}$ nanocrystals depicted in Figure 3.2B. At the later stage of the reaction (titration with 2.7 mL of 0.4 mM PtCl_6^{2-}), further Pt deposition led to an increase of particle size to 31.0 ± 2.8 nm and shell thickness to ~ 11 nm (Fig. 3.4C). The atomic percentages of Pt obtained for the products during the galvanic reaction (Fig. 3.4, A-C) were 44.3, 69.5 and 81.6, respectively. The corresponding EDX spectra for the products are shown in Figure 3.4D. Although the $\text{Pd}_{\text{cube}}\text{-Pt}$ displayed a higher atomic percentage of Pt at the early stage of the reaction as compared to $\text{Pd}_{\text{oct.}}\text{-Pt}$, (44.3% vs. 16.8%), the Pt atomic percentages for the $\text{Pd}_{\text{oct.}}\text{-Pt}$ and $\text{Pd}_{\text{cube}}\text{-Pt}$ nanocrystals were similar at the later stages.

Figure 3.5, A and B shows HRTEM images for the Pd_{cube}-Pt product shown in Fig. 3.4A. Similarly to what was observed for the Pd_{oct}-Pt system, the formation of Pt islands on the surface of the nanocube was epitaxial and the Pd_{cube}-Pt product was single-crystal. Figure 3.5, C and D, displays HRTEM images for the Pd_{cube}-Pt nanocrystals shown in Fig. 3.4B. Here, the Pt branches that were formed directly at the surface of the Pd nanocubes displayed an epitaxial relationship with the Pd template, as shown by HRTEM and FFT operation (inset) in Figure 3.5D. These results indicate that the utilization of Pd octahedra and nanocubes as sacrificial templates for the galvanic replacement reaction with PtCl₆²⁻ did not lead to significant differences for the mechanisms of Pt nucleation and growth. In these cases, with the exception of the shape of the core, the Pd-Pt products obtained after the galvanic replacement reaction displayed essentially the same morphology.

Figure 3.6A shows a TEM image of the product obtained after Pd nanorods had been titrated with 1.8 mL of 0.4 mM PtCl₆²⁻ under similar conditions as described for the octahedra and nanocubes (Pd_{rod}-Pt). Here, Pd oxidation from the nanorods accompanied by the Pt deposition at their surface started to take place. The HRTEM images (Figure 3.7, A and B) for the Pd_{rod}-Pt sample produced at this stage reveals the epitaxial deposition of a thin Pt shell (~1 nm) over the entire surface of the Pd nanorod. After the addition of 2.7 mL of 0.4 mM PtCl₆²⁻ (Figure 3.6B), Pt deposition over the entire surface of the nanorod led to an increase in width to 5.8±0.9 nm. However, Pt deposition did not yield a smooth layer over the surface of the nanorods. The TEM and HRTEM images for this Pd_{rod}-Pt product (Figure 3.7, C and D) reveals the epitaxial deposition of a thin Pt

layer (1 nm in thick) together with the formation of Pt islands (bumps) over the surface of the nanorod. The Pd_{rod}-Pt nanocrystal presented a core-shell structure and was single-crystalline. At the late stage of the reaction (Figure 3.6C, titration with 3.6 mL of 0.4 mM PtCl₆²⁻), the product was dismantled into smaller fragments due to considerable Pd corrosion from multiple sites in the nanorod's side surface. Differently from both the octahedra and nanocubes, no branched arms of Pt were observed on the surface of Pd nanorods. Owing to their small dimensions (specially their small width), it is plausible that the Pd oxidation from each individual nanorod (that lead to the formation of Pt nuclei) could not take place to the extent to enable the growth of Pt branches on the surface of the nanorods (Pd is consumed before the Pt branches can start to grow). According to the EDX spectra displayed in Figure 3.6D, the Pt atomic percentage for the Pd_{rod}-Pt products shown in Fig. 3.6, A-C corresponded to 52.3, 71.3 and 83.2, respectively. Figure 3.8 presents TEM and HRTEM images and EDX spectra for products obtained after titration of Pd nanobars (enclosed by {100} facets) with different volumes of PtCl₆²⁻. It is clear that the utilization of Pd nanobars as sacrificial templates led to identical results as previously observed for the Pd nanocubes, indicating that shape anisotropy did not influence the Pt growth mechanism over the surface of the Pd sacrificial templates.

According to the theory of heterogeneous nucleation, there are three types of growth mechanisms: *i*) layer-by-layer growth (Frank-van der Merwe mode); *ii*) island growth (Volmer-Weber mode); and *iii*) island-on-layer growth (Stranski-Krastanow mode).²³ In layer-by-layer growth, small domains of the depositing material are formed

on the substrate during the early stages of deposition. As heterogeneous nucleation proceeds, the depositing material settles preferentially over the surface of the lowest unfilled material layer, leading to epitaxial growth monolayer-by-monolayer. In the island-growth, small islands of depositing material are formed over the surface of the substrate in the early stages. Then, as deposition progresses, the depositing material nucleates and grows preferentially into the existing islands of depositing material instead of over the surface of the underlying substrate. Finally, in the island-on-layer mechanism, layer-by-layer growth is predominant in the early stages of nucleation and growth. As deposition continues, a transition from layer-by-layer to island growth takes place.²³ When these concepts are applied to heterogeneous nucleation in colloidal synthesis, it is believed that lattice mismatch, supersaturation conditions, surface energies and the interaction between the depositing material and the substrate are the key factors that determine the growth mode.^{13a,24} As the experimental conditions were similar for all the template nanocrystals in the galvanic replacement reactions reported herein, the surface energy should be the most important parameter to explain the differences in growth modes detected for the nanorods with respect to the octahedra and nanocubes. In general, different growth mechanisms can be observed according to the values of overall excess energy $\Delta\gamma$:

$$\Delta\gamma = \gamma_d + \gamma_i + \gamma_{\text{strain}} - \gamma_s \quad (3.2)$$

where γ_d and γ_s refer to the surface energy of the depositing material and substrate, respectively. γ_{strain} refers to the positive strain energy induced by lattice mismatch. Finally, γ_i refers to the interfacial energy due to the formation of the interface between the depositing material and substrate. If the lattice mismatch is small, layer-by-layer growth takes place when the sum of surface energy of the depositing material and interfacial energy equals the surface energy of the substrate:

$$\gamma_s = \gamma_d + \gamma_i \quad (\Delta\gamma \leq 0) \quad (3.3)$$

On the other hand, island-growth is favored when the mismatch between the two materials is relatively large (high γ_{strain}) and/or the sum of surface energy of the depositing material and interfacial energy is bigger than the surface energy of the substrate:

$$\gamma_s < \gamma_d + \gamma_i \quad (\Delta\gamma > 0) \quad (3.4)$$

Finally, in the island-on-layer mechanism, layer-by-layer growth is favored at the initial stages. As deposition progresses, $\Delta\gamma$ becomes positive (due to an increase in γ_{strain} , for example) and the growth mode transitions to island growth.

The Pt deposition via an island growth mechanism on the surface of Pd octahedra and nanocubes is in agreement with the prediction from heterogeneous nucleation theory. Theoretical calculations suggest that Pt has higher surface energy than Pd (thus $\gamma_s < \gamma_d$). Although these calculations don't include the effect of capping agents and ions during

solution phase synthesis, they can be used qualitatively as a general guideline. As the Pd octahedra and nanocubes are enclosed by low surface energy $\{111\}$ and $\{100\}$ facets, respectively, the term γ_s can be lowered so that, under my reactions conditions, γ_{111} and γ_{100} (Pd octahedra and nanocubes) was smaller than γ_d for the Pt nuclei, enabling the island-growth mechanism (eq. 3.4). Conversely, when the nanorods were employed as sacrificial templates in the galvanic replacement reaction, a layer-by-layer growth mechanism was observed at the early stages of the reaction (Fig 3.7, A and B). Then, as Pt deposition continued, a transition from layer-by-layer to island growth occurred. As the Pd nanorods display a side the surface enclosed by a mix of $\{100\}$ and $\{110\}$ facets, it is possible that the increased surface energy of the $\{110\}$ facet relative to $\{111\}$ and $\{100\}$ was high enough to allow γ_s to become comparable to the sum $\gamma_d + \gamma_i$, inducing layer-by-layer growth during the early stages of the reaction (eq. 3.3). As the reaction progressed, the increased nucleation rates associated with the utilization of increased volumes of PtCl_6^{2-} could favor the transition to island-growth mode. In this context, molecular dynamic simulations regarding the heterogeneous nucleation and growth of Argon vapor at polyethylene surfaces have demonstrated that a transition from layer-by-layer to island-on-layer growth as the nucleation rate was increased by using higher supersaturation levels.²⁵ Due to the minor lattice mismatch between Pd and Pt (0.77%), it is unlikely that the strain energy induced the transition to island growth.

The $\text{Pd}_{\text{oct.}}\text{-Pt}$, $\text{Pd}_{\text{cube}}\text{-Pt}$ and $\text{Pd}_{\text{rod}}\text{-Pt}$ bimetallic nanocrystals that were obtained after titration with 1.8 mL ($\text{Pd}_{\text{oct.}}\text{-Pt}$ and $\text{Pd}_{\text{cube}}\text{-Pt}$) and 2.7 mL ($\text{Pd}_{\text{rod}}\text{-Pt}$) of 0.4 mM PtCl_6^{2-} were tested as electrocatalysts for the ORR and their activity was benchmarked against

the commercial Pt/C catalyst (E-TEK, 20 % by wt. of 3.2 nm Pt nanoparticles on Vulcan XC-72 carbon support). Figure 3.9 shows cyclic voltammetry (CV) curves of these catalysts. The CV curves exhibited two distinctive potential regions associated with hydrogen adsorption/desorption processes between $0 < E < 0.37$ V and the hydroxyl species adsorption/desorption processes beyond 0.6 V.²⁶ The sharp peaks at 0.0-0.09 V detected for the Pd_{oct.}-Pt and Pd_{cube}-Pt samples can be assigned to hydrogen adsorption/desorption process at the Pd surface.^{19c,27} In this case, the more intense peak for the Pd_{oct.}-Pt sample is due to the increased number of hydrogen adsorption/desorption sites at {111} as compared to the {100} Pd facets.^{27,28} The Pd_{rod}-Pt sample does not display any sharp peaks in this region. This result agrees with the presence of a complete Pt layer covering the Pd nanorod's surface. The calculated electrochemically active surface area (ECSA) per weight of metal was calculated as 67.1, 80.6 and 30.1 m²/g_{Pt+Pd} for the Pd_{oct.}-Pt, Pd_{cube}-Pt and Pd_{rod}-Pt, respectively. These results indicate that both Pd_{oct.}-Pt and Pd_{cube}-Pt display high ECSAs that are comparable to that for the Pt/C catalyst (74.0 m²/g). The higher ECSA for the Pd_{cube}-Pt as compared to the Pd_{oct.}-Pt is in agreement with the less densely packed arrangement of the Pt branches at the surface of the nanocubes as compared to the octahedra (Fig. 3.2B and Fig. 3.4B). It is important to note that, due to the small size of the Pt nanoparticles in the Pt/C catalyst, it is very challenging to obtain new catalysts displaying ECSA comparable to Pt/C. Here, I believe that the both the Pt branched morphology in Pd_{oct.}-Pt and Pd_{cube}-Pt nanocrystals and their hollow interiors were essential to obtain high ECSAs. This result confirms that the galvanic replacement reaction is an attractive approach to the synthesis of Pd-Pt

bimetallic nanocrystals for catalytic applications. The absence of Pt branches in Pd_{rod}-Pt nanocrystals was responsible for its decreased ECSA as compared to the other catalysts. Figure 3.10A shows ORR polarization curves for the catalysts. The kinetic currents were calculated from the polarization curves by using the mass-transport correction and normalized with respect to the metal loading in order to compare the mass activities for the different catalysts, as shown in Figure 3.10B. Based on the total mass of Pd and Pt, the Pd_{oct}-Pt, Pd_{cube}-Pt and Pd_{rod}-Pt catalysts displayed mass activities of 0.115, 0.078 and 0.029 mA/μg_{Pd+Pt}, respectively. This corresponds to an increase of 1.2 times in the Pd_{oct}-Pt as compared to the Pt/C catalyst (0.095 mA/μg). The mass activities for Pd_{cube}-Pt and Pd_{rod}-Pt corresponded to 82 and 31 %, respectively, as compared to Pt/C. If only the mass of Pt is taken into consideration, the mass activities for the Pd_{oct}-Pt, Pd_{cube}-Pt and Pd_{rod}-Pt become 0.157, 0.104 and 0.041 mA/μg_{Pt}, respectively. In this case, the mass activity of Pd_{oct}-Pt and Pd_{cube}-Pt were 1.7 and 1.1 times higher than that for Pt/C, respectively. For Pd_{rod}-Pt, the electrocatalytic activity was corresponded to 43 % relative to Pt/C. The lower mass activities for the Pd_{rod}-Pt nanocrystals could be directly associated with their significantly decreased ECSA.

In order to gain further insight into the observed differences in ORR activity, the specific activities were calculated by normalizing the kinetic currents against the ECSA for each catalyst (Figure 3.10C). The specific activity for Pd_{oct}-Pt (0.171 mA/cm²_{Pd+Pt}) was 1.3 times higher than that for Pt/C. However, the specific activities for Pd_{cube}-Pt and Pd_{rod}-Pt were equal to 0.097 mA/cm²_{Pd+Pt}, corresponding to 75 % relative to Pt/C. It is well established that the ORR activity on low-index crystallographic facets of Pt in a non-

adsorbing electrolyte such as perchloric acid increases on the order of Pt(100) \ll Pt(111) $<$ Pt(110), with the difference in activity between Pt(111) and Pt(110) being minor.²⁹ This difference in ORR activity most likely arises from the structure-sensitive inhibiting effect for the adsorption of hydroxyl species on Pt (*hkl*), which blocks the active site for O₂ adsorption and retards the ORR kinetics.²⁴ As the formation of Pt branches directly at the surface of the template was epitaxial, it is plausible that Pd_{oct.}-Pt product has a higher percentage of exposed {111} facets as compared to the Pd_{cube}-Pt. Moreover, it is possible that the surface of Pd core also contributes to the ORR activities. It has been reported that the ORR activity of Pd and Pd-Pt alloys increase in the order Pd(100) $<$ Pd(111) $<$ Pd(110).²⁸ Therefore, the preferential exposure of {111} facets at the surface of the octahedron core as compared to {100} facets at the surface of the nanocube core could also contribute to the higher specific activity for the Pd_{oct.}-Pt product as compared to Pd_{cube}-Pt. The fact that the Pd_{cube}-Pt and Pd_{rod}-Pt displayed the same specific activity suggest that, considering both the core and shell, the Pd_{cube}-Pt displayed a similar overall ratio of exposed {111} with respect to {100} facets as the overall ratio of {110} and {111} with respect to {100} facets in the Pd_{rod}-Pt.

3.3. Summary

I have systematically investigated the galvanic replacement reaction between PtCl₆²⁻ ions and Pd nanocrystals with well-defined shapes including octahedra, nanocubes, and nanorods. When Pd octahedra and nanocubes were employed in the galvanic replacement reaction, Pt deposition followed an island growth mechanism

generating branched arms of Pt on the surface of the template. In this case, the Pd-Pt bimetallic nanocrystals displayed a core-shell structure in which the core was composed of a hollow octahedron or nanocube and the shell was composed of Pt branches. Conversely, Pt deposition followed an island-on-layer growth mechanism when Pd nanorods were employed as sacrificial templates. Here, epitaxial deposition of a thin Pt shell containing a significant number of Pt islands (bumps) was detected over the surface of the nanorods. The different Pt growth modes observed for the nanorods, as compared to both octahedra and nanocubes, could be explained based on the presence of high surface-energy {110} facets on nanorod's side surface. The Pd-Pt bimetallic nanocrystals obtained from the different Pd templates were tested as electrocatalysts for the oxygen reduction reaction (ORR). Owing to their branched morphology and hollow interiors, the Pd_{oct.}-Pt and Pd_{cube}-Pt nanocrystals possessed high ECSAs that were comparable to that for commercial Pt/C catalyst. The Pd_{oct.}-Pt displayed the highest ORR activity, being 1.7 times more active based on equivalent Pt mass than the commercial Pt/C catalyst. The results presented herein indicate that the galvanic replacement reaction represents a facile and versatile approach to produce Pd-Pt bimetallic nanocrystals with well-defined shapes, compositions and high surface areas. The optimization of the reaction conditions for each template nanocrystal is expected to enable further control over the Pt growth mechanism and, consequently, the morphology of the Pd-Pt bimetallic materials. A systematic study regarding the deposition of Pt in a variety of Pd seed nanocrystals by using different surfactants and reducing agents is currently being conducted in our group.

3.4. Experimental Section

Chemical and Materials. Ethylene glycol (EG, J. T. Baker, 99.9%), sodium tetrachloropalladate (II) (Na_2PdCl_4 , Aldrich, 99.998%), chloroplatinic acid hydrate ($\text{H}_2\text{PtCl}_6 \cdot x\text{H}_2\text{O}$, Aldrich, 99.995%), potassium bromide (KBr, Fisher Scientific), poly(vinyl pyrrolidone) (PVP, MW \approx 55,000, Aldrich), Ascorbic acid ($\text{C}_6\text{H}_8\text{O}_6$, Aldrich, 99+%), Citric acid ($\text{C}_6\text{H}_8\text{O}_7$, Fisher Scientific, 99.8%) acetone (EMD) and ethanol (Pharmco Products Inc., 200 proof) were all used as received. All aqueous solutions were prepared with deionized water (18.1 M Ω cm). The syntheses of the Pd template nanocrystals were carried out in a 25-mL three-neck flask equipped with a reflux condenser and a Teflon-coated magnetic stirring bar.

Synthesis of Pd Octahedra. In a typical synthesis, 0.0445 g of PVP and 0.06 g of citric acid were dissolved in 8 mL of H_2O and heated at 90 °C in air under magnetic stirring for 10 min. Then, a solution containing 0.0235 g of Na_2PdCl_4 in 3 mL of water was added dropwise to the reaction mixture using a glass pipette. This solution was heated at 90 °C in air for another 26 h before the product was collected by centrifugation and washed with acetone once and with ethanol three times to remove excess PVP. The final product was dispersed in 6 mL of ethanol.

Synthesis of Pd Nanocubes. 0.105 g of PVP was dissolved in 8 mL of H_2O . This solution was heated at 100 °C for 10 min (in air under magnetic stirring). Next, 0.057 g of Na_2PdCl_4 and 0.6 g of KBr dissolved in 3 mL of water was added dropwise to the reaction solution using a glass pipette. The reaction was allowed to proceed at 100 °C in air for

another 3 h. Finally, the product was collected by centrifugation, washed as described for the Pd octahedra and dispersed in 6 mL of ethanol.

Synthesis of Pd Nanorods. 5 mL of EG was heated at 110 °C in air under magnetic stirring for 1 h. Meanwhile, 0.0486 g of Na₂PdCl₄ and 0.2574 g of KBr were dissolved in 3 mL of water, and 0.0916 g of PVP was dissolved in 3 mL of EG at room temperature. These two solutions were then injected simultaneously into the pre-heated 5 mL EG using a two-channel syringe pump (KDS-200, Stoelting, Wood Dale, IL) at a rate of 45 mL/h. The reaction mixture was heated at 110 °C in air for another 1 h. Lastly, the product was collected by centrifugation, washed as described for the Pd octahedra and dispersed in 6 mL of ethanol.

Synthesis of Pd Nanobars. 0.035 g of PVP, 0.02 g of ascorbic acid, and 0.2 g of KBr were dissolved in 8 mL of water. After this system had been kept at 115 °C in air under magnetic stirring for 15 min, 0.019 g of Na₂PdCl₄ in 3 mL of water was added dropwise to the reaction solution using a glass pipette. This system was kept at 115 °C in air for 3 h. The product was then collected by centrifugation, washed as described for the Pd octahedra and dispersed in 3 mL of ethanol.

Galvanic Replacement Reactions. A fixed volume of the ethanol solution containing the sacrificial template nanocrystals (200 μL for octahedra and 100 μL for nanocubes, nanorods and nanobars) was dispersed in 5 mL of water containing PVP (1 mg/mL) in a 50-mL flask under magnetic stirring. This system was heated at 100 °C for 10 min and a specific volume (as indicated in the text) of 0.4 mM H₂PtCl₆ was added through a syringe pump at a rate of 45 mL/h under magnetic stirring. The solution was

heated for another 10 min and then cooled down to room temperature. Then, the solution was centrifuged and washed with water and ethanol three times to remove PVP before characterization.

Instrumentation. Transmission electron microscopy (TEM) studies were performed with a Hitachi H-7500 microscope operated at 100 kV or with a Tecnai G2 Spirit Twin (FEI) microscope operated at 80 kV. High-resolution TEM images (HRTEM) were taken on a JEOL field-emission transmission electron microscope (2100F) operated at 200 kV. Filtered images were generated by inverse FFT with a Gatan Digital Micrograph program. Samples for TEM and HRTEM studies were prepared by drying drops of the aqueous suspension of the nanostructures on carbon-coated copper grids (SPI, West Chester, PA) under ambient conditions. Energy-dispersive X-ray spectroscopy (EDX, Genesis 2000, Mahwah, NJ) was performed at an acceleration voltage of 10 kV. Samples for EDX were prepared by drying drops of the aqueous suspension of the nanostructures on silicon wafer.

Electrochemical measurements. The electrochemical measurements were performed at room temperature using a rotating disk electrode (Pine Research Instrumentation) connected to a PARSTAT 283 potentialstat (Princeton Applied Research). A leak-free AgCl/Ag/KCl (3 M) electrode (Warner Instrument) was used as the reference. The counter electrode was a Pt mesh ($1 \times 1 \text{ cm}^2$) connected to a Pt wire. All potentials were converted to scales relative to the Reversible Hydrogen Electrode (RHE). To prepare the working electrode, 15 μL of the dispersion containing the catalyst was transferred to the glassy carbon rotating disk electrode. For all Pd-Pt nanostructures and

Pt/C catalyst, the catalyst loading was 3 μg based on the mass of the metal(s). Upon drying under air for 2 h, the electrode was covered with 15 μL Nafion dispersed in water (0.05%). After evaporation of water, the electrode was put under vacuum for 30 min before measurement. The electrolyte was 0.1 M perchloric acid diluted from a 70% commercial solution (ACS Reagent grade, Baker) using Millipore ultrapure water. The cyclic voltammetry curves recorded at room temperature in an Ar-purged (ultrahigh purity, Airgas) 0.1 M HClO_4 solution with a sweep rate of 50 mV/s. The electrochemically active surface area (ECSA) was calculated by integrating the charges associated with hydrogen adsorption using 210 $\mu\text{C}/\text{cm}^2$ for monolayer adsorption of hydrogen on Pt surface. The ORR measurements were performed at a sweep rate of 10 mV/sec from 0.05 to 1.1 V at 1,600 rpm under flow of Ar. The Kouteck-Levich equation was applied to calculate the kinetic current density which can be described as:²¹

$$1/j = 1/j_k + 1/j_d \quad (3.5)$$

where i is the experimentally measured current, j_d is the diffusion-limiting current, and j_k is the kinetic current. Thus, the kinetic current can be extracted from equation (3.5). For each catalyst, the kinetic current was normalized to the loading amount of metal (both Pt and Pd or only Pt) and ECSA in order to obtain mass and specific activities, respectively.

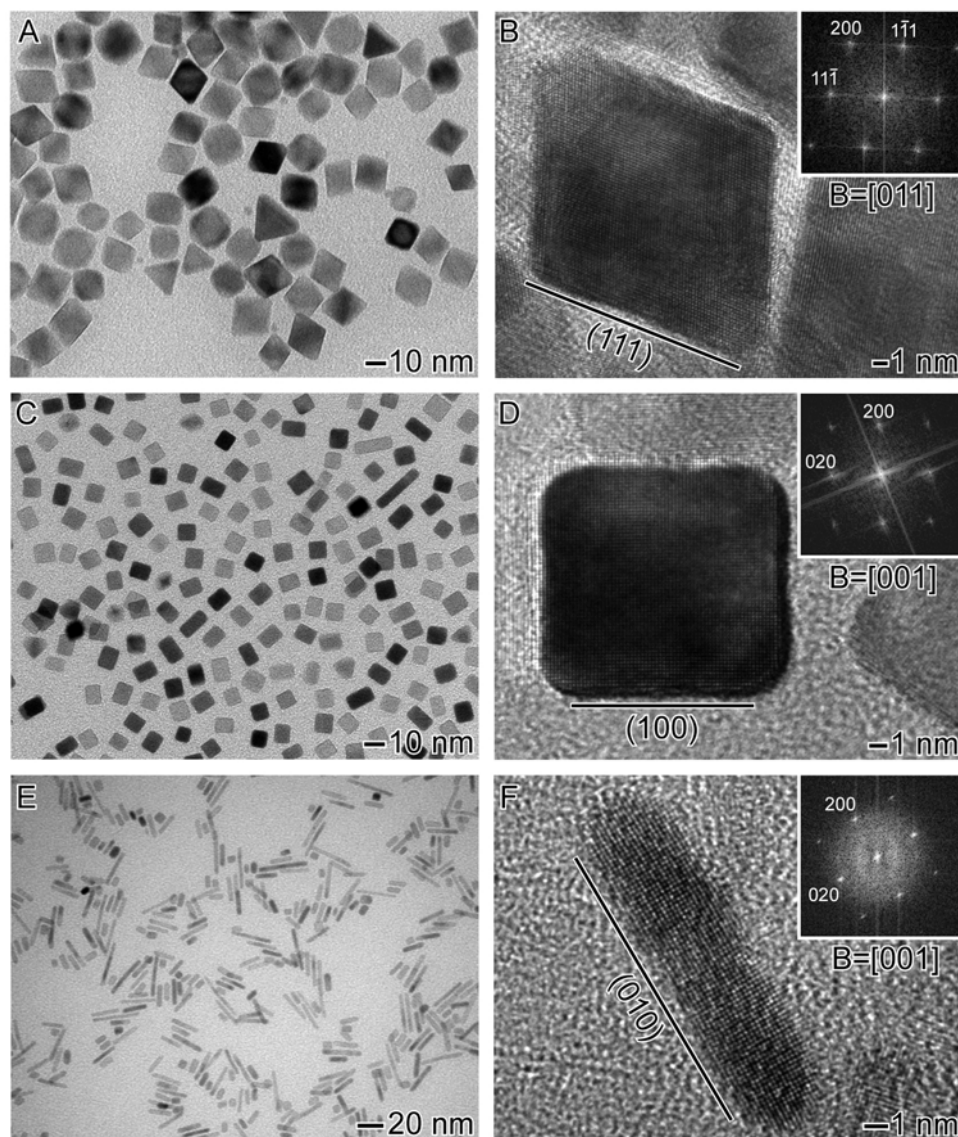


Figure 3.1. TEM and HRTEM images Pd nanocrystals employed as sacrificial templates for the galvanic reaction with PtCl_6^{2-} : (A, B) octahedra, (C, D) nanocubes and (E, F) nanorods. The insets show FFT patterns of the HRTEM images, respectively. In (B), the hexagonal FFT pattern suggests that the nanocrystal was enclosed by $\{111\}$ facets. In (D), the square pattern confirms that the nanocrystal was enclosed by $\{100\}$ facets. In (F), the square pattern indicates that the nanorod sits on the grid against one of its $\{110\}$ facets.

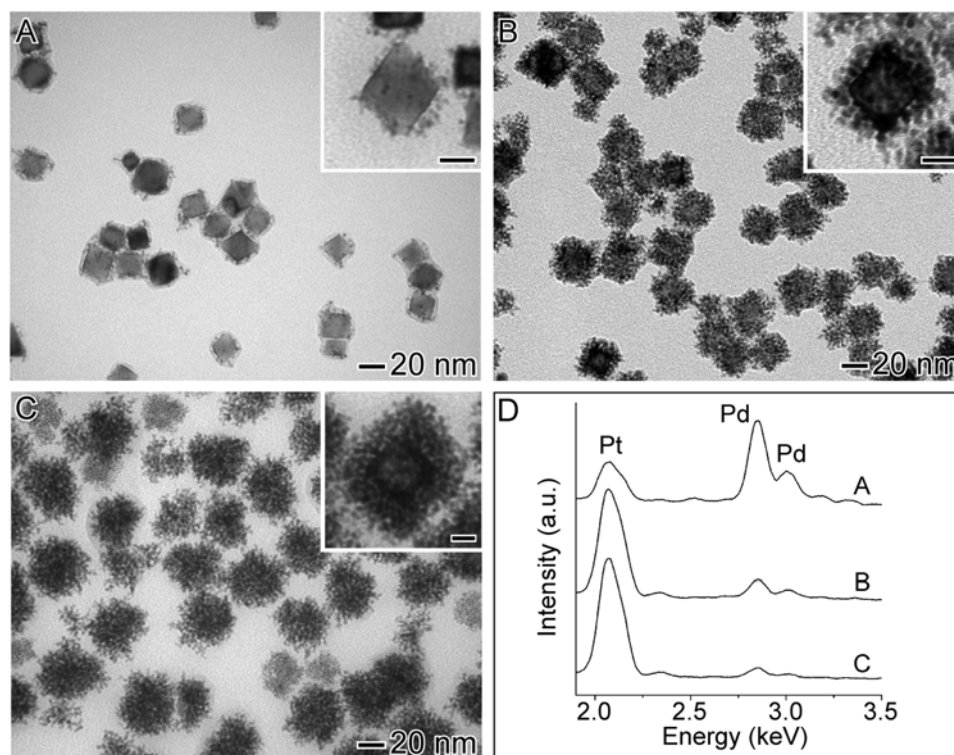


Figure 3.2. (A-C) TEM images of samples that were obtained by titrating the Pd octahedra with different volumes of 0.4 mM PtCl_6^{2-} : (A) 0.9, (B) 1.8, and (C) 2.7 mL. The scale bars in the insets correspond to 10 nm. (D) EDX spectra of the products shown in (A-C). The Pt atomic percentages obtained for the samples depicted in (A-C) were 16.8, 72.5 and 84.6, respectively.

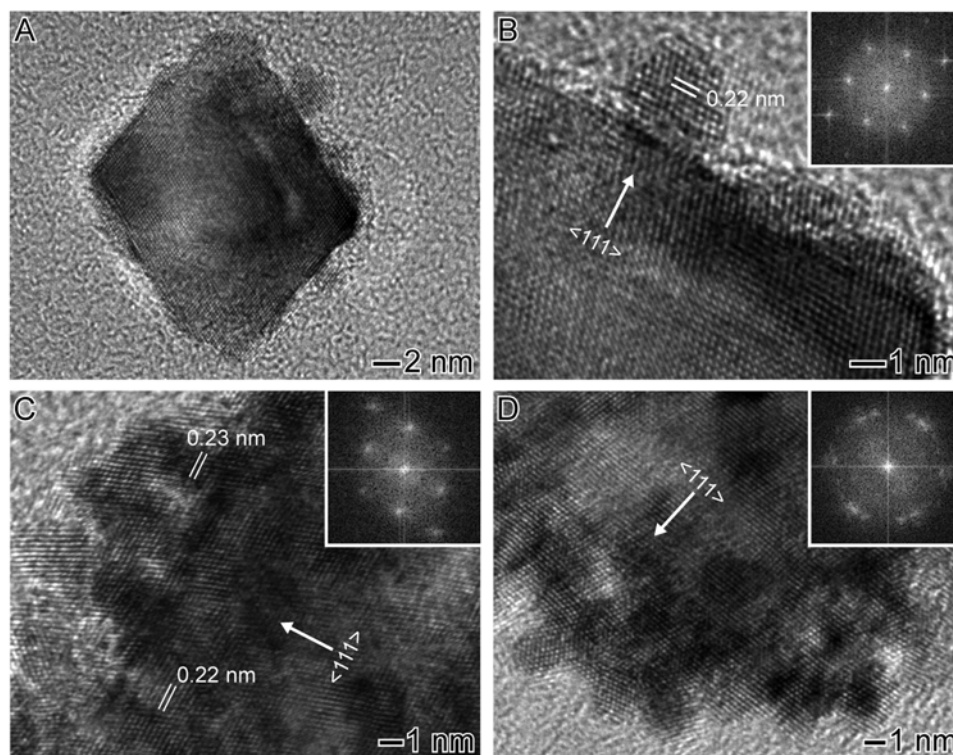


Figure 3.3. HRTEM images of the samples obtained by titrating the Pd octahedra with: (A, B) 0.9 mL and (C, D) 1.8 mL of 0.4 mM PtCl_6^{2-} . The insets show FFT patterns of the corresponding HRTEM images. In the early stage of the reaction (A, B), one can clearly observe the epitaxial growth of small Pt islands on the surface of the Pd octahedron. At a later stage (C, D), epitaxial correlation was only observed for the Pt branches that grew directly from the surface of the Pd octahedron.

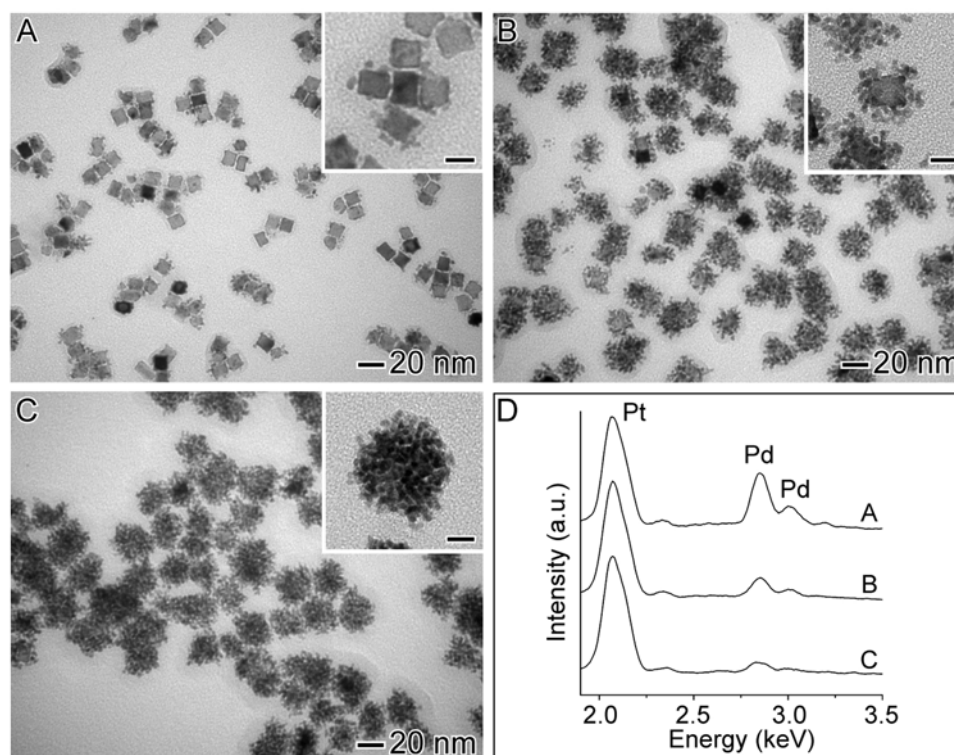


Figure 3.4. (A-C) TEM images of samples that were obtained by titrating the Pd nanocubes with different volumes of 0.4 mM PtCl_6^{2-} : (A) 0.9, (B) 1.8, and (C) 2.7 mL. The scale bars in the insets correspond to 10 nm. (D) EDX spectra obtained for the samples shown in (A-C). The Pt atomic percentage increased from 44.3 to 69.5 and 81.6 as the reaction proceeded.

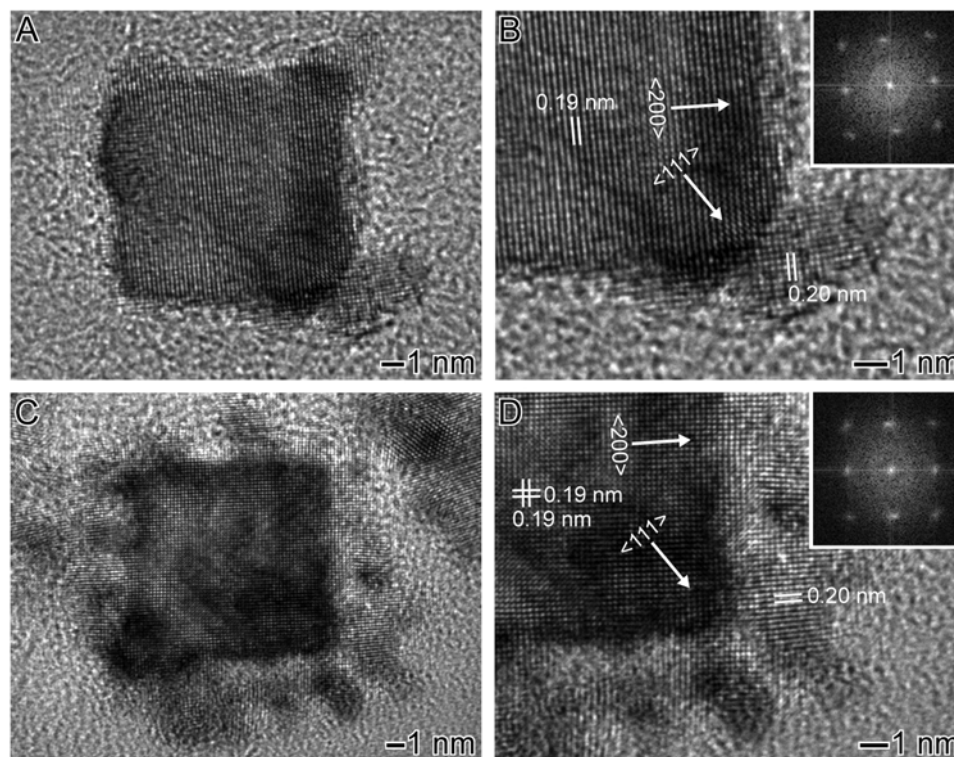


Figure 3.5. HRTEM images of the samples obtained by titrating the Pd nanocubes with: (A, B) 0.9 and (C, D) 1.8 mL of 0.4 mM PtCl_6^{2-} . The insets display FFT patterns of the corresponding HRTEM images. Similar to what was observed for Pd octahedra, small Pt islands and branches were found to grow epitaxially on the surface of the nanocube in the (A, B) early stage and (C, D) late stages of the reaction, respectively.

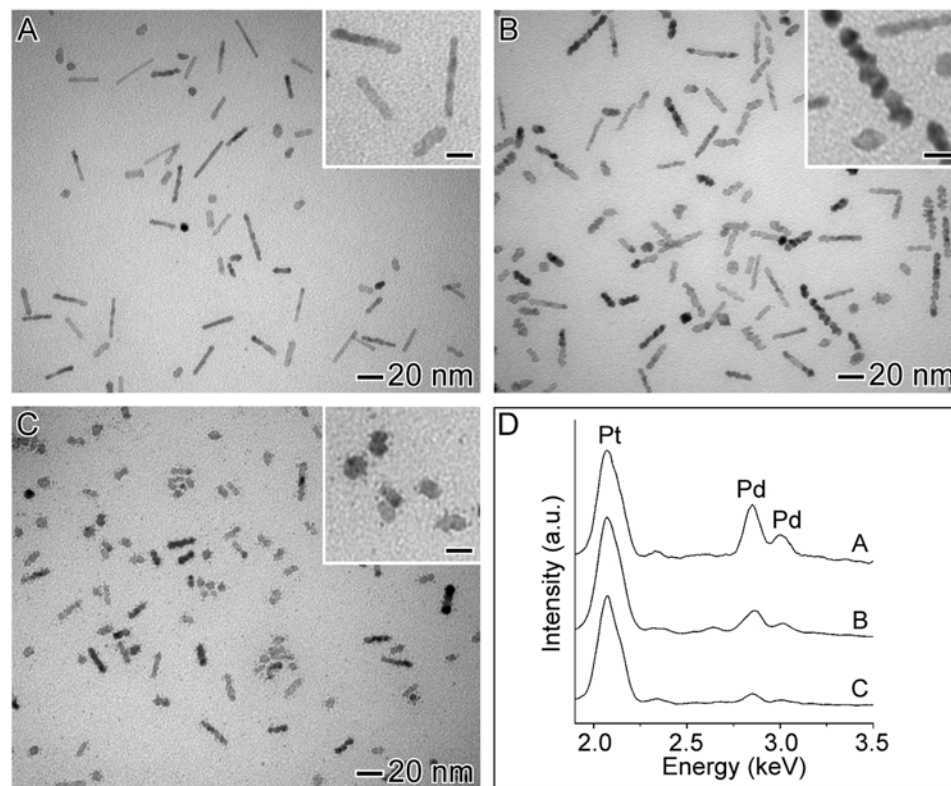


Figure 3.6. TEM images for the Pd_{rod}-Pt nanocrystals that were obtained by titrating the Pd nanorods with: (A) 1.8 and (B) 2.7 and (C) 3.6 mL of 0.4 mM PtCl₆²⁻. The scale bar in the inset corresponds to 10 nm. (D) EDX spectra obtained for the samples shown in (A-C). The Pt atomic percentage increased from 44.3 to 69.5 and 81.6 as the reaction proceeded.

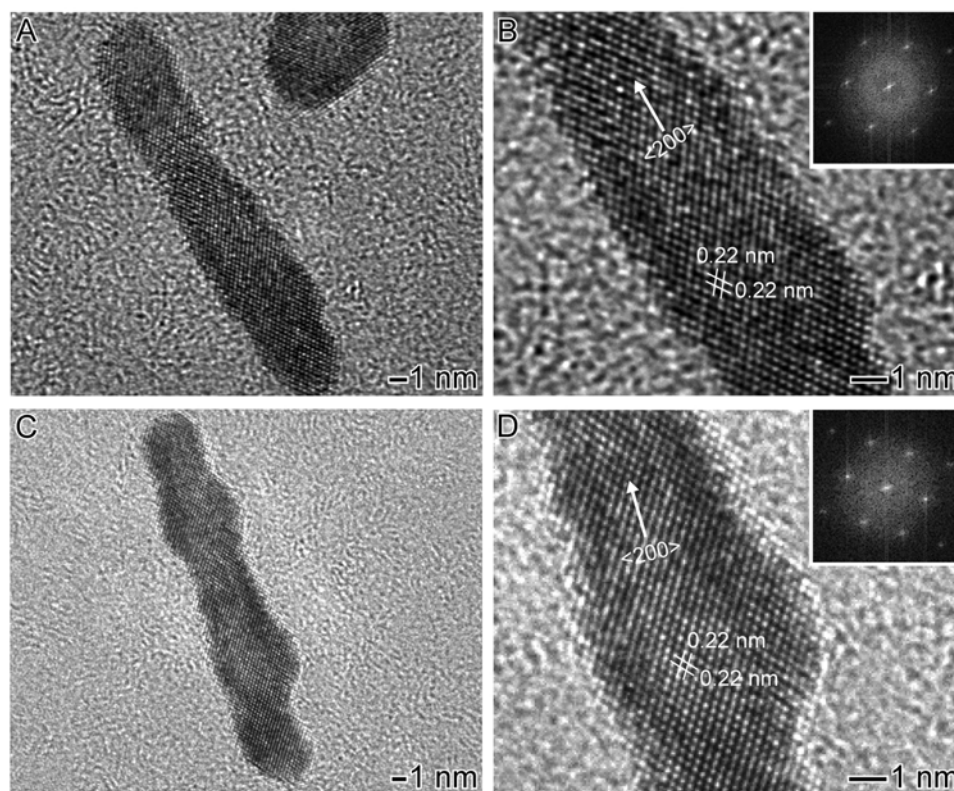


Figure 3.7. HRTEM images of the samples obtained by titrating the Pd nanorods with: (A, B) 1.8 and (C, D) 2.7 mL of 0.4 mM PtCl_6^{2-} . The insets display FFT patterns of the corresponding HRTEM images. In the early stage of the reaction (A, B), the epitaxial deposition of a thin Pt shell over the surface of the Pd nanorod can be observed. No significant island-growth was detected at this stage. As the reaction progressed (C, D), the epitaxial deposition of a thin Pt shell containing a large number of Pt islands (bumps) on the surface of the nanorods took place. The FFT pattern (inset in D) shows that the $\text{Pd}_{\text{rod}}\text{-Pt}$ nanocrystal was single-crystalline.

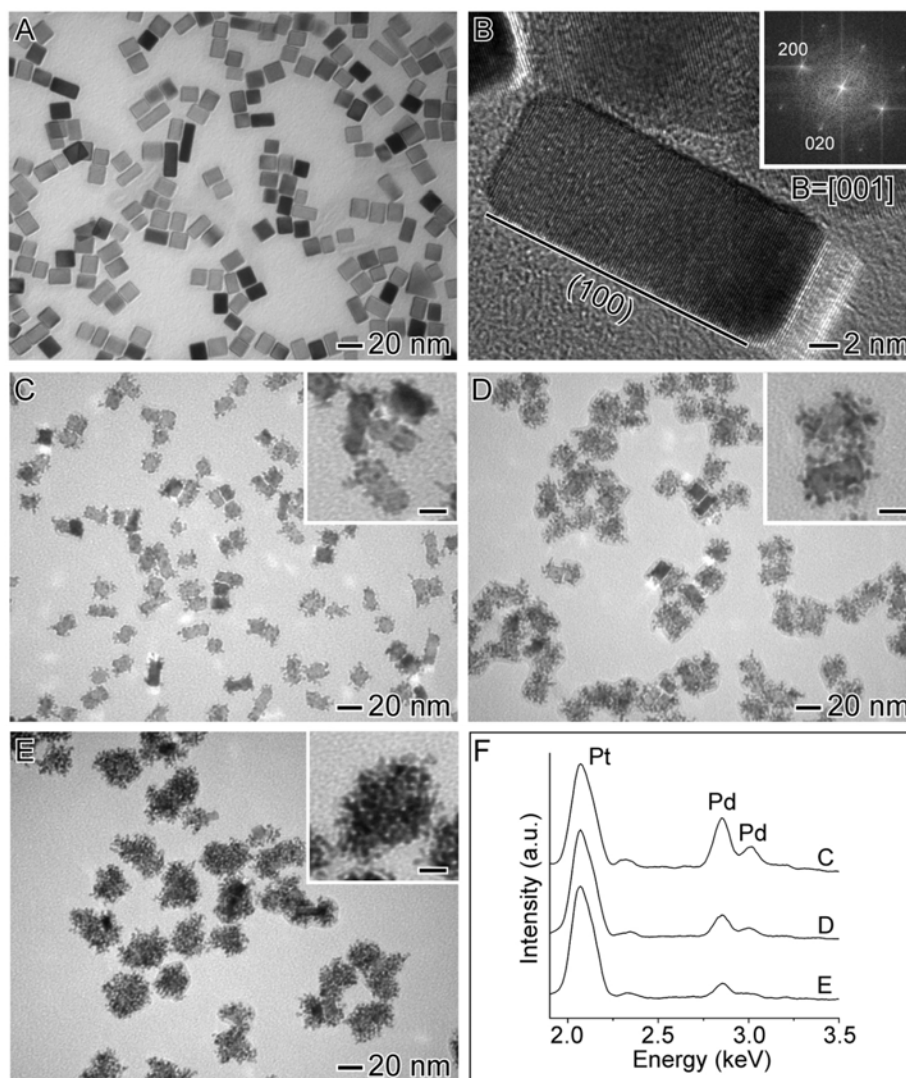


Figure 3.8. (A) TEM and (B) HRTEM image of Pd nanobars employed as sacrificial templates in the galvanic reaction with PtCl_6^{2-} . In (B), a cubic pattern confirms that the nanobar is enclosed by $\{100\}$ facets. (C-E) TEM images of samples that were obtained by titrating the Pd nanobars with different volumes of 0.4 mM PtCl_6^{2-} : (C) 0.9, (D) 1.8 and (E) 2.7 mL. The scale bars in the insets correspond to 10 nm. (F) EDX spectra obtained for the products shown in (C-E). The utilization of Pd nanobars as sacrificial templates in the galvanic reaction led to identical results as previously observed for the Pd nanocubes, indicating that shape anisotropy did not influence the Pt growth mechanism.

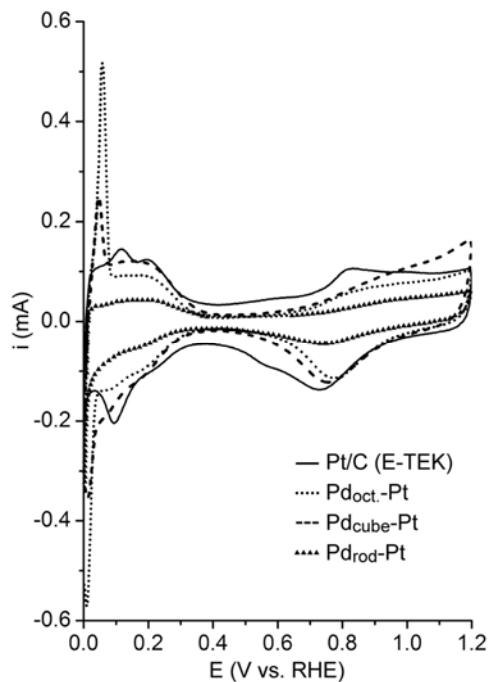


Figure 3.9. Cyclic voltammogram curves for commercial Pt/C (E-TEK, solid line), Pd_{oct}-Pt (dotted line), Pd_{cube}-Pt (dashed line) and Pd_{rod}-Pt (triangles). The calculated ECSA for Pt/C, Pd_{oct}-Pt, Pd_{cube}-Pt and Pd_{rod}-Pt were 79.8, 73.2, 86.6 and 32.6 m²/g_{Pd+Pt}, respectively, based on the total mass of metals.

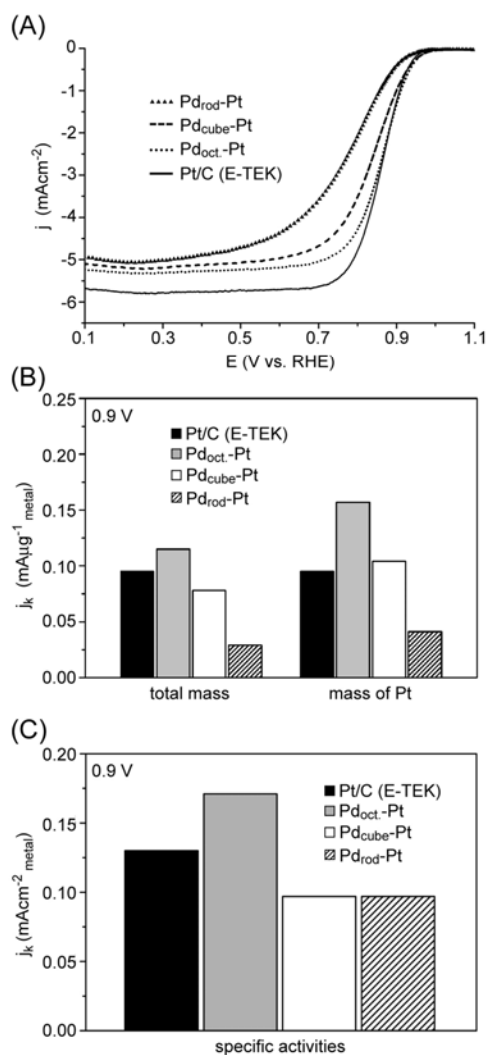


Figure 3.10. (A) ORR polarization curves for commercial Pt/C (E-TEK) and Pd_{oct}-Pt, Pd_{cube}-Pt and Pd_{rod}-Pt bimetallic nanocrystals that were obtained after titration with 1.8 mL (for Pd_{oct}-Pt and Pd_{cube}-Pt) and 2.7 mL (for Pd_{rod}-Pt) of 0.4 mM PtCl₆²⁻. In (A), the current densities were normalized in reference to the geometric area of a RDE (i.e., 0.196 cm²). (B, C) Bar graphs illustrating the mass activities (B) and specific activities (C) obtained for the catalysts shown in (A). The mass and specific activities are given as kinetic current densities (j_k) normalized in reference to the loading amount and ECSA of metal, respectively.

3.5. Notes to Chapter 3

- [1] (a) Lu, X.; Chen, J.; Skrabalak, S. E.; Xia, Y. *Proc. IMechE Part N: J. Nanoengineering and Nanosystems* **2008**, *221*, 1. (b) Sun, Y.; Mayers, B. T.; Xia, Y. *Nano Letters* **2002**, *2*, 481. (c) Sun, Y.; Mayers, B.; Xia, B. *Adv. Mater.* **2003**, *15*, 641.
- [2] (a) Sun, Y.; Xia, Y. *J. Am. Chem. Soc.* **2004**, *126*, 3892. (b) Sun, Y.; Xia, Y. *Science* **2002**, *298*, 2176.
- [3] (a) Cobley, C. M.; Campbell, D. J.; Xia, Sun, Y. *Adv. Mater.* **2008**, *20*, 748. (b) Skrabalak, S. E.; Au, L.; Li, X.; Xia, Y. *Nat. Protoc.* **2007**, *2*, 2182. (c) Chen, J.; McLellan, J. M.; Siekkinen, A.; Xiong, Y.; Li, Z.-Y.; Xia, Y. *J. Am. Chem. Soc.* **2006**, *128*, 14776. (d) Chen, J.; Wiley, B.; McLellan, J.; Xiong, Y.; Li, Z.-Y.; Xia, Y. *Nano Lett.* **2005**, *5*, 2058.
- [4] (a) Kim, M. H.; Lu, X.; Wiley, B.; Lee, E. P.; Xia, Y. *J. Phys. Chem. C* **2008**, *112*, 7872. (b) Lu, X.; Tuan, H.-Y.; Chen, J.; Li, Z.-Y.; Korgel, B. A.; Xia, Y. *J. Am. Chem. Soc.* **2007**, *129*, 1733.
- [5] Sun, Y.; Wiley, B.; Li, Z.-Y.; Xia, Y. *J. Am. Chem. Soc.* **2004**, *126*, 9399.
- [6] (a) Chen, J.; Wiley, B. J.; Xia, Y. *Langmuir* **2007**, *23*, 4120. (b) Sun, Y.; Xia, Y. *Adv. Mater.* **2004**, *16*, 264.
- [7] Huang, X.; Zhang, H.; Guo, C.; Zhou, Z.; Zheng, N. *Angew. Chem. Int. Ed.* **2009**, *48*, 4808.

- [8] (a) Mallouk, T. E. *Nature* **1990**, *343*, 515. (b) Steele, B. C. H.; Heinzl, A. *Nature* **2001**, *414*, 345. (c) Perry, M. L.; Fuller, T. F. *J. Electrochem. Soc.* **2002**, *149*, S59. (d) Ertl, G. *Handbook of Heterogeneous Catalysis*, Wiley-VCH: Weinheim, 2008.
- [9] Gasteiger, H.; Kocha, S. S.; Sompalli, B.; Wagner, F.T. *Appl. Catal. B* **2005**, *56*, 9.
- [10] (a) Marković, N. M.; Schmidt, T. J.; Stamenković, V.; Ross, P. N. *Fuel Cells* **2001**, *1*, 105. (b) Marković, N. M.; Ross, P. N. *Surf. Sci. Rep.* **2002**, *45*, 117. (c) Chen, W.; Kim, J.; Sun, S.; Chen, S. *J. Phys. Chem. C* **2008**, *112*, 3891.
- [11] (a) Guo, S.; Dong, S.; Wang, E. *Chem. Eur. J.* **2008**, *14*, 4689. (b) Chen, Z.; Waje, M.; Li, Z.; Yan, Y. *Angew. Chem. Int. Ed.* **2007**, *46*, 4060.
- [12] (a) Chen, G.; Xia, D.; Nie, Z.; Wang, Z.; Wang, L.; Zhang, L.; Zhang J. *Chem. Mater.* **2007**, *19*, 1840. (b) Liang, H. -P.; Zhang, H. -M.; Hu, J. -S.; Guo, Y. -G.; Wan, L. -G.; Bai, C. -L. *Angew. Chem. Int. Ed.* **2004**, *43*, 1540
- [13] (a) Fan, F. -R.; Liu, D. -Y.; Wu, Y. -F.; Duan, S.; Xie, Z. -X.; Jiang Z. -Y.; Tian, Z. -Q. *J. Am. Chem. Soc.* **2008**, *130*, 6949. (b) Guo, S.; Fang, Y.; Dong, S.; Wang, E. *J. Phys. Chem. C* **2007**, *111*, 17104. (c) Zhou, S.; McIlwrath, K.; Jackson, G.; Eichhorn, B. *J. Am. Chem. Soc.* **2006**, *128*, 1780.
- [14] Lim, B.; Wang, J.; Camargo, P. H. C.; Jiang, M.; Kim, M. J.; Xia, Y. *Nano Lett.* **2008**, *8*, 2535.
- [15] Lim, B.; Jiang, M.; Camargo, P. H. C.; Cho, E. C.; Tao, J.; Lu, X.; Zhu, Y.; Xia, Y. *Science* **2009**, *324*, 1302
- [16] Yang, J.; Lee, J. Y.; Zhang, Q.; Zhou, W.; Liu, Z. *J. Electrochem. Soc.* **2008**, *155*, B776.

- [17] (a) Lim, B.; Jiang, M.; Tao, J.; Camargo, P. H. C.; Zhu, Y.; Xia, Y. *Adv. Funct. Mater.* **2009**, *19*, 189. (b) Lim, B.; Xiong, Y.; Xia, Y. *Angew. Chem. Int. Ed.* **2007**, *46*, 9279.
- [18] (a) Xiong, Y.; Cai, H.; Wiley, B. J.; Wang, J.; Kim, M. J.; Xia, Y. *J. Am. Chem. Soc.* **2007**, *129*, 3665. (b) Camargo, P. H. C.; Xiong, Y.; Ji, L.; Zuo, J. M.; Xia, Y. *J. Am. Chem. Soc.* **2007**, *129*, 15452.
- [19] (a) Mukerjee, S.; Srinivasan, S. *J. Electroanal. Chem.* **1993**, *357*, 201. (b) Mukerjee, S.; Srinivasan, S.; Soriaga, M. P.; McBreen, J. *J. Electrochem. Soc.* **1995**, *142*, 1409.
- [20] (a) Zhang, J.; Vukmirovic, M. B. V.; Xiu, Y.; Mavrikakis, M.; Adzic, R. R. *Angew. Chem. Int. Ed.* **2005**, *44*, 2132. (b) Shao, M. H.; Huang, T.; Liu, P.; Zhang, J.; Sasaki, K.; Vukmirovic, M. B.; Adzic, R. R. *Langmuir* **2006**, *22*, 10409. (c) Zhang, J.; Mo, Y.; Vukmirovic, M. B.; Klie, R.; Sasaki, K.; Adzic, R. R. *J. Phys. Chem. B* **2004**, *108*, 10955.
- [21] (a) Bard A. J.; Faulkner, L. R. *Electrochemical Methods Fundamentals and Application*, 2nd ed.; John Wiley & Sons: New York, 2001. (b) Schmidt, T. J.; Gasteiger, H. A.; Stäb, G. D.; Urban, P. M.; Kolb, D. M.; Behm, R. J. *J. Electrochem. Soc.* **1998**, *145*, 2354.
- [22] (a) Lim, B.; Lu, X.; Jiang, M.; Camargo, P. H. C.; Cho, E. C.; Lee, E. P.; Xia, Y. *Nano Lett.* **2008**, *8*, 4043. (b) Mahmoud, M. A.; Tabor, C. E.; El-Sayed, M. A.; Ding, Y.; Wang, Z. L. *J. Am. Chem. Soc.* **2008**, *130*, 4590.

- [23] (a) Chambers, S. A.; *Surf. Sci. Rep.* **2000**, *39*, 105. (b) Bauer, E.; van der Merwe, J. H.; *Phys. Rev. B* **1986**, *33*, 3657.
- [24] Peng, Z.; Yang, S. *Nano Today* **2009**, *4*, 143.
- [25] Rozas, R.; Kraska, T. *J. Phys. Chem. C* **2007**, *111*, 15784.
- [26] Gomez, R.; Orts, J. M.; Alvarez-Ruiz, B. L.; Feliu, J. J. *Phys. Chem. B* **2004**, *108*, 228.
- [27] Zhang, J.; Huang, M.; Ma, H.; Tian, F.; Pan, W.; Chen, S. *Electrochem. Commun.*, **2007**, *9*, 63.
- [28] Xiao, L.; Zhuang, L.; Liu, Y.; Abruna, H. D. *J. Am. Chem. Soc.*, **2009**, *131*, 602.
- [29] (a) Stamenkovic, V. R.; Fowler, B.; Mun, S.; Wang, G. F.; Ross, P. N.; Lucas, C. A.; Marković, N. M.; *Science* **2007**, *315*, 493. (b) Marković, N. M.; Ross, P. N. *Surf. Sci. Rep.* **2002**, *45*, 117. (c) Marković, N. M.; Gasteiger, H.; Ross, P. N. *J. Electrochem. Soc.* **1997**, *144*, 1591. (d) Marković, N. M.; Adzic, R. R.; Cahan, B. D.; Yeager, E. B. *J. Electroanal. Chem.* **1994**, *377*, 249.

Chapter 4

Facile Synthesis of Tadpole-Like Nanostructures Consisting of Au Heads and Pd Tails

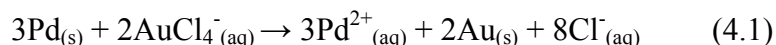
4.1. Introduction

Hybridization provides an effective strategy for enhancing the functionality of materials.¹ It is also possible to tune the electronic and optical properties of nanoparticles by forming a hybrid system.² Palladium serves as a major catalyst in many industrial applications.³ It has been shown that incorporation of Au into Pd nanoparticles can reduce the material cost while enhancing their catalytic activity, selectivity, and stability.⁴ Here I report the synthesis of Pd-Au hybrid nanostructures in a tadpole shape, with the head being a Au nanoparticle and the tail being a Pd nanorod. The synthesis is based upon the galvanic replacement reaction between single-crystal Pd nanorods and AuCl_4^- ions. Different from previous systems that involved Ag-based templates and AuCl_4^- ions,⁵ the Au atoms resulting from the galvanic reaction did not coat the entire surface of a Pd nanorod to generate a core-sheath or hollow structure. Instead, the nucleation and deposition of Au was localized to the end(s) of a Pd nanorod, leading to the formation of a Pd-Au tadpole.

4.2. Results and Discussion

Figure 4.1A shows a TEM image of the initial Pd nanorods that had an octagonal cross section, with the side surface enclosed by a mix of {110} and {100} facets. They had an average diameter of 4.0 ± 0.3 nm and length of 17.4 ± 2.4 nm (78% of them were rods). The nanorods were synthesized by reducing PdCl_4^{2-} ions with ethylene glycol in water in the presence of poly(vinyl pyrrolidone) (PVP) and Br^- ions.⁶ According to our proposed mechanism, cuboctahedral seeds were formed in the nucleation stage, whose surfaces were passivated by Br^- ions.⁷ Oxidative etching due to the presence of oxygen (from air) and chloride (from PdCl_4^{2-}) could break the cubic symmetry of a seed, leading to the formation of an octagonal nanorod.⁸

Figures 4.1, B-D, shows TEM images of the products after the Pd nanorods had reacted with different volumes of 0.4 mM HAuCl_4 . Specifically, after the addition of 1 mL of HAuCl_4 (Figure 4.1B), both ends of each Pd nanorod started to be enlarged and became rounded due to the deposition of Au via the following reaction:



The nanorods shown in Figure 4.1B had an average diameter of 3.5 ± 0.3 nm and length of 18.4 ± 2.9 nm (75% of them were rods). It is important to note that Pd oxidation can occur from any place on the entire surface of a nanorod, including the {100} and {110} side faces and the {100} ends. However, Au deposition only occurs at the ends (Figure 4.2). This can be attributed to the fact that the electrons resulting from oxidation of Pd tend to

be separated as far as possible (in this case, to the ends of a nanorod) due to a strong repulsion between them. Pd is also a good conductor, in which electrons can migrate freely.

As more HAuCl_4 was added, more Pd would be dissolved from the nanorod accompanying the further deposition of Au onto both ends. Interestingly, a transition from two-end to one-end growth was observed, producing a Pd-Au tadpole consisting of a Au head and a Pd tail (Figure 4.1C). In this case, Ostwald ripening occurred for each nanostructure that shifted Au from one end to the other. This behavior was first proposed for the growth of Au tips on CdSe nanorods and can be understood as the following:^{9a} as the Au heads became bigger, their size difference also increased to create a driving force for Ostwald ripening.⁹ The presence of a Pd segment between the two Au heads greatly facilitates the ripening process as Pd is a good conductor for electrons. After further addition of HAuCl_4 (Figure 4.1D), more Pd consumption from the rods caused deposition of more Au at the pre-formed Au heads, increasing their diameter to 11 nm. At the same time, it can be observed that the width and length of the Pd tails in Figures 4.1, C and D, (W/L: $3.4 \pm 0.4 / 11.9 \pm 1.8$ and $2.9 \pm 0.4 / 11.6 \pm 2.5$ nm, respectively; 75% of them were rods) were both reduced relative to the initial Pd nanorods (4.0 nm and 17.4 nm).

When an excess amount of HAuCl_4 was introduced, the Pd-Au tadpoles were dismantled into smaller/shorter Pd nanorods and spherical Au nanoparticles (Figure 4.3). At this point, even though the amount of HAuCl_4 added was enough to consume all the Pd from the nanorods, complete Pd oxidation was not observed. This can be attributed to the coverage of side surface by Au atoms at a late stage of the reaction, preventing the Pd

nanorods from further oxidation. This is supported by STEM/EDS data (see discussion below), in which a small content of Au was detected along the Pd tail. It is worth pointing out that the samples shown in Figures 4.1, C and D, appear to present fewer Au heads than Pd tails. It is possible that after the transition from two-end to one-end growth, Ostwald ripening of the Au tips continued to take place resulting in fewer, large Au heads. It is also possible that each Pd nanorod was broken into several segments to double or triple its number. Figure 4.4 shows the UV-vis spectra taken from the solution at various stages of the reaction, clearly showing the evolution of a surface localized plasmon resonance (LSPR) peak associated with the Au nanoparticles. Because the LSPR peak of Pd nanorods (i.e., tails) is located in the UV region, it is expected that the coupling between these two SPR peaks is relatively weak and can be neglected.

Figure 4.5A shows a high-resolution TEM image recorded along the [110] axis (with respect to the Pd tail). It can be observed that the hybrid nanostructure is a piece of single crystal. Due to a close matching between the {111} lattice spacings of Au and Pd (4% mismatch), the Au atoms could nucleate and grow epitaxially from the end faces of a Pd nanorod along the [100] direction, producing parallel fringes between the tail and the spherical head. The {111} fringes show a period of 2.24 and 2.36 Å, as expected for *fcc* Pd and Au, respectively.

I also performed a STEM/EDS line scanning analysis to reveal the compositional variation along the long axis of the tadpole-shaped nanostructure (Figure 4.5B). As illustrated on the dark-field STEM image, the percentages of Pd and Au were determined for six different sites, *a* to *f*, where *a* is located at the bottom of the tail and *f* at the top of

the head. The results show that the tail (*a* to *c*) is indeed composed mostly of Pd. The atomic percentage for Au was 2.1%, 9.5% and 7.0%, respectively. The low percentages of Au in the tail can probably be attributed to the surface diffusion of Au along the Pd tail. This result also explains the incomplete oxidation of Pd observed at later stages of the galvanic reaction. Site *d*, which is from the region connecting the tail to the head, contains both Pd and Au (64.8% and 36.2%, respectively). Finally, the atomic percentages for sites *e* and *f* confirm that the heads contain mostly Au (~93%). Figure 4.6 summarizes all major steps involved in the localized deposition of Au as a result of the galvanic replacement reaction.

4.3. Summary

I have demonstrated the synthesis of a new type of hybrid nanostructure in the tadpole shape consisting of a Au head and a Pd tail. The formation of such a morphology involved a localized galvanic replacement mechanism. In the earlier stages of the reaction, localized deposition of Au onto both ends of a rod was observed because the electrons tend to be pushed to the ends of the rod as a result of the repulsive forces. At a later stage, a transition from two-end to one-end growth occurred as a result of Ostwald ripening, leading to the formation of a Pd-Au tadpole composed of a Au head and a Pd tail. It is worth pointing out that this localized deposition of Au is unique for Pd nanorods. No such phase segregation was observed when Pd nanoparticles were used in place of the rods. A similar structure was also observed by Wetz *et al.*¹⁰ for the galvanic reaction between Co nanorods and Au compounds. However, these authors did not

provide detailed elemental analysis on each hybrid nanostructure; did not observe the transition from two-end to one-end growth; and did not recognize the importance of rod shape in promoting the localized deposition of Au. It is expected that these Pd-Au tadpoles, combining the properties from both Pd nanorods and Au nanoparticles, may find use in catalysis and LSPR sensing owing to the exceptional sensitivity of Pd towards H₂. This method can also be extended to other metals, such as Pt, to produce a variety of Pd-based hybrid nanostructures.

4.4. Experimental Section

Chemicals and Materials. Ethylene glycol (EG, J. T. Baker, 99.9%), sodium palladium(II) chloride (Na₂PdCl₄, Aldrich, 99.998%), potassium bromide (KBr, Fisher), sodium chloride (NaCl, J. T. Baker), poly(vinyl pyrrolidone) (PVP, MW≈55,000, Aldrich), and ethanol (AAPER Alcohol and Chemical Co., 200 proof) were all used as received.

Synthesis of Pd Nanorods. In a typical synthesis, 5 mL of EG was added to a 25-mL three-neck flask equipped with a reflux condenser and a Teflon-coated magnetic stirring bar. This system was heated at 140 °C in air under magnetic stirring for 1 h. Meanwhile, 0.0486 g of Na₂PdCl₄ and 0.2574 g of KBr were dissolved in 3 mL of water, and 0.0916 g of PVP was dissolved in 3 mL of EG at room temperature. These two solutions were then injected simultaneously into the flask using a two-channel syringe pump (KDS-200, Stoelting, Wood Dale, IL) at a rate of 45 mL per hour. The reaction mixture was heated at 140 °C in air for another 3 h before the product was collected by

centrifugation and washed with acetone once and with ethanol three times to remove most of the EG and excess PVP.

Galvanic Replacement Reactions. In a typical synthesis, a fixed amount (15 mM, 200 μ L) of Pd nanorods was dispersed in 5 mL of water containing PVP (1 mg/mL) in a 50-mL flask under magnetic stirring. This system was heated at 100 $^{\circ}$ C for 10 min. A specific amount (as indicated in the text) of 0.4 mM H₂AuCl₄ was added to the flask through a syringe pump at a rate of 45 mL per hour under magnetic stirring. The solution was heated for another 10 min and then cooled down to room temperature. After that, the solution was centrifuged and washed with saturated NaCl solution to ensure that all Pd(II) species were in the form of [PdCl₄]²⁻ to avoid the precipitation of PdCl₂. Finally, the sample was centrifuged and washed with water several times to remove PVP and NaCl before characterization.

Instrumentation. Transmission electron microscopy (TEM) studies were performed with a Phillips CM100 microscope operated at 100 kV. The TEM images were obtained with a Gatan digital camera. High-resolution TEM images (HRTEM) were taken on a JEOL field-emission transmission electron microscope (2100F) operated at 200 kV. Filtered images were generated by inverse FFT with a Gatan Digital Micrograph program. The STEM/EDS measurements were collected using a Vacuum Generator HB501 STEM microscope equipped with an EDS - Oxford ISIS 30mm ATW detector. Samples for TEM/HRTEM were prepared by drying drops of the aqueous suspension of the nanostructures on carbon-coated copper grids (SPI, West Chester, PA) under ambient

conditions. UV-visible (UV-vis) absorption spectra were taken on a Hewlett-Packard 8452A spectrometer using quartz cuvettes with an optical path length of 1 cm.

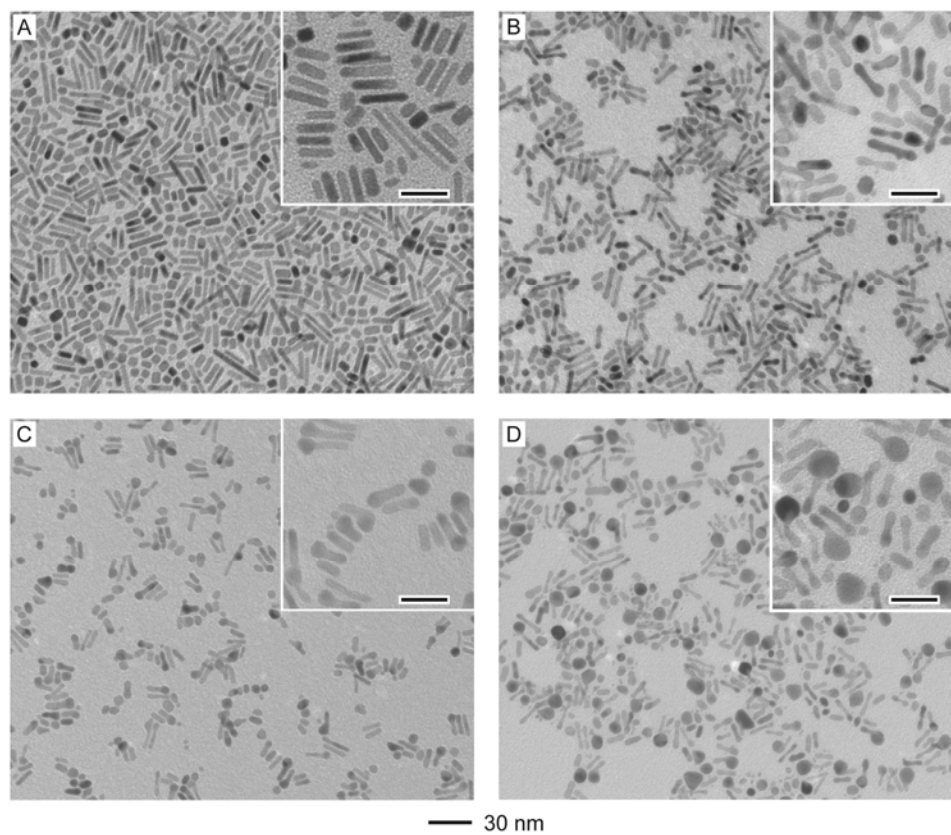


Figure 4.1. TEM images of (A) Pd nanorods and (B-D) samples that were obtained by titrating the Pd nanorods with different volumes of 0.4 mM H_{Au}Cl₄ solution: B) 1, C) 2, and D) 4 mL. The scale bars in the insets correspond to 20 nm.

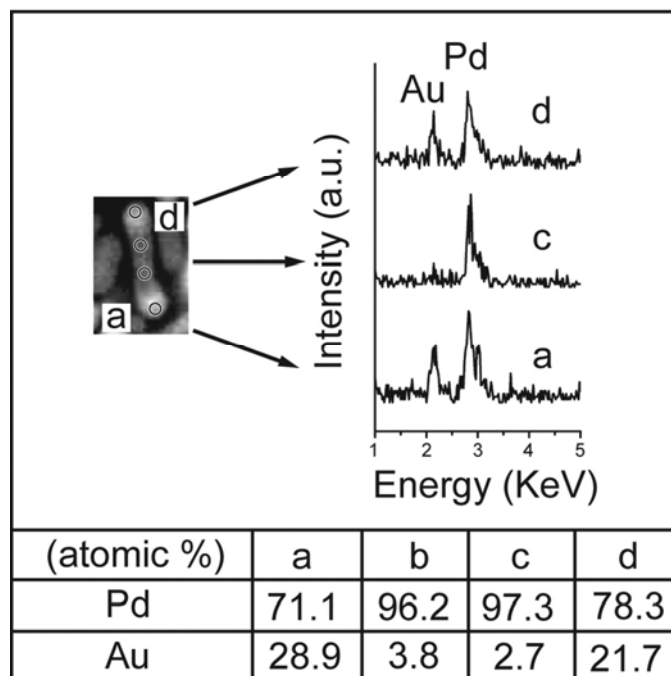


Figure 4.2. STEM/EDS analysis at 4 different sites (*a-d*) along the Pd-Au hybrid nanostructure shown in Figure 4.1B. The STEM image indicates that Au was mainly deposited on both ends of the Pd nanorod. The enclosed table presents the EDS atomic percentages for Pd and Au at sites *a-g*. The EDS spectra taken from *a*, *g* and *g* are also included.

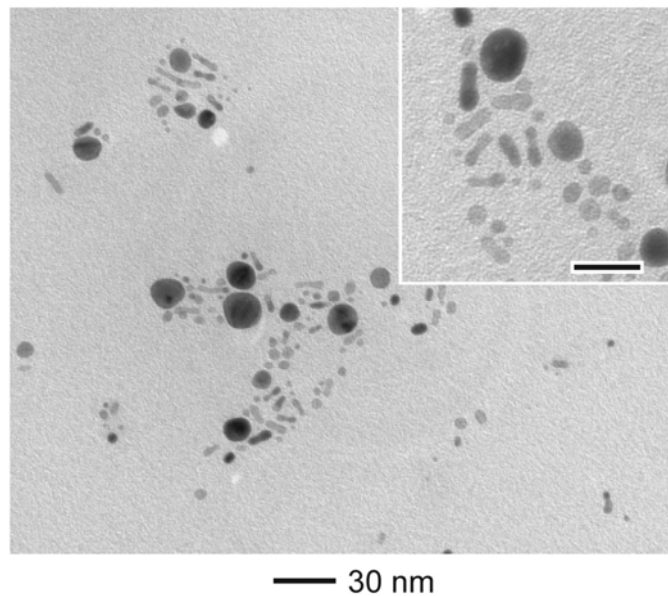


Figure 4.3. Titration of Pd nanorods with 10 mL of 0.4 mM HAuCl₄. In this case, the Pd-Au tadpoles were dismantled into Au nanoparticles and smaller/shorter Pd fragments. The scale bar in the inset corresponds to 20 nm.

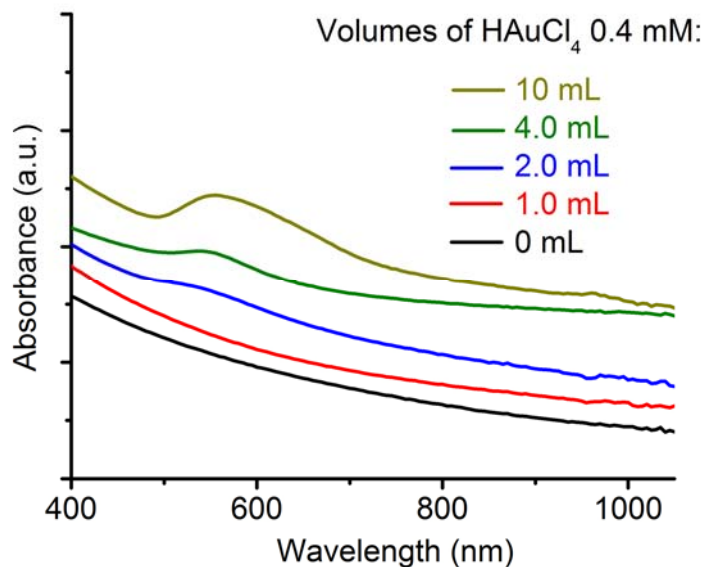


Figure 4.4. UV-vis spectra taken from a suspension of Pd nanorods after they had been titrated with 1, 2, 4 and 10 mL of 0.4 mM H_{AuCl}₄. A broad peak around 560 nm developed as the volume of H_{AuCl}₄ was increased from 2 to 10 mL, clearly showing the evolution of a localized surface plasmon resonance (LSPR) mode associated with the Au nanoparticles either located at the tips of the Pd-Au tadpoles (Au heads) or de-attached from the Pd segments.

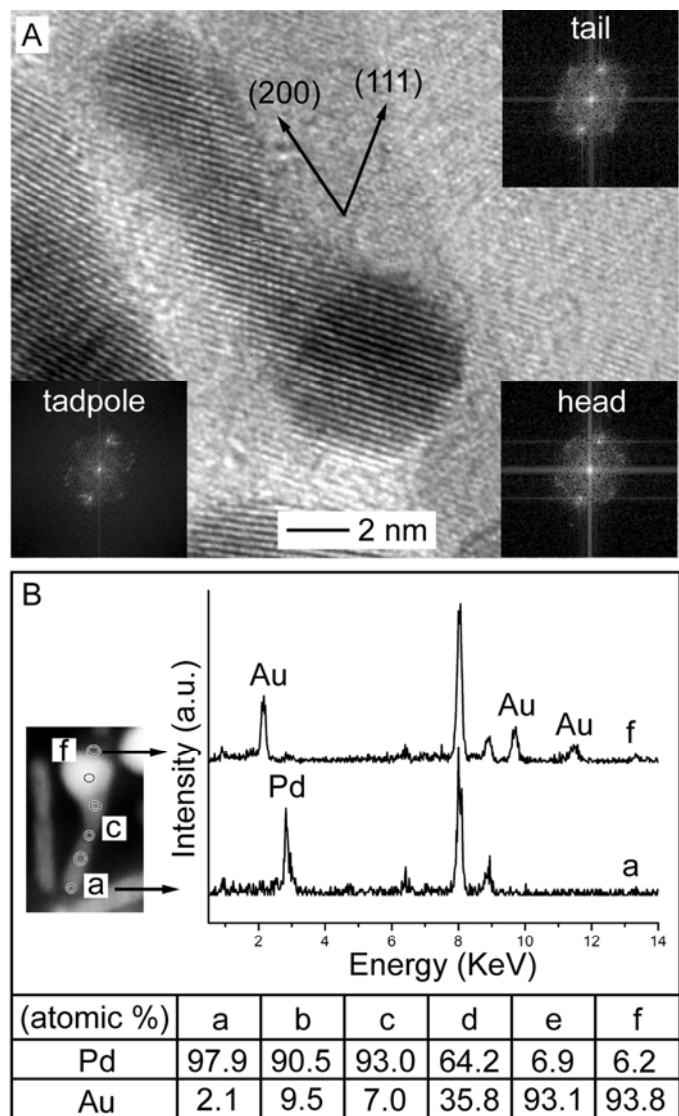


Figure 4.5. (A) High-resolution TEM image recorded along $[110]$ for the Pd-Au tadpoles shown in Figure 4.1C. The insets show FFT operations for the Pd tail, Au head and for the overall tadpole. In all cases, a hexagonal pattern of 6 points is observed, as expected for both *fcc* Au and Pd in the $[011]$ beam direction. (B) STEM/EDS analysis on 6 different sites along the Pd-Au tadpole (*a-f*), as marked on the DF STEM image. The table shows the EDS atomic percentages for Pd and Au obtained for each position. The EDS spectra for points *a* and *f* are also included.

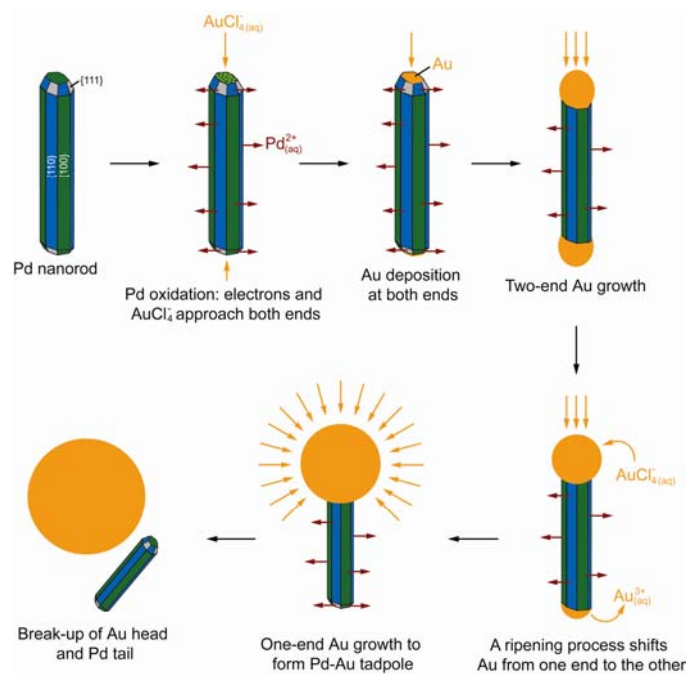


Figure 4.6. Schematic detailing all major steps involved in the galvanic replacement reaction between a Pd nanorod and AuCl_4^- ions. In the first step, Pd atoms are oxidized from certain sites on the nanorod, producing electrons that are quickly pushed to the ends of the nanorod due to the strong repulsion between them. AuCl_4^- ions are reduced by the electrons and epitaxially deposited onto both ends (two-end growth). As more Pd oxidation and AuCl_4^- reduction take place, the Au tips grow and reach a critical size at which a ripening process shifts Au from one end to the other, leading to a transition from two-end to one-end growth and production of a Pd-Au tadpole. The driving force for this ripening process comes from the stabilization of one Au head relative to the other one on each nanorod when the size difference between these two Au heads becomes sufficiently large as the tips grow and reach a critical size. In this scenario, the difference in surface energy favors the growth of larger particles at the expense of smaller ones. The Pd nanorod can provide a conductive path for electron migration from one tip to the other. As Pd oxidation further continues, more Au atoms will be deposited onto the Au head, and this growth can continue until the Pd-Au tadpoles are dismantled into short Pd fragments and a Au nanoparticle.

4.5. Notes to Chapter 4

- [1] See, for example: (a) Xiang, Y.; Wu, X.; Liu, D.; Jiang, X.; Chu, X.; Li, Z.; Ma, L.; Zhou, W.; Xie, S. *Nano. Lett.* **2006**, *6*, 2290. (b) Gao, J. H.; Liang, G. L.; Zhang, B.; Kuang, Y.; Zhang, X. X.; Xu, B. *J. Am. Chem. Soc.* **2007**, *129*, 1428. (c) Gao, J. H.; Zhang, B.; Gao, Y.; Pan, Y.; Zhang, X. X.; Xu, B. *J. Am. Chem. Soc.* **2007**, *129*, 11928. (d) Maksimuk, S.; Yang, S. C.; Peng, Z. M.; Yang, H. *J. Am. Chem. Soc.* **2007**, *129*, 8694.
- [2] (a) Xiong, Y.; Wiley, B.; Chen, J.; Li, Z. -Y.; Yin, Y.; Xia, Y. *Angew. Chem. Int. Ed.* **2005**, *44*, 7913. (b) Xiong, Y.; McLellan, J. M.; Chen, J.; Yin, Y.; Li, Z. -Y.; Xia, Y. *J. Am. Chem. Soc.* **2005**, *127*, 17118. (c) Xiong, Y.; Chen, J.; Wiley, B.; Xia, Y.; Yin, Y.; Li, Z. -Y. *Nano Lett.* **2005**, *5*, 1237. (d) Xu, Z.; Hou, Y.; Sun, S. *J. Am. Chem. Soc.* **2007**, *129*, 8698.
- [3] (a) Nishihata, Y.; Mizuki, J.; Akao, T.; Tanaka, H.; Uenishi, M.; Kimura, M.; Okamoto, T.; Hamada, N. *Nature* **2002**, *418*, 164. (b) Trzeciak, A. M.; Ziólkowski, J. J. *Coord. Chem. Rev.* **2007**, *251*, 1281.
- [4] See, for example: (a) Chen, M.; Kumar, D.; Yi, C.-W.; Goodman, D. W. *Science* **2005**, *310*, 291. (b) Enache, D. A.; Edwards, J. K.; Landon, P.; Solsona-Espriu, B.; Carley, A. F.; Herzing, A. A.; Watanabe, M.; Kiely, C. J.; Knight, D. W.; Hutchings, G. J. *Science*, **2006**, *311*, 362. (c) Ferrer, D.; Torres-Castro, A.; Gao, X.; Sepúlveda-Guzmán, S.; Ortiz-Méndez, U.; José-Yacamán, M. *Nano Lett.* **2007**, *7*, 1701.

- [5] See, for example: (a) Sun, Y.; Xia Y. *Science* **2002**, 298, 2176. (b) Chen, J.; Wiley, B.; McLellan, J.; Xiong, Y.; Li, Z.-Y.; Xia, Y., *Nano Lett.* **2005**, 5, 2058-2062. (c) Chen, J.; McLellan, J. M.; Siekkinen, A.; Xiong, Y.; Li, Z.-Y.; Xia, Y. *J. Am. Chem. Soc.* **2006**, 128, 14776. (d) Lu, X.; Tuan, H.-Y.; Chen, J.; Li, Z.-Y.; Korgel, B. A. and Xia, Y. *J. Am. Chem. Soc.* **2007**, 129, 1733.
- [6] Xiong, Y.; Cai, H.; Wiley, B. J.; Wang, J.; Kim, M. J.; Xia, Y. *J. Am. Chem. Soc.* **2007**, 129, 3665.
- [7] (a) Lucas, C. A.; Marković, N. M.; Ross, P. N. *Phys. Rev. B* **1997**, 55, 7964. (b) Zou, S.; Gao, X.; Weaver, M. J. *Surf. Sci.* **2000**, 452, 44.
- [8] (a) Newman, R. C.; Sieradzki, K. *Science* **1994**, 263, 1708. (b) Scully, J. C. *The Fundamentals of Corrosion*, 3rd ed.; Pergamon Press: Oxford, New York, 1990; pp 1-57. (c) Tsung, C.-K.; Kou, X.; Shi, Q.; Zhang, J.; Yeung, M. H.; Wang, J.; Stucky, G. D. *J. Am. Chem. Soc.* **2006**, 128, 5352. (d) Sun, Y.; Xia, Y. *J. Am. Chem. Soc.* **2004**, 126, 3892.
- [9] (a) Mokari, T.; Sztrum, C. G.; Salant, A.; Rabani, E. and Banin, U. *Nature Mater.* **2005**, 4, 855. (b) Saunders, A. E.; Popov, I. and Banin U. *J. Phys. Chem. B* **2006**, 110, 25421 (d) Redmond, P. L.; Hallock, A. J. and Brus, L. E. *Nano Lett.* **2005**, 5, 131.
- [10] Wetz, F.; Soulantica, K.; Falqui, A.; Respaud, M.; Snoeck, E. and Chaudret B. *Angew. Chem. Int. Ed.* **2007**, 119, 7209.

Chapter 5

Synthesis and Application of RuSe_{2+δ} Nanotubes as a Methanol Tolerant Electrocatalyst for the Oxygen Reduction Reaction

5.1. Introduction

Recent concerns regarding fossil fuel shortage and global warming have placed a great demand for devices that can generate power at a high efficiency with little or no emission. Direct methanol fuel cells (DMFCs), in particular, have attracted great interest as an alternative power source to internal combustion engines in vehicles and to batteries for portable electronic devices.¹⁻³ In addition to high costs associated with current DMFCs,^{4,5} the utilization of Pt at the cathode can cause significant performance losses due to methanol crossover between the anode and cathode.^{6,7} Therefore, the quest for Pt-free cathode electrocatalysts that are both active towards the ORR and is insensitive to methanol represents one of the major challenges in the DMFC technology.²

Several Pt-free catalysts have been proposed as ORR active materials.⁸⁻¹⁰ Among them, Ru-based selenides have emerged as the most promising alternatives to replace Pt-based cathode materials. Ru-based selenides have shown with high tolerance to methanol, as well as good ORR catalytic performances.¹⁰⁻¹² Although the importance of chalcogen additives toward ORR has been recognized, the mechanism behind their ORR activity

and methanol tolerance it is not fully understood. The Ru-based selenides typically employed as ORR electrocatalysts are composed of amorphous Ru_xSe_y cluster compounds. They are prepared by coating Ru nanoparticles with Se, a Ru-Se phase, a Ru-Se-O phase or Ru-C-O groups, which can be present as complete or incomplete thin shells.^{10,13} These Ru_xSe_y cluster compounds have been synthesized via a variety of methods and their composition and morphology generally varies with the protocols. The most common approach is via the thermolysis of Ru-carbonyls in organic solvents (xylene or 1,2-dichlorobenzene) in the presence of Se.¹⁴ In addition, Ru_xSe_y cluster compounds have been prepared via the reaction between Ru nanoparticles and selenous acid (H_2SeO_3) or by the dissolution of RuCl_3 in THF ($\text{C}_4\text{H}_8\text{O}$), followed by their reduction to produce Ru nanoparticles which are further treated with selenous acid (H_2SeO_3).¹⁵ Precipitation methods based on RuCl_3 and Na_2SeO_3 as precursors for Ru and Se, respectively, have also been described.¹⁶ As a final example, Ru_xSe_y catalysts supported on porous carbon have been produced via impregnation and reduction of Ru salts, followed by their reduction and treatment with H_2SeO_3 or SeCl_4 .¹⁷

It is important to note that all these aforementioned synthetic procedures present many limitations. For example, the carbonyl approach involves multi-step chemical reactions that may lead to poor control over the chemical homogeneity and composition of the final material. Moreover, this method is limited for mass production due to the high costs of carbonyl precursors, questionable reproducibility and high toxicity of the solvents. Comparatively, colloidal and impregnation methods also employ toxic solvents and do not allow a tight control over the chemical homogeneity, composition,

morphology and reproducibility of the sample. Due to these synthetic limitations, the exact nature and composition of the Ru_xSe_y materials produced from the above methods are typically difficult to determine with precision and are often inferred from EXAFS and XPS data.^{10,13-17} Hence, the utilization of a fabrication approach that is simple, inexpensive, reproducible and that yields Ru-based chalcogenides with well-defined morphology, controllable shape, composition and chemical uniformity is very attractive from both fundamental (understanding of mechanism of ORR activity and methanol tolerance) and practical aspects (applications).

I describe in this chapter the utilization of a facile and versatile ethanol-based synthesis to produce uniform $\text{RuSe}_{2+\delta}$ nanotubes, followed by the investigation of their ORR activity and durability. My synthetic approach involves the utilization of uniform *t*-Se nanowires as the starting material in a template-engaged reaction with elemental Ru (produced *in situ*) to generate *t*-Se@ $\text{RuSe}_{2+\delta}$ core-sheath nanowires, which, after removal of the unreacted *t*-Se cores, are converted into $\text{RuSe}_{2+\delta}$ nanotubes.¹⁸ My approach has many interesting features. First of all, it can be easily scaled up for mass production, as it is simple, reproducible, inexpensive and does not require sophisticated techniques, toxic solvents or high temperatures. Secondly, the produced $\text{RuSe}_{2+\delta}$ nanotubes present well-defined composition, morphology and chemical uniformity, which is highly desirable for DMFCs applications. Finally, the 1-D morphology may lead to improved long-term stabilities.¹⁹ Due to the micrometer length size of the nanotubes, they do not require a support and are less vulnerable to dissolution, Ostwald ripening, and aggregation than their nanoparticles counterparts during fuel cell operation.²⁰

5.2. Results and Discussion

5.2.1. Synthesis of RuSe_{2+δ} Nanotubes

The synthesis of RuSe_{2+δ} nanotubes followed a template-engaged approach developed by group.¹⁸ The first step involved the preparation of *t*-Se nanowires via a sonochemical route. Then, the *t*-Se nanowires were used as starting material in the reaction with Ru(acac)₃ in ethanol at 80 °C to produce *t*-Se@RuSe_{2+δ} core-sheath nanowires. In this process, elemental Ru⁰ was generated *in situ* via the reduction of Ru³⁺ from Ru(acac)₃ by ethanol, which then reacts with *t*-Se according to the following equation:



Due to the low melting point of *t*-Se (~217°C)²² as compared to RuSe₂, the unreacted *t*-Se cores could be removed by heating the samples at 230 °C for 10 min to yield uniform RuSe_{2+δ} nanotubes. As previously demonstrated, the thickness of the RuSe_{2+δ} sheath could be controlled by changing the Ru:Se molar ratio and by controlling the reaction time.¹⁸ Figure 5.1 shows electron microscopy images of the morphological changes involved in this template-engaged reaction. Figure 5.1A shows both SEM and TEM (inset) images of initial *t*-Se nanowires. It can be seen that the nanowires were uniform in size, together with smooth surfaces. The average width was ~53 nm and

>5 μm in length. Figure 5.1, B-D, shows TEM and HRTEM images of the $\text{RuSe}_{2+\delta}$ nanotubes produced by reacting the *t*-Se nanowires with Ru^0 followed by selective removal of the unreacted *t*-Se cores. The contrast differences clearly depict a tubular morphology. It can be observed the wall thickness of the nanotubes was ~ 9 nm and their outer diameter was ~ 55 nm. The absence of well-defined phase contrast in HRTEM images (Figure 5.1, C and D) reveals the low crystallinity of the produced $\text{RuSe}_{2+\delta}$ nanotubes. This is further confirmed by XRD (Figure 5.2a), in which no diffraction peaks assigned to RuSe_2 was detected. It is important to note that the XRD for the initial *t*-Se nanowires contains sharp, intense diffraction peaks. Consequently, this result shows the complete removal of the unreacted *t*-Se cores in the $\text{RuSe}_{2+\delta}$ product. Figure 5.2B shows EDX spectra recorded for the initial *t*-Se nanowires and the $\text{RuSe}_{2+\delta}$ nanotubes product. As expected, the spectra for the *t*-Se nanowires contain only the peak assigned to Se. For $\text{RuSe}_{2+\delta}$, the EDX spectrum contains peaks from both Se and Ru. The corresponding Ru and Se atomic percentages are 28.8 and 71.2%, respectively, which is in reasonable agreement with 33.3 and 66.4% expected for RuSe_2 .

5.2.2. Evaluation of Electrochemical Performance

In order to investigate and compare the effect of the presence of 0.1 M methanol on the ORR electrochemical characteristics and performance for both $\text{RuSe}_{2+\delta}$ nanotubes and commercial Pt/C (TKK), I used two electrolyte compositions for each catalyst during the electrochemical studies: 0.1 M HClO_4 and 0.1 M HClO_4 containing 0.1 M methanol.

Figure 5.3A shows the cyclic voltammograms (CVs) recorded for Pt/C (TKK) at

room temperature in a solution of O₂-free 0.1 M HClO₄ (solid curve) and in a solution of O₂-free 0.1 M HClO₄ containing 0.1 M methanol (dashed curve). In the absence of methanol, the CVs curves for Pt/C (TKK) showed the standard hydrogen adsorption potential peaks in the 0.05-0.4 V region.²³ The electrochemical surface area (ECSA) was estimated to be 42.8 m²/g. The anodic/cathodic peaks observed above 0.6 V can be assigned to adsorption/desorption of surface hydroxyl (oxide) species. Significant changes can be observed in the CV for Pt/C (TKK) in the presence of 0.1 M methanol (dashed curve). First, there is a reduction in the area under the curve, corresponding to the hydrogen adsorption/desorption region (0.05-0.4 V), as a result of the reduction of the ECSA after methanol adsorption. Secondly, typical methanol oxidation peaks can be observed at 0.7 and 0.8 V, confirming that the Pt/C (TKK) catalyst is active towards methanol oxidation.²⁴ As shown in Figure 5.3B, no such behavior was observed for the RuSe_{2+δ} nanotubes. In this case, there was no change to the CVs curves as 0.1 M methanol was added to the electrolyte solution, demonstrating the inactivity of this material towards methanol oxidation. The CV curves for RuSe_{2+δ} nanotubes differ substantially when compared to the Pt/C (TKK) catalyst. No peaks due to hydrogen adsorption/desorption were detected in the 0.05-0.4 V region, indicating that the adsorption and desorption of hydrogen were suppressed. Also, significant anodic currents above ~0.9 V were observed. This anodic currents can be assigned to oxidation and partial dissolution of Se²⁻ as well as adsorption/desorption of surface hydroxyl (oxide) species.²⁵ The cathodic peak feature at ~0.49 V indicates the anodic dissolution of oxidation products (removal of Se surface oxides, for example).²⁵

The ORR polarization curves for RuSe_{2+δ} in the absence and in the presence of 0.1 M methanol are shown in Figure 5.4A (solid and dashed curves, respectively). It can be clearly observed that no change to the polarization curves took place when methanol was introduced into the electrolyte, indicating that the RuSe_{2+δ} catalyst was insensitive to 0.1 M methanol. The cathodic currents produced in the ORR reach zero at 0.8 V and the half-wave potentials were 0.61 V. Figure 5.4B illustrates the ORR polarization curves for commercial Pt/C (TKK) catalysts. In this case, a significant decrease in the ORR activity in the 0.5-1.0 V region can be observed when 0.1M methanol was introduced into the electrolyte (dashed curve). In the absence of methanol, the cathodic current reaches zero at 0.95 V and the half-wave potential is 0.78 V. In the presence of 0.1 M methanol, these values shift to 0.84 V and 0.72 V, respectively.

In order to quantify the ORR activities and the methanol tolerance for the RuSe_{2+δ} nanotubes and compare with those from commercial Pt/C (TKK), kinetic current densities (j_k) of the samples were obtained from the rotating disc electrode mass-transport correction. The kinetic current density was calculated according to the Koutecky-Levich equation:²⁶

$$1/j = 1/j_k + 1/Bw^{1/2} \quad (5.2)$$

Where j is the measured current density, in mA/cm² and w is the rotation speed, in rpm. The constant B is defined as $0.62nFAC_{O_2}v^{-1/6}D^{2/3}$ (n is the number of electrons transferred per oxygen molecule and equals to four, F is the Faraday constant, A is the geometrical

area of the electrode, C_{O_2} is the concentration of oxygen in the solution, ν is the kinematic viscosity of the solution, and D is the oxygen diffusion coefficient). B can be experimentally determined by calculating the slope in a $1/j$ versus $1/w^{1/2}$ plot. In my experiments, the value of B was experimentally determined as $0.14 \text{ cm}^2 \text{rpm}^{1/2} \text{mA}^{-1}$ using Pt/C (TKK) catalysts. Figure 5.4C shows the mass-specific kinetic currents (j_{mk}) for the RuSe_{2+ δ} nanotubes and commercial Pt/C (TKK) catalysts in the absence and in the presence of 0.1 M methanol. In these cases, the j_{mk} values at a specific potential provide a direct measure of the ORR activities of the two catalysts. It can be observed that j_{mk} for Pt/C (TKK) was higher than the j_{mk} for RuSe_{2+ δ} in the 0-0.8 V interval. However, there was considerable decrease in j_{mk} for Pt/C (TKK) in the presence of 0.1 M methanol, while no significant changes were observed for the RuSe_{2+ δ} nanotubes. Figure 5.4D shows a bar graph displaying the j_{mk} obtained from Figure 5.4C at 0.7 V. At 0.7 V, j_{mk} for commercial Pt/C (TKK) and RuSe_{2+ δ} were 695.4 mA/mg_{Pt} and 22.8 mA/mg_{Ru}, respectively, indicating that the ORR activity for RuSe_{2+ δ} was ~30 times lower compared to Pt/C (TKK). In the presence of 0.1 M methanol, the j_{mk} for Pt/C (TKK) dropped to 315.1 mA/mg_{Pt}, which corresponds to a performance loss of ~55%. Conversely, j_{mk} for RuSe_{2+ δ} increased to 25.3 mA/mg_{Ru} in the presence of 0.1 M methanol, representing a gain of ~11% in the ORR activity. Even though the increase in current density was insignificant and could be within the typical errors of such measurements, this result demonstrates that RuSe_{2+ δ} was tolerant to 0.1 M methanol at 0.7 V. Upon the addition of 0.1 M methanol, the ORR activity for the RuSe_{2+ δ} nanotubes became ~12 times lower compared to Pt/C (TKK).

Durability tests by chronoamperometry were performed in order to investigate and compare the long-term stability of the RuSe_{2+δ} nanotubes and Pt/C (TKK) catalysts. For the durability tests, the potential was fixed at 0.7 V. Figure 5.5, A and B, shows chronoamperometry curves for RuSe_{2+δ} nanotubes and Pt/C (TKK), respectively, in the presence and in the absence of 0.1 M methanol. As shown in the chronoamperometry curves for the RuSe_{2+δ} nanotubes (Figure 5.5A), the presence of 0.1M methanol did not cause significant changes to the detected *j* during the entire 0-1,800 s interval. No change to the current decay over time was observed either, indicating similar stability both in the presence and absence of 0.1 M methanol. While a slight decrease in the detected *j* was observed in the presence of 0.1 M methanol up to 850 s (the maximum decrease was 6.0%), no loss in activity was observed after 850 s of operation. Even after 1,800s, the difference in the detected *j* with and without the addition of 0.1 M methanol was very small and within 5% under the measuring conditions. This indicates that the presence of 0.1 M methanol did not affect the long-term stability of the RuSe_{2+δ} nanotubes.

The chronoamperometry curves for commercial Pt/C (TKK) catalyst (Figure 5.5B) show a significant decrease in detected *j* after 0.1 M methanol was added into the electrolyte solution. The graph illustrated in Figure 5.5C shows the detected *j* after 5 and 1,800 s in the durability test. While no changes on the detected *j* were observed for RuSe_{2+δ} upon the addition of methanol, the detected *j* for Pt/C (TKK) decreased considerably. Figure 5.5D illustrates the effects of the addition of 0.1 M methanol on the detected *j* for these two catalysts. For Pt/C (TKK), the *j* in the presence of 0.1 M methanol after 5 and 1,800 s corresponds to 67 % and 73 % of the *j* registered in the

absence of methanol, corresponding to a drop of 33 and 27 %, respectively. For RuSe_{2+δ} nanotubes, the *j* in the presence of 0.1 M methanol after 5 and 1,800 s corresponds to 96 and 100 % of the *j* registered in the absence of methanol, suggesting 100 % tolerance to methanol even after 1,800 s.

The fact that the mass-specific ORR activity for RuSe_{2+δ} is close to ~8 % of the activity of commercial Pt/C (TKK) in the presence of 0.1 M methanol makes this material attractive for DMFCs applications. While the prices for Pt have peaked at 2,200 USD/ounce in 2008, Ru only costs 250 USD/ounce (~11 % of Pt price). Therefore, the utilization of increased loadings of RuSe_{2+δ} nanotubes would allow one to obtain a cathode with ORR activity similar to the commercial Pt/C catalysts for the same price and with the advantage of being methanol tolerant. This would circumvent existing limitations and performance loss shown by current Pt/C catalysts due to methanol crossover. It is also important to note that the RuSe_{2+δ} nanotubes described in this work are expected to present smaller electrochemical surface area than the commercial Pt/C (TKK). Thus, additional improvements on the RuSe_{2+δ} ORR activities may be achieved by controlling the dimensions of the nanotubes and by using different morphologies with higher surface areas.

Although most studies employing Ru-based selenides for ORR catalysis focus on cluster compounds based on metallic Ru, no definite conclusion regarding the nature of the catalytic active sites and the constitution of the Ru_xSe_y has been drawn. The results presented here show that the presence of metallic Ru is not a pre-requisite, as RuSe_{2+δ} nanotubes (containing Ru⁴⁺) also present ORR catalytic activity and methanol tolerance.

Similarly to what is described for single-crystalline RuO₂, RuS₂, and RuTe₂, the electron transfer for ORR in the RuSe_{2+δ} nanotubes would involve the Ru⁴⁺ *d*-states, where the adsorbed oxygen molecule can directly exchange electrons with the catalyst upon cathodic polarization.²⁷ In this case, the Ru⁴⁺ *d*-states would support the selective interaction with adsorbed molecular oxygen to the extent that methanol oxidation does not take place.

5.3. Summary

I have demonstrated the use of RuSe_{2+δ} nanotubes as an active and methanol tolerant electrocatalyst for the ORR. In the presence of 0.1 M methanol, the mass-specific ORR activity for the RuSe_{2+δ} nanotubes was ~12 times lower than that of Pt/C (TKK) at 0.7 V. Durability tests showed that while the addition of 0.1 M led to significant performance loss for Pt/C (TKK), the RuSe_{2+δ} nanotubes were 100% tolerant to 0.1 M methanol even after 1,800 s of operation. The results described herein indicate that the RuSe_{2+δ} nanotubes are attractive for applications as Pt-free cathode electrocatalysts in DMFCs. Since they are methanol tolerant, high catalyst loadings may lead to mass-specific ORR activity comparable to commercial Pt/C (TKK). Furthermore, additional improvements on the RuSe_{2+δ} ORR activities may be achieved by controlling the dimensions of the nanotubes and by using different morphologies with higher surface areas.

5.4. Experimental Section

Chemicals and Materials. Ruthenium(III) acetylacetonate ($\text{Ru}(\text{acac})_3$, 97%), selenious acid (H_2SeO_3 , 99.999%), hydrazine monohydrate ($\text{N}_2\text{H}_4 \cdot \text{H}_2\text{O}$, 98%) and poly(vinyl pyrrolidone) (PVP, M.W.=55,000) were all purchased from Aldrich. Ethanol (CH_3OH , 99.8%) was obtained from EMD. All chemicals were used as received.

Synthesis of $\text{RuSe}_{2+\delta}$ Nanotubes. The *t*-Se nanowires were synthesized using the sonochemical approach.²¹ In a typical procedure, an aqueous solution of selenious acid (4.2 mL, 1 M) was added dropwise to an aqueous hydrazine solution (10 mL, 3 M) under magnetic stirring in a 50-mL round bottom flask, yielding an orange suspension. After 20 min, the spherical colloids of amorphous Se (*a*-Se) were filtered over 0.2 μm polymer membrane, rinsed with pure water, and dried under ambient conditions. The *a*-Se colloids (0.1 g) were then added to a 200-mL beaker containing 100 mL of ethanol. The beaker were sonicated for 30 s (1510R-DTH, Branson) and then kept in dark at room temperature for 12 h to generate uniform *t*-Se nanowires. The *t*-Se nanowires were centrifuged, washed with ethanol twice, and dried under ambient conditions.

For the template-engaged synthesis of $\text{RuSe}_{2+\delta}$ nanotubes, the *t*-Se nanowires (0.1 g, 1.27 mmol), $\text{Ru}(\text{acac})_3$ (0.5g, 1.27 mmol) and 0.5 g of PVP were dispersed in 20 mL of absolute ethanol hosted in a 50-ml flask. The mixture was then heated at 80 °C under vigorous magnetic stirring for 72 h. After the reaction mixture had been cooled down, the product was collected as a brown precipitate through centrifugation. The sample was submitted to successive rounds of centrifugation and washing with ethanol to remove unreacted metal salts. Uniform nanotubes of $\text{RuSe}_{2+\delta}$ could be readily obtained by

removal of the *t*-Se cores by heating the sample at 230 °C for 10 min, yielding a black precipitate.

Instrumentation. Scanning electron microscopy (SEM) images were captured using a field-emission microscope (FEI NanoSEM, Hillsboro, OR) operated at an acceleration voltage of 15 kV. The samples were directly imaged without coating their surfaces with conductive layers. Energy-dispersive X-ray spectroscopy (EDX, Genesis 2000, Mahwah, NJ) was performed at an acceleration voltage of 10 kV. TEM images were acquired using a Hitachi H-7500 microscope operated at 100 kV. High-resolution TEM was performed using a JEOL JEM-2100F operated at 200 kV. TEM samples were prepared by drop-casting a dispersion of the products onto carbon-coated copper grids (Formvar/Carbon, 200 mesh, Ted Pella). X-ray diffraction (XRD) was performed on Philips PW-1710 diffractometer with a resolution of 0.02° in 2 θ .

Electrochemical measurements. The ORR electrochemical characteristics of the RuSe_{2+ δ} nanotubes were studied using a rotating disk electrode. The catalyst was prepared by dispersing the RuSe_{2+ δ} nanotubes in a mixture of distilled water, 2-propanol and 5% in weight Nafion solution ($V_{\text{H}_2\text{O}}:V_{\text{propanol}}:V_{5\% \text{ Nafion}}=0.8 : 0.2 : 0.005$) at concentration of 1 mg/mL. The dispersion was sonicated for 10 min to obtain the catalyst ink. 10 μL of ink (containing 10 μg of RuSe_{2+ δ}) was drop-cast onto a glassy carbon electrode (5 mm in diameter) and dried under gentle airflows. The electrochemical properties were examined with a CHI 760 dual channel electrochemical workstation (CH instruments) using a three-electrode system, which consists of a rotating-disk working electrode, a Pt wire counter electrode, and a hydrogen reference electrode (Gaskatel,

HydroFlex). For the oxygen reduction reaction test, an Ag/AgCl reference electrode was used instead of the HydroFlex electrode but the data were converted to hydrogen reference electrode.

Cyclic voltammetry (CV) was tested in O₂-free 0.1M HClO₄ and O₂-free 0.1M HClO₄ containing 0.1 M methanol at a sweep rate of 50 mV/s. For ORR polarization curves, the electrolyte was protected by O₂ during test and consisted of either O₂-saturated 0.1 M HClO₄ or O₂-saturated 0.1 M HClO₄ containing 0.1 M methanol. The electrode was rotated at rate of 1,600 rpm. The potential was swept anodically from 0 to 1 V vs. RHE at a rate of 10 mV/s. For durability tests (chronoamperometry), the potential was fixed to be 0.7 V (vs. RHE). The electrode was rotated at rate of 1,600 rpm during the experiment. Each time before test, the potential was preconditioned at 0 V vs. RHE for 30 s. Aiming at the evaluation of RuSe_{2+δ} catalyst performance, catalyst inks of commercial Pt/C (47% in weight of Pt, TKK) were also prepared and tested using similar procedures. The catalyst loading was 3 μg of Pt.

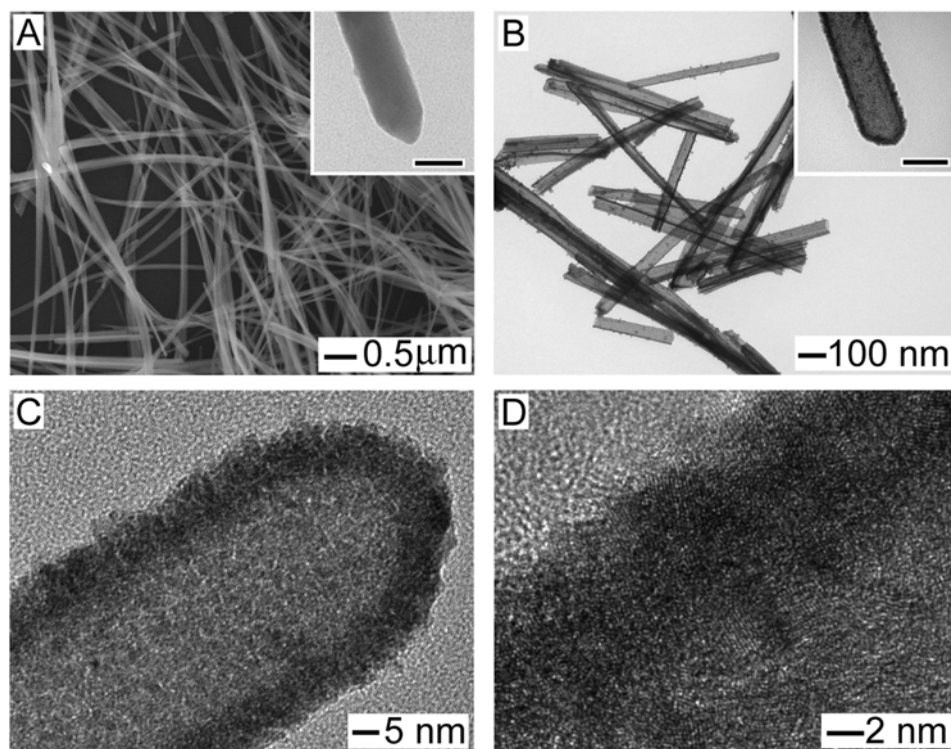


Figure 5.1. (A) SEM and TEM (inset) images of the *t*-Se nanowires employed in the template-engaged reaction with Ru(acac)₃. (B) TEM images of the RuSe_{2+δ} nanotubes produced by reacting Ru(acac)₃ with *t*-Se nanowires, followed by selective removal of the unreacted *t*-Se cores. The nanotubes had a wall thickness of approximately 9 nm. (C, D) HRTEM images of the RuSe_{2+δ} nanotubes. The scale bars in the insets correspond to 50 nm.

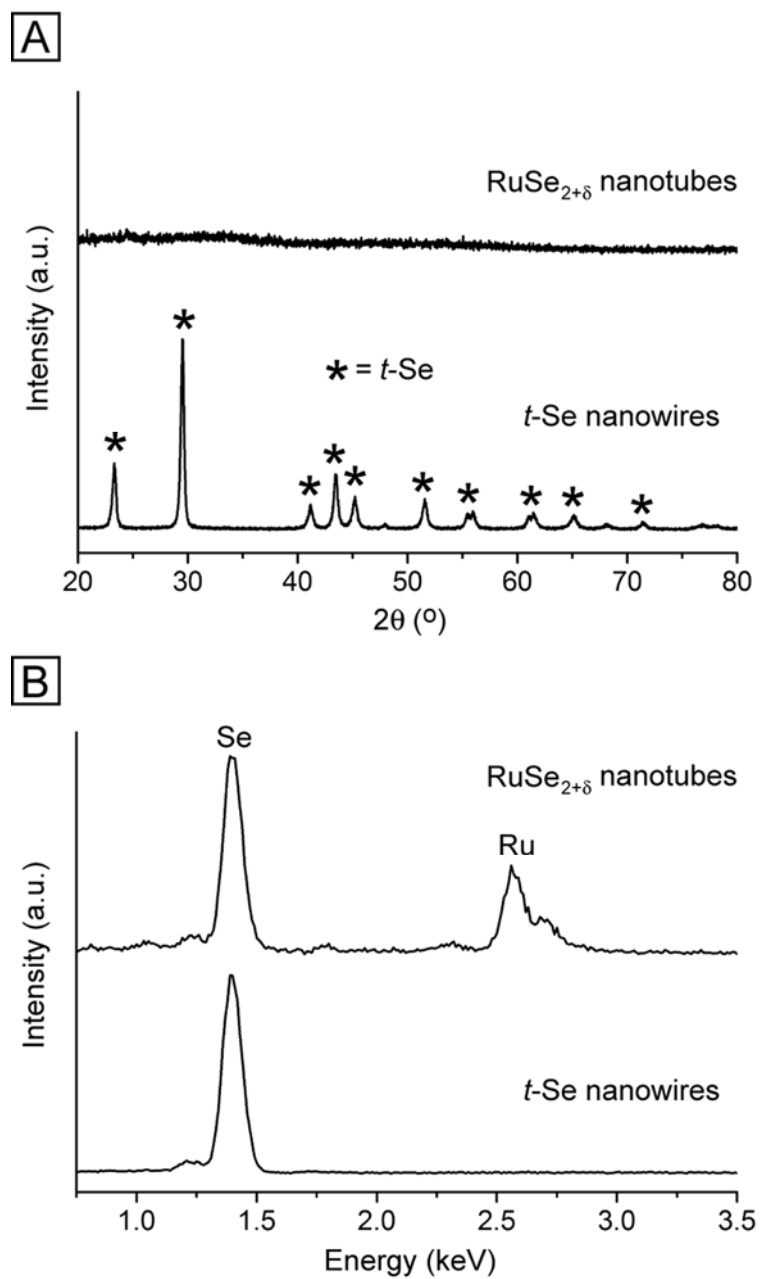


Figure 5.2. (A) XRD diffractograms and (B) EDX spectra taken from the t -Se nanowires and $\text{RuSe}_{2+\delta}$ nanotubes shown in Figure 1, respectively.

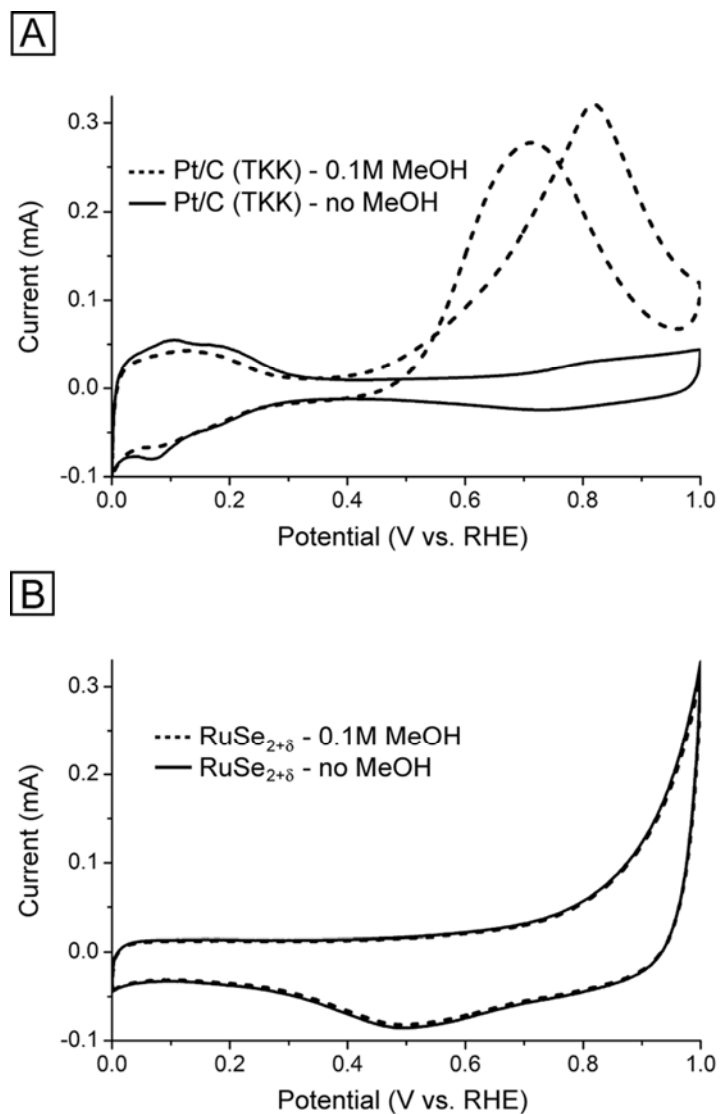


Figure 5.3. CV curves of (A) commercial Pt/C (TKK, 46.7% by weight) and (B) RuSe_{2+δ} nanotubes in acidic electrolyte solutions. Electrolyte: 0.1 M HClO₄ (solid curves) or 0.1 M HClO₄ containing 0.1 M methanol (dashed curves).

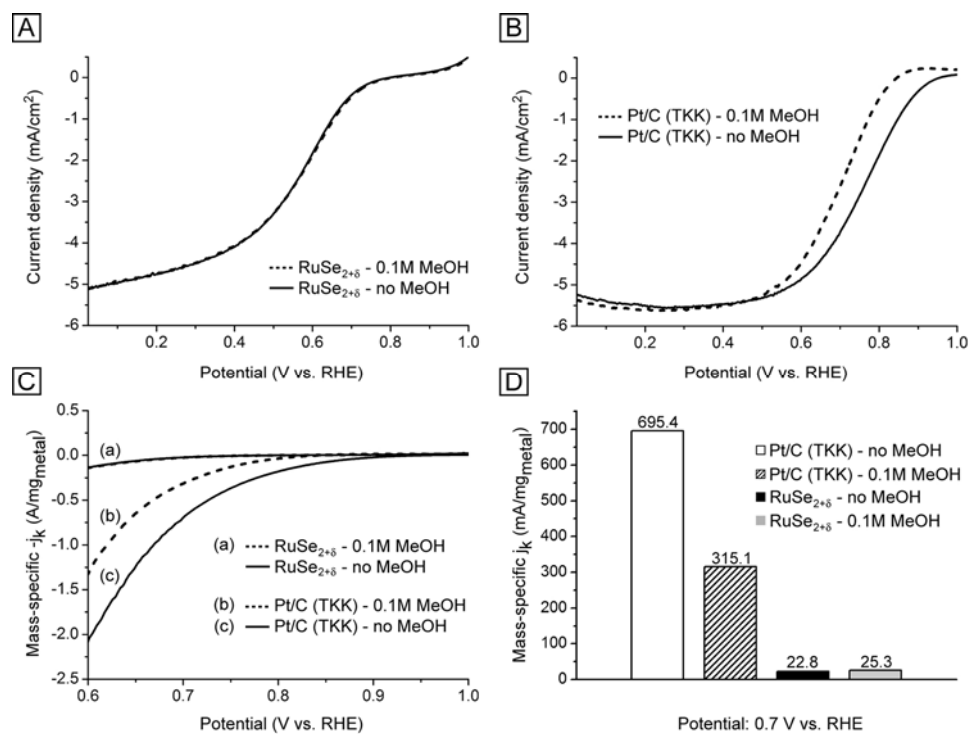


Figure 5.4. ORR polarization curves for (A) RuSe_{2+δ} nanotubes and (B) commercial Pt/C (TKK, 46.7% by weight) in the absence (solid curves) and in the presence of 0.1 M methanol (dashed curves). (C) Mass-specific kinetic current densities (j_{mk}) for the RuSe_{2+δ} nanotubes and commercial Pt/C (TKK) calculated from (A) and (B) using the Koutecky-Levich equation. (D) Bar graph showing the j_{mk} obtained at 0.7 V. The numbers in the graph represent j_{mk} and are expressed in mA/mg_{metal}.

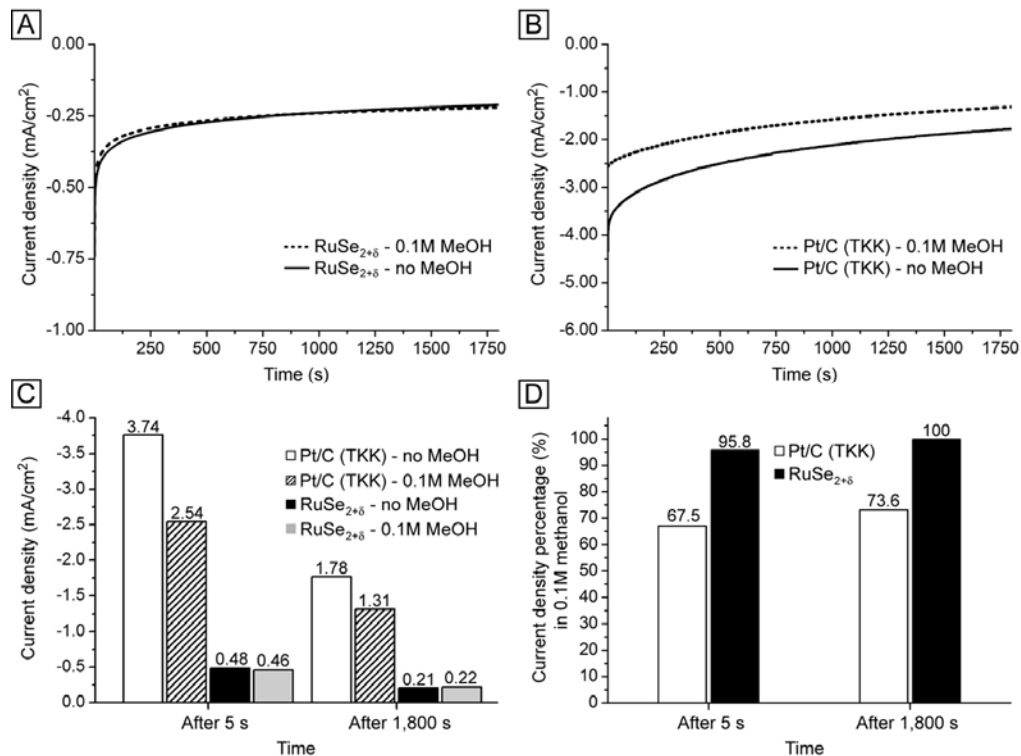


Figure 5.5. Chronoamperometry curves for (A) RuSe_{2+δ} nanotubes and (B) commercial Pt/C (TKK, 46.7% by weight) in an O₂-saturate 0.1 M HClO₄ and in an O₂-saturate 0.1 M HClO₄ containing 0.1 M methanol electrolyte. (C, D) Bar graphs illustrating the current densities (C) and the current density percentages in 0.1M methanol (D) for RuSe_{2+δ} nanotubes and Pt/C (TKK) obtained from curves (A) and (B) after 5 and 1,800 s in the durability test. The current density percentages in 0.1M methanol were calculated relative to the respective current densities registered without 0.1M methanol in the electrolyte.

5.5. Notes to Chapter 5

- [1] Steele, B. C. H.; Heinzl, A. *Nature* **2001**, *414*, 345.
- [2] (a) Aricò, A. S.; Srinivasan, S.; Antonucci, V. *Fuel Cells* **2001**, *2*, 133. (b) Winter, M.; Brodd, R. J. *Chem. Rev.* **2004**, *104*, 4245. (c) Dresselhaus, M. S.; Thomas, I. L. *Nature* **2001**, *414*, 332. d) Wasmus, S.; Küver, A. *J. Electroanal. Chem.* **1999**, *461*, 14.
- [3] Shukla, A. K.; Raman, R. K. *Annu. Rev. Mater. Res.* **2003**, *33*, 155.
- [4] (a) Liu, H.; Song, C.; Zhang, L.; Zhang, J.; Wang, H.; Wilkinson, D. P. *J. Power Sources* **2006**, *155*, 95. (b) Gasteiger, H.; Kocha, B.; Sompalli, B.; Wagner, F. T. *Appl. Catal., B* **2005**, *56*, 9. (c) Paulus, U. A.; Schmidt, T. J.; Gasteiger, H. A.; Behm, R. J. *J. Electroanal. Chem.* **2001**, *495*, 134.
- [5] (a) Greeley J.; Mavrikakis, M. *Nat. Mater.* **2004**, *3*, 810. (b) Stamenkovic, V. R.; Mun, B. S.; Mayrhofer, K. J. J.; Ross, P. N.; Markovic, N. M. *Am. Chem. Soc.* **2006**, *128*, 8813. (c) Yang, H.; Vogel, W.; Lamy, C.; Alonso-Vante, N. *J. Phys. Chem. B* **2004**, *108*, 11024. (d) Yang, H.; Alonso-Vante, N.; Leger, J. M.; Lamy, C. *J. Phys. Chem. B* **2004**, *108*, 1938.
- [6] (a) Wang, B. *J. Power Sources*, **2005**, *152*, 1. (b) Sawai, K.; Suzuki, N. *J. Electrochem. Soc.* **2004**, *151*, A682. (c) Kallo, J.; Lehnert, W.; von Helmolt, R. *J. Electrochem. Soc.* **2003**, *150*, A765.
- [7] Jusys, Z.; Behn, R. *J. Electrochim. Acta* **2004**, *49*, 3891.
- [8] (a) Lefevre, M.; Dodelet, J. P.; P. Bertrand, *J. Phys. Chem. B* **2002**, *106*, 8705. (b) Baranton, S.; Coutanceau, C.; Roux, C.; Hahn, F.; Leger, J. -M. *J. Electroanal.*

- Chem.* **2005**, 577, 223. (c) Matter, P. H.; Zhang, L.; Ozkan, U. S. *J. Catal.* **2006**, 239, 83. (d) Liu, L.; Kim, H.; Lee, J. W.; Popov, B. N. *J. Electrochem. Soc.* **2007**, 154, A123.
- [9] (a) Alonso-Vante, N.; Tributsch, H. *Nature* **1986**, 323, 431. (b) Alonso-Vante, N.; Jaegermann, W.; Tributsch, H.; Honle, W.; Yvon, K. *J. Am. Chem. Soc.* **1987**, 109, 3251.
- [10] (a) Colmenares, L.; Jusys, Z.; Behm, R. J. *Langmuir* **2006**, 22, 10437. (b) Colmenares, L.; Jusys, Z.; Behm, R. J. *J. Phys. Chem. C* **2007**, 111, 1273. (c) Zaikovskii, V. I.; Nagabhushana, K. S.; Kriventsov, V. V.; Loponov, K. N.; Cherepanova, S. V.; Kvon, R. I.; Bolnnemann, H. D.; Kochubey, I.; Savinova, E. R. *J. Phys. Chem. B* **2006**, 110, 6881. (d) Fiechter, S.; Dorbandt, I.; Bogdanoff, P.; Zehl, G.; Schulenburg, H.; Tributsch, H.; Bron, M.; Radnik, J.; Fieber-Erdmann, M. *J. Phys. Chem. C* **2007**, 111, 477.
- [11] (a) Lee, J.-W.; Popov, B. N. *J. Solid State Electrochem.* **2007**, 11, 1355. (b) Gonzales-Huerta, R. G.; Chavez-Carvayar, R. G.; Solorza-Feria, O. *J. Power Sources* **2006**, 153, 11. (c) Suárez-Alcántara, K.; Rodríguez-Castillano, A.; Dante, R.; Solorza-Feria, O. *J. Power Sources* **2006**, 157, 114.
- [12] (a) Schulenburg, H.; Hilgendorff, M.; Dorbandt, I.; Radnik, J.; Bogdanoff, P.; Fiechter, S.; Bron, M.; Tributsch, H. *J. Power Sources* **2006**, 155, 47. (b) Serov, A. A.; Min, M.; Chai, G.; Han, S.; Kang, S.; Kwak, C. *J. Power Sources* **2008**, 175, 175.
- [13] (a) Zhang, L.; Zhang, J.; Wilkinson, D. P.; Wang, H. *J. Power Sources* **2006**, 156,

171. (b) Zaikowskii, V. I.; Nagabhushana, K. S.; Kriventsov, V. V.; Loponov, K. N.; Cherepanova, S. V.; Kvon, R. I.; Bönnemann, H.; Kochubey, D. I.; Savinova, E. *R. J. Phys. Chem.* **2006**, *110*, 6881.
- [14] Alonso-Vante, N. *Fuel Cells* **2006**, *6*, 182.
- [15] (a) Tributsch, H.; Bron, M.; Hilgendorff, M.; Schulenburg, H.; Dorbandt, I.; Eyert, V.; Bogdanoff, P.; Fiechter, S. *J. Appl. Electrochem.* **2001**, *31*, 739. (b) Schulenburg, H.; Hilgendorff, M.; Dorbandt, I.; Radnik, J.; Bogdanoff, P.; Fiechter, S.; Bron, M.; Tributsch, H. *J. Power Sources* **2006**, *155*, 47.
- [16] Liu, G.; Zhang, H.; Hu, J. *Electrochem. Comm.* **2007**, *9*, 2643.
- [17] Zehl, G.; Schmithals, G.; Hoell, A.; Haas, S.; Hartnig, C.; Dorbandt, I.; Bogdanoff, P.; Fiechter, S. *Angew. Chem. Int. Ed.* **2007**, *46*, 7311.
- [18] Jiang, X.; Mayers, B.; Wang, Y.; Cattle, B.; Xia, Y. *Chem. Phys. Lett.* **2004**, *385*, 472.
- [19] Chen, Z.; Waje, M.; Li, W.; Yan, Y. *Angew. Chem. Int. Ed.* **2007**, *46*, 4060.
- [20] (a) Zhang, J.; Sasaki, K.; Sutter, E.; Adzic, R. R. *Science* **2007**, *315*, 220. (b) Ferreira, P. J.; la O', G. J.; Shao-Horn, Y.; Morgan, D.; Makharia, R.; Kocha, S.; Gasteiger, H. A. *J. Electrochem. Soc.* **2005**, *152*, A2256.
- [21] (a) Mayers, B.; Liu, K.; Sunderland, D.; Xia, Y. *Chem. Mater.* **2003**, *20*, 3852. (b) Gates, B.; Mayers, B.; Grossman, A.; Xia, Y. *Adv. Mater.* **2002**, *14*, 1749.
- [22] Chizhikov, D. M.; Shchastlivyi, V. P. *Selenium and Selenides* (E.M. Elkin, Trans.), Collet's LTD, London and Wellingborough, 1968.
- [23] Gomez, R.; Orts, J. M.; Alvarez-Ruiz, B. L.; Feliu, J. *J. Phys. Chem. B* **2004**, *108*,

228.

- [24] Formo, E.; Peng, Z.; Lee, E.; Lu, X.; Yang, H.; Xia, Y. *J. Phys. Chem. C* **2008**, *112*, 9970.
- [25] Cao, D.; Wieckowski, A.; Inukai, J.; Alonso-Vante, N. *J. Electrochem Soc.* **2006**, *153*, A869.
- [26] (a) Bard A. J.; Faulkner, L. R. *Electrochemical Methods Fundamentals and Application*, 2nd ed.; John Wiley & Sons: New York, 2001. (b) Schmidt, T. J.; Gasteiger, H. A.; Stäb, G. D.; Urban, P. M.; Kolb, D. M.; Behm, R. J. *J. Electrochem. Soc.* **1998**, *145*, 2354.
- [27] Alonso-Vante, N.; Bogdanoff, P.; Tributsch, H. *J. Catal.* **2000**, *190*, 240.

Chapter 6

Cation-Exchange: A Simple and Versatile Route to Inorganic Colloidal Spheres with the Same Size but Different Compositions and Properties

6.1. Introduction

Monodispersed colloidal spheres have received a great deal of attention due to their use as building blocks to fabricate photonic crystals by self-assembly.^{1,2} Most studies in this area have been focused on dielectric materials such as silica and polystyrene because it is feasible to synthesize them as monodispersed samples, in copious quantities, and with controllable dimensions. As limited by their low refractive indices, these two materials can only yield photonic crystals with relatively narrow and weak stop bands. In contrast, utilization of metals and semiconductors associated with higher refractive indices provides a promising alternative.³ Another advantage is that metals and semiconductors often have interesting electrical, optical, magnetic, and optoelectronic properties that can be further exploited to produce photonic crystals with tunable or switchable band gaps.⁴ However, it has been a great challenge to synthesize monodispersed colloidal spheres of metals and semiconductors that are uniform in size,

shape, composition, and structure. The major issue is that these materials tend to crystallize and grow anisotropically into non-spherical shapes.⁵⁻⁸

Another technical barrier associated with the synthesis of colloidal spheres is the difficulty in producing particles with the same size but different compositions. Even though the size can often be controlled for an individual colloidal system, it is challenging to fine-tune the size so that a very close match will be achieved for colloidal spheres of different compositions. For instance, semiconductor colloidal spheres with the same size but different refractive indices can be employed as building blocks to fabricate photonic crystals with novel properties. In particular, spheres with a lower or higher refractive index than the major component can be regarded as dopants in a 3D photonic crystal, generating defect states in the photonic bands.⁹⁻¹¹ Such a system can serve as an model to study the photonic band gap properties as a function of the concentration of “defects” and allow one to tailor the photonic structure of a particular system.¹²

In this chapter, I am interested on the utilization of cation-exchange as a generic approach to produce monodispersed colloidal spheres of various semiconductors with the same size but different compositions. Ion-exchange reactions are attractive to this end because the morphology of the starting materials can be preserved during the exchange process.¹³⁻¹⁷ Inspired by our previous success with the synthesis of Se@CdSe colloids from Se@Ag₂Se via cation-exchange,^{8c} I decided to fully explore the potential of this approach by increasing the scope of cations used in the ion-exchange processes. More specifically, I describe in this chapter the synthesis of monodisperse Se@MSe (M=Zn, Cd, and Pb) core-shell colloidal spheres with the same diameter via cation-exchange with

the same batch Se@Ag₂Se.¹⁸ Figure 6.1 shows a schematic of the approach. The unique feature of this route relies on the fact that the sizes of the products are determined by the size of the starting core-shell spheres and the balance between density and molar volume of ZnSe, CdSe, and PbSe relative to Ag₂Se. I am interested in these materials for a number of reasons. Owing to their sizes and high refractive indices (>2.5), they are ideal candidates for fabricating photonic crystals with band gaps in the optical regime. In addition to their interesting properties (luminescence, thermoelectricity, and photoelectricity),^{18,19,4} the difference on their refractive indices can be directly exploited to fabricate 3D photonic crystal containing controlled defects in an effort to engineer their band structures. Finally, the ion-exchange process can be combined with other methodologies to add new functions to the core-shell spheres. For example, it is feasible to incorporate superparamagnetic nanoparticles into the *a*-Se cores to obtain magnetoactive colloidal spheres that can be addressed with an external magnetic field. Taken together, I envision a new platform that will enable the production of multifunctional colloidal spheres with a range of different compositions and properties.

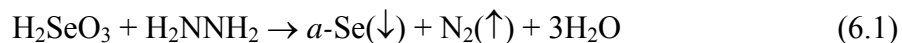
6.2. Results and Discussion

6.2.1. Synthesis of *a*-Se and Se@Ag₂Se Monodispersed Colloidal

Spheres

The experimental procedure employed in this synthesis followed the method previously reported by our group.^{8a,b} The formation of *a*-Se colloidal spheres occurs via

the reduction of selenious acid with hydrazine at room temperature (15-20 °C) in EG according to the following equation:



Because the reaction took place below the glass-transition temperature of selenium ($T_g = 32$ °C), all Se was precipitated in the amorphous form. The size of the Se colloids could be controlled by changing the molar ratio between N_2H_4 and H_2SeO_3 during the syntheses. The use of a viscous solvent like EG, instead of water, allowed a better control over the transport of elemental selenium, the number of nucleation events, and the growth kinetics, leading to monodispersed samples. After removal of hydrazine from the reaction mixture, the next step involved a reaction of the as-formed $a\text{-Se}$ colloids with AgNO_3 in EG at room temperature to yield $\text{Se@Ag}_2\text{Se}$, which would serve as the starting material for the cation-exchange reactions. In this process, Ag^+ was reduced by EG to Ag, which reacted with Se to form uniform colloidal spheres consisting of $a\text{-Se}$ core and Ag_2Se shell (Figure 6.1). In this case, the thickness of the resulting shell could be controlled by changing the molar ratio of AgNO_3 to Se. Since hydrazine is a strong reductant, the removal of hydrazine before AgNO_3 addition is crucial to avoiding the production of Ag precipitates and agglomerates in the reaction mixture. Figure 6.2A shows SEM image of the $\text{Se@Ag}_2\text{Se}$ spheres obtained using this protocol. They had a mean diameter of 325 ± 4.2 nm. It is clear that the spherical particles were uniform in size

and their surfaces were free of irregularities. The TEM image in the inset indicates that the Ag₂Se shell was ~30 nm thick, with a variation below 5 nm.

6.2.2. Synthesis of Se@MSe (M=Zn, Cd, Pb) Colloidal Spheres via Cation-Exchange Reactions

In order to perform the cation-exchange reactions, the Se@Ag₂Se colloids were dispersed in methanol and PVP was added as a stabilizer to prevent any possible agglomeration during the cation-exchange process. Nitrate salts were employed as the precursors because they are highly soluble in methanol, the solvent used for all cation-exchange reactions.

For cation-exchange reactions carried out in aqueous solutions containing the respective salt precursors, a large difference in solubility provides the driving force for the ion replacement. Generally, the starting material present in a solution containing an appropriate precursor will spontaneously undergo cation-exchange to yield the product with a lower solubility. On the other hand, when the solubility of the desired product is higher than the solubility of the precursor material, new strategies are needed. As reported by Alivisatos and coworkers, excess Cd²⁺ ions and a small amount of TBP were required to enable the exchange between Cd²⁺ and Ag⁺ in nanocrystals (Ag₂Se → CdSe).¹⁷ Our group has recently demonstrated that this method was also extendable to colloidal spheres with larger dimensions. In this case, TBP also played a pivotal role because no cation-exchange was observed without TBP. It is believed that TBP can bind to both Ag⁺ ions in the shells and Cd²⁺ ions in solution forming intermediate complexes. In this context, the

stronger interaction between TBP and Ag^+ allows the association of Cd^{2+} with the anion sublattice, leading to the replacement of Ag^+ by Cd^{2+} . Methanol seems to be required for the cation-exchange reactions. It may act as a ligand, together with TBP, in the formation of intermediate complexes. It is worth emphasizing that heating (to ~ 50 °C) was necessary to facilitate this process and allow the $\text{Ag}^+ \rightarrow \text{Cd}^{2+}$ substitution. This is because the reverse reaction, i.e., the replacement of Cd^{2+} by Ag^+ , is spontaneous due to the large difference in solubility between Ag_2Se and CdSe ($s=2.0 \times 10^{-22}$ mol/L for Ag_2Se and 3.2×10^{-17} mol/L for CdSe).²⁰ Similarly, ZnSe and PbSe have $s=1.9 \times 10^{-10}$ and 8.9×10^{-22} mol/L, respectively; both are higher than that of Ag_2Se . Based on these numbers, it is expected that the replacement of Ag^+ by Zn^{2+} or Pb^{2+} will not be spontaneous at room temperature, similar to the replacement of Ag^+ by Cd^{2+} . Therefore, for the synthesis of both Se@ZnSe and Se@PbSe , I had to employ experimental conditions (i.e., a small amount of TBP together with heating to 60 °C) similar to those previously established for the Se@CdSe system.

Figure 6.2 shows SEM and TEM images of the $\text{Se@Ag}_2\text{Se}$ spheres, together with the products derived from the cation-exchange reactions with Zn^{2+} , Cd^{2+} and Pb^{2+} . All samples display a spherical shape, and are characterized by monodispersed size and smooth surface. These features are reproducible and routinely achievable for all the samples described in this article. The $\text{Se@Ag}_2\text{Se}$ spheres were 325 ± 4.2 nm in diameter, while the Se@MSe (M=Zn, Cd, Pb) spheres had a mean diameter of 315 ± 4.7 nm. The shell thickness of the Se@MSe core-shell particles was determined to be 25 nm by TEM. It is clear that all the products of cation-exchange reactions, i.e., Se@MSe colloidal

spheres, had essentially the same diameter and shell thickness. This is a unique feature as it allows for the synthesis of semiconductor colloidal spheres with the same size but different compositions. In this case, the dimension of the core-shell particles is determined by the size of the starting Se@Ag₂Se spheres. The reduction in shell thickness after cation-exchange can be attributed to the changes in unit cell symmetry and lattice constants. For the Se²⁻ sublattice of each cation-exchange product, there was a slight decrease in the volume occupied by each individual Se²⁻ anion relative to that of Ag₂Se. These changes agree, within experimental errors, with the ~5 nm reduction observed for shell thickness.

The chemical transformations were followed using both XRD and EDX, as shown in Figures 2.3 and 2.4, respectively. The XRD pattern taken from the Se@Ag₂Se sample can be assigned to the orthorhombic lattice of β -Ag₂Se, with lattice constants being $a=4.33$ Å, $b=7.06$ Å, and $c=7.76$ Å. No peaks assigned to the α -Se cores were detected because of their amorphous nature. The XRD patterns of the Se@MSe (M=Zn, Cd, Pb) spheres indicate a complete cation-exchange between Ag⁺ and Zn²⁺, Cd²⁺, and Pb²⁺, respectively. All β -Ag₂Se peaks disappeared after the cation-exchange conversion. For the Se@ZnSe colloids, XRD data shows the formation of hexagonal ZnSe (würzite structure). The lattice constants are $a=3.99$ Å and $c=6.55$ Å. For Se@CdSe, the XRD pattern can also be indexed to the hexagonal phase (würzite structure). The lattice constants are $a=4.30$ Å and $c=7.01$ Å. For Se@PbSe, all peaks can be assigned to cubic PbSe with $a=6.12$ Å.

Figure 6.4 compares the EDX spectra taken from Se@Ag₂Se and the ion-exchanged products. The EDX results also indicates a complete replacement of Ag⁺ by Zn⁺², Cd⁺², and Pb⁺² ions in the cation-exchange reactions. For Se@Ag₂Se, the corresponding atomic percentage of Se and Ag is 62% and 38%, respectively. All peaks assigned to silver in Se@Ag₂Se colloids disappeared after the cation-exchange reaction, while peaks assigned to Zn, Cd or Pb arose. The atomic percentages obtained from EDX data for Se@ZnSe were Se=56% and Zn=44%. For Se@CdSe, the atomic percentages were Se=59% and Cd=41%. As for Se@PbSe, the atomic percentages were Se=63% and Pb=37%. These results are in agreement with a complete replacement of the Ag⁺ ions by Zn⁺², Cd⁺², and Pb⁺². It is worth noting that the *a*-Se cores are slightly dissolved in the reactions involving Zn⁺² and Cd⁺² due to the medium solubility of *a*-Se in methanol, which was the solvent employed in these two systems.

The effectiveness in the cation-exchange between Ag⁺ and Cd²⁺ can be explained based on the crystal structures of Ag₂Se and CdSe. The anion sublattice in Ag₂Se (orthorhombic) and CdSe (würzite) have a topotactic relationship. The *a*- and *b*-axis of Ag₂Se are almost the same as the *a*- and *c*-axis of CdSe. As a result, the matching of anion positions facilitates the in- and out-diffusion of Ag⁺ and Cd²⁺ through the lattice, leading to the formation of CdSe without substantial rearrangement for the Se²⁻ sublattice and preservation of the anion sublattice connectivity. Our results indicate that a topotactic relationship between the anion sublattices is not necessarily required in order to achieve cation-exchange in colloidal systems, since ZnSe (würzite) and PbSe (cubic) do not exhibit any topotactic relationship with either Ag₂Se or CdSe. This fact might explains

why a higher temperature was required to perform the cation-exchange reactions with Zn^{+2} and Pb^{+2} (60 °C) than for Cd^{+2} (50 °C). It is clear that the cation-exchange can be more easily performed when the starting and final solids display a topotactic relationship for the anion sublattice. When I tried to carry out the cation-exchange reactions with Zn^{+2} and Pb^{+2} at 50 °C, the products always showed a silver content around 10% (atomic percent). Interestingly, a small increase of the reaction temperature from 50 to ~60 °C was sufficient to achieve complete conversion.

All the cation-exchange reactions could not be completed at temperatures below 50 °C, even with increase of TBP concentration. At higher temperatures (~70 °C), the colloids malformed and became irregular in shape (Figure 6.5). This observation suggests that the connectivity of the anion sublattice could be significantly disturbed at 70 °C, contributing to the shell's collapse. Another aspect is that the reactions involving Zn^{2+} and Cd^{2+} took place faster than the reaction with Pb^{2+} . For Zn^{2+} and Cd^{2+} , the cation-exchange could be achieved in 30 min. I allowed the reaction to proceed up to 2 h in order to assure that all the cation-exchange processes were completed. It was observed that the molar ratios did not change for periods longer than 2 h. On the other hand, the cation-exchange with Pb^{2+} required 4 h to complete. No significant effect on the cation-exchange reactions rates was observed as the concentration of $\text{M}(\text{NO}_3)_2$ was increased from 0.12 to 0.5 M. This difference can be attributed to two main factors. Firstly, the reaction is faster for anion sublattices that have topotactic relationship. In this regard, würtzite CdSe is the only structure having a topotactic relationship with $\beta\text{-Ag}_2\text{Se}$. Since ZnSe also has a würtzite structure, the ZnSe lattice resembles the CdSe structure. This

similarity could make the rate of ion-exchange more or less similar for Cd^{2+} and Zn^{2+} . On the other hand, PbSe has a cubic lattice that does not have any topotactic relationship with either $\beta\text{-Ag}_2\text{Se}$ or CdSe, contributing to a more difficult cation-exchange. Secondly, ZnSe and CdSe (both wurtzite) have fairly lower densities than Ag_2Se , while the densities for PbSe and Ag_2Se are similar. It is expected that the cation-exchange process is more favorable for reactions that lead to products presenting lower densities than the starting material.

6.2.3. Crystallization of MSe (M=Zn, Cd, Pb) Hollow Spheres

The monodispersity in size and spherical shape of these new colloidal spheres make them well-suited as building blocks to fabricate 3D photonic crystals by self-assembly. To this end, I focused on the crystallization of CdSe hollow spheres, as well as its mixtures with ZnSe hollow spheres. The hollow spheres were prepared from their core-shell precursors by selectively dissolving the *a*-Se core with hydrazine at room temperature. Crystallization was achieved with the packing cells described in our previous publications.²¹ The hollow spheres are 390 nm in outer diameter, together with a shell thickness of 35 nm. Due to the large difference in refractive index for CdSe (2.54) and ZnSe (2.89), incorporation of ZnSe hollow spheres into the lattice of CdSe hollow spheres can be regarded as a simple method to fabricate photonic crystals with controllable levels of defects. Figure 6.6 shows SEM images of three different samples of colloidal crystals: pure CdSe hollow spheres; CdSe hollow spheres doped with 5% ZnSe, and CdSe hollow spheres doped with 20% ZnSe. It is clear that all of these samples

displayed a face-centered cubic (*fcc*) structure with the (111) planes oriented parallel to the surface of the glass substrate.

Figure 6.7 shows the near-IR reflectance spectra recorded for these crystals after they had been dried in air. For CdSe hollow spheres, the spectrum displayed a peak at 970 nm. No shift in the peak position was observed for the crystal fabricated from CdSe hollow spheres doping with 5% ZnSe hollow spheres. When the doping level was increased to 20%, the peak position was shifted to 990 nm. These results can be quantitatively explained based on the Bragg equation:²²

$$m\lambda_{\max} = 2d_{hkl}(n^2 - \sin^2\theta)^{1/2} \quad (6.2)$$

where m is order of diffraction; d_{hkl} is the spacing between (hkl) planes; n is the refractive index of the crystal; and θ is the angle between the incident light and the surface of the diffraction planes ($\theta=10^\circ$ in our measurements). For the *fcc* lattice, $d_{111}=4r/(6)^{1/2}$, where r is the radius of the spheres ($r=195$ nm). If a linear relationship between the refractive index (n) and the volume fraction (X) is assumed,²³ the n for CdSe and ZnSe hollow spheres can be calculated according to the equations:

$$n_{\text{CdSe,sphere}} = n_{\text{core}}X_{\text{core}} + n_{\text{CdSe}}X_{\text{shell}} \quad (6.3)$$

$$n_{\text{ZnSe,sphere}} = n_{\text{core}}X_{\text{core}} + n_{\text{ZnSe}}X_{\text{shell}} \quad (6.4)$$

Taking into consideration that the α -Se core had been completely removed before crystallization and assuming that the core as completely filled with air in the dry crystal, $n_{\text{core}}=n_{\text{air}}=1.0$, $X_{\text{core}}=0.55$, $X_{\text{shell}}=0.45$, $n_{\text{CdSe}}=2.54$, and $n_{\text{ZnSe}}=2.89$. Equations 3 and 4 yield $n_{\text{CdSe,sphere}}=1.69$ and $n_{\text{ZnSe,sphere}}=1.85$.

The refractive index ($n_{\text{CdSe,crystal}}$) for the crystal made of pure CdSe hollow spheres can then be calculated according to the equation:

$$n_{\text{CdSe,crystal}} = n_{\text{voids}}f_{\text{voids}} + n_{\text{CdSe,sphere}}(1-f_{\text{voids}}) \quad (6.5)$$

where $n_{\text{voids}}=n_{\text{air}}=1.0$ for the dry crystal and $f_{\text{voids}}=0.26$ for an fcc lattice (f =volume fraction in the crystal). Similarly, the refractive indices for the crystals made of CdSe doped with 5% ZnSe and CdSe doped with 20% ZnSe ($n_{\text{CdSe,dopedcrystal}}$) can be calculated according to the following:

$$n_{\text{CdSe,dopedcrystal}} = n_{\text{voids}}f_{\text{voids}} + (n_{\text{CdSe,sphere}}X_{\text{CdSe,sphere}} + n_{\text{ZnSe,sphere}}X_{\text{ZnSe,sphere}})(1-f_{\text{voids}}) \quad (6.6)$$

where $X_{\text{CdSe,sphere}}=0.95$ and 0.80 for the crystals doped with 5% and 20% ZnSe, respectively ($X_{\text{ZnSe,sphere}}=0.05$ and 0.20 , respectively). Therefore, equations 5 and 6 yield $n = 1.51$, 1.51 and 1.53 for CdSe, CdSe doped with 5% ZnSe, and CdSe doped with 20% ZnSe, respectively. The band positions calculated from the Bragg equation are 956, 959 and 971 nm, respectively. These results indicate that there is a red-shift of 15 nm for the peak position when the crystal was doped with 20% ZnSe hollow spheres. These values

are in reasonable agreement with our experimental results, in which a 20 nm shift was detected.

In addition to the red-shift of peak position, the spectra showed a gradual decrease in peak intensity as the concentration of ZnSe dopants was increased. This result can be attributed to an increased number of diffusive scattering sites introduced as optical defects in the opaline lattice as the concentration of ZnSe hollow spheres was increased.¹²

6.2.4. Synthesis of Superparamagnetic Colloidal Spheres of Fe₃O₄/*a*-Se, (Fe₃O₄/Se)@Ag₂Se, and (Fe₃O₄/Se)@CdSe

Cation-exchange can also be combined with other procedures to synthesize colloidal spheres with superparamagnetic features.²⁴ This can be achieved by incorporating Fe₃O₄ superparamagnetic nanoparticles into the *a*-Se spheres during their synthesis. The *a*-Se spheres can then be converted into Ag₂Se, and further into CdSe by cation-exchange. Figure 6.8 shows a schematic of the synthesis. The success of this approach is built upon the ability to control the encapsulation of Fe₃O₄ nanoparticles into the *a*-Se spheres versus the pure deposition of *a*-Se by regulating the reaction temperature relative to the T_g (32 °C) of selenium.²⁴

In the first step, hydrazine, selenious acid, and the Fe₃O₄ nanoparticles were added to EG and kept at -10 °C. At this temperature, the reduction rate was very slow, enabling the Fe₃O₄ nanoparticles to act as exotic nuclei for *a*-Se growth. At this point, the product was mainly Se-coated Fe₃O₄ nanoparticles. In the next step, the temperature was raised to 43 °C and held for 7 min. At this point, the surface of *a*-Se spheres were

softened as a result of the glass transition temperature of selenium ($T_g = 32\text{ }^\circ\text{C}$), allowing the incorporation of Fe_3O_4 nanoparticles into the growing a -Se spheres. Moreover, the increased reduction rate and growth allows further encapsulation of Fe_3O_4 nanoparticles into the a -Se spheres in this step. Finally, the temperature was decreased to $20\text{ }^\circ\text{C}$ (below the T_g) in order to harden the surface of a -Se spheres, slow their growth, and avoid further encapsulation of Fe_3O_4 nanoparticles. This two-step procedure yields $\text{Fe}_3\text{O}_4/a$ -Se colloidal spheres. In the next step, $\text{Fe}_3\text{O}_4/a$ -Se serves as the starting material to react with AgNO_3 in EG to generate $(\text{Fe}_3\text{O}_4/\text{Se})@\text{Ag}_2\text{Se}$ in the same manner as discussed and described for Se and $\text{Se}@\text{Ag}_2\text{Se}$ spheres. Additionally, as shown in Figure 6.8, $(\text{Fe}_3\text{O}_4/\text{Se})@\text{Ag}_2\text{Se}$ can be further cation-exchanged with Cd^{2+} to produce superparamagnetic $(\text{Fe}_3\text{O}_4/\text{Se})@\text{CdSe}$ spheres.

Figure 6.9, A-C, shows SEM and TEM (inset) images of $\text{Fe}_3\text{O}_4/a$ -Se, $(\text{Fe}_3\text{O}_4/\text{Se})@\text{Ag}_2\text{Se}$, and $(\text{Fe}_3\text{O}_4/\text{Se})@\text{CdSe}$ spheres, respectively. All samples show monodispersity in size, spherical shape, and smooth surface. The size of the $\text{Fe}_3\text{O}_4/a$ -Se spheres shown in Figure 6.9A was $214\pm 3.1\text{ nm}$. After reacting with AgNO_3 , the size increased to $228\pm 3.5\text{ nm}$ for $(\text{Fe}_3\text{O}_4/\text{Se})@\text{Ag}_2\text{Se}$. Finally, after cation-exchange, the size of $(\text{Fe}_3\text{O}_4/\text{Se})@\text{CdSe}$ spheres became $220\pm 4.5\text{ nm}$. The shell thickness, as revealed by the TEM images, was 30 and 26 nm for these colloidal spheres, respectively.

The formation of $(\text{Fe}_3\text{O}_4/\text{Se})@\text{Ag}_2\text{Se}$ and $(\text{Fe}_3\text{O}_4/\text{Se})@\text{CdSe}$ were also confirmed by XRD and EDX analyses. The results are similar to those reported for $\text{Se}@\text{Ag}_2\text{Se}$ and $\text{Se}@\text{CdSe}$. However, no iron signal was detected in these measurements. This is because the concentration of encapsulated Fe_3O_4 nanoparticles was not high enough to give rise to

any diffraction peaks on XRD and/or bands on EDX spectra assigned to Fe_3O_4 . It is important to note that, in the presence of Fe_3O_4 , the $\text{Ag}^+ \rightarrow \text{Cd}^{2+}$ cation exchange was performed with a larger amount of TBP and at room temperature. In this case, the decrease in the reaction temperature was compensated by the increase of TBP. When the reaction was carried out at 50°C with a normal amount of TBP, the colloidal spheres collapsed, instead of maintaining the spherical shape. This result indicates that some of the Fe_3O_4 nanoparticles had been incorporated into the Ag_2Se shells. It is probable that this small amount of Fe_3O_4 nanoparticles acted as impurities, causing the shells to collapse at 50°C during the cation-exchange process.

Figure 6.9D shows optical microscopy images of the $(\text{Fe}_3\text{O}_4/\text{Se})@\text{CdSe}$ spheres. It can be seen that the spheres were randomly oriented when no magnetic field was applied. The inset shows parallel alignment of the spheres with respect to an external magnetic field. This result indicates that the superparamagnetic spheres could be effectively manipulated under an external magnetic field. In order to further characterize the magnetic properties, magnetization was measured for the $(\text{Fe}_3\text{O}_4/\text{Se})@\text{Ag}_2\text{Se}$ and $(\text{Fe}_3\text{O}_4/\text{Se})@\text{CdSe}$ colloids. Figure 6.10 shows the typical M-H curves recorded at room temperature for both $(\text{Fe}_3\text{O}_4/\text{Se})@\text{Ag}_2\text{Se}$ and $(\text{Fe}_3\text{O}_4/\text{Se})@\text{CdSe}$. The variation of M as a function of H is characteristic of a superparamagnetic behavior. The saturation magnetization was found to be 0.18 and 0.12 emu/g for $(\text{Fe}_3\text{O}_4/\text{Se})@\text{CdSe}$ and $(\text{Fe}_3\text{O}_4/\text{Se})@\text{Ag}_2\text{Se}$, respectively. This difference can be attributed to the difference in density and molar mass between CdSe (5.67 g/cm^3 , 191.37 g/mol) and Ag_2Se (8.25 g/cm^3 , 294.7 g/mol).

6.3. Summary

I have demonstrated the use of cation-exchange as a generic and effective approach to core-shell colloidal spheres characterized by the same size but a variety of compositions and properties. This work focused on the synthesis of Se@MSe (M=Zn, Cd, Pb) via the cation-exchange between the Ag⁺ in Se@Ag₂Se and the M²⁺ in solution. All the products showed monodispersity in size, spherical shape, and smooth surface. In these systems, the large difference in solubility makes the reaction Ag₂Se → MSe non-spontaneous at room temperature. As a result, the cation replacement relied on the use of both TBP and elevation of temperature. Our results show that a topotactic relationship between the anion sublattices was not a prerequisite for cation-replacement, since both ZnSe and PbSe do not show topotactic relationship with respect to Ag₂Se. As a result, it is feasible to use cation-exchange reactions to significantly expand the scope of II-IV semiconductors that can be synthesized as colloidal spheres with sizes >100 nm. These colloids can be employed as building blocks for 3D photonic crystals. In this context, I have crystallized colloidal spheres having the same size but different compositions and refractive indices, i.e., CdSe hollow spheres and its mixtures with ZnSe hollow spheres prepared by selectively removing their *a*-Se cores with hydrazine. A gradual attenuation in the stop band was observed with increasing ZnSe concentration. Furthermore, a shift of 20 nm in the peak position was detected when the concentration of ZnSe in the mixture reached 20%. Finally, superparamagnetic feature has been successfully introduced into these colloidal spheres by incorporating Fe₃O₄ nanoparticles into the *a*-Se cores. This method provides a simple and versatile approach to the synthesis of magnetoactive

spheres with a variety of compositions and the same size, which are potentially useful as building blocks to fabricate photonic crystals that can be addressed using an external magnetic field.

6.4. Experimental Section

Chemicals and Materials. Selenious acid (H_2SeO_3 , 99.999%), hydrazine monohydrate ($\text{N}_2\text{H}_4\cdot\text{H}_2\text{O}$, 98%), poly(vinyl pyrrolidone) (PVP, M.W.=55,000), silver nitrate (AgNO_3 , 99.9%), cadmium nitrate tetrahydrate ($\text{Cd}(\text{NO}_3)_2\cdot 4\text{H}_2\text{O}$, 98%), lead nitrate ($\text{Pb}(\text{NO}_3)_2$, 99+%), zinc nitrate hexahydrate ($\text{Zn}(\text{NO}_3)_2\cdot 6\text{H}_2\text{O}$, 98%), tributylphosphine ($\text{C}_{12}\text{H}_{27}\text{P}$ or TBP, 97%) were purchased from Aldrich. Magnetite nanoparticles (Fe_3O_4 , EMG 308 ferrofluid) were obtained from Ferrotec Corporation (Nashua, NH). Ethylene glycol ($\text{HOCH}_2\text{CH}_2\text{OH}$, EG, 99.9%) and methanol (CH_3OH , 99.8%) were obtained from Fluka and EMD, respectively. All chemicals were used as received.

Synthesis of Monodispersed Amorphous Se (*a*-Se) Colloidal Spheres. In a typical procedure, a solution of hydrazine hydrate in EG (20 mL, 0.7 M) was added to 80 mL of pure EG in a 250-mL round bottom flask. The temperature was maintained between 15 and 20 °C using a water bath. After 10 min under magnetic stirring, 20 mL of selenious acid solution (0.07 M, in EG) was introduced and the reaction was allowed to proceed for 1 h.

Synthesis of Se@Ag₂Se Core-Shell Colloidal Spheres. A solution containing 2.4 g of PVP in 80 mL of EG was added to the above *a*-Se suspension. After complete

removal of hydrazine via vacuum distillation, a AgNO_3 solution (0.1 g in 1.5 mL EG) was added dropwise in 10 min, leading to a color change from light red to dark brown. The reaction was allowed to proceed for 2 h. 210 mL of water was then added to the mixture and the core-shell particles were centrifuged and washed four times with water to remove EG and excess PVP. Finally, the product was dried by evaporation under ambient conditions.

Synthesis of Se@MSe (M=Zn, Cd, Pb) Core-Shell Colloidal Spheres by Cation-Exchange Reactions. The $\text{Se}@Ag_2\text{Se}$ spheres produced above (0.25 g) were washed three times with methanol and re-dispersed in 100 mL of methanol to be used for the cation-exchange reactions. For the synthesis of $\text{Se}@M\text{Se}$ spheres, either 5 mL (for Zn) or 10 mL (for both Cd and Pb) of the $\text{Se}@Ag_2\text{Se}$ suspension in methanol was added to a 80-mL round bottom flask containing 35 mL of methanol and 0.6 g of PVP. After 5 min magnetic stirring, $\text{Zn}(\text{NO}_3)_2 \cdot 6\text{H}_2\text{O}$, $\text{Cd}(\text{NO}_3)_2 \cdot 4\text{H}_2\text{O}$, or $\text{Pb}(\text{NO}_3)_2$ pre-dissolved either in a 1:1 water/methanol mixture (for both Zn and Cd) or water (for Pb) was added (0.85, 1.00, and 1.05 g in 5 mL, respectively). The reaction was performed at 60 °C for Zn and Pb and at 50 °C for Cd in an oil bath. When 50 μL of TBP was introduced dropwise, the color of the reaction mixture changed to dark yellow (for Zn) or to brown (for Cd), in 10 min. For Pb, the reaction mixture changed to dark grey instantaneously. 20 min later, another 5 mL of the $\text{Zn}(\text{NO}_3)_2 \cdot 6\text{H}_2\text{O}$, $\text{Cd}(\text{NO}_3)_2 \cdot 4\text{H}_2\text{O}$, or $\text{Pb}(\text{NO}_3)_2$ solution was added. The reaction was allowed to proceed for another 2 h in the case of Zn and Cd and for 4 h in the case of Pb. The solids were centrifuged and washed three times with methanol.

Synthesis of Monodispersed Fe_3O_4/a -Se Colloidal Spheres. In a typical procedure, 80 mL of EG, 20 mL of a hydrazine hydrate solution in EG (0.7 M) and 4 mL of a magnetite suspension in EG (0.5 mL of iron oxide nanoparticles dispersed in 40 mL EG) were placed into a 250-mL round bottom flask held at -10 °C. 20 mL of H_2SeO_3 (0.7 M, in EG) was added to the reaction mixture. The color turned to light orange in 6 min and deep orange after 10 min. After 20 min at -10 °C, the temperature was increased to 43 °C. The reaction mixture was kept at this temperature for 7 min. Then, the temperature was reduced to 20 °C to slow down the growth of a -Se and harden its surface. The reaction was allowed to proceed for another 30 min until the reaction mixture became orange red.

Synthesis of Monodispersed $(Fe_3O_4/Se)@Ag_2Se$ Core-Shell Colloidal Spheres. A solution containing 2.4 g of PVP in 80 mL of EG was added to the above Fe_3O_4/a -Se suspension. All following steps for the preparation of $(Fe_3O_4/Se)@Ag_2Se$ were the same as those described for the synthesis of $Se@Ag_2Se$ spheres.

Synthesis of $(Fe_3O_4/Se)@CdSe$ Core-Shell Colloidal Spheres via Cation Exchange. All the steps for the synthesis of $(Fe_3O_4/Se)@CdSe$ spheres via cation-exchange from $(Fe_3O_4/Se)@Ag_2Se$ were similar to those described for the synthesis of $Se@CdSe$ spheres from $Se@Ag_2Se$ except two variations in the experimental procedure: the reaction was performed at room temperature and the volume of TBP was 500 μ L.

Instrumentation. Scanning electron microscopy (SEM) images were captured using a field-emission microscope (Sirion XL, FEI, Hillsboro, OR) operated at an acceleration voltage of 5 kV. The samples were directly imaged without coating their

surfaces with conductive layers. Energy-dispersive X-ray spectroscopy (EDX, Genesis 2000, Mahwah, NJ) was performed at an acceleration voltage of 10 kV. Transmission electron microscopy (TEM) images were obtained using a JEOL JEM 1200 EX II microscope operated at 120 kV. X-ray diffraction (XRD) was performed on Philips PW-1710 diffractometer with a resolution of 0.02° in 2θ . The magnetic measurements were performed at room temperature using a SQUID Magnetometer MPMS-5S (Quantum Design, San Diego, CA). The applied field ranged from -10000 to +15000 Oe. The near-IR reflection spectra were recorded using a fiber optic spectrometer (NIR-128, Control Development, South Bend, IN) with an incident/detection angle of 10° from the normal to the surface.

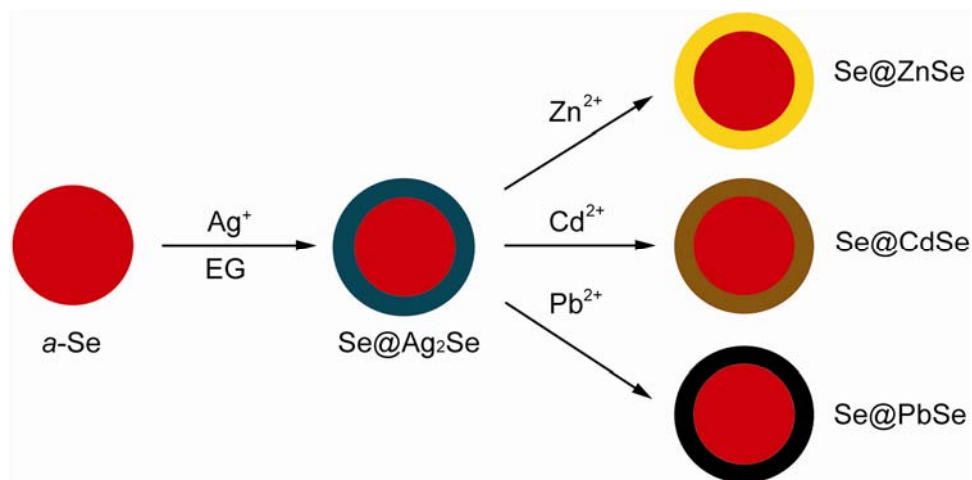


Figure 6.1. Schematic showing the synthesis of core-shell colloidal spheres of $\text{Se@Ag}_2\text{Se}$ by reacting *a*-Se with Ag; and the synthesis of Se@ZnSe , Se@CdSe and Se@PbSe via cation-exchange reactions.

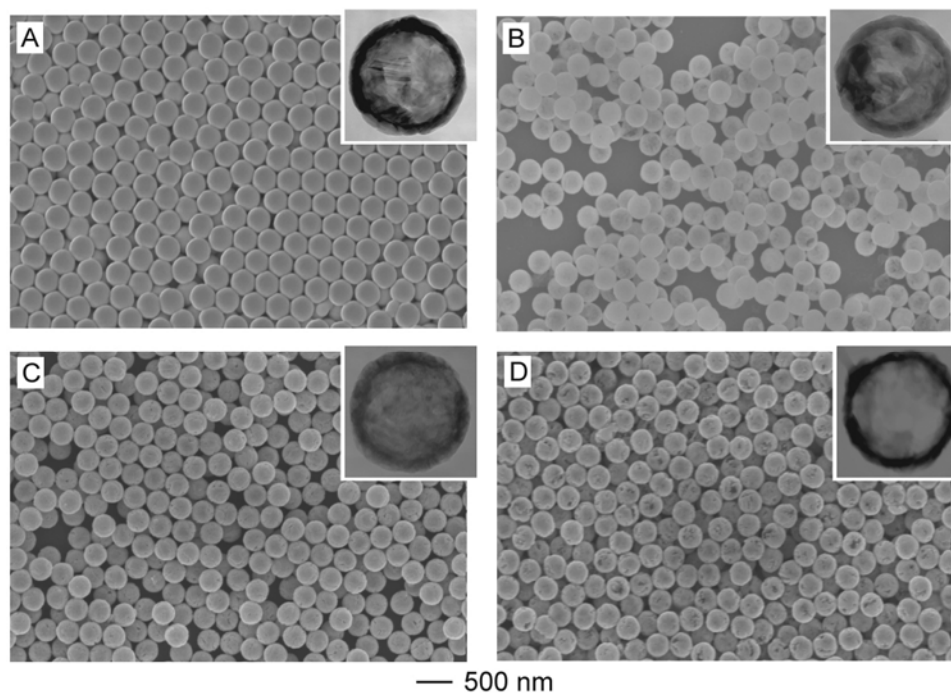


Figure 6.2. SEM images of (A) Se@Ag₂Se; (B) Se@ZnSe; (C) Se@CdSe; and (D) Se@PbSe colloidal spheres. The insets show TEM images of the corresponding sample after the *a*-Se cores had been removed with hydrazine. The outer diameter of the sphere in the inset was 325, 315, 315, and 315 nm, respectively.

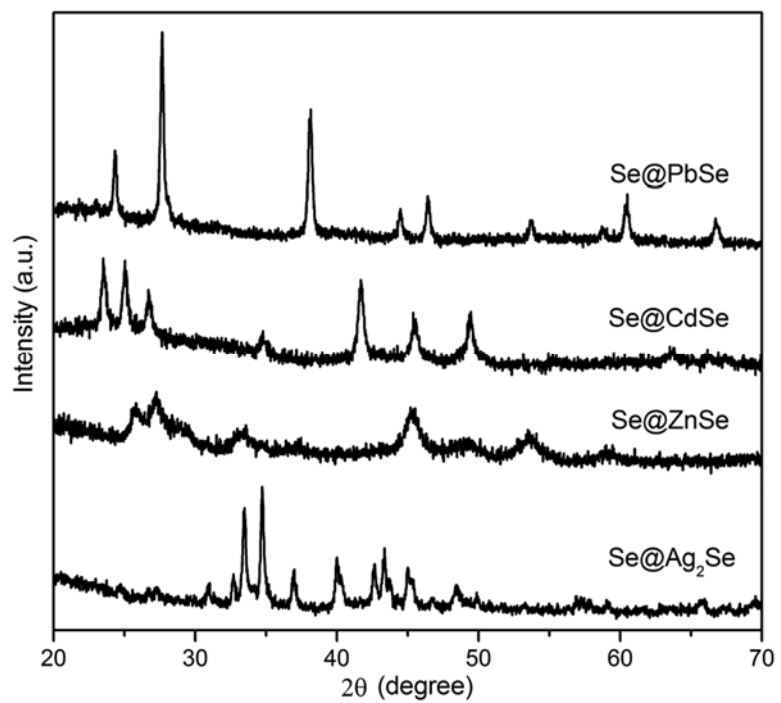


Figure 6.3. XRD patterns taken from the as-synthesized samples of Se@Ag₂Se, Se@ZnSe, Se@CdSe, and Se@PbSe colloidal spheres.

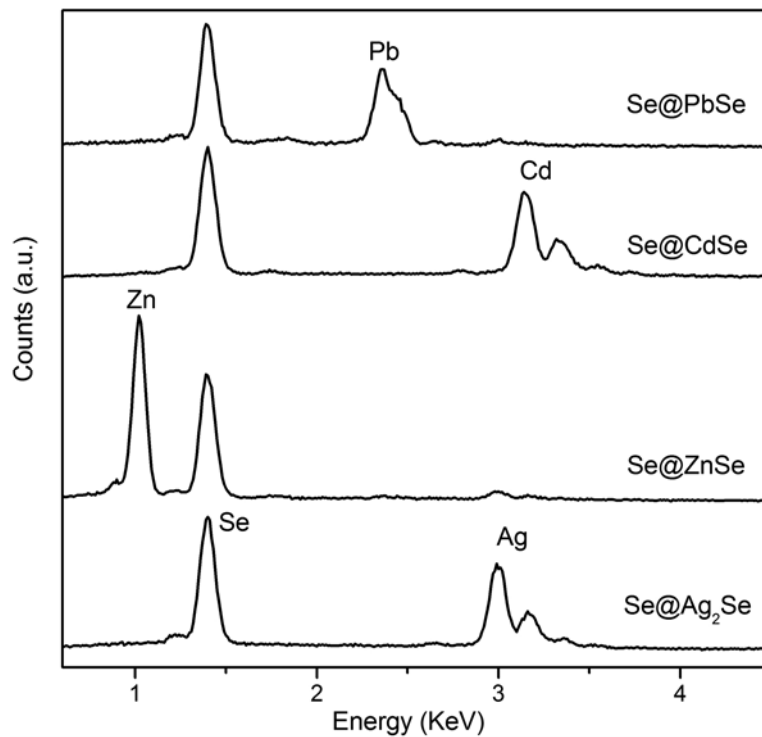


Figure 6.4. EDX spectra recorded from the as-synthesized samples of Se@Ag₂Se, Se@ZnSe, Se@CdSe, and Se@PbSe colloidal spheres.

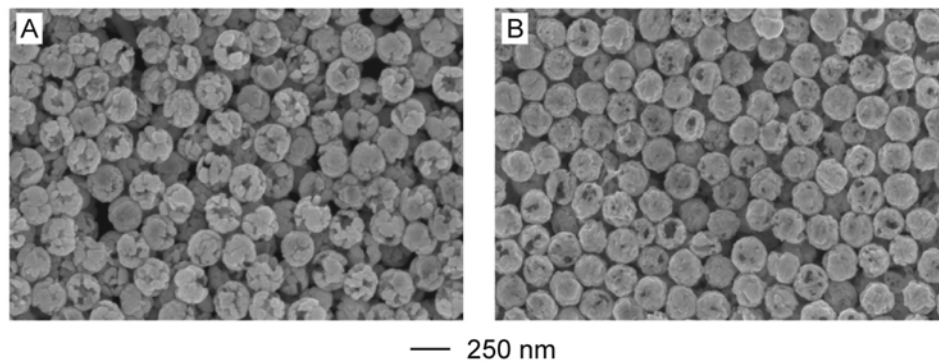


Figure 6.5. SEM images of (A) Se@CdSe and (B) Se@PbSe colloidal spheres prepared via cation-exchange with Se@Ag₂Se at 70 °C.

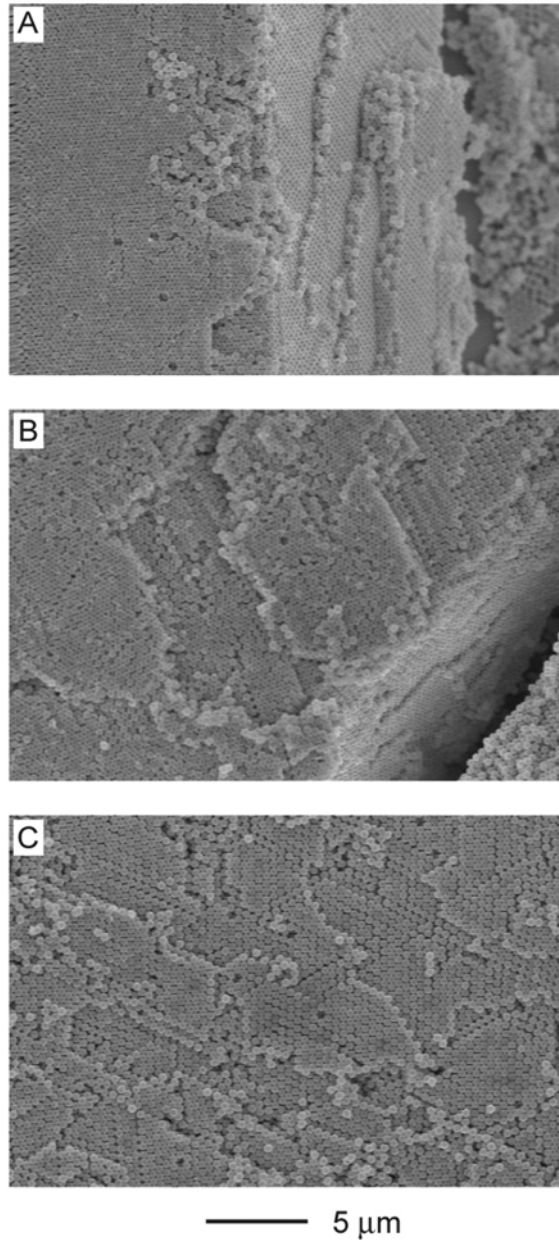


Figure 6.6. SEM images of colloidal crystals assembled from hollow spheres of 390 nm in outer diameter and 35 nm in shell thickness: (A) CdSe hollow spheres; (B) CdSe hollow spheres doped with 5% ZnSe hollow spheres; and (C) CdSe hollow spheres doped with 20% ZnSe hollow spheres.

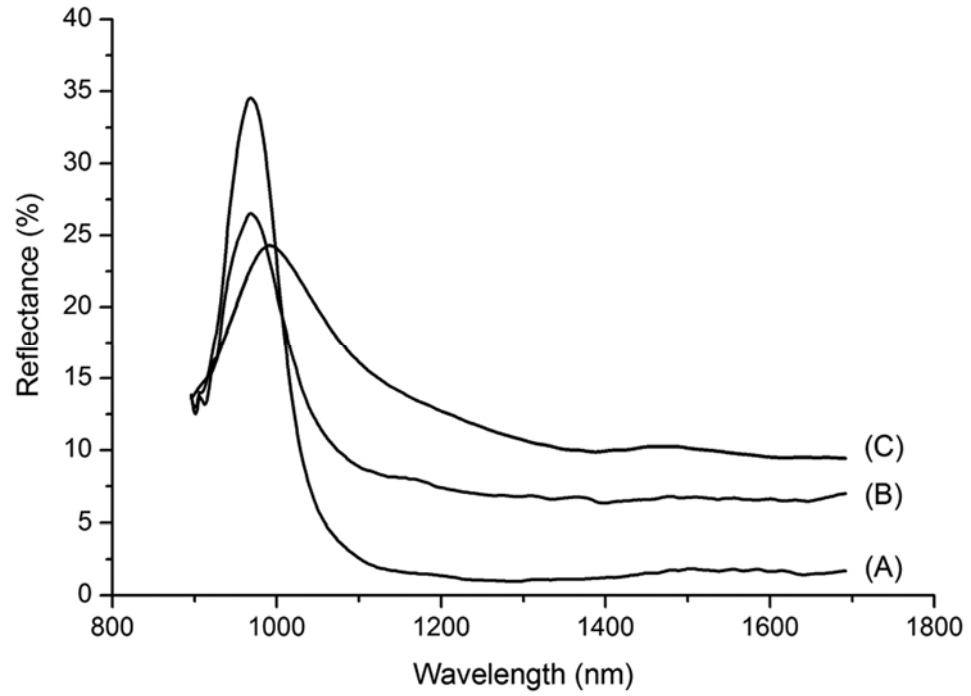


Figure 6.7. Near-IR reflectance spectra taken from the colloidal crystals shown in Figure 5: (A) CdSe hollow spheres; (B) CdSe hollow spheres doped with 5% ZnSe hollow spheres; and (C) CdSe hollow spheres doped with 20% ZnSe hollow spheres.

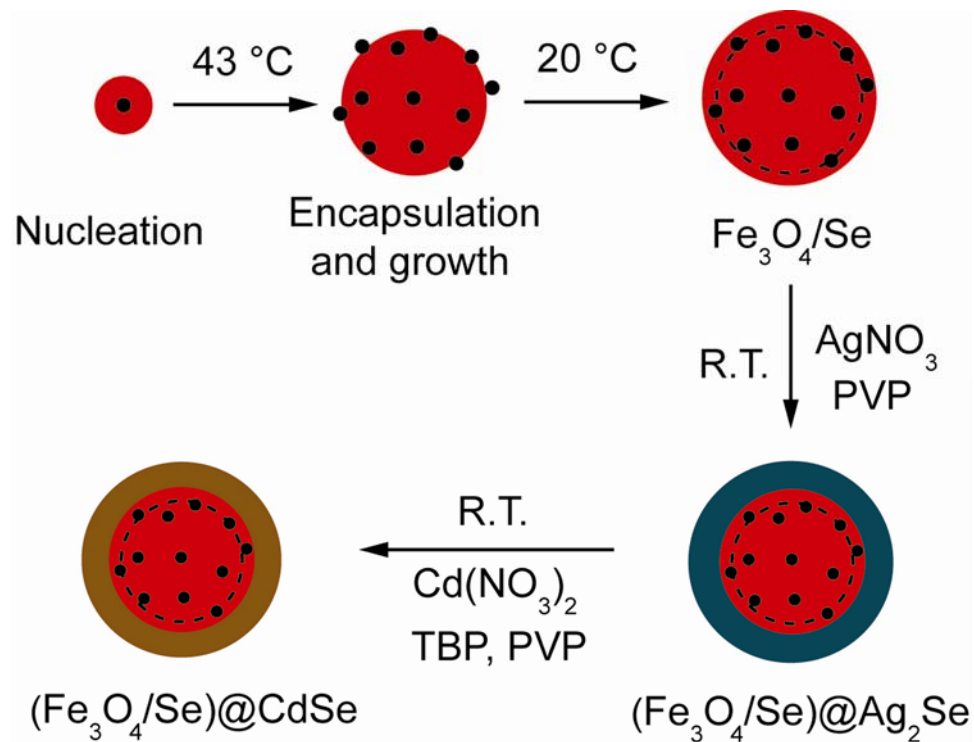


Figure 6.8. Schematic illustrating the synthesis of $(\text{Fe}_3\text{O}_4/\text{Se})@\text{Ag}_2\text{Se}$ and $(\text{Fe}_3\text{O}_4/\text{Se})@\text{CdSe}$ core-shell colloidal spheres with the superparamagnetic feature.

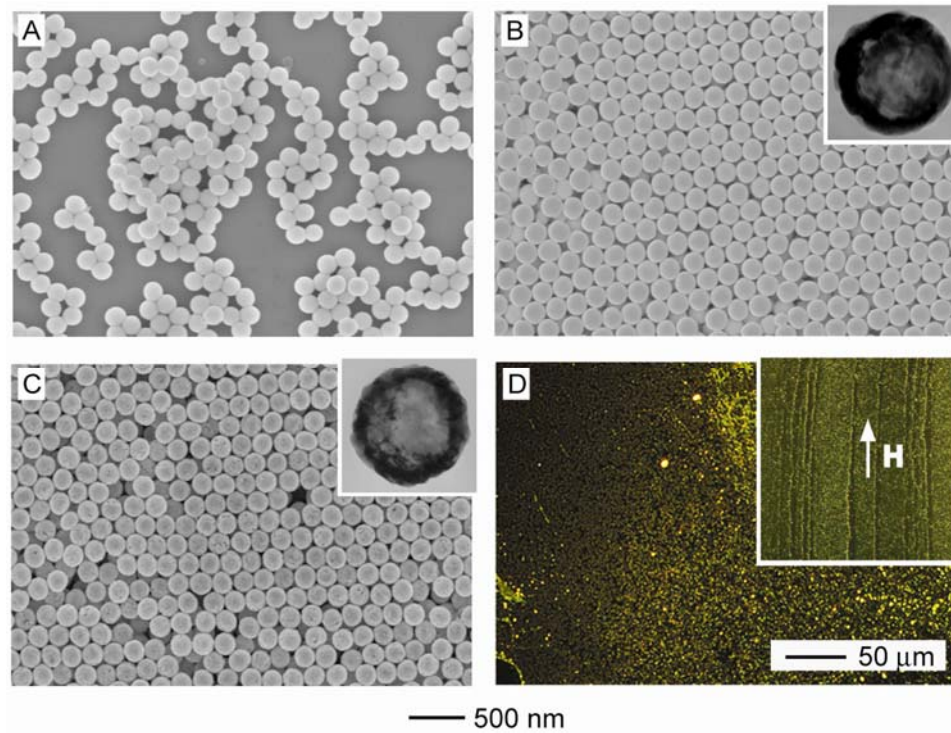


Figure 6.9. SEM and TEM (insets) images of (A) $\text{Fe}_3\text{O}_4/\text{Se}$; (B) $(\text{Fe}_3\text{O}_4/\text{Se})@\text{Ag}_2\text{Se}$; and (C) $(\text{Fe}_3\text{O}_4/\text{Se})@\text{CdSe}$. The diameter of the particle in the inset was 228 and 220 nm, respectively. The *a*-Se cores had been selectively removed before TEM imaging. (D) Optical micrograph of $(\text{Fe}_3\text{O}_4/\text{Se})@\text{CdSe}$ colloidal spheres, which were randomly distributed on a glass slide when no magnetic field was applied. The inset shows magnetic alignment of these colloidal spheres after an external field was applied. The sample was prepared by slowly evaporating a drop of the suspension under a magnetic field.

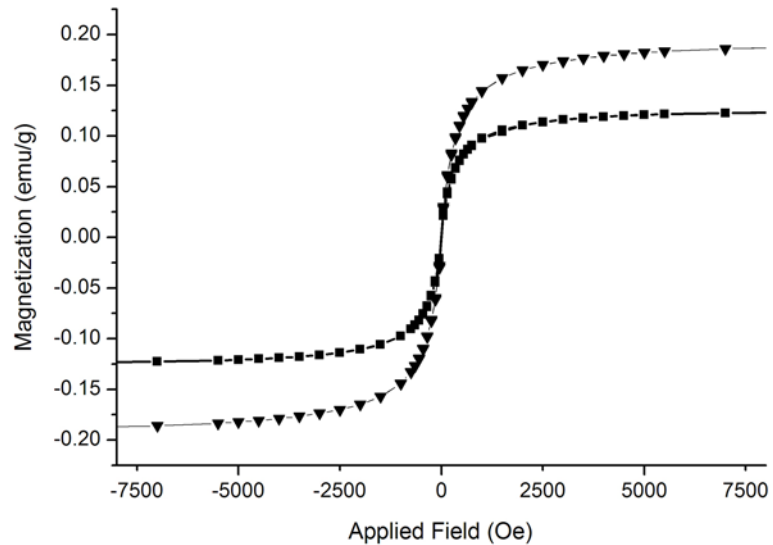


Figure 6.10. Magnetization curves measured at room temperature for both $(\text{Fe}_3\text{O}_4/\text{Se})@Ag_2\text{Se}$ (■) and $(\text{Fe}_3\text{O}_4/\text{Se})@CdSe$ (▼) colloidal spheres.

6.5. Notes to Chapter 6

- [1] Russel, W. B.; Saville, D. A.; Schowalter, W. R. *Colloidal Dispersions*; in Cambridge Monographs on Mechanics, Cambridge University Press: New York, 1989.
- [2] Recent reviews: (a) López, C. *Adv. Mater.* **2003**, *15*, 1679. (b) Xia, Y.; Gates, B.; Yin, Y. D.; Lu, Y. *Adv. Mater.* **2000**, *12*, 693. (c) Velev, O. D.; Lenhoff, A. M. *Curr. Opin. Colloid Interface Sci.* **2000**, *5*, 56. (d) Stein, A.; Schroden, R. C. *Curr. Opin. Solid State Mater. Sci.* **2001**, *5*, 553. (e) Braun, P. V.; Rinne, S. A.; Garcia-Santamaría, F. *Adv. Mater.* **2006**, *18*, 2665.
- [3] (a) Brown, E. R.; McMahon, O. B. *Appl. Phys. Lett.* **1995**, *67*, 2138. (b) McCalmont, J. S.; Sigalas, M. M.; Tuttle, G.; Ho, K. M.; Soukolis, C. M. *Appl. Phys. Lett.* **1996**, *68*, 2759. (c) Gupta, S.; Tuttle, G.; Sigalas, M.; Ho, K. M. *Appl. Phys. Lett.* **1997**, *71*, 2412. (d) McIntosh, K. A.; Mahoney, L. J.; Molvar, K. M.; McMahon, O. B.; Verghese, S.; Rothschild, M.; Brown, E. R. *Appl. Phys. Lett.* **1997**, *70*, 2937.
- [4] Bhargava, R. *Properties of Wide Bandgap II-IV Semiconductors*, in EMIS data Reviews Series No. 17, INSPEC/Institution of Electrical engineers, London 1997.
- [5] (a) Xia, Y.; Yang, P. *Special Issue on One-Dimensional Nanostructures, Adv. Mater.* **2003**, *15*, 353. (b) Yin, Y.; Alivisatos, A. P. *Nature* **2005**, *437*, 664.
- [6] (a) Murray, C. B.; Norris, D. J.; Bawendi, M. G. *J. Am. Chem. Soc.* **1993**, *115*, 8706. (b) Alivisatos, A. P. *Science* **1996**, *271*, 933. (c) Peng, X. G.; Manna, L.; Yang W.; Wickham, J.; Scher, E.; Kadavanich, A.; Alivisatos, A. P. *Nature*, **2000**,

- 404, 59. (d) Jun, Y. W.; Lee, S. M.; Kang, N. J.; Cheon, J. *J. Am. Chem. Soc.* **2001**, *123*, 5150. (e) Zhao, N.; Pan, D.; Nie, W.; Ji, X. *J. Am. Chem. Soc.* **2006**, *128*, 10118. (f) Wang, X.; Zhuang, J.; Peng, Q.; Li, Y. *Langmuir* **2006**, *22*, 7364.
- [7] (a) Matijevic, E.; Murphy-Wilhelmy, D. *J. Colloid Interface Sci.* **1982**, *86*, 476. (b) Murphy-Wilhelmy, D. J.; Matijevic, E. *J. Chem Soc. Faraday Trans.* **1984**, *80*, 563. (c) Velikov, K. P.; Van Blaaderen, A. *Langmuir* **2001**, *17*, 4779. (d) Breen, M. L.; Dinsmore, A. D.; Pink, R. H.; Qadri, S. B.; Ratna, B. R. *Langmuir* **2001**, *17*, 903.
- [8] (a) Jeong, U.; Xia, Y. *Adv. Mater.* **2005**, *17*, 102. (b) Jeong, U.; Xia, Y. *Angew. Chem. Int. Ed.* **2005**, *44*, 3099. (c) Jeong, U.; Kim, J.-U.; Xia, Y. *Nano Lett.* **2005**, *5*, 937. (d) Jiang, X.; Herricks, T.; Xia, Y. *Adv. Mater.* **2003**, *15*, 1205. (e) Wang, Y.; Xia, Y. *Nano Lett.* **2004**, *4*, 2047. (f) Wang, Y.; Cai, L.; Xia, Y. *Adv. Mater.* **2005**, *17*, 473. (g) Jeong, U.; Wang, Y.; Ibisate, M.; Xia, Y. *Adv. Funct. Mater.* **2005**, *15*, 1907.
- [9] Pradhan, R. D.; Tarhan, I. I.; Watson, G. H. *Phys. Rev. B* **1996**, *54*, 13721.
- [10] Vlasov, Y. A.; Astratov, V. N.; Baryshev, A. V.; Kaplyanskii, A. A.; Karimov, O. Z.; Limonov, M. F. *Phys. Rev. E* **2000**, *61*, 5784.
- [11] Gates, B.; Xia, Y. *Appl. Phys. Lett.* **2001**, *78*, 3178.
- [12] Lee, W.; Pruzinsky, S. A.; Braun, P. V. *Adv. Mater.* **2002**, *14*, 271.
- [13] (a) Cheetham, A. K.; Day, P. *Solid State Chemistry: Techniques*; Clarendon Press: Oxford, U.K., 1987. (b) Rao, C. N. R.; Gopalakrishnan, J. *New Directions in Solid State Chemistry*; Cambridge University Press: Cambridge, U.K., 1997.

- [14] (a) Krustok, J.; Madasson, J.; Altosaar, M.; Kukk, P. E. *J. Phys. Chem. Solids* **1990**, *51*, 1013. (b) Lokhande, C. D.; Bhad, V. V.; Dhumure, S. S. *J. Phys.* **1992**, *25*, 315. (c) Lokhande, C. D.; Gadave, K. M. *Mater. Chem. Phys.* **1993**, *36*, 119. (d) Ristova, M.; Ristov, M. *Appl. Surf. Sci.* **2001**, *181*, 68.
- [15] (a) Dloczik, L.; Engelhardt, R.; Ernst, K.; Fiechter, S.; Sieber, I.; Könenkamp, R. *Appl. Phys. Lett.* **2001**, *78*, 3687. (b) Dloczik, L.; Könenkamp, R. *Nano Lett.* **2003**, *3*, 651.
- [16] Lubeck, C. R.; Han, T. Y.-J.; Gash, A. E.; Satcher, Jr., J. H.; Doyle, F. M. *Adv. Mater.* **2006**, *18*, 781.
- [17] Son, D. H.; Hughes, S. M.; Yin, Y.; Alivisatos, A. P. *Science* **2004**, *306*, 1009.
- [18] Steigerwald, M. L.; Brus, L. E. *Annu. Rev. Mater. Sci.* **1989**, *19*, 471.
- [19] Harman, T. C.; Taylor, P. J.; Walsh, M. P.; LaForge, B. E. *Science* **2002**, *297*, 2229.
- [20] Hankare, P. P.; Bhuse, V. M.; Garadkar, K. M.; Delekar, S. D.; Mulla, I. S. *Mater. Chem. Phys.* **2003**, *82*, 711.
- [21] (a) Park, S. H.; Qin, D.; Xia, Y. *Adv. Mater.* **1998**, *10*, 1028. (b) Lu, Y.; Yin, Y.; Gates, B.; Xia, Y. *Langmuir* **2001**, *17*, 6344.
- [22] Park, S. H.; Xia, Y. *Langmuir* **1999**, *15*, 266.
- [23] Takeda, H.; Yoshino, K. *Appl. Phys. Lett.* **2002**, *80*, 4495.
- [24] Jeong, U.; Herricks, T.; Shahar, E.; Xia, Y. *J. Am. Chem. Soc.* **2005**, *127*, 1098.

Bibliography

- Albrecht, M. G.; Creighton, J. A. *J. Am. Chem. Soc.* **1977**, *99*, 5215.
- Alivisatos, A. P. *Science* **1996**, *271*, 933.
- Alonso-Vante, N. *Fuel Cells* **2006**, *6*, 182.
- Alonso-Vante, N.; Jaegermann, W.; Tributsch, H.; Honle, W.; Yvon, K. *J. Am. Chem. Soc.* **1987**, *109*, 3251.
- Alonso-Vante, N.; Bogdanoff, P.; Tributsch, H. *J. Catal.* **2000**, *190*, 240.
- Alonso-Vante, N.; Tributsch, H. *Nature* **1986**, *323*, 431.
- Aricò, A. S.; Bruce, P.; Scrosati, B.; Tarascon, J. M.; Van Schalkwijk, W. *Nature Mater.* **2005**, *4*, 366.
- Aricò, A. S.; Srinivasan, S.; Antonucci, V. *Fuel Cells*, **2001**, *2*, 133.
- B. C. H. Steele and A. Heinzl, *Nature*, 2001, **414**, 345.
- Baranton, S.; Coutanceau, C.; Roux, C.; Hahn, F.; Leger, J. -M. *J. Electroanal. Chem.* **2005**, *577*, 223.
- Bard A. J.; Faulkner, L. R. *Electrochemical Methods Fundamentals and Application*, 2nd ed.; John Wiley & Sons: New York, 2001.
- Bauer, E.; van der Merwe, J. H.; *Phys. Rev. B* **1986**, *33*, 3657.
- Bhargava, R. *Properties of Wide Bandgap II-IV Semiconductors*, in EMIS data Reviews Series No. 17, INSPEC/Institution of Electrical engineers, London 1997.
- Bhushan, B. (ed.), *Springer Handbook of Nanotechnology*, Springer, Verlag Berlin Heidelberg **2004**.
- Boisselier, E.; Astruc, D. *Chem. Soc. Rev.* **2009**, *38*, 1759.
- Brandl, D. W.; Oubre, C.; Nordlander, P. *J. Chem. Phys.* **2005**, *123*, 024701.
- Braun, P. V.; Rinne, S. A.; Garcia-Santamaría, F. *Adv. Mater.* **2006**, *18*, 2665.

- Breen, M. L.; Dinsmore, A. D.; Pink, R. H.; Qadri, S. B.; Ratna, B. R. *Langmuir* **2001**, *17*, 903.
- Brown, E. R.; McMahon, O. B. *Appl. Phys. Lett.* **1995**, *67*, 2138.
- Camargo, P. H. C.; Cobley, C. M.; Rycenga, M.; Xia, Y. *Nanotechnology* **2009**, in press
- Camargo, P. H. C.; Li, Z. -Y.; Xia, Y. *Soft Matter*, **2007**, *3*, 1215.
- Camargo, P. H. C.; Rycenga M, Au L and Xia Y 2009 *Angew. Chem. Int. Ed.* **48**, 2180.
- Camargo, P. H. C.; Xiong, Y.; Ji, L.; Zuo, J. M.; Xia, Y. *J. Am. Chem. Soc.* **2007**, *129*, 15452.
- Camden, J. P.; Dieringer, J. A.; Wang, Y.; Masiello, D. J.; Marks, L. D.; Schatz, G. C.; Van Duyne, R. P. *J. Am. Chem. Soc.* **2008**, *130*, 12616.
- Campion, A.; Kambhampati, P. *Chem. Soc. Rev.* **1998**, *27*, 241.
- Cao, D.; Wieckowski, A.; Inukai, J.; Alonso-Vante, N. *J. Electrochem Soc.* **2006**, *153*, A869.
- Cao, G. *Nanostructures & Nanomaterials*, Imperial College Press, London **2004**
- Chambers, S. A.; *Surf. Sci. Rep.* **2000**, *39*, 105.
- Cheetham, A. K.; Day, P. *Solid State Chemistry: Techniques*; Clarendon Press: Oxford, U.K., 1987.
- Chen J.; Wiley, B.; Xia, Y. *Langmuir* **2007**, *23*, 4120.
- Chen, G.; Xia, D.; Nie, Z.; Wang, Z.; Wang, L.; Zhang, L.; Zhang J. *Chem. Mater.* **2007**, *19*, 1840.
- Chen, J.; McLellan, J. M.; Siekkinen, A.; Xiong, Y.; Li, Z.-Y.; Xia, Y. *J. Am. Chem. Soc.* **2006**, *128*, 14776.
- Chen, J.; McLellan, J. M.; Siekkinen, A.; Xiong, Y.; Li, Z.-Y.; Xia, Y. *J. Am. Chem. Soc.* **2006**, *128*, 14776.
- Chen, J.; Wiley, B. J.; Xia, Y. *Langmuir* **2007**, *23*, 4120.

- Chen, J.; Wiley, B.; McLellan, J.; Xiong, Y.; Li, Z.-Y.; Xia, Y. *Nano Lett.* **2005**, *5*, 2058.
- Chen, M.; Kumar, D.; Yi, C.-W.; Goodman, D. W. *Science* **2005**, *310*, 291.
- Chen, W.; Kim, J.; Sun, S.; Chen, S. *J. Phys. Chem. C* **2008**, *112*, 3891.
- Chen, Z.; Waje, M.; Li, W.; Yan, Y. *Angew. Chem. Int. Ed.* **2007**, *46*, 4060.
- Chen, Z.; Waje, M.; Li, Z.; Yan, Y. *Angew. Chem. Int. Ed.* **2007**, *46*, 4060.
- Chizhikov, D. M.; Shchastlivyi, V. P. *Selenium and Selenides* (E.M. Elkin, Trans.), Collet's LTD, London and Wellingborough, 1968.
- Cho, S. H.; Han, H. S.; Jang, D. -J.; Kim, K.; Kim, M. S. *J. Phys. Chem.* **1995**, *99*, 10594.
- Cobley, C. M.; Campbell, D. J.; Xia, Sun, Y. *Adv. Mater.* **2008**, *20*, 748.
- Colmenares, L.; Jusys, Z.; Behm, R. J. *J. Phys. Chem. C* **2007**, *111*, 1273.
- Colmenares, L.; Jusys, Z.; Behm, R. J. *Langmuir* **2006**, *22*, 10437.
- Dagata, J. A. *Science* **1995**, *270*, 1625.
- Dloczik, L.; Engelhardt, R.; Ernst, K.; Fiechter, S.; Sieber, I.; Könenkamp, R. *Appl. Phys. Lett.* **2001**, *78*, 3687.
- Dloczik, L.; Könenkamp, R. *Nano Lett.* **2003**, *3*, 651.
- Dmitriev, A.; Hägglund, C.; Chen, S.; Fredriksson, H.; Pakizeh, T.; Käll M.; Sutherland, D. S. *Nano Lett.* **2008**, *8*, 3893.
- Doering, W. E.; Nie, S. *J. Phys. Chem. B* **2002**, *106*, 311.
- Dresselhaus, M. S.; Thomas, I. L. *Nature* **2001**, *414*, 332.
- Dunn, P. N. *Solid State Technology* **1994**, *June*, 49.
- Enache, D. A.; Edwards, J. K.; Landon, P.; Solsona-Espriu, B.; Carley, A. F.; Herzing, A. A.; Watanabe, M.; Kiely, C. J.; Knight, D. W.; Hutchings, G. J. *Science*, **2006**, *311*, 362.
- Ertl, G. *Handbook of Heterogeneous Catalysis*, Wiley-VCH: Weinheim, 2008.

- Etchegoin, P. G.; Le Ru, E. C. *Phys. Chem. Chem. Phys.* **2008**, *10*, 6079.
- Etchegoin, P. G.; Le Ru, E. C.; Meyer, M. *J. Am. Chem. Soc.* **2009**, *131*, 2713.
- Fan, F. -R.; Liu, D. -Y.; Wu, Y. -F.; Duan, S.; Xie, Z. -X.; Jiang Z. -Y.; Tian, Z. -Q. *J. Am. Chem. Soc.* **2008**, *130*, 6949.
- Ferreira, P. J.; la O', G. J.; Shao-Horn, Y.; Morgan, D.; Makharia, R.; Kocha, S.; Gasteiger, H. A. *J. Electrochem. Soc.* **2005**, *152*, A2256.
- Ferrer, D.; Torres-Castro, A.; Gao, X.; Sepúlveda-Guzmán, S.; Ortiz-Méndez, U.; José-Yacamán, M. *Nano Lett.* **2007**, *7*, 1701.
- Ferry, D. K. *Science* **2008**, *319*, 579.
- Fiechter, S.; Dorbandt, I.; Bogdanoff, P.; Zehl, G.; Schulenburg, H.; Tributsch, H.; Bron, M.; Radnik, J.; Fieber-Erdmann, M. *J. Phys. Chem. C* **2007**, *111*, 477.
- Fleming, J. G.; Lin, S. Y.; El-Kady, I.; Biswas, R.; Ho, K. M. *Nature* **2002**, *417*, 52.
- Formo, E.; Peng, Z.; Lee, E.; Lu, X.; Yang, H.; Xia, Y. *J. Phys. Chem. C* **2008**, *112*, 9970.
- Gao, J. H.; Liang, G. L.; Zhang, B.; Kuang, Y.; Zhang, X. X.; Xu, B. *J. Am. Chem. Soc.* **2007**, *129*, 1428.
- Gao, J. H.; Zhang, B.; Gao, Y.; Pan, Y.; Zhang, X. X.; Xu, B. *J. Am. Chem. Soc.* **2007**, *129*, 11928.
- Garcia-Vidal, F. J.; Pendry, J. B. *Phys. Rev. Lett.* 1996, *77*, 1163.
- Gasteiger, H. A.; Kocha, S. S.; Sompalli, B.; Wagner, F. T. *Appl. Catal. B* **2005**, *56*, 9.
- Gates, B. D.; Xu, Q.; Stewart, M.; Ryan, D.; Willson, C. G.; Whitesides, G. M. *Chem. Rev.* **2005**, *105*, 1171.
- Gates, B.; Mayers, B.; Grossman, A.; Xia, Y. *Adv. Mater.* **2002**, *14*, 1749.
- Gates, B.; Xia, Y. *Appl. Phys. Lett.* **2001**, *78*, 3178.
- Gibson, J. M. *Phys. Today* **1997**, *October*, 56.
- Gomez, R.; Orts, J. M.; Alvarez-Ruiz, B. L.; Feliu, J. *J. Phys. Chem. B* **2004**, *108*, 228.

- Gonzales-Huerta, R. G.; Chavez-Carvayar, R. G.; Solorza-Feria, O. *J. Power Sources* **2006**, *153*, 11.
- Greeley J.; Mavrikakis, M. *Nat. Mater.* **2004**, *3*, 810.
- Gui, J. Y.; Stern, D. A.; Frank, D. G.; Lu, F.; Zapien, D. C.; Hubbard, A. T. *Langmuir* **1991**, *7*, 955.
- Guo, S.; Dong, S.; Wang, E. *Chem. Eur. J.* **2008**, *14*, 4689.
- Guo, S.; Fang, Y.; Dong, S.; Wang, E. *J. Phys. Chem. C* **2007**, *111*, 17104.
- Gupta, S.; Tuttle, G.; Sigalas, M.; Ho, K. M. *Appl. Phys. Lett.* **1997**, *71*, 2412.
- Hankare, P. P.; Bhuse, V. M.; Garadkar, K. M.; Delekar, S. D.; Mulla, I. S. *Mater. Chem. Phys.* **2003**, *82*, 711.
- Hao, E.; Schatz, G. C. *J. Chem. Phys.* **2004**, *120*, 357.
- Harman, T. C.; Taylor, P. J.; Walsh, M. P.; LaForge, B. E. *Science* **2002**, *297*, 2229.
- Haynes, C. L.; McFarland, A. D.; Van Duyne, R. P. *Anal. Chem.* **2005**, *77*, 338A.
- Hong, S. H.; Mirkin, C. A. *Science* **1999**, *286*, 523.
- Huang, X.; Zhang, H.; Guo, C.; Zhou, Z.; Zheng, N. *Angew. Chem. Int. Ed.* **2009**, *48*, 4808.
- Hutchison, J. A.; Centeno, S. P.; Odaka, H.; Fukumura, H.; Hofkens, J.; Uji-i, H. *Nano Lett.* **2009**, *9*, 995.
- Im, S. H.; Lee, Y. T.; Wiley, B.; Xia, Y. *Angew. Chem. Int. Ed.* **2005**, *44*, 2154.
- Inoue, M.; Ohtaka, K. *J. Phys. Soc. Jpn.* **1983**, *52*, 3853.
- Jeanmaire, D. L.; Duyne, R. P. V. *J. Electroanal. Chem.* **1977**, *84*, 1.
- Jeong, D. H.; Zhang, Y. X.; Moskovits, M. *J. Phys. Chem. B* **2004**, *108*, 12724.
- Jeong, U.; Herricks, T.; Shahar, E.; Xia, Y. *J. Am. Chem. Soc.* **2005**, *127*, 1098.
- Jeong, U.; Kim, J.-U.; Xia, Y. *Nano Lett.* **2005**, *5*, 937.
- Jeong, U.; Wang, Y.; Ibisate, M.; Xia, Y. *Adv. Funct. Mater.* **2005**, *15*, 1907.

- Jeong, U.; Xia, Y. *Adv. Mater.* **2005**, *17*, 102.
- Jeong, U.; Xia, Y. *Angew. Chem. Int. Ed.* **2005**, *44*, 3099.
- Jiang, X.; Herricks, T.; Xia, Y. *Adv. Mater.* **2003**, *15*, 1205.
- Jiang, X.; Mayers, B.; Wang, Y.; Cattle, B.; Xia, Y. *Chem. Phys. Lett.* **2004**, *385*, 472.
- Joannopoulos, J. D.; Johnson, S. G.; Winn, J. N.; Meade, R. D. *Photonic Crystals: Molding the Flow of Light*, 2nd edition, Princeton University Press, Princeton, 2008.
- Joo, S. W.; Han, S. W.; Kim, K. *J. Colloid Interface Sci.* **2001**, *240*, 391.
- Jun, Y. W.; Lee, S. M.; Kang, N. J.; Cheon, J. *J. Am. Chem. Soc.* **2001**, *123*, 5150.
- Jusys, Z.; Behn, R. *J. Electrochim. Acta* **2004**, *49*, 3891.
- Kallo, J.; Lehnert, W.; von Helmolt, R. *J. Electrochem. Soc.* **2003**, *150*, A765.
- Kamat, P. V.; *J. Phys. Chem. C* **2008**, *112*, 18737.
- Kelly, K. L.; Coronado, E.; Zhao, L. L.; Schatz, G. C. *J. Phys. Chem. B* **2003**, *107*, 668.
- Khan, M. A.; Hogan, T. P.; Shanker, S. *J. Raman Spectrosc.* **2008**, *39*, 893.
- Kim, M. H.; Lu, X.; Wiley, B.; Lee, E. P.; Xia, Y. *J. Phys. Chem. C* **2008**, *112*, 7872.
- Kneipp, K.; Kneipp, H.; Itzkan, I.; Dasari, R. R.; Feld, M. S. *Chem. Rev.* **1999**, *99*, 2957.
- Kneipp, K.; Kneipp, H.; Kneipp, J. *Acc. Chem. Res.* **2006**, *39*, 443.
- Kneipp, K.; Wang, Y.; Kneipp, H.; Perelman, L. T.; Itzkan, I.; Dasari, R. R.; Feld, M. S. *Phys. Rev. Lett.* **1997**, *78*, 1667.
- Krustok, J.; Madasson, J.; Altosaar, M.; Kukk, P. E. *J. Phys. Chem. Solids* **1990**, *51*, 1013.
- Kwon, S. G.; Hyeo, T. *Acc. Chem. Res.* **2008**, *41*, 1696.
- Le Ru, E. C.; Blackie, E.; Meyer, M.; Etchegoin, P. G. *J. Phys. Chem. C* **2007**, *111*, 13794.
- Le Ru, E. C.; Etchegoin, P. G.; Meyer, M. *J. Phys. Chem.* **2006**, *125*, 104701.

- Le Ru, E. C.; Meyer, M.; Blackie, E.; Etchegoin, P. G. *J. Raman Spectrosc.* **2008**, *39*, 1127.
- Lee, J.-W.; Popov, B. N. *J. Solid State Electrochem.* **2007**, *11*, 1355.
- Lee, S. J.; Baik, J. M.; Moskovits, M. *Nano Lett.* **2008**, *8*, 3244.
- Lee, W.; Pruzinsky, S. A.; Braun, P. V. *Adv. Mater.* **2002**, *14*, 271.
- Lefevre, M.; Dodelet, J. P.; P. Bertrand, *J. Phys. Chem. B* **2002**, *106*, 8705
- Levenson, D. V. *Solid State Technology*, **1995**, *September*, 81.
- Li, W.; Camargo, P. H. C.; Au, L.; Zhang, Q.; Xia, Y. *Adv. Mater.* **2009**, in press.
- Li, W.; Camargo, P. H. C.; Lu, X.; Xia, Y. *Nano Lett.* **2009**, *9*, 485.
- Liang, H. -P.; Zhang, H. -M.; Hu, J. -S.; Guo, Y. -G.; Wan, L. -G.; Bai, C. -L. *Angew. Chem. Int. Ed.* **2004**, *43*, 1540
- Lim, B.; Jiang, M.; Camargo, P. H. C.; Cho, E. C.; Tao, J.; Lu, X.; Zhu, Y.; Xia, Y. *Science* **2009**, *324*, 1302
- Lim, B.; Jiang, M.; Tao, J.; Camargo, P. H. C.; Zhu, Y.; Xia, Y. *Adv. Funct. Mater.* **2009**, *19*, 189.
- Lim, B.; Jiang, M.; Tao, J.; Camargo, P. H. C.; Zhu, Y.; Xia, Y. *Adv. Funct. Mater.* **2009**, *19*, 189.
- Lim, B.; Lu, X.; Jiang, M.; Camargo, P. H. C.; Cho, E. C.; Lee, E. P.; Xia, Y. *Nano Lett.* **2008**, *8*, 4043.
- Lim, B.; Wang, J.; Camargo, P. H. C.; Jiang, M.; Kim, M. J.; Xia, Y. *Nano Lett.* **2008**, *8*, 2535.
- Lim, B.; Xiong, Y.; Xia, Y. *Angew. Chem. Int. Ed.* **2007**, *46*, 9279.
- Lim, B.; Xiong, Y.; Xia, Y. *Angew. Chem. Int. Ed.* **2007**, *46*, 9279.
- Liu, G.; Zhang, H.; Hu, J. *Electrochem. Comm.* **2007**, *9*, 2643.
- Liu, H.; Song, C.; Zhang, L.; Zhang, J.; Wang, H.; Wilkinson, D. P. *J. Power Sources* **2006**, *155*, 95.
- Liu, L.; Kim, H.; Lee, J. W.; Popov, B. N. *J. Electrochem. Soc.* **2007**, *154*, A123.

- Lokhande, C. D.; Bhad, V. V.; Dhumure, S. S. *J. Phys.* **1992**, *25*, 315.
- Lokhande, C. D.; Gadave, K. M. *Mater. Chem. Phys.* **1993**, *36*, 119.
- López, C. *Adv. Mater.*, 2003, **15**, 1679
- Lu, X.; Chen, J.; Skrabalak, S. E.; Xia, Y. *Proc. IMechE Part N: J. Nanoengineering and Nanosystems* **2008**, *221*, 1
- Lu, X.; Rycenga, M.; Skrabalak, S. E.; Wiley, B. and Xia, Y. *Ann. Rev. of Phys. Chem.* **2009**, *60*, 167.
- Lu, X.; Tuan, H.-Y.; Chen, J.; Li, Z.-Y.; Korgel, B. A. and Xia, Y. *J. Am. Chem. Soc.* **2007**, *129*, 1733.
- Lu, Y.; Yin, Y.; Gates, B.; Xia, Y. *Langmuir* **2001**, *17*, 6344.
- Lubeck, C. R.; Han, T. Y.-J.; Gash, A. E.; Satcher, Jr., J. H.; Doyle, F. M. *Adv. Mater.* **2006**, *18*, 781.
- Lucas, C. A.; Marković, N. M.; Ross, P. N. *Phys. Rev. B* **1997**, *55*, 7964.
- Macilwain, C. *Nature* **2006**, *441*, 1046.
- Mahmoud, M. A.; Tabor, C. E.; El-Sayed, M. A.; Ding, Y.; Wang, Z. L. *J. Am. Chem. Soc.* **2008**, *130*, 4590.
- Maksimuk, S.; Yang, S. C.; Peng, Z. M.; Yang, H. *J. Am. Chem. Soc.* **2007**, *129*, 8694.
- Malinsky, M. D.; Kelly, K. L.; Schatz, G. C.; Van Duyne, R. P. *J. Phys. Chem. B* **2001**, *105*, 2343.
- Mallouk, T. E. *Nature* **1990**, *343*, 515.
- Marković, N. M.; Adzic, R. R.; Cahan, B. D.; Yeager, E. B. *J. Electroanal. Chem.* **1994**, *377*, 249.
- Marković, N. M.; Gasteiger, H.; Ross, P. N. *J. Electrochem. Soc.* **1997**, *144*, 1591.
- Marković, N. M.; Ross, P. N. *Surf. Sci. Rep.* **2002**, *45*, 117.
- Marković, N. M.; Schmidt, T. J.; Stamenković, V.; Ross, P. N. *Fuel Cells* **2001**, *1*, 105.
- Matijevic, E.; Murphy-Wilhelmy, D. *J. Colloid Interface Sci.* **1982**, *86*, 476

- Matsui, S.; Ochiachi, Y. *Nanotechnology* **1996**, *7*, 247.
- Matter, P. H.; Zhang, L.; Ozkan, U. S. *J. Catal.* **2006**, *239*, 83.
- Mayers, B.; Liu, K.; Sunderland, D.; Xia, Y. *Chem. Mater.* **2003**, *20*, 3852.
- McCalmont, J. S.; Sigalas, M. M.; Tuttle, G.; Ho, K. M.; Soukolis, C. M. *Appl. Phys. Lett.* **1996**, *68*, 2759.
- McCreery, R. L. *Modern Techniques in Raman Spectroscopy*, ed. J. J. Laserna, John Wiley & Sons, Chichester-NY, Brisbane-Toronto-Singapore, **1996**.
- McFarland, A. D.; Young, M. A.; Dieringer, J. A.; Van Duyne, R. P. *J. Phys. Chem. B* **2005**, *109*, 11279.
- McIntosh, K. A.; Mahoney, L. J.; Molvar, K. M.; McMahan, O. B.; Verghese, S.; Rothschild, M.; Brown, E. R. *Appl. Phys. Lett.* **1997**, *70*, 2937.
- McLellan, J. M.; Li, Z. -Y.; Siekkinen, A. R.; Xia, Y. *Nano Lett.* **2007**, *7*, 1013.
- McLellan, J. M.; Siekkinen, A.; Chen, J.; Xia, Y. *Chem. Phys. Lett.* **2006**, *427*, 122.
- Mohanty, P.; Yoon, I.; Kang, T.; Seo, K.; Varadwaj, K. S. K.; Choi, W.; Park, Q. -H.; Ahn, J. P.; Suh, Y. D.; Ihee, H.; Kim, B. *J. Am. Chem. Soc.* **2007**, *129*, 9576.
- Mokari, T.; Sztrum, C. G.; Salant, A.; Rabani, E. and Banin, U. *Nature Mater.* **2005**, *4*, 855.
- Mukerjee, S.; Srinivasan, S. *J. Electroanal. Chem.* **1993**, *357*, 201.
- Mukerjee, S.; Srinivasan, S.; Soriaga, M. P.; McBreen, J. *J. Electrochem. Soc.* **1995**, *142*, 1409.
- Murphy-Wilhelmy, D. J.; Matijevic, E. *J. Chem Soc. Faraday Trans.* **1984**, *80*, 563.
- Murray, C. B.; Norris, D. J.; Bawendi, M. G. *J. Am. Chem. Soc.* **1993**, *115*, 8706.
- Muthu, M. S.; Singh, S. *Nanomedicine* **2009**, *4*, 105.
- Natan, N. J. *Faraday Discuss.* **2006**, *132*, 321.
- Newman, R. C.; Sieradzki, K. *Science* **1994**, *263*, 1708.
- Nie, S.; Emory, S. R. *Science* **1997**, *275*, 1102.

- Nishihata, Y.; Mizuki, J.; Akao, T.; Tanaka, H.; Uenishi, M.; Kimura, M.; Okamoto, T.; Hamada, N. *Nature* **2002**, *418*, 164.
- Noda, S.; Imada, M.; Okano, M.; Ogawa, S.; Mochizuki, M.; Chutinan, A. *IEEE J. Quantum Electron.* **2002**, *38*, 726.
- Odom, T. M.; Pileni, M. –P. *Acc. Chem. Res.* **2008**, *41*, 1565.
- Olk, P.; Renger, J.; Härtling, T.; Wenzel, M. T.; Eng, L. M. *Nano Lett.* **2007**, *7*, 1736.
- Osawa, M.; Matsuda, N.; Yoshii, K.; Uchida, I. *J. Phys. Chem.* **1994**, *98*, 12702.
- Otto, A. *J. Raman Spectrosc.* **2006**, *37*, 937.
- Park, S. H.; Qin, D.; Xia, Y. *Adv. Mater.* **1998**, *10*, 1028.
- Park, S. H.; Xia, Y. *Langmuir* **1999**, *15*, 266.
- Paulus, U. A.; Schmidt, T. J.; Gasteiger, H. A.; Behm, R. J. *J. Electroanal. Chem.* **2001**, *495*, 134.
- Peng, X. G.; Manna, L.; Yang W.; Wickham, J.; Scher, E.; Kadavanich, A.; Alivisatos, A. P. *Nature*, **2000**, *404*, 59.
- Peng, Z.; Yang, S. *Nano Today* **2009**, *4*, 143.
- Perry, M. L.; Fuller, T. F. *J. Electrochem. Soc.* **2002**, *149*, S59.
- Pieczonka, N. P. W.; Aroca, R. F. *Chem. Soc. Rev.* **2008**, *37*, 946.
- Pinchuk, A.; Hilger, A.; von Plessen, G. Kreibig, U. *Nanotechnology* **2004**, *15*, 1890.
- Pradhan, R. D.; Tarhan, I. I.; Watson, G. H. *Phys. Rev. B* **1996**, *54*, 13721.
- Raman, C. V.; Krishnan, K. S. *Nature* **1928**, *121*, 501.
- Rao, C. N. R.; Gopalakrishnan, J. *New Directions in Solid State Chemistry*; Cambridge University Press: Cambridge, U.K., 1997.
- Redmond, P. L.; Hallock, A. J. and Brus, L. E. *Nano Lett.* **2005**, *5*, 131.
- Riehemann, K.; Schneider, S. W.; Thomas, A. L.; Godin, B.; Ferrari, M.; Fuchs, H. *Angew. Chem. Int. Ed.* **2009**, *48*, 872.

- Ristova, M.; Ristov, M. *Appl. Surf. Sci.* **2001**, *181*, 68.
- Rozas, R.; Kraska, T. *J. Phys. Chem. C* **2007**, *111*, 15784.
- Russel, W. B.; Saville, D. A.; Schowalter, W. R. *Colloidal Dispersions*; in Cambridge Monographs on Mechanics, Cambridge University Press: New York, 1989
- Rycenga, M.; Kim, M. H.; Camargo, P. H. C.; Cobley, C.; Li, Z. -Y.; Xia, Y. *J. Phys. Chem. A*, **2009**, *113*, 3932.
- Sauer, G.; Brehm, G.; Schneider, S. *J. Raman Spectrosc.* **2004**, *35*, 568.
- Saunders, A. E.; Popov, I. and Banin U. *J. Phys. Chem. B* **2006**, *110*, 25421
- Sawai, K.; Suzuki, N. *J. Electrochem. Soc.* **2004**, *151*, A682.
- Schatz, G. C.; Van Duyne, R. P. In *Handbook of Vibrational Spectroscopy*, Eds. Chalmers, J. M.; Griffiths, P. R. John Wiley & Sons: New York, **2002**.
- Schmidt, T. J.; Gasteiger, H. A.; Stäb, G. D.; Urban, P. M.; Kolb, D. M.; Behm, R. J. *J. Electrochem. Soc.* **1998**, *145*, 2354.
- Schmidt, T. J.; Gasteiger, H. A.; Stäb, G. D.; Urban, P. M.; Kolb, D. M.; Behm, R. J. *J. Electrochem. Soc.* **1998**, *145*, 2354.
- Schulenburg, H.; Hilgendorff, M.; Dorbandt, I.; Radnik, J.; Bogdanoff, P.; Fiechter, S.; Bron, M.; Tributsch, H. *J. Power Sources* **2006**, *155*, 47.
- Scully, J. C. *The Fundamentals of Corrosion*, 3rd ed.; Pergamon Press: Oxford, New York, 1990; pp 1-57.
- Seo, K.; Borguet, E. *J. Phys. Chem. C* **2007**, *111*, 6335.
- Serov, A. A.; Min, M.; Chai, G.; Han, S.; Kang, S.; Kwak, C. *J. Power Sources* **2008**, *175*, 175.
- Shao, M. H.; Huang, T.; Liu, P.; Zhang, J.; Sasaki, K.; Vukmirovic, M. B.; Adzic, R. R. *Langmuir* **2006**, *22*, 10409.
- Sherry, L. J.; Chang, S. H.; Schatz, G. C.; Van Duyne, R. P.; Wiley, B. J.; Xia, Y. *Nano Lett.* **2005**, *5*, 2034.
- Shukla A. K.; Raman, R. K.; *Annu. Rev. Mater. Res.*, **2003**, *33*, 155.
- Skrabalak, S. E.; Au, L.; Li, X.; Xia, Y. *Nat. Protoc.* **2007**, *2*, 2182.

- Son, D. H.; Hughes, S. M.; Yin, Y.; Alivisatos, A. P. *Science* **2004**, *306*, 1009.
- Stamenkovic, V. R.; Fowler, B.; Mun, S.; Wang, G. F.; Ross, P. N.; Lucas, C. A.; Marković, N. M.; *Science* **2007**, *315*, 493.
- Stamenkovic, V. R.; Mun, B. S.; Mayrhofer, K. J. J.; Ross, P. N.; Markovic, N. M. *Am. Chem. Soc.* **2006**, *128*, 8813.
- Steele, B. C. H.; Heinzl, A. *Nature* **2001**, *414*, 345.
- Steigerwald, M. L.; Brus, L. E. *Annu. Rev. Mater. Sci.* **1989**, *19*, 471.
- Stein, A.; Schroden, R. C. *Curr. Opin. Solid State Mater. Sci.* **2001**, *5*, 553.
- Stewart, M. E.; Anderton, C. R.; Thompson, L. B.; Maria, J.; Gray, S. K.; Rogers, J. A.; Nuzzo, R. G. *Chem. Rev.* **2008**, *108*, 494.
- Stiles, P. L.; Dieringer, J. A.; Shah, N. L.; Van Duyne, R. P. *Annu. Rev. Anal. Chem.* **2008**, *1*, 601.
- Suárez-Alcántara, K.; Rodríguez-Castllano, A.; Dante, R.; Solorza-Feria, O. *J. Power Sources* **2006**, *157*, 114.
- Sun, Y.; Mayers, B. T.; Xia, Y. *Nano Letters* **2002**, *2*, 481.
- Sun, Y.; Mayers, B.; Herricks, T.; Xia, Y. *Nano Lett.* **2003**, *3*, 955.
- Sun, Y.; Mayers, B.; Xia, B. *Adv. Mater.* **2003**, *15*, 641.
- Sun, Y.; Wiley, B.; Li, Z.-Y.; Xia, Y. *J. Am. Chem. Soc.* **2004**, *126*, 9399.
- Sun, Y.; Xia Y. *Science* **2002**, *298*, 2176.
- Sun, Y.; Xia, Y. *Adv. Mater.* **2004**, *16*, 264.
- Sun, Y.; Xia, Y. *J. Am. Chem. Soc.* **2004**, *126*, 3892.
- Sun, Y.; Xia, Y. *Science* **2002**, *298*, 2176.
- Svedberg, F.; Li, Z.; Xu, H.; Käll, M. *Nano Lett.* **2006**, *6*, 2639.
- Takeda, H.; Yoshino, K. *Appl. Phys. Lett.* **2002**, *80*, 4495.
- Talley, C. E.; Jackson, J. B.; Oubre, C.; Grady, N. K.; Hollars, C. W.; Lane, S. M.;

- Huser, T. R.; Nordlander, P.; Halas, N. J. *Nano Lett.* **2005**, *5*, 1569.
- Tao, A. R.; Yang, P. *J. Phys. Chem. B* **2005**, *109*, 15687.
- Tao, A.; Kim, F.; Hess, C.; Goldberger, J.; He, R.; Sun, Y.; Xia, Y.; Yang, P. *Nano Lett.* **2003**, *3*, 1229.
- Tributsch, H.; Bron, M.; Hilgendorff, M.; Schulenburg, H.; Dorbandt, I.; Eyert, V.; Bogdanoff, P.; Fiechter, S. *J. Appl. Electrochem.* **2001**, *31*, 739.
- Trzeciak, A. M.; Ziólkowski, J. J. *Coord. Chem. Rev.* **2007**, *251*, 1281.
- Tsung, C.-K.; Kou, X.; Shi, Q.; Zhang, J.; Yeung, M. H.; Wang, J.; Stucky, G. D. *J. Am. Chem. Soc.* **2006**, *128*, 5352.
- Velev, O. D.; Lenhoff, A. M. *Curr. Opin. Colloid Interface Sci.* **2000**, *5*, 56.
- Velikov, K. P.; Van Blaaderen, A. *Langmuir* **2001**, *17*, 4779.
- Vlasov, A.; O'Boyle, M.; Harmann, H. F.; McNab, S. J. *Nature* **2005**, *438*, 65.
- Vlasov, Y. A.; Astratov, V. N.; Baryshev, A. V.; Kaplyanskii, A. A.; Karimov, O. Z.; Limonov, M. F. *Phys. Rev. E* **2000**, *61*, 5784.
- Wang Y.; Cai L.; Xia Y. *Adv. Mater.* **2005**, *17*, 473.
- Wang, B. *J. Power Sources*, **2005**, *152*, 1.
- Wang, H.; Halas, N. J. *Nano Lett.* **2006**, *6*, 2945.
- Wang, X.; Zhuang, J.; Peng, Q.; Li, Y. *Langmuir* **2006**, *22*, 7364.
- Wang, Y.; Xia, Y. *Nano Lett.* **2004**, *4*, 2047.
- Wasmus, S.; Küver, A. *J. Electroanal. Chem.* **1999**, *461*, 14.
- Wei, H.; Hao, F.; Huang, Y.; Wang, W.; Nordlander, P.; Xu, H. *Nano Lett.* **2008**, *8*, 2497.
- Wetz, F.; Soulantica, K.; Falqui, A.; Respaud, M.; Snoeck, E. and Chaudret B. *Angew. Chem. Int. Ed.* **2007**, *119*, 7209.
- Whitesides, G. M.; Grzybowski, B. *Science* **2002**, *295*, 241.

- Wiley, B. J.; Im, S. H.; Li, Z.-Y.; McLellan, J.; Siekkinen, A.; Xia, Y. *J. Phys. Chem. B* **2006**, *110*, 15666.
- Willems, K. A.; Van Duyne, R. P. *Annu. Rev. Phys. Chem.* **2007**, *58*, 267.
- Winter, M.; Brodd, R. J. *Chem. Rev.* **2004**, *104*, 4245.
- Wu, M. C.; Solgaard, O.; Ford, J. E. *J. Lightw. Technol.* **2006**, *24*, 4433.
- Xia, Y.; Gates, B.; Yin, Y. D.; Lu, Y. *Adv. Mater.* **2000**, *12*, 693.
- Xia, Y.; Rogers, J. A.; Paul, K. E.; Whitesides, G. M. *Chem. Rev.* **1999**, *99*, 1823.
- Xia, Y.; Xiong, Y.; Lim, B.; Skrabalak, S. E. *Angew. Chem. Int. Ed.* **2009**, *48*, 60.
- Xia, Y.; Yang, P. *Special Issue on One-Dimensional Nanostructures, Adv. Mater.* **2003**, *15*, 353.
- Xiang, Y.; Wu, X.; Liu, D.; Jiang, X.; Chu, X.; Li, Z.; Ma, L.; Zhou, W.; Xie, S. *Nano. Lett.* **2006**, *6*, 2290.
- Xiao, L.; Zhuang, L.; Liu, Y.; Abruna, H. D. *J. Am. Chem. Soc.*, **2009**, *131*, 602.
- Xiao, T.; Ye, Q.; Sun, L. *J. Phys. Chem. B* **1997**, *101*, 632.
- Xiong, Y.; Cai, H.; Wiley, B. J.; Wang, J.; Kim, M. J.; Xia, Y. *J. Am. Chem. Soc.* **2007**, *129*, 3665.
- Xiong, Y.; Chen, J.; Wiley, B.; Xia, Y.; Yin, Y.; Li, Z. -Y. *Nano Lett.* **2005**, *5*, 1237.
- Xiong, Y.; McLellan, J. M.; Chen, J.; Yin, Y.; Li, Z. -Y.; Xia, Y. *J. Am. Chem. Soc.* **2005**, *127*, 17118.
- Xiong, Y.; Wiley, B.; Chen, J.; Li, Z. -Y.; Yin, Y.; Xia, Y. *Angew. Chem. Int. Ed.* **2005**, *44*, 7913.
- Xu, Z.; Hou, Y.; Sun, S. *J. Am. Chem. Soc.* **2007**, *129*, 8698.
- Yang, H.; Alonso-Vante, N.; Leger, J. M.; Lamy, C. J. *J. Phys. Chem. B* **2004**, *108*, 1938.
- Yang, H.; Vogel, W.; Lamy, C.; Alonso-Vante, N. *J. Phys. Chem. B* **2004**, *108*, 11024.

Yang, J.; Lee, J. Y.; Zhang, Q.; Zhou, W.; Liu, Z. *J. Electrochem. Soc.* **2008**, *155*, B776.

Yin, Y.; Alivisatos, A. P. *Nature* **2005**, *437*, 664.

Zaikovskii, V. I.; Nagabhushana, K. S.; Kriventsov, V. V.; Loponov, K. N.; Cherepanova, S. V.; Kvon, R. I.; Bolnnemann, H. D.; Kochubey, I.; Savinova, E. R. *J. Phys. Chem. B* **2006**, *110*, 6881.

Zehl, G.; Schmithals, G.; Hoell, A.; Haas, S.; Hartnig, C.; Dorbandt, I.; Bogdanoff, P.; Fiechter, S. *Angew. Chem. Int. Ed.* **2007**, *46*, 7311.

Zeman, E. J.; Schatz, G. C. *J. Phys. Chem.* **1987**, *91*, 634-43.

Zhang, J.; Huang, M.; Ma, H.; Tian, F.; Pan, W.; Chen, S. *Electrochem. Commun.*, **2007**, *9*, 63.

Zhang, J.; Mo, Y.; Vukmirovic, M. B.; Klie, R.; Sasaki, K.; Adzic, R. R. *J. Phys. Chem. B* **2004**, *108*, 10955.

Zhang, J.; Sasaki, K.; Sutter, E.; Adzic, R. R. *Science* **2007**, *315*, 220

Zhang, J.; Vukmirovic, M. B. V.; Xiu, Y.; Mavrikakis, M.; Adzic, R. R. *Angew. Chem. Int. Ed.* **2005**, *44*, 2132.

Zhang, L.; Zhang, J.; Wilkinson, D. P.; Wang, H. *J. Power Sources* **2006**, *156*, 171.

Zhao, N.; Pan, D.; Nie, W.; Ji, X. *J. Am. Chem. Soc.* **2006**, *128*, 10118.

Zhou, S.; McIlwrath, K.; Jackson, G.; Eichhorn, B. *J. Am. Chem. Soc.* **2006**, *128*, 1780.

Zou, S.; Gao, X.; Weaver, M. J. *Surf. Sci.* **2000**, *452*, 44.